Infrared Interferometric Observations of Dust In The Nuclei of Active Galaxies

Infrared Interferometric Observations of Dust In The Nuclei of Active Galaxies

Proefschrift

ter verkrijging van
de graad van Doctor aan de Universiteit Leiden,
op gezag van de Rector Magnificus prof. mr. P.F. van der Heijden,
volgens besluit van het College voor Promoties
te verdedigen op dinsdag 24 november 2009
klokke 13.45 uur

door

David Raban

geboren te Israël
in 1976

Promotiecommissie

Promotores: Prof. dr. H. Röttgering
       Dr. W. Jaffe

Overige leden: Prof. dr. K. Meisenheimer (Max-Planck-Institut für Astronomie)
       Prof. dr. K. H. Kuijken
       Prof. dr. M. Elitzur (University of Kentucky)
       Prof. dr. G. Miley
       Prof. dr. F . Israël

Dedicated to my parents Ellen and Erez

Table of contents

Chapter 1

Introduction

1.1 Goals of this thesis

$\mathbf{A}$CTIVE Galactic Nuclei (AGN) are fascinating objects. They emit more energy from an area as small as our solar system to rival the energy output of an entire galaxy. All AGNs are powered by matter accreting into the super-massive black hole at the centre of the galaxy. This much they have in common, and many are the observed differences between the types of AGNs. Some are highly variable, and some stable. Some show the accretion disk, and for some it is obscured, to name but a few of the differences. The number of different types of AGNs depends on one's classification system, but in any case it is more than a handful. Fortunately, there is theory which unites the different properties of AGNs. Known as the 'AGN unification model', or 'standard model', it declares all the observed differences between AGNs in the same class to be an effect caused by looking at the same object but from a different angle. Specifically, in the case of 'radio quiet AGNs' the unification model holds that an obscuring torus-shaped structure of dust surrounds the accretion disk and broad line region. Since the obscuring structure is torus-shaped, and therefore possesses a 'hole', it can be viewed either face-on or side on, thereby hiding or revealing the physical processes which take place on smaller scales. The main goal of this thesis is to verify to what extent this simple model is true, by use of interferometric observations in the mid-infrared which directly probe the obscuring torus. Our main goal is to take advantage of the unprecedented spatial resolution in the infrared which the interferometer offers in order to establish via direct measurements the physical properties of the torus, such as size and temperature, and related these properties to the expectations of the unification models.

1.2 Active Galactic Nuclei

There is now considerable evidence that at the centre of every galaxy resides a super-masssive black hole (SMBH). In most cases, such as the case in our own galaxy, the SMBH is in a quiescent state, i.e. it does not accrete matter, except on occasion.

Accretion onto a compact object such as a black hole is the most efficient way of producing energy known to men, with a mass to energy efficiency factor of $\eta \sim 10\%$ (i.e. $E = \eta mc^2$). When there is a stable stream of matter accreting into the SMBH, the resulting release of energy makes the nucleus very bright, emitting across the electromagnetic spectrum. In those cases, the galaxy is called 'active', and its nucleus is an 'AGN'. Some of the main component of an active nucleus, which are relevant to this
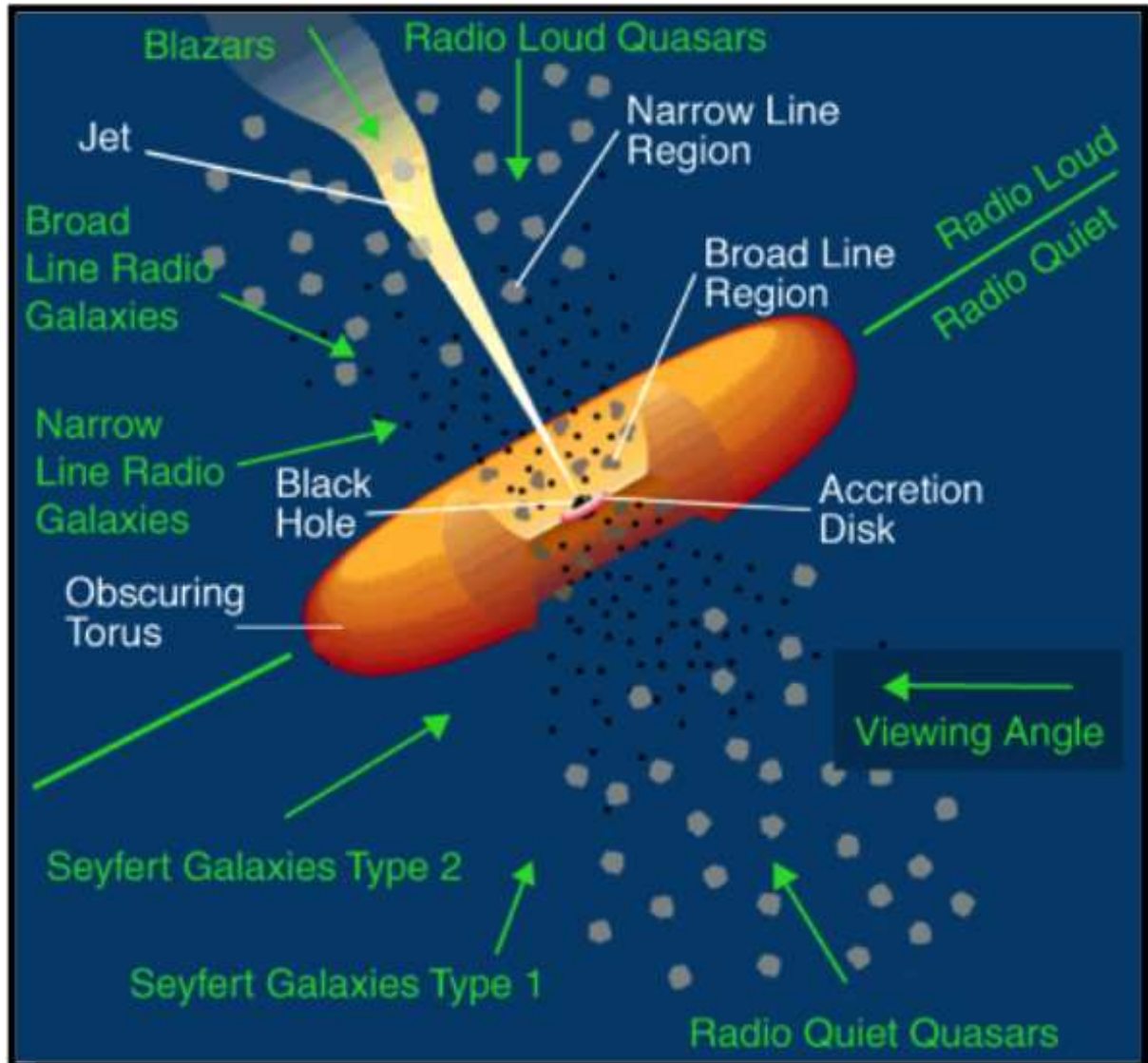
Figure 1.1 — A cartoon showing the main components of an AGN, along with the basic idea behind the unification schemes (Urry & Padovani 1995). The white labels describe the different AGN components. The green labels note some of the different AGN types, and the arrows show how these different types are named differently depending on the observer's line of sight. For example, the differences between Seyfert galaxies type 2 and type 1 are attributed here to viewing the AGN either from the side of the obscuring torus (type 2), or through the opening (type 1). The different types of AGN are discussed in §1.2.5.

work are:

1.2.1   The dusty torus

This component is the main concern of this work. Although it is discussed in more detail in section 1.4, a brief description is needed to put the rest of this section in context.

The dusty torus, also referred to as the 'obscuring' torus, surrounds the central engine and the broad line region. Since is has a 'hole', it allows for the central engine and broad line region to be seen if the hole is viewed face-one (an 'unobscured' AGN), and blocks our view if positioned edge-on. In the standard, simple, picture of an AGN, the properties of the torus, i.e. size, orientation, temperature, etc. are closely coupled to those of the other elements of the AGN (Antonucci & Miller 1985) . Thus, by measuring the properties of the torus, and then comparing them to the predictions of the model, we are able to gain more knowledge on the validity of the standard model.

1.2.2   The central engine

The central engine (CE), also known as the 'accretion disk', is where most of the energy of an AGN is produced. When visible, it appears on the sky as a bright point-soure, as its size is too small to be resolved even by interferometers. The accretion disk emits light across the entire spectrum, from radio to X-rays. In the context of this work, the accretion disk does not play an important role, since emission from thermal dust dominates the mid-infrared, where we observe. The most common use we make here of the accretion disk is to use its luminosity in order to estimate the expected inner radius of the dusty structure which surrounds it. Other circumstances which required us to examine emission from the CE are when the object is variable (the CE being the main source of variability), or when debating whether a bright unresolved source we (or others) have observed is in fact the accretion disk, or compact emission from hot thermal dust.

1.2.3   Broad and narrow lines regions

All AGNs show narrow emission lines in the optical regime, with line widths < 1200 km/s. In some AGNs broad emission lines are detected as well. The broad lines are broader since the matter emitting them is moving at larger velocities, and hence is situated closer to the black hole. The narrow lines are then emitted from a region further away from the central engine.

It was early discovered that the broad lines are only seen together with the accretion disk (Antonucci 1984), which led to the natural suggestion that both the broad line region and the accretion disk are surrounded by an obscuring structure.

The narrow lines are often found in cone-shaped structure, the 'ionization cone'. The shape of the cone indicates that it is also bounded by a toroidal distribution of obscuring matter (Wilson & Tsvetanov 1994). This structure was termed 'the obscuring torus'.

In this work, we make two uses of the broad and narrow lines, both in chapter 3. First, we compare the shape of the ionization cone in the galaxy NGC 1068 with the
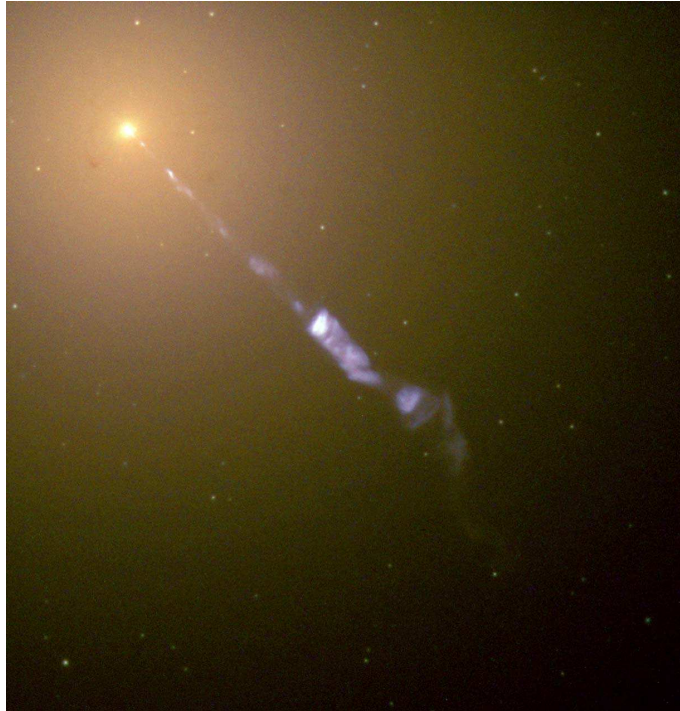
Figure 1.2 — An optical image taken by the *Hubble Space Telescope* of the jet of M87

shape of the dust distribution we observed (i.e. the obscuring torus), as it is a consequence of the above statement that the two structured are related. Second, in NGC 1068 (an obscured galaxy), broad lines were discovered in reflection. Thus, for this specific object we already know that it harbours an un-obscured nucleus, and hence for this object the standard model holds. This knowledge allows us to determine that the dust distribution is inclined mostly edge-one, and its size is therefore and estimation of its thickness.

1.2.4 The Jet

The precise mechanism which produces jets in AGN is not yet established. The current prevailing view (Blandford & Payne 1982) is that magnetic field lines in the inner accretion disk wrap around until they are 'locked' in a double-helix configuration which causes charged particles to accelerate to velocities close to the speed of light. The emission mechanism of jets is synchrotron radiation, which has a power-law spectrum. The emission from the jet is highly beamed, and can therefore appear very bright. There are two main ways in which jets are relevant for this work. The first is that jets also emit in the infrared. In some cases emission from the base of the jet dominates over other emission mechanisms. This is the case in the galaxy Centaurus A, and chapter 7 discusses the spectral properties of the jet at microwave wavelengths. The second is that the orientation of the jet is related (normally perpendicular) to the angular momentum of the inner accretion disk. The accretion disk's angular momentum is related to the angular momentum of the captured (accreting) material. Thus, the orientation of the jet is determined by the sum of the angular momenta of individual accreted

Table 1.1. The main differences between the different AGN types

Type.	Narrow lines	broad lines	X-rays	UV excess	far-IR excess	Radio loud	variable
Seyfert 1	yes	yes	yes	some	yes	no	some
Seyfert 2	yes	no	no	no	yes	no	no
Quasar	yes	yes	yes	yes	yes	no	yes
Blazar	some	no	yes	some	no	some	strong
BL LAC	no	some	yes	yes	no	yes	strong
OVV	some	some	yes	yes	no	yes	strong

material. This orientation may be compared to the orientation of the dusty structure we observe in the infrared. In chapter 3 we show that the position angles of the jet and of the inner part of the dusty torus we observe are not what one would normally expect, i.e. they are not perpendicular. This is a strong hint that this particular AGN had a rather complex accretion history, with the current accreting material possessing a different angular momentum than that of the material captured at earlier times. This would also imply that the accretion disk itself is highly warped. An example of a jet of M87 is shown in Fig.1.2.

1.2.5 AGN Types

The major division between different types of AGNs starts with 'radio loud' AGN vs. 'radio quiet' AGN, the two main AGN classes. In radio loud AGN the most dominant emission source is the jet, while with radio quiet AGNs the jet is relatively weak and the other components of the AGN dominate the emission. The main types of AGN along with a summary of their main properties are listed in Table. 1.1. In the AGN unification models, the differences between the different AGN types (belonging to the same class) comes from the differences in our line of sight to the objects, and are not intrinsic to the objects. Thus, there are two components which break the symmetry of the AGN structure: the obscuring torus, which could be viewed either from the side or through the 'hole'; and the jet, which could be pointed towards the observer (Blazars) , away (Seyferts) , or point directly at the observer's line of sight (optically violent variables, OVVs).

The bulk of this thesis is concerned with radio-quiet AGNs, with the exception of chapter 7 which is concerned with Centaurus A, a radio-loud object. The distinction between Seyfert 1's and Quasars is somewhat arbitrary and is made for historical reasons. Quasars are Seyfert 1 objects that are very luminous, and for that reason they were discovered first and given a particular name. The differences and types of AGNs are further explained in the next section.

1.3 Unification models

When first encountering an unknown, diverse phenomena, the first step to understanding it is classification. Next, an attempt is made to use this classification in order

to get better insight on the physical nature of the phenomena. In the case of AGNs, the classification presented in the previous section form the basis of the unification models (Antonucci 1993). These models attempt to explain the diversity of AGNs by a combination of orientation effects and luminosity effects, i.e. objects are essentially the same, only viewed from different lines-of-sight, and with different luminosities resulting from different accretion rates and black hole masses. Although attempts have been made to attribute *all* the observed differences between AGN types to orientation effects (e.g.Barthel (1989)), these have not proven successful. Most notably, radio-loud and radio-quiet AGNs cannot be united in such a way. As a result, unification models now concentrate on unifying AGNs within the same class. Since this work is mainly concerned with the unification of Seyfert galaxies, which are radio quiet, the rest of the discussion will concentrate on unification of radio quiet AGNs. We already know from direct observations of the existence of a linear, beamed jet in most AGNs. The jet is an obvious source of asymmetry, and the orientation of the jet with respect to the observer's line of sight is naturally expected to affect the properties of the object as we see it. The other source of asymmetry, the obscuring torus, is not as evident as the jet, being much smaller in size. For a considerable time, it was considered putative, since all the evidence in favour of the torus have been indirect (see §1.4.1). The main idea is that there is a torus-shaped structure made of dust, which surrounds the central engine and the broad line region. The 'hole' in the torus is the second source of asymmetry. When viewed edge-on, it hides the central engine and the broad line region, and we name the object a Seyfert 2. When viewed face-on, we see the central object and the broad line region through the 'hole', exposing the central engine and the high energy photons produced there. In this case the AGN would appear as a Seyfert 1. By considering different combinations of the orientation with respect to the jet or the torus, combined with luminosity dependent effects, the differences between radio quiet AGNs are explained.

The unification models are indeed very simple. Despite that, they do remarkably well in explaining the AGN phenomena, in particular the relationship between Seyfert galaxies. The obscuring torus, which lies at the heart of the unification of radio-quiet AGNs, is the subject of the next section.

1.4   The obscuring torus

The obscuring torus in the main subject of this thesis. We now give a more detailed description of the historical background and of the known properties of the torus, including some discussion of its origins and dynamical state.

1.4.1   Indirect Observational evidence

The obscuring torus has a central role in unification models for AGN. However, until recently (Jaffe et al. 2004), no direct evidence (i.e. a direct observation of its toroidal shape) for its existence was available. This is due to the compact (pc-scale) size of the torus, too small to be resolved by even the largest of the single-dish telescopes.

Nevertheless, even without direct observations, there is a considerable body of indirect evidence supporting the existence of the torus. Below is an overview of the most

suggestive discoveries.

1.4.1.1   The infrared bump

Many AGN show an excess in their infrared emission (Barvainis 1987). The infrared spectra of $\sim 60\%$ of all Seyfert galaxies are dominated by thermal 'bumps'. These were interpreted as emission from dust heated by the nucleus. However, these observations could not tell exactly where the dust is located with respect to the nucleus, or what shape the dust structure must have.

1.4.1.2   Spectropolarimetry

Perhaps the most compelling evidence in favour of an obscuring structure comes from spectropolarimetric observations of Seyfert 2 galaxies. These observations showed that the broad lines characteristic of Seyfert 1 galaxies are also seen in the polarised spectrum of the Seyfert 2 galaxy NGC 1068 (Antonucci & Miller 1985). Later, the same was found for other Seyfert 2 galaxies. The discovery of the hidden broad lines has important consequences. It establishes the existence of a hidden Seyfert 1 nucleus inside a Seyfert 2 nucleus, thereby uniting the two type of AGNs. It also places the obscuring material between the narrow line region and the broad line region. Finally, it suggests a thick distribution of the obscuring matter.

1.4.1.3   The Seyfert 1/2 ratio

The discoveries mentioned in the previous sections strongly suggest the existence of a thick (and therefore torus-like) body of dust which occupies the space between the narrow and broad lines regions. The question remains exactly how thick the structure is. Assuming that obscuration is solely responsible for the differences between Seyfert galaxies (as unification models do), the relative number of Seyfert 1's vs. Seyfert 2's would be indicative of the (average) opening angle of the structure. If f_2 is the fraction of type 2 sources, then it is related to the angular width σ of the torus by $f_2 = \sin\sigma$. Schmitt et al. (2001) find that $f_2 \simeq 70\%$, and hence $\sigma \simeq 45$ degrees. In contrast, Hao et al. (2005) find the ratio to be 50%, hence $\sigma \simeq 30$ degrees. In any case, the torus is thick.

1.4.1.4   The conical shape of the ionisation cones

Cones of ionised matter are often seen in the nuclei of active galaxies. An example of the ionisation cone of NGC 1068 is shown in Fig.1.3. Such cones can result from collimation in the emission of the ionising photons, or by absorption. In the case of absorption, the absorbing matter must then be distributed in the torus-shaped structure (Wilson & Tsvetanov 1994). The opening angle of the cone, which can be measured directly, should match the opening angle of the putative torus. This scenario is sketched is Fig.1.3. Note, however, that once again this consideration cannot constrain the size of the torus.
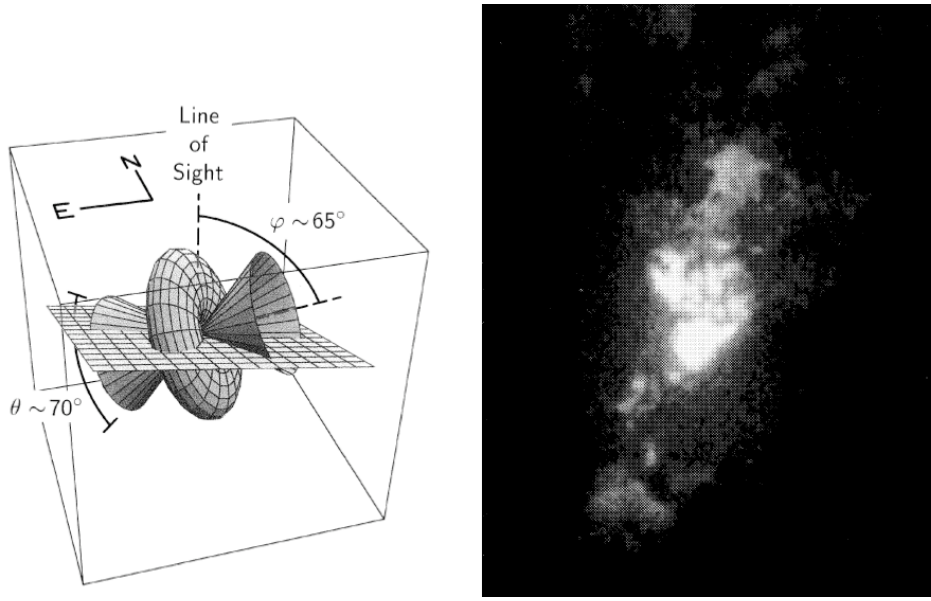
Figure 1.3 — Left: A sketch showing the relation between the ionisation cone and the dusty torus (Evans et al. 1993). Right: The ionisation cone of NGC 1068, as seen by the *Hubble Space Telescope* (Macchetto et al. 1994)

1.4.1.5 The 'receding torus'

The 'receding-torus' refers to the fact the the fraction of obscured AGN decreases with the bolometric luminosity of the AGN (Lawrence 1991; Simpson 2005). This fact strongly implies that the obscuring structure is thick: as the luminosity of the AGN increases, the dust reaches sublimation temperature further away from the nucleus, thus increasing the opening angle of the obscuring structure which in turn makes the appearance of unobscured AGNs more common. It is also possible to determine how changes in the fraction of (un)obscured sources depends upon the assumes shape of the torus. The most simple geometry is that of a torus with a constant height. In this case, the AGN type is related to the luminosity by (Simpson 2005):

$$f_1 = 1 - (1 + 3L/L_0)^{-0.5} \tag{1.1}$$

where f_1 is the fraction of type 1 sources, and L_0 is the luminosity at which the numbers of type 1 and type 2 sources are equal, i.e. an opening angle of 60 degrees. A schematic representation of the receding torus model is shown is Figure 1.4 along with a comparison between the fraction of type 1 sources as a function of luminosity and the expected relationship from Equation 1.1. It can be seen that Equation 1.1 does indeed follow the general shape of the data, but is not an exact fit. Differences can result from a number of factors, one of them being the oversimplified geometry which is assumed. Nevertheless, the data does strongly support the basic assumptions of the receding torus model.
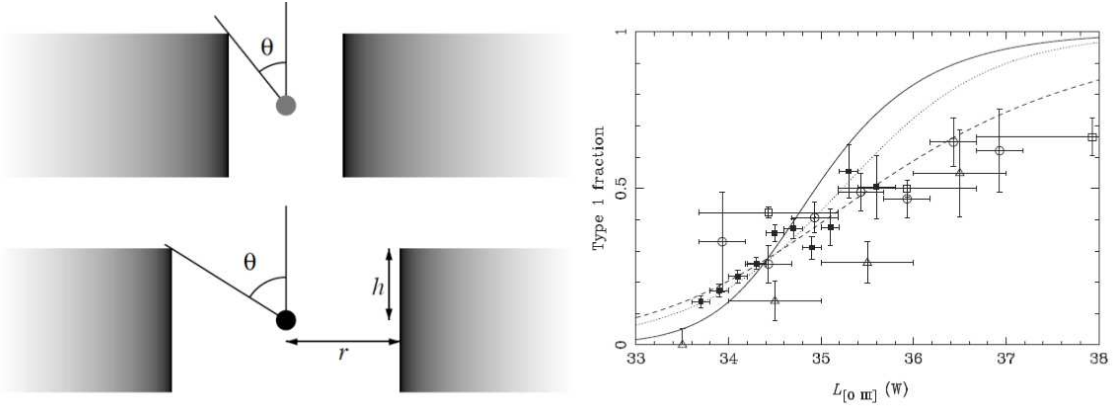
Figure 1.4 — Left: A schematic representation of the receding torus model (Simpson 1998), showing how the opening angle increases with luminosity. Right: The relationship between the fraction of type 1 sources versus the luminosity of the AGN. The solid line represents the expectations from the geometry of the sketch on the left, which assumes that h is constant with r and is the same for every AGN (Simpson 2005).

1.4.2 The 10μm spectral feature

At the mid-infrared there are two spectral features (lines) which are associated with dust, at wavelength of 9.7 and 18μm. These lines are caused by Si-O stretching and O-Si-O bending modes. They are therefore commonly named 'the 10μm silicate feature and 'the 18μm silicate feature', since they are lines associated with silicate dust.

These lines play a vital role in our understanding of the physical conditions which produce the mid-infrared emission from AGNs, and observing and detecting these lines is the major tool by which the mid-infrared properties of AGN are investigated. The two physical processes which govern the appearance of a spectral feature are line-emission and self absorption. In now briefly discuss the conditions for the appearance an absorption or emission feature.

1.4.2.1 Absorption feature

Based on the geometry of the dust distribution with relation to the central heat source and its optical thickness, the features can appear either in absorption or emission. An optically thick medium with a uniform temperature can never produce an emission or absorption feature. In this case, self-absorption and emission are perfectly balanced, producing a featureless Planck function. For an absorption feature to appear, two conditions must be satisfied:

1. A decreasing temperature profile (towards the observer).
2. The dust must be optically thick.

Optically thick dust is needed in order to allow some of the radiation to propagate, while still maintaining a temperature difference, from hot regions towards colder regions. Thus, the colder regions absorb the photons which originated from the hotter regions, and this absorption is not compensated by emission from these regions since they are colder. Therefore, the detection of a feature in absorption is a clear indication of the presence of optically thick dust with a temperature profile which decreases to-

wards the observer. Furthermore, the strength of the absorption feature is then related to the temperature profile of the dust. A large temperature gradient will produce a deeper absorption feature.

1.4.2.2 Emission feature

The conditions for the appearance of an emission feature are less strict. An emission feature can appear for dust at a single temperature if the dust is optically thin. In the general case, an emission feature is observed when looking at optically thin dust with a temperature profile which increases towards the observer, or when the illuminated surface of the dust is directly visible.

1.4.3 Implication on unified models

From the above discussion, it is clear that for nuclei where the obscuring torus it observed edge-on, the spectral features should appear in absorption, while for nuclei which are observed face-on, the features should appear in emission. This is one of the main predictions of unification models.

In the case of Seyfert 2 galaxies, the silicate feature is well detected in absorption. However, in the case of Seyfert 1 galaxies, a featureless continuum is commonly observed. This can be seen in Fig. 1.5, which shows Spitzer spectra for a sample of Seyfert galaxies. Currently, more and more type 1 objects showing the silicate feature in emission are found. This progress is mostly due to the shift towards space-based infrared telescopes, e.g. the *Spitzer* space observatory. However, in the general case of type 1 objects, the feature is still not detected. This non-detection of the silicate feature in emission poses a challenge to unification models.

Currently, the main approach into solving this problem is by looking for physical mechanisms which will suppress the emission feature. One such mechanism is the introduction of a clumpy medium for the distribution of the dust in the obscuring torus (Nenkova et al. 2002).

With MIDI, we are able to obtain a high-resolution correlated flux in the wavelength range of 8-13 μm. We therefore have an opportunity to detect the 10μm silicate feature in emission/absorption. For type 2 objects, the feature in absorption is well detected in the case of the Seyfert 2 galaxy NGC 1068. Unfortunately, there happens to be no nearby type 1 AGNs which are as bright as NGC 1068, a coincidence which limits out capacity to observe type 1 sources, and hopefully detect the elusive emission feature.

This lack of prominent bright Seyfert 1 galaxies did not deter us from still attempting to use the superior resolution of MIDI in order to shed light on this issue. We have therefore attempted to observe the brightest Seyfert 1 galaxy NGC 4151, although its declination is northern (+39), and our observing facilities are situated in the southern Hemisphere, and therefore the object is barely observable. The results, presented in chapter 4, clearly detect the silicate emission feature in our correlated flux, and constrain the location of the silicate emitting region to with the central ~ 2 pc of the galaxy. This is an improvement of a factor ~ 15 over the current limit of the size of the silicate emitting region (Mason et al. 2009). Furthermore, the emission feature is tentatively detected as well for several other type 1 objects, although not as clearly as in NGC
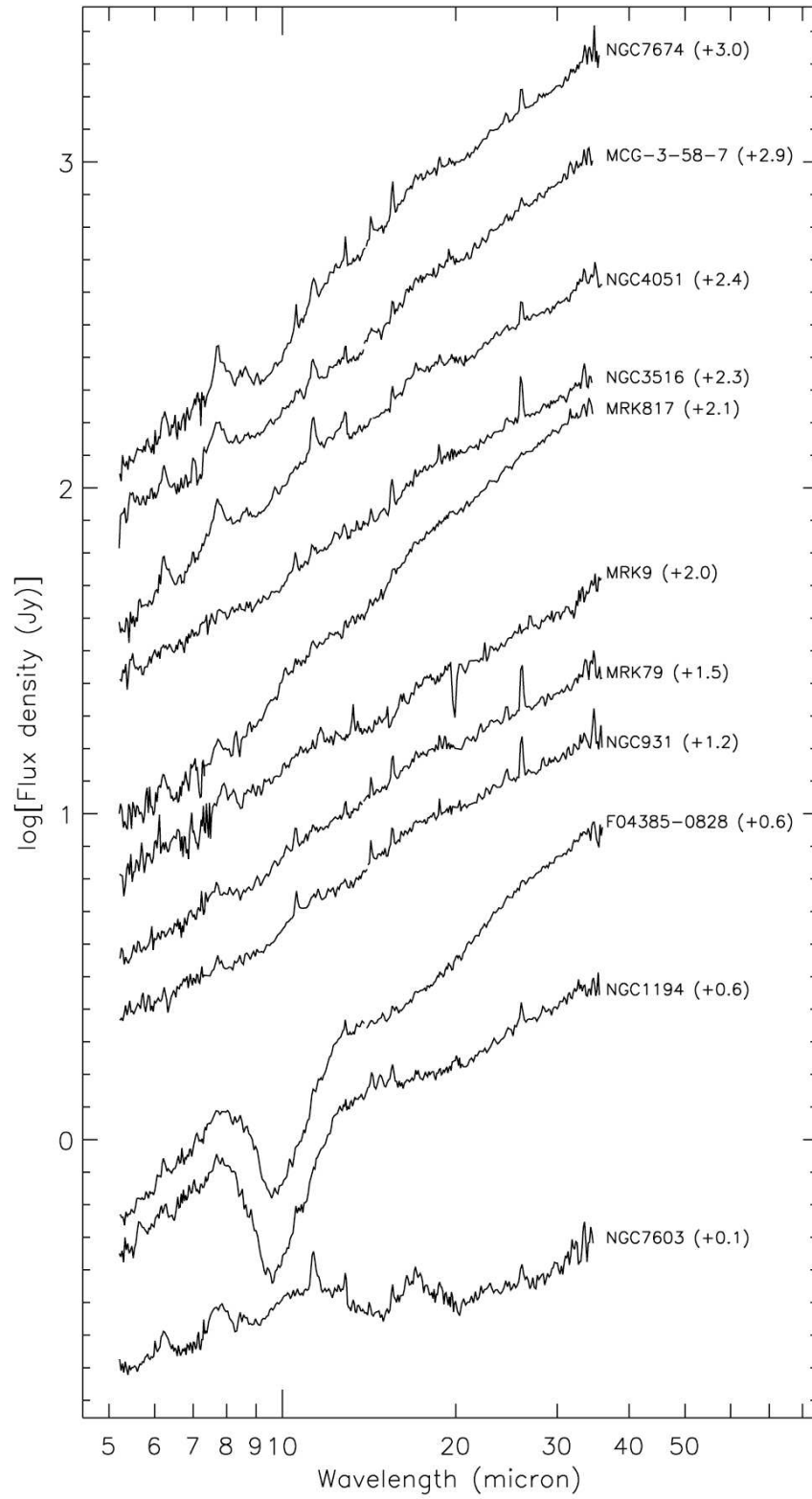
Figure 1.5 — Infrared spectra of a sample of AGNs from Buchanan et al. (2006) displaying the strong absorption feature seen at 10μm for Seyfert 2 galaxies, and the same very weak (at best) feature in emission in the case of Seyfert 1 galaxies.

4151. These objects are presented in chapter 6

1.4.4 The dust L-r-T relation

The circum-nuclear dust in AGNs is heated by absorbing *UV* radiation from the central engine. Naturally, the further the dust is from the *UV* source, or the less powerful the *UV* source is, the lower the temperature of the dust is expected to be. This is expressed in the following relationship between the dust temperature T, the bolometric luminosity of the AGN, L, and the distance from the energy source ,r, which we label 'the dust $L - r - T$ relation'. The quantitative relations in this section are based on the discussion of Nenkova et al. (2008).

$$r \simeq 0.4 \left(\frac{L}{10^{45} \, \mathrm{erg \, s^{-1}}} \right)^{1/2} \left(\frac{1500 \, K}{T} \right)^{2.6} \mathrm{pc} \tag{1.2}$$

or, alternatively

$$T(r, L) \simeq 680 \left(\frac{L}{10^{44} \, \mathrm{erg \, s^{-1}}} \right)^{0.2} \left(\frac{1 \, \mathrm{pc}}{r} \right)^{0.38} \mathrm{K} \tag{1.3}$$

The bolometric luminosity of an AGN may be directly measured or derived. The dust temperature and the its spatial scale may also be derived from MIDI observations. We are therefore in a position to test this relation.

1.4.4.1 Derivation

The spectral infrared luminosity (L_{ir}) of a single grain with temperature T , size a, and absorption coefficient Q_ν is given by:

$$L_{ir} = 4\pi a^2 Q_\nu B_\nu(T) \, \mathrm{ergs \, s^{-1} Hz^{-1}} \tag{1.4}$$

When exposed to a *UV* radiation field on energy density u_ν, an equilibrium state will be reached when the energy absorption rate equals the rate at which it is radiated:

$$\pi a^2 \int u_\nu c Q_{UV} \mathrm{d}\nu = \int L_{ir} \mathrm{d}\nu \tag{1.5}$$

where Q_{UV} is the ultraviolet absorption efficiency of the grains. Eqs. 1.2, 1.3 are a solution to the last equation.

Given the elementary physics involved, it is clear that if the L-r-T relation is found inaccurate, them there are basically just three options:
- Dust grains are wither smaller or bigger than expected
- Q_ν is different, i.e.
- Q_{UV} is different.

1.4.4.2 Empirical evidence in favour of relation

Let us consider the evidence in favour of Eqs. 1.2 ,1.3. To the best of our knowledge, empirical evidence for the $L - r - T$ relation comes from measurements of the time-delayed responses of the K-band flux variations to the V-band flux variations in a sample of nearby Seyfert 1 objects (Suganuma et al. 2006). The K-band emission originates from the putative torus, while the V-band emission from the accretion disk. The time lag between the two, if indeed found, is then an estimation of the inner radius of the torus. The results of this study show the the above mentioned time-lag, Δt, is proportional to the square root of the luminosity, i.e. the same relation between r and L as expressed Eq.1.2.

1.4.4.3 significance of the relation

From the discussion above we can see that the $L - r - T$ relation is another form of representing the way UV rediation interacts with the dust grains. It therefore has implication on every field in Astronomy where centrally heated dust is concerned. This includes studies of galactic objects such as proto-planetary disks, for example. Any information we obtain using MIDI about the $L - r - T$ relation therefore might apply to different physical environments as well.

1.4.5 Masers

Masers are molecules such as OH and H_2O, which have undergone a population inversion and emit stimulated emission. The radiation is emitted at a single wavelength corresponding to the transition between the levels in question. Masers are very similar to man-made lasers in principle, but they do not employ resonant feedback as lasers do. Masers require a pumping mechanism to supply the energy input and stimulate the emission.

Masers in AGN are usually referred to as 'megamasers' due to their exceptional isotropic luminosities. Masers are a very useful tool in astronomy. They can be used to measure distances, determining very accurate rotation curves, and may reveal the geometry of the disks they occupy.

Masers require specific astrophysical conditions to be formed (Elitzur 1992), and can only be formed where the density and temperature of the interstellar material falls within a certain range. For water masers, for example, a temperature of 300-900 K is needed.

For this reason, it was early speculated that masers are related to the dusty torus, as dust clouds are a fertile environment to maser formation (Claussen & Lo 1986). However, the high resolution data necessary to confirm this was not available. Now, after the successful operation of the VLTI, we have managed to prove the relation between the masers and the dust distribution in two galaxies: Circinus and NGC 1068 (chapter 3). In both cases, the masers are distributed in a ring with an orientation and size matching those of the dust structure we observe. The geometrical properties of the maser ring in NGC 1068, and its edge-on inclination, both provided substantial support to the interpretation of our finding in NGC 1068.

1.4.5.1   our findings

As discussed, MIDI observations let us directly test the $L - r - T$ relation if we can estimate a size and a temperature for the dust emitting region, providing the bolometric luminosity of the AGN is known. We consistently find that the $L - r - T$ relation is not properly scaled. i.e. while the size of the dust is still proportional to the luminosity, the dust is nevertheless found to be cooler than Eq.1.2 predicts. We attribute this difference to either larger grains, or to the existence of dust species which absorb less UV than normal dust.

1.4.6   Outlook to the future: 3D radiative transfer models

The observational effort to detect and measure the properties of the torus is accompanied by a theoretical effort to constrain its physical properties with the help of state-of-the-art 3-D computer simulations. The first such simulations where relatively simple and only considered a smooth distribution for the dust.

During the last decade, more complicated radiative transfer models have been introduced. These models now enable us to consider clumpy distributions for the dust. The handling of clumpy media was pioneered by Nenkova et al. (2002), and there are now several groups who are busy perfecting their models, each with a different approach.

Most such radiative transfer models make several assumptions about the optical depth of the individual dust clouds. The clouds are then distributed in an arbitrary manner which would nevertheless provide toroidal obscuration, and the resulting images and SEDs as a function of the model parameters and its inclination are compared to available data. As an example, Fig.1.6 shows images of the torus model of Hönig et al. (2006) as a function of its inclination and cloud arrangement.

Most models, however, still do not address the issue of how the dust clouds ended up in their locations, or what is the dynamical state of the clouds. An exception is the work of Schartmann et al. (2009) who attempt to use stellar feedback processes to explain the dynamical state of the torus. The temporal evolution of the torus density from their latest models is shown in Fig.1.7.

It is safe to say that currently our ability to create complicated models outshines our ability to obtain data which would constrain such models. The data presented in this work is the most extensive of its kind. And yet, to fully constrain the models with this data, a much higher resolution is needed. The true impact of the radiative transfer models will take place in the future, when better instruments are available.

1.4.7   Origin and dynamical state

As stated before, the dynamical state of the torus is still unknown. Still, there are two main scenarios for the dynamical state of the torus: the *outflowing* and *inflowing* scenarios, which we will shortly describe. The issues we address in this section are actually not addressed at all in the thesis. The main reason is that the observations, which are the basis for this work, are unable to distinguish between the different scenarios. However, this work is concerned with the torus, so an overview of the current speculation as to its origin and dynamical state is given.
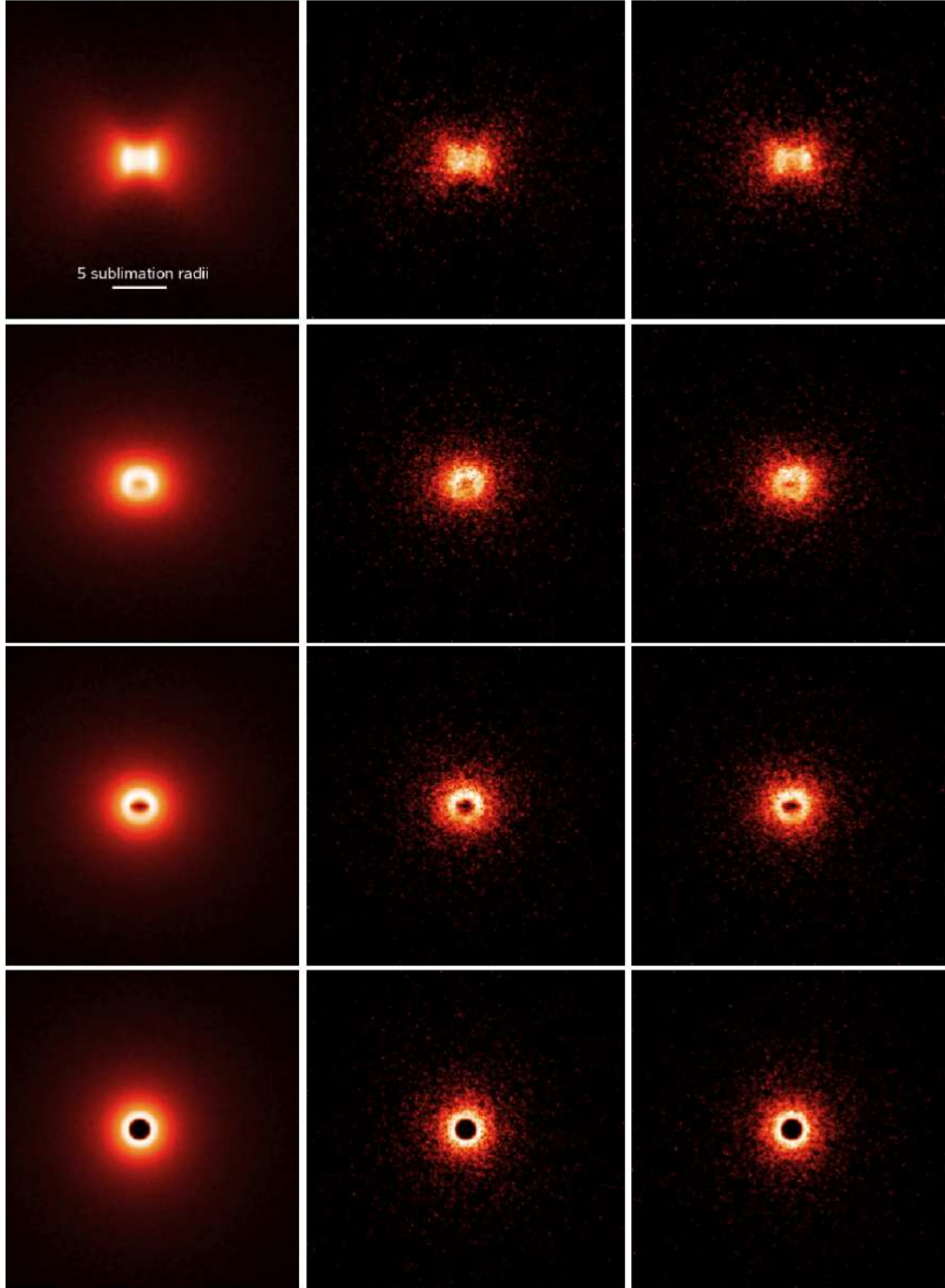
Figure 1.6 — L-band model images of the torus of Hönig et al. (2006) as a function of its inclination, i. *Left column:* images obtained by averaging model images of ~ 200 different random cloud arrangements. *Middle and right columns:* model images for two particular random cloud arrangements. *From top to bottom:* $i = 90°, 45°, 30°$ and $0°$
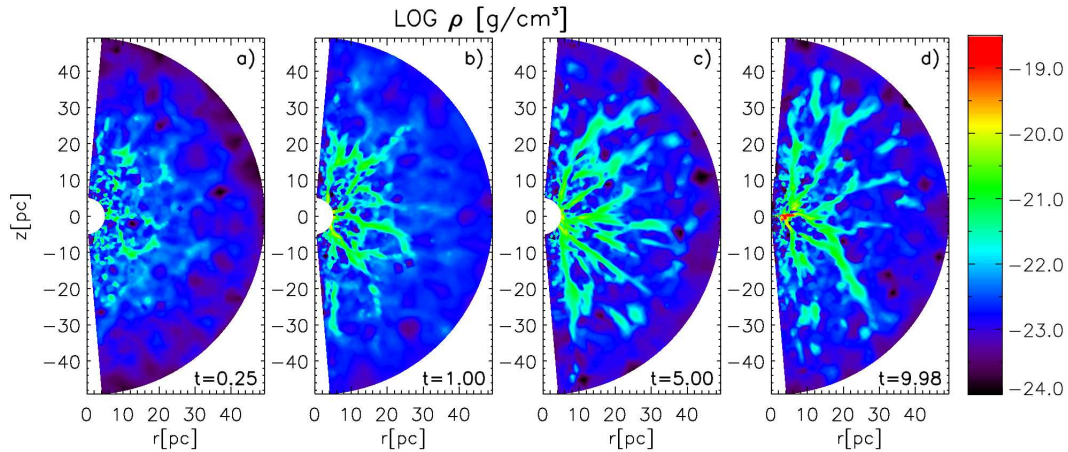
Figure 1.7 — Temporal evolution of the density in the model of Schartmann et al. (2009), given in a meridional slice of the torus. Shown are four stages of the torus at 0.25, 1.0, 5.0 and roughly 10.0 global orbits. The scaling is logarithmic.

1.4.7.1   The inflowing secnario

In this scenario, which is the dominant one at the moment, the torus is a somewhat separate entity from the broad line region (BLR). The dust originates from stars in the host galaxy, slowly making their way to the nucleus. Below is a qualitative description for the scenario of Schartmann et al. (2009), which is the most detailed one currently available. This model is not only able to account for the origin of the dust clouds, but is also able to explain its vertical structure.

The main assumption of the model is that a young star cluster exists in those AGN which posses a torus, which was build up during a short duration (40 Myr) starburst period. After the first violent phase of the evolution of the cluster double systems of lower mass stars are able to form, and the rate of supernova type Ia begin to rise sharply. At the same time, planetary nebulae formed by stars in the intermediate mass range (1.5-8 $M_{\odot}$) begin to inject mass into the interstellar medium. The injection velocity matches the velocity dispersion plus the rotational velocity of the stars. The injected mass begins to cool and loose energy, making its way towards the central engine. The combination of cooling instabilities, shock fronts from supernova explosions and planetary nebula collisions lead to the creation of a geometrically thin, but optically thick and very turbulent disk. As more and more matter falls towards the minimum of the potential, a turbulent and fluffy disk emerges, possessing a very filamentary structure with strings of material in the azimuthal direction, in a torus-like shape. The torus, then, is not a stable structure. It's height is maintained by constant injection of mass and energy from the nuclear star cluster and supernova explosions. Without this constant mass and energy injection, the torus will collapse to a thin disk. The temporal evolution of the density in this model is shown in Fig.1.7

1.4.7.2   The outflowing scenario

The outflow scenario offers a radically different outlook on the torus. Here, the torus is not an independent entity. Rather, the torus, accretion disk and broad line region

are all basically the same phenomena, with the BLR being a wind of ionized material lifted out of the accretion disk, and the torus being the condensed, molecular part of the wind.

This scenario started to take shape after Blandford & Payne (1982) proposed that energy and angular momentum are removed from the accretion disk by field lines that leave the disk surface, extending to large distances. This idea was originally intended to explain the production of jets in AGN. About ten years later, Emmering et al. considered what happens to the material lifted off the accretion disk in the more extended regions of the disk, which are not directly related to the jet. They proposed that this material is ionised by the AGN, and is seen as the broad line region. Thus, the accretion disk and BLR are united in this scheme, in the sense that if you have and accretion disk, then you have a BLR as well. The next step was to consider what happens to the BLR ionized clouds when they are sufficiently away from the nucleus. If the uplifting force is sufficient, the clouds will eventually condense and become molecular and optically thick, obscuring the nucleus. Thus, in this case, the obscuring torus is not a structure which exists on its own, but is the part of the wind which has condensed. This scheme may be termed the 'Grand unification theory' since it requires only a SMBH accreting matter in order to account for the CE, the BLR, and the torus.

1.5   Introduction to Interferometry

Interferometry can be most simply described as the careful combination of light from telescopes placed at distance. The fringe pattern produced due to the wave-like nature of the light contains information on the spatial distribution of the emitter, but with a resolution $\theta = 2.2\lambda/B$, where λ is the observed wavelength and B the projected separation between the telescopes. The higher the separation between the telescopes, the higher the resolution gained. The Very Long Baseline Array, for example, has a network of radio telescopes across North America.

While the spatial resolution depends on the distance between the telescopes, the amount of information gained depends mostly on how many different telescopes positions were used in the observation. The distribution of the telescopes (or antennas) is referred to as the 'u-v plane', where each point on the plane is the projected position of each telescope. The signal recorded after combining the light is nothing else than the Fourier transform of the source's brightness distribution. This may be formally written as:

$$V(u',v') = \int_{\infty}^{\infty} \int_{\infty}^{\infty} I(l',m')e^{-2\pi i(u'l'+v'm')} \frac{dl'dm'}{\sqrt{l-l^2-m^2}} \tag{1.6}$$

where (l',m') are direction cosines measured with respect to the relative position of the telescopes (u',v'), $V(u',v')$ is the visibility for each pair of (u,v) points , and I the spatial distribution of the source on the sky.

Equation 1.5 is all one needs in order to analyse interferometric data. If enough u-v points were gathered, then one has determined sufficient values of V in order to use the inverse transform and recover I, the image of the source, as is normally the case with radio astronomy. At shorter wavelengths, such as the infrared, the process

of collecting and combining the light is more complicated. The practical implication is that infrared interferometric arrays are very small compared to their radio counterparts, and therefore provide considerably less information. In Chapter 3 we present one of the most extensive infrared interferometric observations to date. These observations are composed of 16 u-v points, combining the data form only two telescopes at a time. With this type of data, the direct imaging method described above cannot be employed. Not only do we not measure enough values of V, but we also lose the phase of V (which is a complex number) and measure only its amplitude.

This lack of information may be overcome by use of either modelling, or by use of clever ways to reconstruct images from partial data. The next section describes both methods.

1.5.1   Modelling

Modelling allows us to determine the basic properties of the source, even when a small number of u-v points are measured. First, a model, often with a few free parameters for I, the source's brightness distribution, is generated. The values of V for each u-v point are then determined according to Eq.1.5, while changing the free parameters to fit the data. Modelling is especially useful when the shape of I is already known. For example, measuring the diameter of a star is possible using a single u-v point, using a circular disk model for I, which has only one free parameter, its radius.

In cases where there is no a-priori information about the shape of the source, one must assume a specific shape for I. Common shapes used in interferometry include a Gaussian distribution, a ring, a circular disk etc.

Modelling is in a way a process of clever guessing, since we have to first guess the basic properties of the source. However, as shown in this thesis, modelling can deliver a large degree of certainty if enough u-v points are measured, and if the model fits the data well.

1.5.2   Image reconstruction

In some situations, there is enough information allowing one to reconstruct an image of the source although some of the data is missing. Suppose we have measured a set of 10 u-v points, while 30 u-v points are enough to apply the inverse Fourier transform and generate the true image. In this case, there are many images which might differ considerably, but nevertheless would fit the measured data points. How does one chose between them?

The answer is: by making a few other assumptions about the flux distribution. The first one, and the most straightforward, is that the image we recover must have all positive values. The second one is less intuitive than the first. Namely, we define a function called the 'entropy', and select the image for which the entropy is in extremum. The most simple definition of entropy here is virtually identical to the classical entropy in thermodynamics: $S = \sum_i P_i \log P_i$, where we sum over the number of pixels and P_i is the pixel value of the ith pixel. In practice, more complicated forms of the entropy can be used. This method is called 'Maximum Entropy' , and in Chapter 3 we employ it for the first time with such data in order to reconstruct an image of the centre of the active

galaxy NGC 1068 at mid-infrared wavelengths.

1.5.3 Spectro-interferometry

Spectro-interferometry is the technique we use in all the interferometric observations presented in this thesis. The idea is to disperse the light before combining the beams using either a prism or a grism. This way we get not just the visibility V, but the visibility for each wavelength we measure, $V(\lambda)$. The direct product of the spectro-interferometer is not the visibility, but the 'correlated flux', which is the the actual flux which is correlated, and may be thought of as the spectrum of the source measured under an aperture set by the spatial resolution of the interferometer[1]. The correlated flux is in fact the visibility times the total flux emitted from the source.

Although the common practice is to use the visibility in analysing interferometric data, it is often more useful to model the correlated flux directly, as we have done throughout this thesis. The main reason for this is that in many cases the uncertainties in the visibility are much higher than in the correlated fluxes.

Spectro-interferometric observations pose an additional challenge due to the correlated fluxes being sensitive to the the spectrum of the source and to its size. For example, suppose we see that the correlated fluxes rises with wavelength. The rise could be due to the source emitting more at longer wavelengths, or may indicate that the source is more resolved spatially at shorter wavelengths. There is no full-proof method to disentangle the two effects. The approach that we have taken in this work in to apply two models to the data. The first model assumes all the differences in flux arise from the spectral properties of the source, i.e. the source has the same size in every wavelength. The second assumes no relationship between the flux at different wavelength, i.e source size (and orientation) may vary with wavelength. By comparing the results of the two models, one may gain some insight into the true nature of the source.

1.6 The Very Large Telescope Interferometer and MIDI

The very large telescope interferometer (VLTI) is composed of four 8.2 meter units telescopes (UTs), and several 1.8 meter auxiliary telescopes (ATs). The telescopes are coupled together by tunnels (the delay lines) designed to carry the photons to a common location, where the beams are combined by the specific instrument used. Since the optical path difference between the telescopes and instrument must be equal, the delay line are equipped with mobile retroflector carriages which are able to move with a precision of a micron. For a successful beam combination, the optical path difference must be controlled with a precision that is better than the shortest observed wavelength, in this case $\sim 2\mu$m. This very high precision needed is the main reason while optical interferometry had to wait to the 21 century, while radio interferometry (with much larger wavelengths) has been practised for half a century. There are several instruments currently coupled to the VLTI with different capabilities. For example the AMBER instrument can simultaneously combine the K-band light from three telescopes.

---

[1] In some cases, usually when the source has a sharp 'edge', the correlated flux behaves rather differently
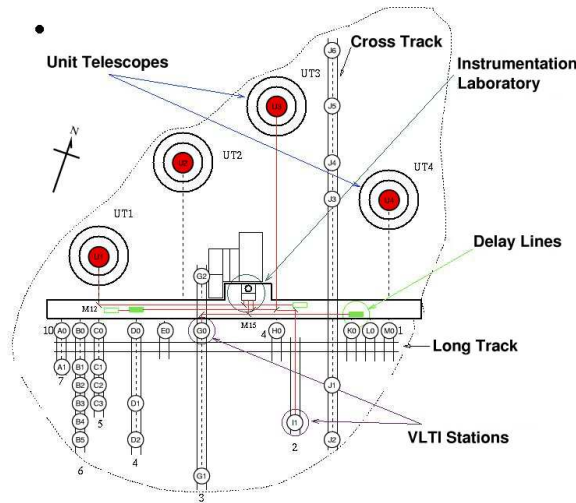
Figure 1.8 — Sketch of the VLTI site and telescope configuration
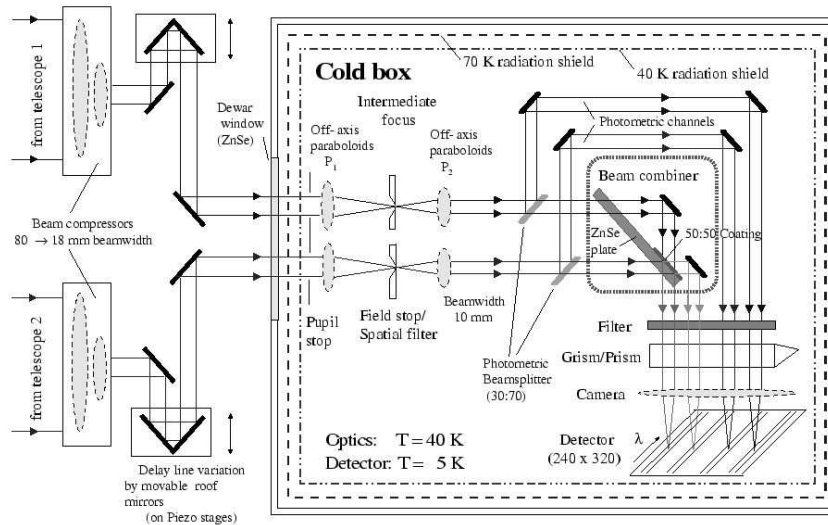
Figure 1.9 — Principle of the MIDI instrument. Image courtesy ESO.

For the observations presented in this work, we use the MIDI instrument, which shall be described ext.

1.6.1   The MIDI instrument

The Mid Infrared Interferometric Instrument (MIDI) is the instrument we use in all the interferometric observations presented in this thesis. It is also the only such interferometer which routinely observes AGNs. Below is a brief description of the instrument. For a more detailed overview see Leinert et al. (2003)

MIDI is a classical Michelson interferometer, combining the light from two UTs or ATs at a time. To protect the instrument from thermal radiation from the environment,

most of the optics is enclosed in a cryostat cooled at about 40 K (the cold box), while the array detector of MIDI is cooled at 10 K, with pupil-stops inside the cryostat reducing the background radiation and stray-light. In order to adjust the optical path difference, the two beams paths are modulated by moveable mirrors motored by piezoelectric transducers, before entering the cold box. In the cold box, the two beams pass through two stops, designed to block stray light and improve the image quality. The beams then continue to the beam combiner, which is made from a ZnSe plate with a 50:50 coating. After the beam combiner, the beams (now called 'channels') pass thorough a dispersive element to generate a spectrum. Two kinds of dispersive elements are used, a grism and a prism. The Prism provided a spectral resolution of $R = \lambda/\Delta\lambda = 30$ and for the grism $R = 230$. The dispersed beam is then recorded on a detector, divided into spectral channels. There is a trade-off between the spectral resolution and the number of photons that reach each pixel on the detector. For strong sources, the grism is used, while for weak sources the prism is used since there are less spectral channels and so each pixel on the detector gets more photons.

The official limiting flux of MIDI is 1 Jy if using the ATs. However, we present here MIDI data for sources with flux as low as 50 mJy. This shows that MIDI as an exceptionally successful instrument, capable of performing observations well beyond its designated limits. In fact, most of the problems which occur when observing very faint sources arise from the other systems of the VLTI, most notably the adaptive optics. The main limitation of MIDI is its lack of phase measurement, as MIDI can only measure Fourier amplitudes. In practice this means that when interpreting MIDI data we cannot distinguish between symmetrical and asymmetrical models.

1.6.2 Observational procedure and data reduction

The observational procedure is described in detail in chapter 6. For reducing the data, we use the Expert Work Station (EWS) data reduction package, developed by Leiden University. EWS uses coherent visibility estimation as the method of data reduction. For a detailed description see Jaffe (2004).

1.7 This thesis

Here is a brief summary of the contents of each chapter.

Chapter 2

Interferometric observations are costly, and observing time is not given easily. We therefore must be sure which objects are worth observing, given the limited time on the interferometer.

In this chapter, we use the 3.6m telescope at La Silla, Chile, to first observe every source which may be a promising MIDI target, a total of 21 sources. We try to determine which sources are bright enough to be observed and for which sources the mid-infrared emission is resolved. Images are also presented when structure is visible.

Chapter 3

In this chapter we present observation of the Seyfert 2 galaxy NGC 1068. For this object we use an extensive $u - v$ coverage composed of 16 different baselines, which is one of the most extensive infrared interferometric observations of an extragalactic object. We were able to fully resolve the dusty structure and measure its main properties such as size and temperature. We also present an image of the source at 8 μm, which was produced using maximum entropy image reconstruction. We find the dust component (the torus) to be co-spatial with the known maser disk and discuss the relation between the dust and the ionisation cone. We also find that the dust is tilted by 45 degrees with respect to the jet, which indicated a complicated history of accretion for this specific object. Due to the side-one position of the torus in NGC 1068, we were able to show that the dust structure we resolve is indeed an inflated torus. The observation of NGC 1068 provide the most convincing case for the obscuring torus, compared with results for other objects.

Chapter 4

In this chapter we present observations which resolve the dust distribution in the Seyfert 1 galaxy NGC 4151. The resolved structure's size and temperature are comparable with those of Seyfert 2 galaxies, which is a strong indication in favour of the unification models. We compare in detail our findings with interferometric observations at shorter wavelengths, and conclude that the unresolved source seen in those observations cannot be a continuation of the resolved structure seen by MIDI. We detect the silicate feature in emission, albeit tentatively, and discuss how the size and temperature we derive for this source fit into the unification models.

Chapter 5

In chapter 5, we present observations of the Quasar 3c273. This source is unique in our sample because it is not a nearby object, allowing us to test the predictions of the unification models on a high-redshift and very luminous object, as well as to compare our findings for this object with our finding on nearby AGNs. We find a resolved and elongated structure at the core of 3C 273. The size of the structure is consistent with the size predicted by unification models for the dusty torus. Similarly with NGC 4151, we also detect the 10 μm silicate feature in emission tentatively.

These observations, for the first time for such high redshift source, resolve the emission from the dust in the centre of the quasar, and provide the first direct evidence that unification scheme hold for this type of objects.

Chapter 6

In this chapter we present observations of a sample of 10 Seyfert galaxies, a combination of both types of Seyfert galaxies. For each source we obtain between one and three u-v points, which allow us to see whether the target is resolved and to measure basic properties such as the size of the mid-IR emitting regions. For seven targets out of the ten observed, we derive sizes of limits on the sizes of the AGN heated dust. In these cases we find that the size of the mid-IR emitting region is parsec-scaled. Further, the

derived sizes roughly scale with the square root of the AGN luminosity. the 10 micron silicate feature is also tentatively detected either in emission or absorption.

Chapter 7

In this chapter we turn our attention away from the obscuring torus and toward the mm and radio emission coming from the jet. Only publicly available data is used, including WMAP data which was obtained for determining the properties of the microwave background radiation. Here, we use WMAP data in order to study the radio emission mechanism of the FR-I AGN NGC 5128 (Centaurus A). We determine the centimeter and millimeter continuum spectrum of the whole Centaurus A radio source and measure at frequencies between 86 GHz (3.5 mm) and 345 GHz (0.85 mm) the continuum emission from the active radio galaxy nucleus at various times between 1989 and 2005. The data shows that the integral radio source spectrum becomes steeper at frequencies above 5 GHz. The SW outer lobe has a steeper spectrum than the NE middle and outer lobes. We find that Millimeter emission from the core of Centaurus A is variable, a variability that correlates appreciably better with the 20-200 keV X-ray variability than with 2 - 10 keV variability. In its quiescent state, the core has a spectral index which steepens when the core brightens. The variability appears to be mostly associated with the inner nuclear jet components that have been detected in VLBI measurements. The densest nuclear components are optically thick below 45-80 GHz. This chapter is an example of how one can use existing and publicly available data to obtain results in a different niche of Astronomy than the data was intended for.

References

Antonucci R., 1984, ApJ278, 499

Antonucci R. R. J., Miller J. S., 1985, ApJ, 297, 621

Antonucci R., 1993, ARA&A, 31, 473

Barthel P. D., 1989, ApJ, 336, 606

Blandford R. D., Payne D. G., 1982, MNRAS, 199, 883

Barvainis R., 1987, ApJ, 320, 537

Buchanan C. L., Gallimore J. F., O'Dea C. P., Baum S. A., Axon D. J., Robinson A., Elitzur M., Elvis M., 2006, AJ, 132, 401

Claussen M. J., Lo K.-Y., 1986, ApJ, 308, 592

Elitzur M., 1992, ARA&A, 30, 75

Emmering R. T., Blandford R. D., Shlosman I., 1992, ApJ, 385, 460

Evans I. N., Tsvetanov Z., Kriss G. A., Ford H. C., Caganoff S., Koratkar A. P., 1993, ApJ, 417, 82

Hao L., Spoon H. W. W., Sloan G. C., Marshall J. A., Armus L., Tielens A. G. G. M., Sargent B., van Bemmel I. M., Charmandaris V., Weedman D. W., Houck J. R., 2005, ApJ, 625, L75

Hönig S. F., Beckert T., Ohnaka K., Weigelt G., 2006, A&A, 452, 459

Jaffe W., Meisenheimer K., Röttgering H. J. A., Leinert C., Richichi A., Chesneau O., Fraix-Burnet D., Glazenborg-Kluttig A., Granato G.-L., Graser U., Heijligers B., Köhler R., Malbet F., Miley G. K., Paresce F., Pel J.-W., Perrin G., Przygodda F., Schoeller M., Sol H., Waters L. B. F. M., Weigelt G., Woillez J., de Zeeuw P. T., 2004, Nature, 429, 47

Jaffe W. J., 2004, SPIE., 5491, 715

Lawrence A., 1991, MNRAS, 252, 586

Leinert C., Graser U., Przygodda F., and 31 coauthors , *Astrophysics and space science* , 286, 73, 2003

Macchetto F., Capetti A., Sparks W. B., Axon D. J., Boksenberg A., 1994, ApJ, 435, L15

Mason R. E., Levenson N. A., Shi Y., Packham C., Gorjian V., Cleary K., Rhee J., Werner M., 2009, ApJ, 693, L136

Nenkova M., Ivezić Ž., Elitzur M., 2002, ApJ, 570, L9

Nenkova M., Sirocky M. M., Nikutta R., Ivezić Ž., Elitzur M., 2008, ApJ, 685, 160

Schartmann M., Meisenheimer K., Klahr H., Camenzind M., Wolf S., Henning T., 2009, MNRAS, 393, 759

Schmitt H. R., Antonucci R. R. J., Ulvestad J. S., Kinney A. L., Clarke C. J., Pringle J. E., 2001, ApJ, 555, 663

Simpson C., 1998, MNRAS, 297, L39

Simpson C., 2005, MNRAS, 360, 565

Suganuma M., Yoshii Y., Kobayashi Y., Minezaki T., Enya K., Tomita H., Aoki T., Koshida S., Peterson B. A., 2006, ApJ, 639, 46

Urry C. M., Padovani P., 1995, PASP, 107, 803

Wilson A. S., Tsvetanov Z. I., 1994, AJ, 107, 1227

Chapter 2

The core flux of the brightest 10μm galaxies in the southern sky

Abstract. Near diffraction-limited images have been taken at 8.9, 11.9, and 12.9 μm for the brightest extragalactic sources in the southern sky, in order to optimally plan N-band observations with MIDI (MID-infrared Interferometric instrument) at the VLTI. We have assembled a sample of 21 objects consisting of all the AGNs observable from Paranal observatory, Chile, plus three non-AGN objects, with an estimated N-band flux greater than 400mJy. We used the TIMMI2 Mid Infrared instrument mounted on the ESO's 3.6m telescope to obtain near diffraction-limited images in order to establish the unresolved core flux within < 0.5 arscsec. Positions and core total fluxes were obtained for all sources in our sample and compared with similar investigations in the literature. We find that 15 AGN and the nuclear starburst in NGC 253 exhibit an unresolved core flux < 300mJy at 11.9μm, making them promising targets for MIDI at the VLTI. For extended sources, near diffraction-limited images are presented and discussed.

D. Raban, B. Heijligers , H. Röttgering, K. Meisenheimer, W. Jaffe, H. U. Käufl and T. Henning

2.1　Introduction

SINCE the operation of MIDI at the VLTI began in 2004, astronomy has entered a new era where it is now possible to reach a resolution of a few milliarcseconds at infrared wavelengths, about 15 times the resolution of the largest single-dish telescopes. MIDI (operates in the N-band (8-13μm) and therefore it is ideal for observing heated dust expected in AGNs and starburst galaxies. Although it is most commonly used in observing galactic objects like circumstellar disks (Leinert et al. 2004) and dust shells around evolved stars (Ohnaka et al. 2005), MIDI has been successfully used to observe extragalactic objects. The main limitation of MIDI in this context is its limiting flux of ~400mJy, so only bright objects can be observed currently. So far, MIDI has been used to observe dusty torii in AGNs, objects which are central to the AGN unification model, and which have proven too small to be resolved by a single dish telescope. With its superior resolution, the presence of a torus-like structure has been established in the galaxy NGC 1068 (Jaffe et al. 2004) by using only two baseline observations, and additional MIDI observations with extensive coverage of up to 21 baselines have measured the geometrical properties of the torus in the Circinus galaxy (Tristram et al. 2007) and NGC 1068 (Raban et at, submitted). A resolved dust structure was also detected in the core of Centaurus A (Meisenheimer et al. 2007). Apart from active galactic nuclei, the only extragalactic objects bright enough for MIDI are starburst galaxies. For such objects, MIDI can be used to measure the size and geometry of the nuclear star-forming region.

Here, we have assembled a list of the brightest extragalactic objects at 10μm, and observed them at 8.9 ,11.9 and 12.9 μm with the TIMMI2 instrument, mounted on the 3.6m telescope in La Silla, Chile. Our goal here is to give the basic information needed in order to plan VLTI observation of cores of galaxies. Positions and core fluxes were determined for all sources, and for those sources which were resolved, we present and discuss images at 8.9, 11.9 and 12.9 μm.

The layout of the paper is as follows: in Section 2.2 we describe how the observed sources were selected; the observations and data reduction are discussed in Sections 6.3 and 2.4; images are presented in Section 6.4 along with a brief description of each object and additional reference information

2.2　Sample selection

The target list consists of *all* AGN's observable from Cerro Paranal ($\delta < 22$) and have an estimated total N-band flux density brighter than $N = 5$ or $S_N = 400$mJy, which is the limiting magnitude for observations with MIDI, estimated from previous N-band measurements available in the literature. This list of 21 objects (without NGC 1068) was taken from the catalogue of Seyfert galaxies by Lipovetsky et al. (1988) to which we added additional sources from the compilations of Granato et al. (1997) and Maiolino et al. (1995), plus the IR luminous galaxy M83, the starburst galaxy NGC 253 and the famous quasar 3C 273. See Table 2.1 for a complete list.

Table 2.1.   Observation list and fluxes for all objects[a]

Name	RA J2000	DEC J2000	D Mpc	11.9μm Flux mJy	8.9μm flux mJy
N 253[1]	00 47 33.1	-25 17 17.2	3.3	2040-2800	1140
N 253[2]				1160	695
N 1365[1]	03 33 36.4	-36 08 25.5	20.7	606	-
N 1365[2]				157	-
N 1365[3]				152	-
IRS 05189-2524	05 21 01.4	-25 21 44.9	172.6	545	-
N 2377	07 24 56.8	-09 39 36.9	31.3	< 60	-
MCG-5-23-16	09 47 40.2	-30 56 54.2	31.9	648	-
Mrk 1239	09 52 19.1	-01 36 43.5	79.7	638	-
N 3256	10 27 51.8	-43 54 08.7	35.4	553	-
N 3281	10 31 52.0	-34 51 13.3	40.9	625	-
N 3758	11 36 29.0	+21 35 47.8	122	< 60	-
N 3783	11 39 01.8	-37 44 18.7	37.2	590	-
3C 273	12 29 06.7	+02 03 08.5	649	345	-
N 4594	12 39 59.4	-11 37 23.0	12.4	< 60	-
MCG-3-34-6	13 10 23.7	-21 41 09.0	95.4	< 60	-
N 5128	13 25 27.6	-43 01 08.8	5.3	1220	635
M 83	13 37 00.8	-29 51 58.6	5.2	232	-
ESO 445-G50	13 49 19.3	-30 18 34.4	64.2	352	-
Mrk 463	13 56 02.9	+18 22 19.5	20.7	338	-
Circinus	14 13 09.3	-65 20 20.6	3.6	9700	4700
N 5506	14 13 15.0	-03 12 27.2	25	908	-
N 7469	23 03 15.6	+08 52 26.4	69.2	414	-
N 7582	23 18 23.5	-42 22 14.0	21.3	670	-

[a]RA and DEC coordinates are coordinates taken directly from the telescope position. Distances are from NED. RA & DEC error: $\pm 5''$. Flux errors are $\pm 15\%$.

2.3   Observations

The mid-infrared observations were carried out with the TIMMI2 instrument on the ESO 3.6m telescope on La Silla, Chile, on the nights of 6 and 7 of August 2001 and 8 to 10 February 2002. TIMMI2 is a mid-infrared imager and spectrograph operating in the M (5 μm), N (10 μm) and Q (20 μm) atmospheric bandpasses. The camera is equipped with a 320×240 pixel Si:As array and can operate at a scale of 0.2 or 0.3 arcsec/pixel. We used the 0.2 arcsec/pixel scale resulting in a total field-of-view of $64'' \times 48''$. For a complete description of the instrument refer to Reimann et al. (2000) and Käufl et al. (2003).

For most of the observations we selected the 1.2μm wide 11.9μm filter since it offered the best signal to noise ratio for a given integration time. A ratio of flux over noise (per pixel) of about a 200 is achieved by 40 minutes of integration time for a 400mJy source. Sources that were significantly brighter were observed for shorter periods of time. Some targets were supplemented with additional images with the the 8.6 μm filter ($\Delta\lambda = 1.2\,\mu$m) and the 12.9 μm filter ($\Delta\lambda = 0.9\,\mu$m). The complete observation log can be found in table 2.1.

Seeing conditions as monitored in the optical were highly variable, ranging between 1 and 1.8 arcseconds on August 6 to 0.36 and 0.8 arcseconds on August 7 2001, while the humidity at ground level remained around 5%. During the February 2002 run the seeing was constant at 1 arcsecond with a very high humidity at ground level of $80\% - 95\%$. In order to remove the strongly variable background radiation of the telescope and atmosphere in the mid infrared we used the standard chopping and nodding method. In this mode the secondary mirror chops with a frequency of typically several Hz North-South and the telescope is nodded approximately every 5 minutes East-West. As all sources turned out to be compact at 10μm, the small field chop and nod mode was used, keeping the objects always in the frame, while still avoiding overlapping of the images which might lead to loss of flux. This effectively cuts the field-of-view of the chip in 4 pieces and is therefore only possible for compact targets. such as extended star forming regions, the relatively small throw we used can substract these from the image, leading to an underestimation of the flux. During chopping the detector is continuously read-out with a frequency of about 40 Hz and each 100 image pairs are subtracted, stacked and saved to disk. The result is a series of chopped frames with both a positive and a negative image of the source, with an exposure time of approximately 25 seconds per frame. Subtracting 2 frames from different nod positions results in 2 positive and 2 negative acquisitions of the object. We used a chop throw of 20 arcsec North-South and a nod of 30 arcsec East-West (except for the observations of M83 where these values were 25 and 30 arcsec respectively), allowing for both the chopped as well as the nodded positions to fall onto the detector, while at the same time preventing any overlap of the positive and negative images.

Due to technical problems with the autoguider there was a slow position drift during the integrations. This was taken into account during data reduction.
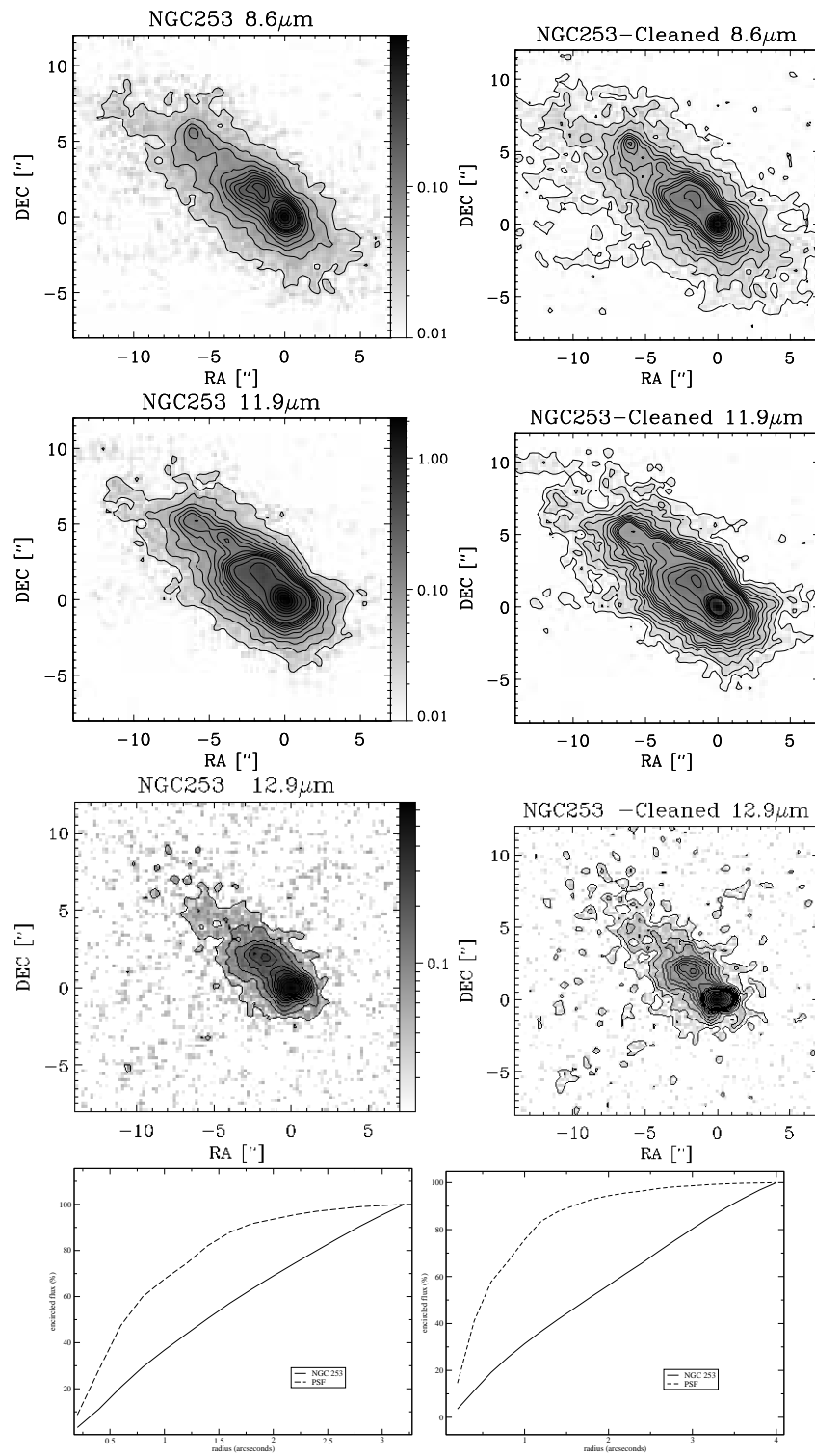
Figure 2.1 — NGC 253 contour and image overlays, Left: Raw data. Right: Central point deconvolved with CLEAN algorithm sdf. Bottom : growth curve of the core and PSF at 11.9μm (left) and 8.9μm (right).

2.4 Reduction

Standard reduction techniques were used to convert a set of raw frames into a final, photometrically calibrated image of the source. Flat field correction was not applied since for all ground-based mid-IR instruments no possibility of a reliable flatfield correction exists up to now (Starck et al. 1999), and since the chopping and nodding method used to eliminate the thermal background results in a relatively flat images. For our data cosmic rays removal is not required since the number of background photons is large, making the cosmic ray's contribution undetectable. Bad pixels were detected using the statistical variation of each pixel, extrapolated and excluded from the measurements. Three different modes for referencing and co-adding were implemented to accommodate different SNR levels. For all these modes the image peak was determined by fitting a Gaussian of appropriate size to the central airy disk:

- For the brightest sources with a flux above 1200 mJy (i.e. Circinus, NGC1068, NGC253, NGC5128) the peak SNR was high enough so that each of the four images (2 positive, 2 negative) in a single frame could be separately fitted, referenced and co-added in order to get the best registration, thus compensating for possible small errors in the chopping distance.
- For the intermediate sources with a core flux above 650 mJy we assumed the chopping distance to be fixed, first combining the positive and negative images before their center point is determined.
- For weak sources below 650 mJy the image pairs are first co-added with a fixed chopping distance. Images taken just before and after each image are also co-added before being fitted. This procedure first averages a subset of images, calculates the peak position and then uses this position for next subset of images, iterating until the corrections are smaller then 0.1 pixel.

Since the transmissivity of the atmosphere is highly variable in the observed wavelengths, absolute calibration is challenging. The system is photometrically calibrated using bright stars of known flux that have been observed every two hours. Care was taken that the stars are observed at similar altitudes to the science objects. For the photometry measurement a distinction is made between objects where the nucleus is a mere point source and objects displaying extended emission. For point sources a $1.6''$ aperture flux was taken, covering the central airy disk out to the first minimum. For extended objects the peak value was used since the PSF is well sampled with $0.2''$ per pixel. Using the peak value minimizes contamination from extended components. For these sources the growth curve of the source and the PSF are also presented in order to make clear which part of the flux comes from an unresolved source. The peak flux corresponds to an aperture of $1.2''$. An exception is NGC 7582, for which the flux was measured with a $2.6''$ aperture. In order to improve the visual appearance all images have also been deconvolved, using a simple but robust, CLEAN method, where a PSF taken from a nearby reference star is iteratively subtracted from the peak position and replaced with a Gaussian with a similar width. Flux errors are dominated by the calibration errors from the reference stars measured by estimating the fluctuations of the transmissivity of the sky by comparing the fluxes of the same objects (stars or AGNs) close in time. Accordingly, the photometric error is about 15% for all sources.
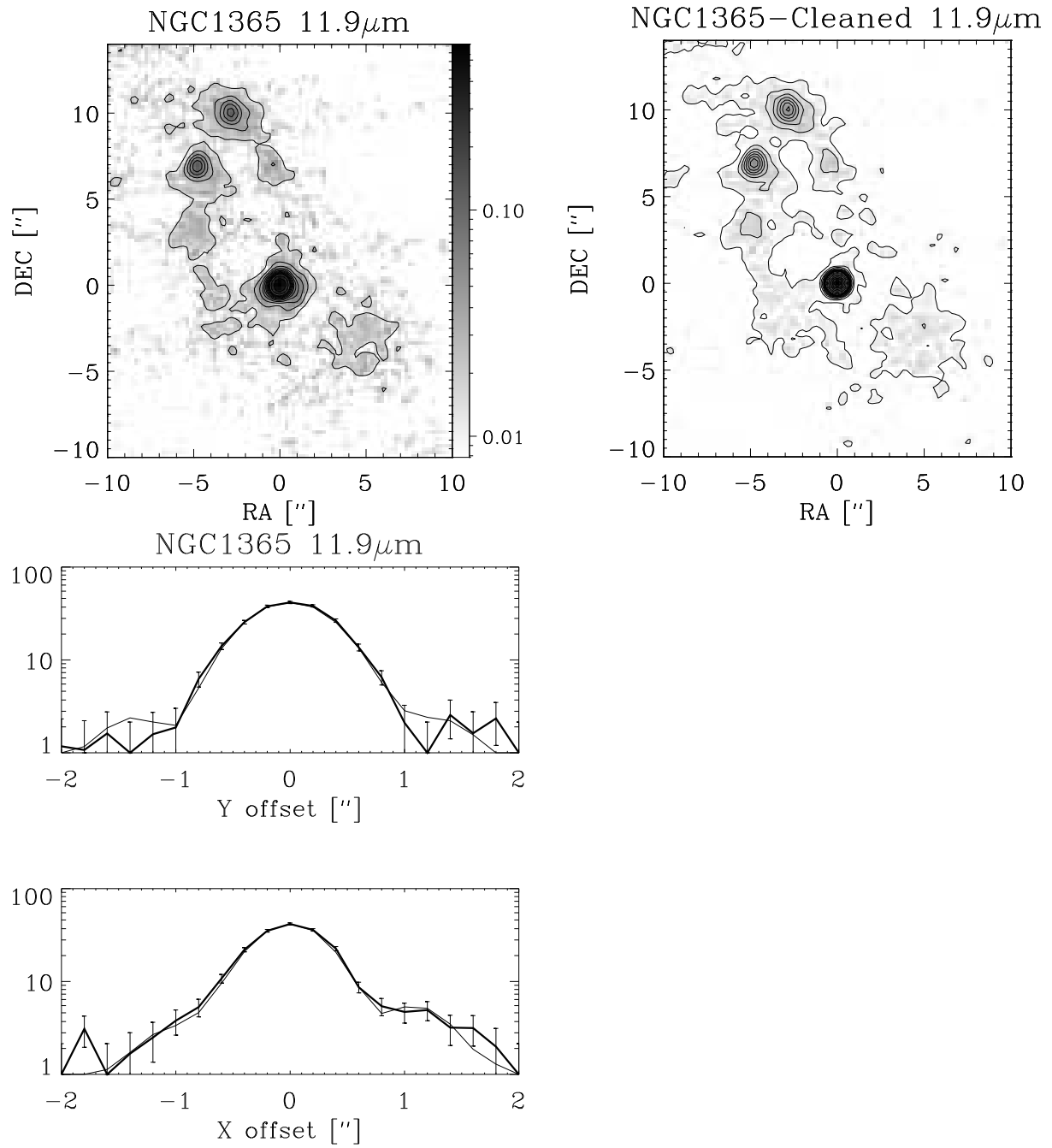
Figure 2.2 — NGC 1365 Contour and image overlays. Left: Raw data. Right: Central point deconvolved with CLEAN algorithm sdf. Bottom: comparison of X and Y axis crosssection with psf, in normalized counts.

2.5   Results

Core flux measurements and core positions for each source are presented in Table 2.1. Figures 2.1 to 2.8 show high resolution contour images of eight objects out of the 21 objects observed, omitting those sources for which more recent images are available and images of unresolved sources. A brief discussion of each source is presented, along with references for other similar or complementary data. All sources show an unresolved core with little or no extended emission, with the exception of NGC 253, NGC 7582, NGC1365, and M83, which show considerable extended emission.

NGC 253   Figure 2.1. This nearby starburst galaxy shows complex extended emission in all observed wavelengths: 8.6, 11.9 and $12.9\mu m$. All images show two sources, the bright source seems to be resolved. The extended emission shows an elongation of 3″ to the north east. An additional peak is seen clearly in the 8.6 μm image, and to a lesser extent in the $11.9\mu m$ image, and corresponds to ″peak 3″ that Kalas & Wynn-Williams (1994) identify at $3.28\mu m$ and is most likely to be PAH emission. The 12.9 μm image, shows the structure boarded by the two peaks reported by Boeker et al. (1998) as well as other authors, and is very similar to the $NeII$ map of these authors and the $NeII$ maps of Keto et al. (1999). It is most likely to be dominated by a combination of $NeII$ emission and $12.7\mu m$ PAH emission (Boeker et al. (1998), Förster Schreiber et al. (2003)). Since the 11.9 filter is centered on $11.66\mu m$ with a FWHM of $1.16\mu m$ it is likely that the $11.9\mu m$ extended emission also includes $11.3\mu m$ PAH emission. Galliano et al. (2005) show $11.9\mu m$ deconvolved images and identify six sources, as opposed to four in our $11.9\mu m$ image Comparing the two images, sources M2 and M3 of Galliano et al. (2005) coincide with our second brightest peak, and sources M5 and M6 with the two peaks to the North-East. The flux measured by Galliano et al. (2005) for the main peak $(5000 \pm 1000\mathrm{mJy})$ is a factor of two higher than the flux measured in this work. This discrepancy can be attributed to the 2″ aperture used by Galliano et al. (2005) as opposed to out method of measuring the peak value (see §2.4) Identifying out second peak with M2+M3 our flux (1150 mJy) is 50 % higher than the combined flux of M2 and M3.

NGC 1365   Figure 2.2. A face-on spiral galaxy with a prominent bar. Our $11.9\mu m$ image shows an unresolved nucleus and two point sources to the north east, identified by Galliano et al. (2005) as M5 and M6. This structure is surrounded by an arm like faint extended emission. In addition, the deconvolved image shows slight point like emission from sources M7 and M4 of Galliano et al. (2005). The authors identify their M4, M5 and M6 sources with radio counterparts of Saikia et al. (1994), and conclude that these sources are embedded young massive star clusters. Flux measurements of the nucleus are in excellent agreement with Galliano et al. (2005), but are higher than those of Siebenmorgen et al. (2004) who measured a flux of 400mJy at $8.5\mu m$ and 460mJy at $10.4\mu m$. This discrepancy can be explained by the multi-source structure of NGC 1365, causing flux measurements very sensitive to telescope positioning. The weak extended emission to the South West of the nucleus also appears as two point sources in the 11.9 and 10.4 μm deconvolved maps of Galliano et al. (2005) and is most likely not an artifact.
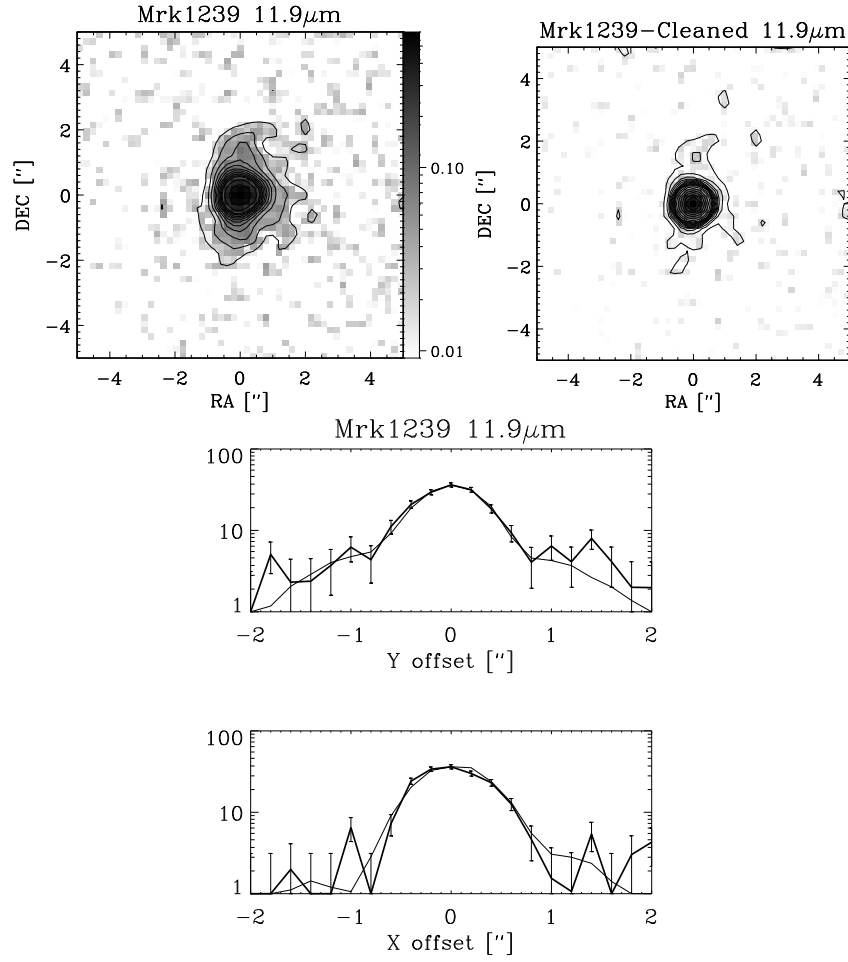
Figure 2.3 — Mrk 1239 contour and image overlays, see Figure 2.2.

IRAS 05189-2524   Observations of this Seyfert 2 galaxy at $11.9\mu m$ show a completely unresolved core with no deviations from the PSF larger then 1σ. An unresolved core is also reported by Siebenmorgen et al. (2004) with 8.6, 10.4 and 11.9μm flux densities of 420,420 and 570 mJy, respectively, and by Soifer et al. (2000), who present a 12.5μm image and 12.5 24.5μm fluxes.

NGC 2377   For this object we give an upper limit for the flux of 60mJy.

MCG 5-23-16   For this S0 galaxy hosting a Seyfert 1.9 nucleus we have an unresolved core with a flux of 646 mJy at 11.9μm .

Mrk1239   Figure 2.3 Observations of this highly polarised narrow-line Seyfert 1 galaxy at 11.9μm shows central source unresolved. The 11.9μm flux is in agreement with Maiolino et al. (1995).

NGC 3256   Our image (not presented here) of this IR-luminous merger system shows an unresolved core, In contrast to Siebenmorgen et al. (2004) who present a resolved,

yet featureless image, taken with shorter exposure time. The difference may be explained by a change in seeing between the calibrator, from which the PSF is determined, and NGC 3256.

NGC 3281 For this Seyfert 2 galaxy we measure 625 mJy for 11.9 μm, which is similar to the N-band flux found at Krabbe et al. (2001) 580 ± 30 mJy, measured with a 2.2m telescope, and therefore a diffraction limit 1.6 times that of our observation. A $18'' \times 20''$ 10.5 μm image of NGC 3281 dominated by a point source and marginal evidence for an extended emission component is Krabbe et al. (2001).

NGC 3758 (Mkn 739) For this double-nuclei Seyfert I/starburst galaxy a low flux of < 60 mJy is measured.

NGC 3783 NGC 3783 is a nearly face-on SBa galaxy with a very bright, highly variable, Seyfert 1 nucleus. The image shows an unresolved point source.

3C273 The image of this well known quasar shows an unresolved core at $11.9\mu m$. The measured $11.9\mu m$ flux is in agreement with the N-band flux of Sitko et al. (1982) but 100mJy higher than the flux quoted in Gorjian et al. (2004).

NGC 4594 "Sombrero Galaxy". For this object the measured $11.9\mu m$ flux, $< 60mJy$, is in agreement with the results found at Maiolino et al. (1995) and Gorjian et al. (2004).

MCG-3-34-6 The low flux measured here, < 60 mJy at $11.9\mu m$ is much smaller than the 440 mJy flux measured by Maiolino et al. (1995) at $10.4\mu m$, with a $5.4''$ aperture. The origin of the discrepancy are unclear since this object has not been studied before apart from the single measurement of Maiolino et al. (1995) mentioned above, and so it is possible that the N-band emission is variable. Our image shows an unresolved point source and therefore it is unlikely that extended emission is responsible for the discrepancy.

NGC 5128 Figure 2.4 Centaurus A, the closest active radio galaxy. The 11.9 μm image shows an unresolved central core, with extended emission at 10% level. The $8.6\mu m$ image shows an unresolved core. For comparison, see Siebenmorgen et al. (2004) for a $10.4\mu m$ image showing an unresolved core of less than $0.5''$.

M 83 Figure 2.5 This near, face-on barred spiral galaxy shows mostly extended emission surrounding a faint central object. The extended emission is dominated by PAHs which account for the majority if the MIR luminosity (Vogler et al. 2005). The $11.9\mu m$ flux measured, 232 mJy, is identical with the $11.9\mu m$ flux measured by Siebenmorgen et al. (2004). Our images, however, show a clear, although faint, central source, while Siebenmorgen et al. (2004) report only fuzzy extended emission. The LW3 filter ($12 - 18\mu m$) of Vogler et al. (2005) show the emission clearly tracing the spiral arms of M83, which is not seen in our image.
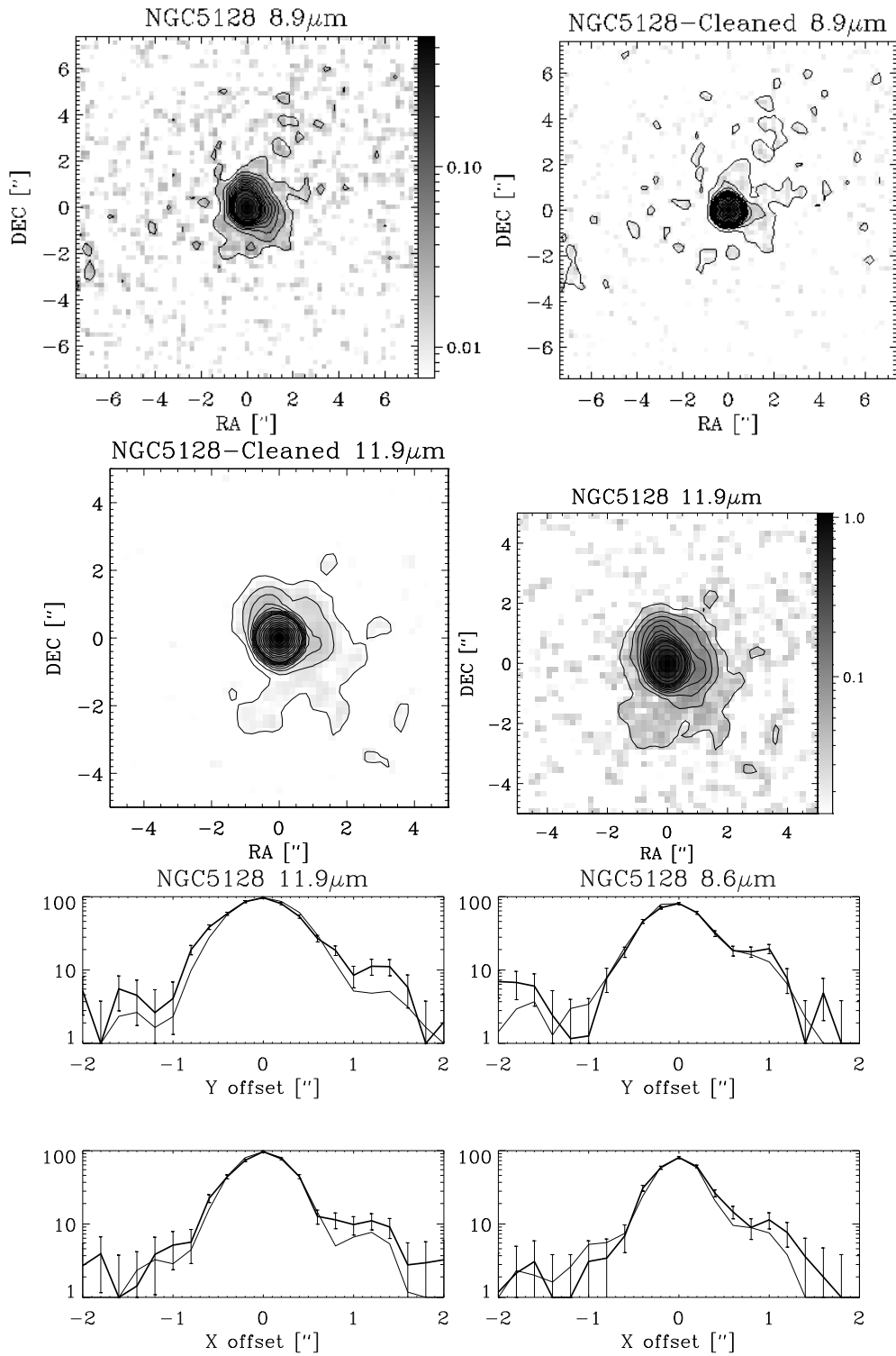
Figure 2.4 — NGC 5128 contour and image overlays, see Figure 2.2.
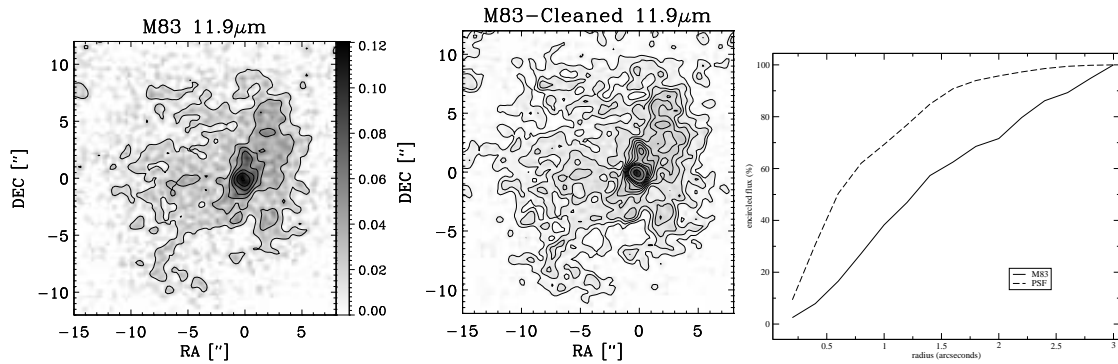
Figure 2.5 — M 83 contour and image overlays, see Figure 2.2. Bottom: growth curve of core compared with the PSF.
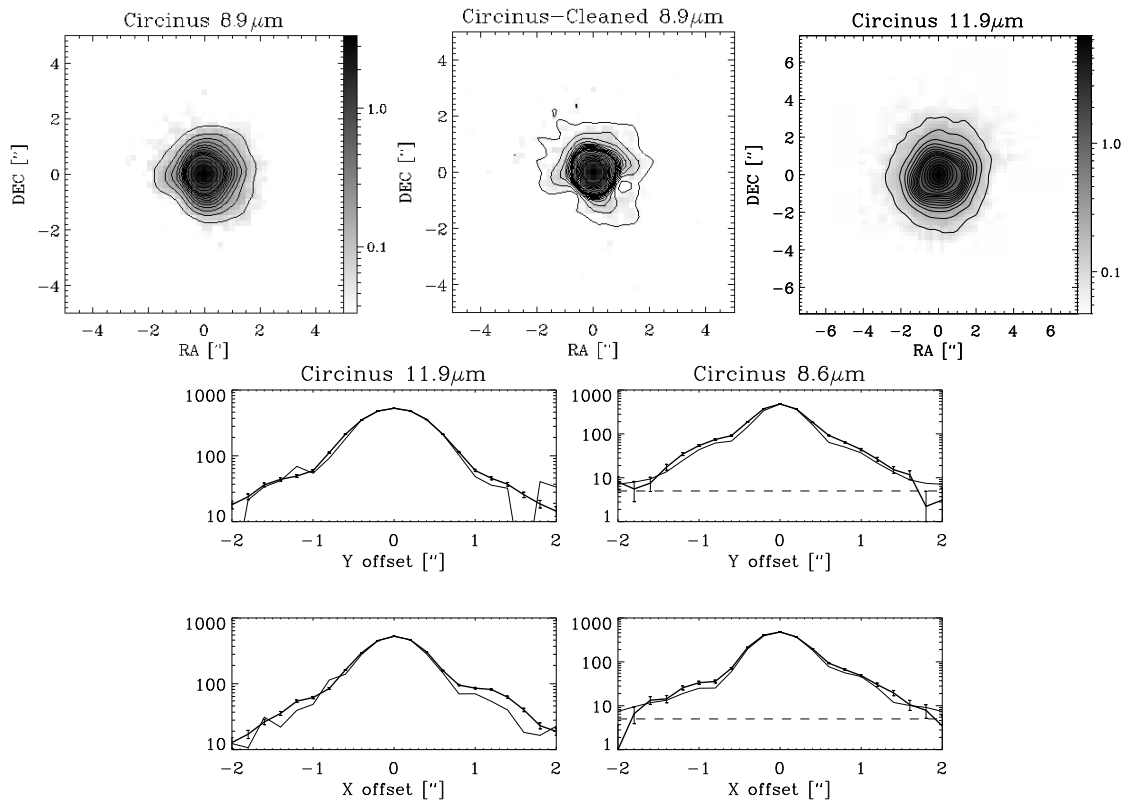
Figure 2.6 — Circinus contour and image overlays, see Figure 2.2.
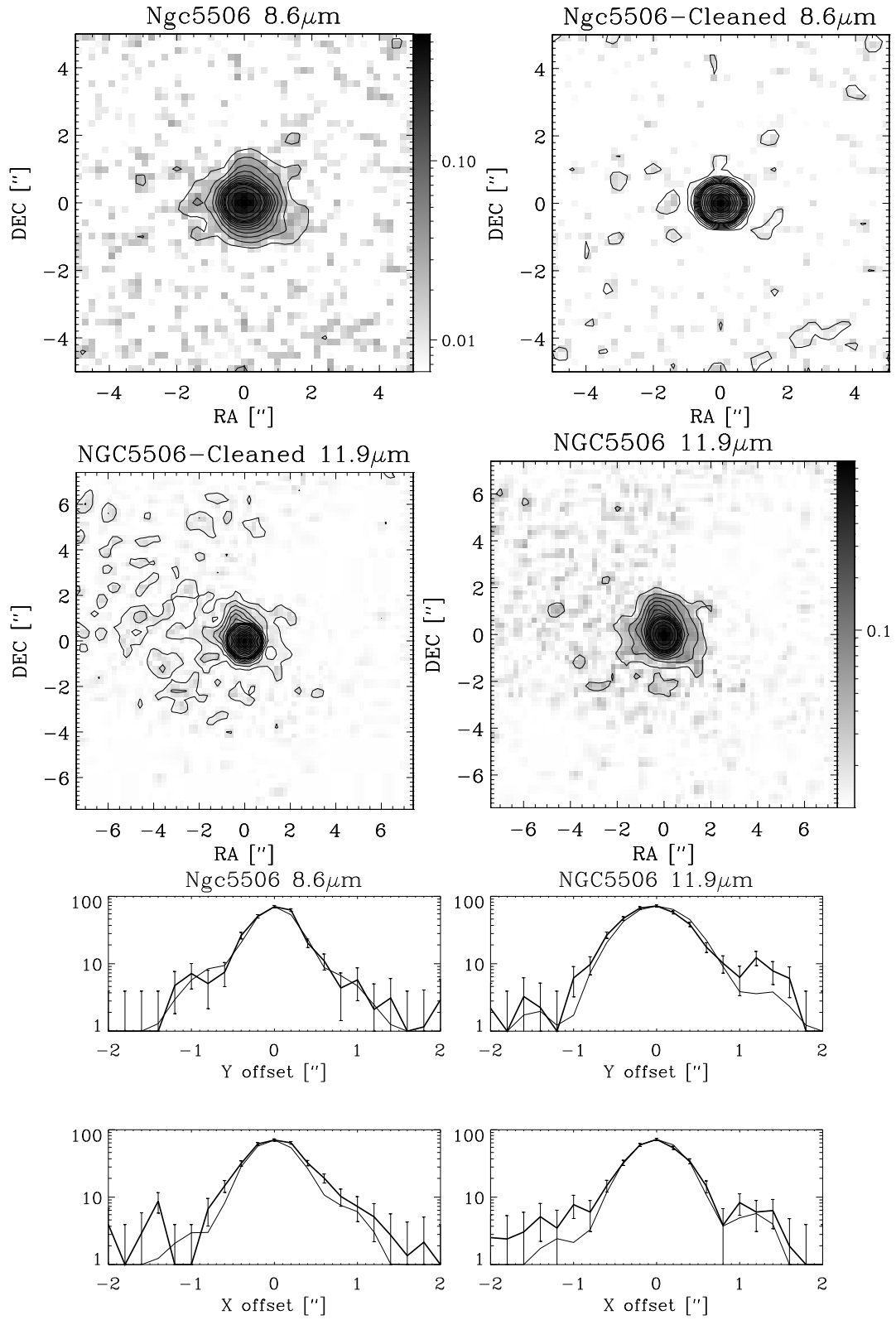
Figure 2.7 — NGC 5506 contour and image overlays, see Figure 2.2.

ESO 445-G50   For this Seyfert I galaxy we measure 352 mJy at 11.9μm . A 10.4 μm flux of 640 mJy can be found at Siebenmorgen et al. (2004).

Mrk463   The image of this double-nuclei Seyfert 2 galaxy shows an unresolved core at 11.9μm , measuring 338 mJy.

Circinus   Figure 2.6 Observations of this nearby spiral were made at 11.9 μm and 8.6 μm . The seeing at for the 11.9 μm point was bad, so no statement can be made whether the central peak is resolved or not. The 8.6 μm does show a slightly resolved background component yet whether this is a disk or circum-nuclear emission (reported by Krabbe et al. (2001) with a radius of $\approx 1''$ is not clear. The image presented here is very similar to the one presented by Siebenmorgen et al. (2004). Recent high resolution 8.74 and 18.33μm images and flux measurements are also presented by Packhamet al. (2005), which also find a higher 8.74μm flux, 5.5-8.4 Jy, for a range of apertures from $1''$ to $5''$.

NGC 5506   Figure 2.7 For this edge-one irregular Seyfert 1 (S1i) galaxy ,we show here the first high resolution images at 8.6 and 11. 9μm . The 8.6μm image shows an unresolved core while extended emission to the north-east is seen in the 11.9μm image. The 11.9μm flux measured, 908 mJy, is similar to the Siebenmorgen et al. (2004) measurement of 1060 mJy.

NGC 7469   For this prototypical Seyfert 1 galaxy we encountered an unknown image quality problem. Soifer et al. (2003) present a high resolution ($4'' \times 4''$) 12.5 μm image of the nucleus of NGC 7469, resolving the ring structure around the nucleus and an extended structure in the nucleus itself.

NGC 7582   NGC 7582 is a classic Seyfert 2 galaxy which, during a period of five months in 1999 showed broad lines characteristic of a Seyfert 1 galaxy, which may indicate the presence of a patchy torus. Aretxaga et al. (1999). 50% of the flux found in extended emission with a peak offset from the center of the extended emission. The extended emission is seen elongated along the South-North direction. The 12.9μm image shows two weak sources to the North and to the South of the main peak, also clearly seen in the 12.9μm image of Acosta-Pulido et al. (2003). The 11.9μm image shows one slightly resolved peak surrounded by extended emission. Flux at 11.9μm is very similar to that of Siebenmorgen et al. (2004), although the 11.9μm image they present shows considerably less extended emission. Similar extended emission can also be seen in the N1 ($\approx 8 - 95.5\mu$m) image of Acosta-Pulido et al. (2003).

2.6   Conclusion

We presented new high resolution mid-infrared images and fluxes at 8.9,11.9 and 12.9μm for the brightest AGN's observable from Cerro-Paranal. Most sources show an unresolved core, with little or no extended emission. Considerable extended emission has

only been detected for NGC 253, NGC 7582 and M83. For each source, a brief discussion is given along with a comparison with other relevant published data. In general we find our images and fluxes to be in agreement with previous papers.
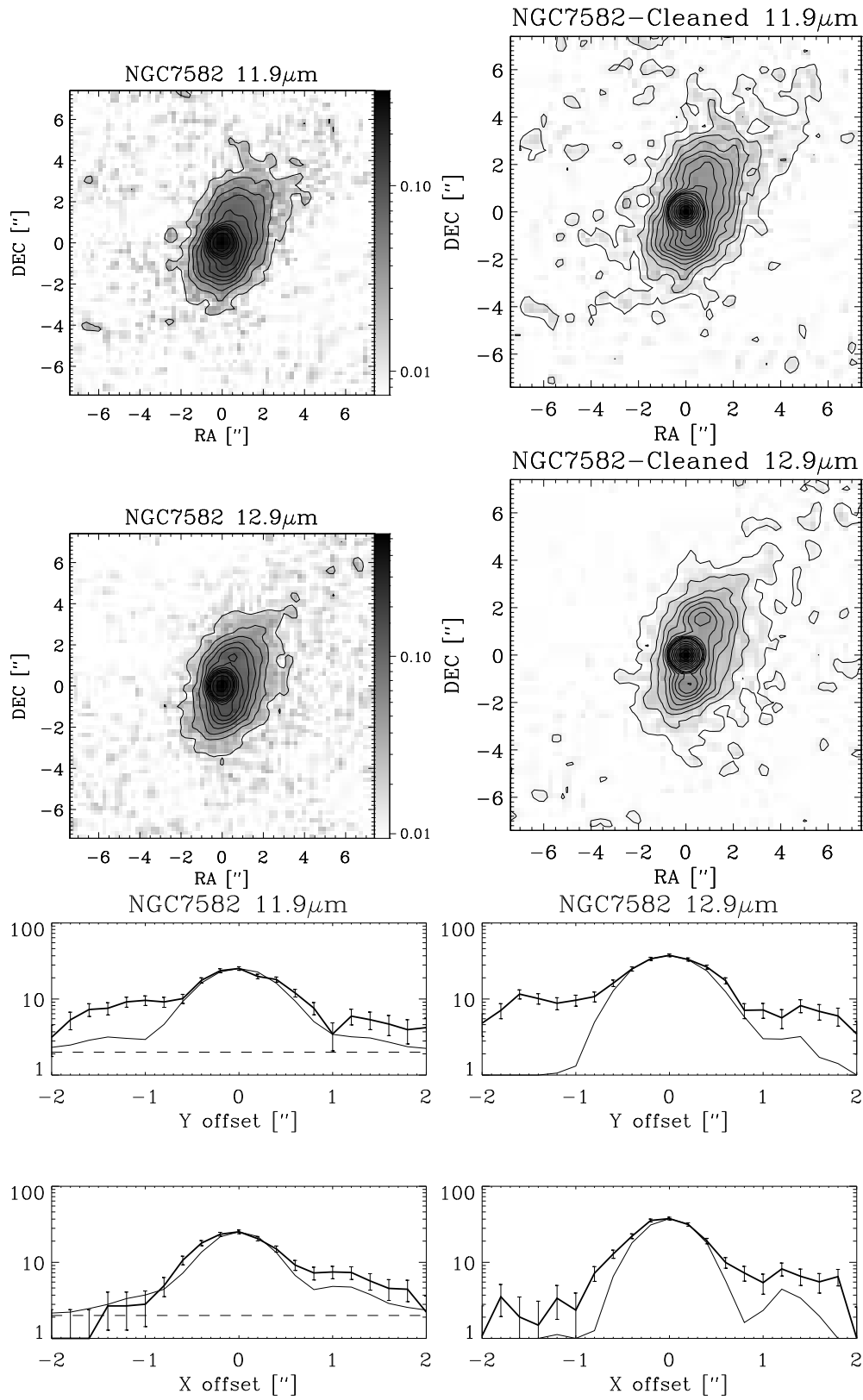
Figure 2.8 — NGC 7582 contour and image overlays, see Figure 2.2.

References

Acosta-Pulido, J. A., Pérez García, A. M., Prieto, M. A., Rodríguez-Espinosa, J. M., & Cairós, L. M. 2003, in Revista Mexicana de Astronomia y Astrofisica Conference Series, 198–201

Aretxaga, I., Joguet, B., Kunth, D., Melnick, J., & Terlevich, R. J. 1999, ApJ, 519, 123

Boeker, T., Krabbe, A., & Storey, J. W. V. 1998, ApJ, 498, L115+

Förster Schreiber, N. M., Sauvage, M., Charmandaris, V., et al. 2003, A&A, 399, 833

Galliano, E., Alloin, D., Pantin, E., Lagage, P. O., & Marco, O. 2005, A&A, 438, 803

Gorjian, V., Werner, M. W., Jarrett, T. H., Cole, D. M., & Ressler, M. E. 2004, ApJ, 605, 156

Granato, G. L., Danese, L., & Franceschini, A. 1997, ApJ, 486, 147

Jaffe W., Meisenheimer K., Röttgering H. J. A., Leinert C., Richichi A., Chesneau O., Fraix-Burnet D., Glazenborg-Kluttig A., Granato G.-L., Graser U., Heijligers B., Köhler R., Malbet F., Miley G. K., Paresce F., Pel J.-W., Perrin G., Przygodda F., Schoeller M., Sol H., Waters L. B. F. M., Weigelt G., Woillez J., de Zeeuw P. T., 2004, Nature, 429, 47

Käufl, H., Sterzik, M. F., Siebenmorgen, R., et al. 2003, in Instrument Design and Performance for Optical/Infrared Ground-based Telescopes. Edited by Iye, Masanori; Moorwood, Alan F. M. Proceedings of the SPIE, Volume 4841, pp. 117-128 (2003)., 117–128

Kalas, P. & Wynn-Williams, C. G. 1994, ApJ, 434, 546

Keto, E., Hora, J. L., Fazio, G. G., Hoffmann, W., & Deutsch, L. 1999, ApJ, 518, 183

Krabbe, A., Böker, T., & Maiolino, R. 2001, ApJ, 557, 626

Leinert, C., van Boekel, R., Waters, L. B. F. M., et al. 2004, A&A, 423, 537

Lipovetsky, V. A., Neizvestny, S. I., & Neizvestnaya, O. M. 1988, Soobshcheniya Spetsial'noj Astrofizicheskoj Observatorii, 55, 5

Maiolino, R., Ruiz, M., Rieke, G. H., & Keller, L. D. 1995, ApJ, 446, 561

Meisenheimer, K., Tristram, K. R. W., Jaffe, W., et al. 2007, A&A, 471, 453

Ohnaka, K., Bergeat, J., Driebe, T., et al. 2005, A&A, 429, 1057

Packham, C., Radomski, J. T. , Roche,et al. 2005, ApJ, 618, L17-L20

Reimann, H., Linz, H., Wagner, R., et al. 2000, in Proc. SPIE Vol. 4008, p. 1132-1143, Optical and IR Telescope Instrumentation and Detectors, Masanori Iye; Alan F. Moorwood; Eds., 1132–1143

Saikia, D. J., Pedlar, A., Unger, S. W., & Axon, D. J. 1994, MNRAS, 270, 46

Siebenmorgen, R., Krügel, E., & Spoon, H. W. W. 2004, A&A, 414, 123

Sitko, M. L., Stein, W. A., Zhang, Y.-X., & Wisniewski, W. Z. 1982, ApJ, 259, 486

Soifer, B. T., Bock, J. J., Marsh, K., et al. 2003, AJ, 126, 143

Soifer, B. T., Neugebauer, G., Matthews, K., et al. 2000, AJ, 119, 509

Starck, J. L., Abergel, A., Aussel, H., et al. 1999, A&AS, 134, 135

Tristram, K. R. W., Meisenheimer, K., Jaffe, W., et al. 2007, A&A, 474, 837

Vogler, A., Madden, S. C., Beck, R., et al. 2005, A&A, 441, 491

Chapter 3

Resolving the dusty torus in NGC 1068

Abstract. We present new interferometric data obtained with MIDI (MID infrared Interferometric instrument) for the Seyfert II galaxy NGC 1068, with an extensive coverage of sixteen *uv* points. These observations resolve the nuclear mid-infrared emission from NGC 1068 in unprecedented detail with a maximum resolution of 7 milliarcseconds.

For the first time, sufficient *uv* points have been obtained, allowing us to generate an image of the source using maximum entropy image reconstruction. The features of the image are similar to those obtained by modelling.

We find that the mid-infrared emission can be represented by two components, each with a Gaussian brightness distribution. The first, identified as the inner funnel of the obscuring torus, is hot ($\sim$800K), 1.35 parsec long, and 0.45 parsec thick in FWHM at a PA=$-42°$ (from north to east). It has an absorption profile different than standard interstellar dust and with evidence for clumpiness.

The second component is 3×4 pc in FWHM with T=$\sim$300K, and we identify it with the cooler body of the torus. The compact component is tilted by $\sim 45°$ with respect to the radio jet and has similar size and orientation to the observed water maser distribution.

We show how the dust distribution relates to other observables within a few parsecs of the core of the galaxy such as the nuclear masers, the radio jet, and the ionization cone. We compare our findings to a similar study of the Circinus galaxy and other relevant studies.

Our findings shed new light on the relation between the different parsec-scale components in NGC 1068 and the obscuring torus.

D. Raban, W. Jaffe, H. Röttgering, K. Meisenheimer and K. Tristram
Monthly Notices of the Roayal Astronomical Society, 394, 1325 (2009)

3.1   Introduction

T HE AGN unification model (Antonucci 1993; Urry & Padovani 1995) explains the
difference between type II Seyferts, which show only narrow emission lines, and
type I, which show both narrow and broad emission lines, by stipulating that a torus-
like structure surrounds the central engine and accretion disk. Thus, when oriented
edge-on, the torus blocks the subparsec-sized broad emission line region making the
object appear as a type II, while harbouring an unseen type I nucleus. Symmetry and
angular momentum considerations suggest that the torus and the accretion disk are
perpendicular to the bipolar jet, whose orientation is likely to be coupled closely to
that of the accreted matter. The relative number of Seyfert I/II demands that the torus
be geometrically thick (Osterbrock & Shaw 1988), although thick structures orbiting
compact objects will quickly lose their height and collapse into a thin disk. In order to
maintain its stable torus structure, the random velocities of the dust clouds need to be
of an order similar to the orbital speed, or a few hundred km/s. Since colliding dust
clouds are destroyed at relative speeds as low as a few meters per second, the dust
clouds are not expected to last very long (Krolik & Begelman 1988). To overcome the
difficulty of maintaining its inflated state different dust configuration other than a torus
have been introduced, such as the warped disk of Sanders et al. (1989). Alternatively,
the dust has been described as a hydrodynamically driven outflow (Kartje & Königl
1996).

NGC 1068 is considered to be the prototype Seyfert II galaxy, where the central
source is obscured by dust. Its relatively small distance of 14.4 Mpc and high mid-
infrared flux make the object ideally suited for the study of the nucleus and obscuring
dust. Previous MIDI observations of NGC 1068 revealed warm (320 K) silicate dust in a
structure 2.1 parsecs thick and 3.4 parsecs in diameter, surrounding a small, hot (800K)
component whose shape and orientation could not be determined in detail (Jaffe et al.
2004) (hereafter J04). These observations were, together with those of Wittkowski et al.
(2004) (W04), the first to spatially resolve direct emission from the putative torus, and
the first to show that a torus-like structure is indeed present in NGC 1068.

The mid-infrared emission from the central region of NGC 1068, as seen by the
largest single dish telescopes, is composed of an unresolved core plus extended emis-
sion. Deconvolved maps at 12μm taken with VISIR (Imager and Spectrometer in the
InfraRed at the Very Large Telescope) by Galliano et al. (2005) reveal a set of discrete
mid-infrared sources: seven in the north-eastern quadrant and five in the south-eastern
quadrant. The central source, observed with the 10m Keck telescope (Bock et al. 2000),
is extended by $\sim$1" in the north-south direction and is unresolved in the east-west
direction. About 2/3 of its flux can be ascribed to a core structure which is itself elon-
gated north-south in a tongue-shaped structure and according to Bock et al. (2000)
does not show a distinct unresolved core. Recent 12.8μm speckle images taken with
VISIR in BURST mode by Poncelet et al. (2007) identify two major sources of emis-
sion at 12.8μm: a compact source (< 85 mas) and an elliptical source of size (< 140)
mas $\times$ 1187 mas and PA$\sim 4°$. It is the unresolved compact source which is associated
with the dusty torus and is the subject of this study. Other parsec scale components
in NGC 1068 that are related to the torus are the compact H$_2$O masers , appearing on

Figure 3.1 — *uv* coverage [m] for NGC1068 and colour coded by date. Due to the ∼0.0 declination of NGC1068, the *uv* tracks are parallel to the u-axis. *uv* coords [u,v] are complex conjugates of uv coords [-u,-v], and both are plotted since they are indistinguishable.
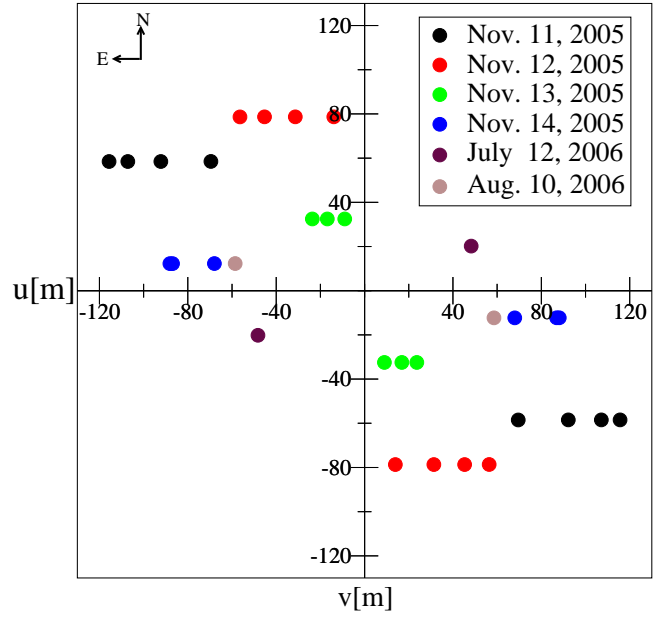
the sky as a set of linear spots (PA=−45°) that are misaligned with the jet and span a velocity range of 600 km/s with a sub-Keplerian velocity profile ($v \propto r^{-0.3}$). The kinematics of the maser spots indicate that the masers are located in a rotating disk with inner radius of ∼0.65 pc and outer radius of ∼1.1 pc (Gallimore et al. 2001). This disk traces the outer, colder part of the accretion disk where conditions allow for the formation of water masers. It was proposed earlier that these masers trace warm molecular dust (Claussen & Lo 1986), a conclusion supported by the observations presented here which reveal the dusty torus to be at the outer edge of the maser disk. VLBA 5 and 8.4GHz radio continuum images show a parsec-sized structure with a major axis at PA≃-75°, most likely indicating free-free emission from hot (T=$10^4 - 10^5$ K) ionized gas (Gallimore et al. 2004). According to the unification model, toroidal obscuration by dust is also responsible for the conical shape of the narrow-line region. The ionization cone in NGC 1068 as seen in HST images is centred around PA=10°, while modelling of HST spectra, based on the kinematics of the gas indicate the ionization cone with an opening angle of 80° centred around PA=30° (Das et al. 2006), roughly perpendicular to the maser spots.

3.2 Observations, *uv* coverage and data reduction

MIDI is the mid-infrared interferometer located on Cerro Paranal in northern Chile and operated by the European Southern Observatory (ESO). MIDI functions as a classical Michelson interferometer, combining the light from two 8-meter unit telescopes (UTs). For a detailed description of the instrument see Leinert et al. (2003). The main data product of MIDI is the correlated flux, which can be explained as the spectrum of the source at a certain spatial resolution projected perpendicular to the baseline, that is to the projected separation of the two telescopes.

A total of 16 interferometric observations were taken together with a single-dish total flux spectrum for each one. Table 3.1 contains the observation log. All observations

Table 3.1.　Log of the observations dates, unit telescopes used and baseline configuration in polar (D[m], PA[degree]) coordinates projected on sky.

No.	Date	# UT's	D	PA	resolution[a]
#1	Nov. 11, 2005	UT1-UT4	90.8	50.0	10.3
#2		"	109.2	57.6	8.6
#3		"	122.	61.4	7.7
#4		"	129.6	63.2	7.2
#5	Nov. 12, 2005	UT1-UT3	79.9	10.0	11.7
#6		"	84.7	21.7	11
#7		"	90.8	29.9	10.3
#8		"	96.8	35.6	9.7
#9	Nov. 13, 2005	UT2-UT3	33.6	15.5	27.9
#10		"	36.6	27.5	25.6
#11		"	40.15	36.1	23.4
#12	Nov. 14, 2005	UT2-UT4	69.0	79.8	13.6
#13		"	89.98	82.1	10.4
#14		"	87.76	82.0	10.7
#15	July 12, 2006	UT3-UT4	52.3	-67.3	17.9
#16	Aug. 10, 2006	UT2-UT4	59.82	78.2	15.6

[a]The spatial resolution in milliarseconds is calculated by $\theta = \lambda/(2.2B)$ where B is the projected baseline separation and $\lambda = 10\mu m$.

were done in GRISM mode with a spectral resolution of $\lambda/\Delta\lambda = 230$. The same calibrator, HD10380, was used for all observations with identical settings. Chopping with $f = 1$Hz, and throw amplitude of 15" at an angle $\alpha = 0°$ was applied during photometric measurement and acquisition. Fringes were tracked in "offset tracking" mode.

A map of the *uv* coverage is shown in Fig. 3.1. Due to the near zero declination of NGC 1068 the tracks are parallel to the u-axis, causing each observation to differ both by baseline length and position angle from its neighbours. The distribution of the tracks is concentrated in the second/fourth quarter of the *uv* plane, with only one observation on a perpendicular baseline, reflecting the fixed physical placement of the VLTI unit telescopes. After each interferometric observation, a total flux measurement (i.e. single-dish spectrum) is taken from each telescope independently, and used to determine the visibility, i.e. the correlated interferometric flux divided by the geometric mean of the single dish fluxes. Only one such observation was rejected due to bad seeing, and the remaining 15 fluxes were averaged together (Fig. 3.2). A typical MIDI observation is recorded in 8000 frames, with an integration time of 0.036 seconds for each frame. We examined the total flux recorded on the detector per frame, and rejected frames where the flux was unstable. Data reduction was done by coherent vis-

ibility estimation with the Expert Work Station (EWS) package written in Leiden. See Jaffe (2004) for a detailed description of the coherent visibility estimation method.

3.2.1 Calibration

Calibration of the interferometric and photometric data was done using HD10380 as the calibrator star for all observations. Each night's observation started with HD10380, and it was observed between observations of NGC 1068. Thus, we obtained a calibration measurement for each *uv* point of NGC 1068. The calibrator's data reduction was done using the same parameters as for NGC 1068 and went through the same tests for consistency as for the science target. Only one calibrator observation was rejected due to bad seeing. Calibration measurements taken just before and after NGC 1068 were compared and, if different, were averaged. For an unresolved point source, the correlated flux should equal the total flux. Assuming this, we can calibrate the correlated fluxes using the calibrators, without a need to use the photometry measurements, which are less reliable due to the strong atmospheric background. The calibrated fluxes are computed by dividing the correlated fluxes of the target by those of the calibrator, and then multiplying by the known flux of the calibrator. For HD 10380 we used the spectral template of Cohen et al. (1999). The calibrated photometric fluxes were produced by the same procedure for the photometric data.

3.2.2 Correlated flux. vs. visibility

Optical/infrared interferometric data is often presented as visibility data, a dimensionless quantity, which measures the fraction of flux that is resolved for a given baseline. Here we prefer to use the correlated fluxes, the actual flux that the interferometer measures for a given baseline, as is common practice in radio interferometry. Determining the visibility, V, directly from the contrast of the interferometric fringes ($V = (I_{max} - I_{min})/(I_{max} + I_{min})$) is not practical since the amount of flux reaching the beam combiner from the two telescopes is generally not equal and therefore affects the contrast of the fringes. Given an isolated source, the visibilities equal the correlated fluxes divided by the total flux of the source. If, however, the source is embedded in emission on larger scales (as seems to be the case for NGC 1068), then the total flux determined by a larger field of view is contaminated by the large scale emission making it difficult to interpret. The correlated fluxes also free us from handling the strong atmospheric background, which is not correlated and is removed easily in the data reduction process.

3.3 Results

3.3.1 The total flux

The total flux of NGC 1068 is shown in Fig. 3.2, as measured by the average of two 8-meter UTs, each with a beam size of 250 mas . It is in rough agreement with previously published spectra from 8m class telescopes. The only spectral feature seen in the total flux is the 9.7μm silicate feature, in absorption. We do not detect the very weak [SIV] emission line reported by Rhee & Larkin (2006) and Mason et al. (2006) with similar
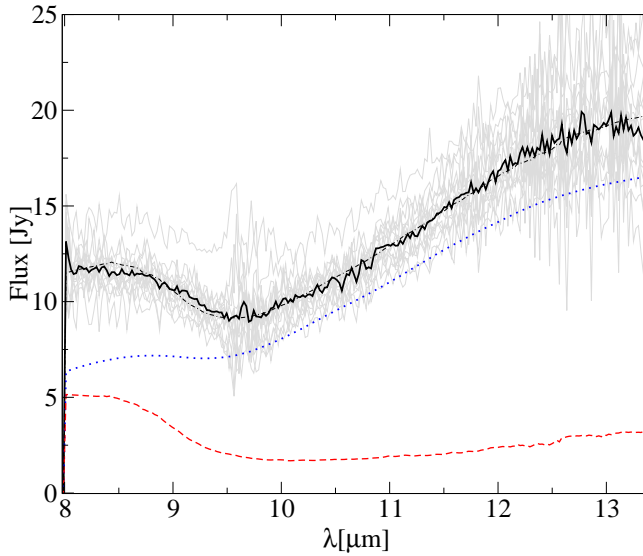
Figure 3.2 — Total (single-dish) flux. All 15 individual spectra are in grey with the mean given in black. The dash-dotted line is the model fit described in section 3.4.1, which is composed of two flux components: component 1 (red-dashed) and component 2 (blue-dotted). Note the atmospheric O_3 feature at 9.7μm.

apertures. Space based instruments show PAH features at $\lambda = 7.6, 9$ and 10.9μm (Sturm et al. 2000). These features are found to occur at larger distances from the nucleus.

3.3.2   The correlated (interferometric) fluxes

The correlated fluxes, shown in Figures 3.3&3.4 display large variations in the shape and depth of the silicate feature centred at 9.7μm, the only spectral feature present in the data. No traces of PAH molecules or the 12.9μm Ne line are seen. The clear relation seen in the data between the baseline length and the correlated flux shows that the source is resolved on every baseline. The 'bump' around 9.7μm seen in baselines #9-14,16 (Figures 3.3&3.4) is due to the atmospheric ozone feature, centred 9.7μm.

3.3.3   Discussion of the results

The correlated fluxes in fact sample the SED of NGC 1068 about a range of different orientations and spatial resolutions. The structure of the spectra, and in particular the 9.7μm silicate feature, varies considerably with baselines, and is quite different from the total flux. The striking differences between the correlated and total fluxes demonstrate how inadequate the total flux is as the sole means to constrain torus models. Indeed, numerous authors have attempted to fit tori models to the SED of NGC 1068, and many different models fit the SED equally well, as was first demonstrated by Galliano et al. (2003).

The depth of the silicate feature in the correlated fluxes is about 0.6 of the continuum level (as defined by the average of the flux at 8 and 13μm) and is independent of baseline length. This suggests that the emitting medium is compact and is located in a region much smaller than the absorbing medium. For the total flux, the silicate feature depth is smaller, ~ 0.3. The total flux can be successfully fitted with a combination of two grey body spectra, a warm ($\sim$300K) component, plus a hot ($\sim$800K) compact component, both behind uniform absorption screens as discussed in §3.4.1. In general we find the total flux to be easily reproducible by our models described in §3.4.1 for a wide range of parameters.
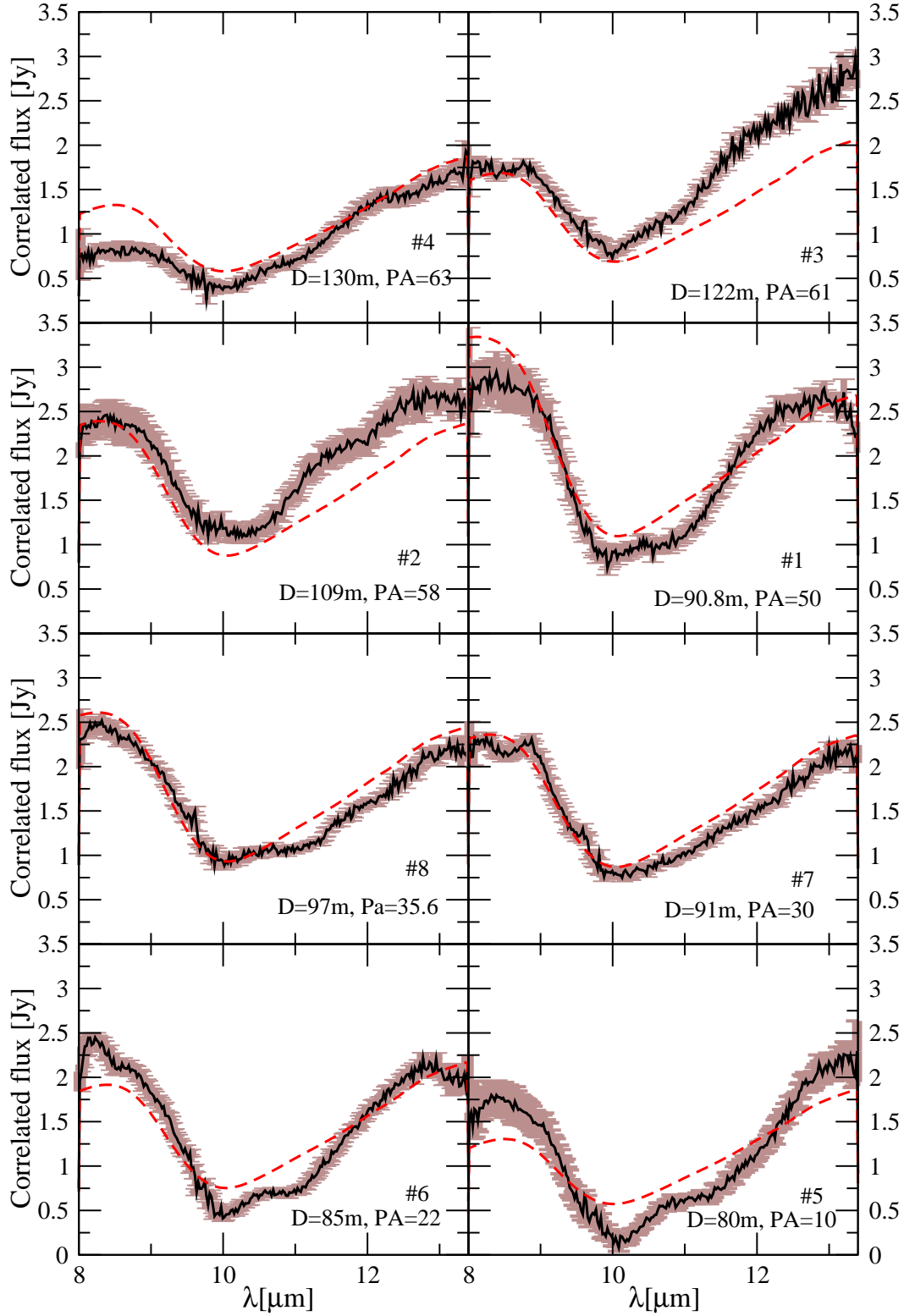
Figure 3.3 — Correlated fluxes #1-8 (solid black) and the model fit from section 3.4.1 (red-dashed). The panels are sorted according to baseline length and the unit telescopes used, and are numbered according to the number in the observation log (Table 3.1).
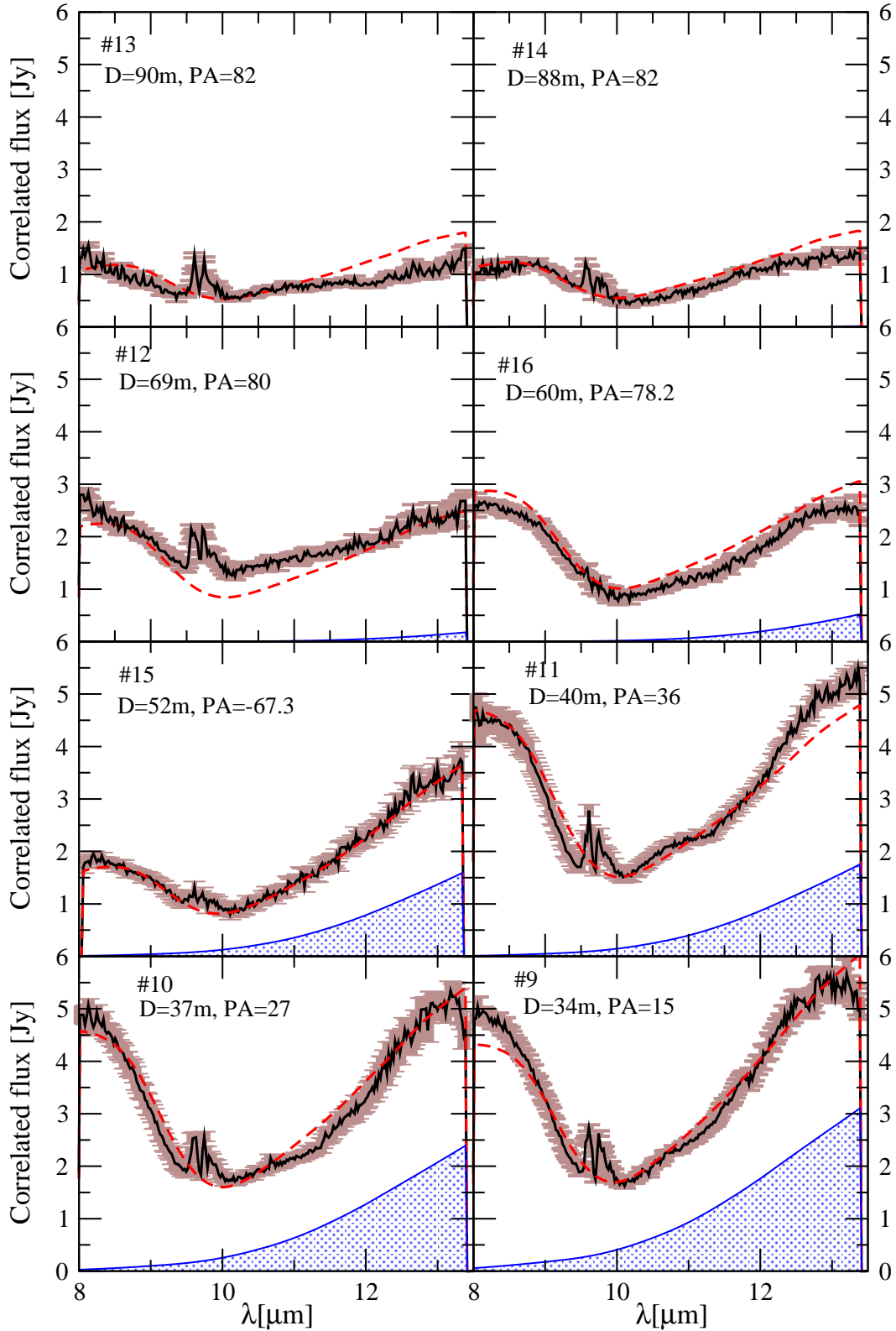
Figure 3.4 — Correlated fluxes #9-16 (solid black) and the model fit described in section 3.4.1 (red-dashed). The blue filled curves show the contribution of component 2 to the correlated fluxes. The 'bump' at 9.7μm visible on fluxes #9-14,16 is due to the atmospheric O_3 feature. The panels are sorted according to baseline length and the unit telescopes used, and are numbered according to the number in the observation log (Table 3.1).

A note on phases and symmetry

Apart from the correlated and total fluxes, one can also recover the differential phase $\phi_{diff}(k)$ of the source from MIDI data. The differential phase is related to the source's true phase, $\phi(k)$, by $\phi_{diff}(k) = \phi(k) - C \times k$, where $k = 2\pi/\lambda$ is the wave number and C is an unknown constant. Thus, any linear dependence of ϕ on k is removed from the differential phase in the data reduction process, and cannot be recovered. This missing information in the differential phase makes it very challenging to include it in our models. We have therefore postponed treatment of the differential phase in NGC 1068 to a second paper. Without the phase information, only models or images which possess inversion symmetry can be applied to the data. Throughout this paper, we assume a symmetric flux distribution. This is an instrumental limitation and we do not claim that the true source brightness possesses such symmetry.

3.4 Modelling

As interferometric data is obtained in Fourier space, interpreting the data is not as straightforward as in direct imaging or spectroscopy. In infrared interferometry, where only a small number of the absolute value of the Fourier components can be measured, the results are often model dependent and difficult to interpret unambiguously. The effective resolution for each uv point is determined by λ/B, the projected separation between the telescopes expressed in number of wavelengths. This relation causes the spectral features of the source, which strongly depend on λ, to become entangled with the spatial flux distribution as observed by telescopes of separation B. We have attempted to disentangle the two effects by using two different modelling approaches. First, we treat the flux distribution as coming from two Gaussian components, each with a fixed size and orientation. Each component is assumed to be a grey body with a fixed temperature and situated behind a uniform absorption screen (§3.4.1). The model results show us that at 8μm only one component contributes to the correlated flux. Therefore, we chose to attempt to reconstruct an image at this wavelength, which is shown and discussed in §3.4.2. The image agrees well with the modelling results. In our third approach (§3.4.3) we look at each wavelength independently and fit a single Gaussian component to each, assuming no relation between the different wavelengths in the data, and assuming all the observed structures in the correlated fluxes arise from the different source sizes and orientation at each wavelength (channel by channel fitting). A good understanding of the observed properties of NGC 1068 can then be achieved by combining the results from the different procedures.

3.4.1 Two grey body model

The first approach to disentangling structure and spectrum is to assume that changes to the correlated fluxes with wavelength are solely due to spectral effects, i.e. a grey body emission undergoing absorption while keeping the spatial parameters constant with wavelength. In this model we treat the infrared emission as coming from two Gaussian grey body components of a fixed size and orientation, each one behind a uniform absorption screen. Two is the minimal number of components necessary to account well for the data, while the addition of more components does not improve
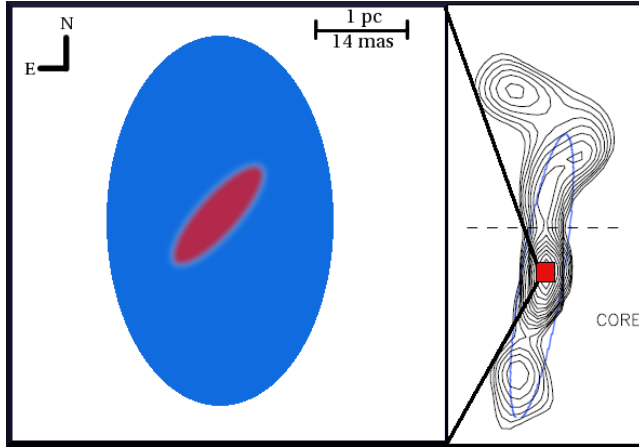
Figure 3.5 — Comparison between the two components in our model and the 12.5μm image of Bock et al. (2000), taken with the 10m Keck telescope. The two components are plotted symmetrically, yet their relative position cannot be determined from the correlated fluxes.

our fit. The correlated flux of each component is given by:

$$F_{corr}(\lambda, u, v) = \eta BB(\lambda)V(u/\lambda, v/\lambda)e^{-\tau \cdot abs} \tag{3.1}$$

where BB$(_\lambda)$ is the emission from a black body of temperature T; V is the visibility of a Gaussian component whose major axis, minor axis, and PA are to be fitted; abs is the absorption curve of a chosen mineral or a combination of a few minerals as described below. The coefficient η is the grey body scaling factor and has a value $0 < \eta < 1$, independent of wavelength.

After computing the Fourier amplitudes corresponding to each uv point in the model, the two sets of amplitudes (one for each component) are then combined to produce the final correlated flux to be compared to the data:

$$F_{corr} = |F_{corr1} + e^{2\pi i(ul+vm)}F_{corr2}| \tag{3.2}$$

The parameters l, m are for the two components to be moved with respect to each other in the plane of the sky, parallel to the RA and DEC directions, respectively. In practice we find that the data does not provide constraints for the relative positions l, m (see also §3.4.1.1) and we have set them to zero (concentric components). Each component in the model has six parameters, making in twelve in total: the major and minor FWHM, the position angle ϕ, the BB temperature T, the optical depth τ, and the scaling factor η. The main features of the data can be reconstructed from values of the correlated flux at about six wavelengths, in the sense that if the model fits the data well at those wavelengths it will fit the rest well. We can then estimate that these 12 parameters are in fact fitting $6 \times 16 = 96$ independent data points. The total flux is treated here as an extra uv point to be fitted, and is computed by setting the u and v coordinates in equation 3.2 to zero for each component. In practice we find that the total flux is easily reproduced in many of our models and for a different range of parameters, and may serve as an upper limit to the flux and size of each component. The most difficult part in our model is to determine the absorption curves in equation 3.1. We have selected several dust absorption templates, including standard galactic dust as observed towards the centre of the Milky Way (Kemper et al. 2004), as well as $Ca_2Al_2SiO_7$, which was found to best fit the previous MIDI data (J04, Speck et al.

Figure 3.6 — A comparison between the absorption template used in fitting the data (dashed) and the other spectral templates for dust particles commonly found in astrophysical environments. The latter includes that of dust seen toward the centre of the Milky Way. These templates only include line absorption and do not include the continuum absorption.
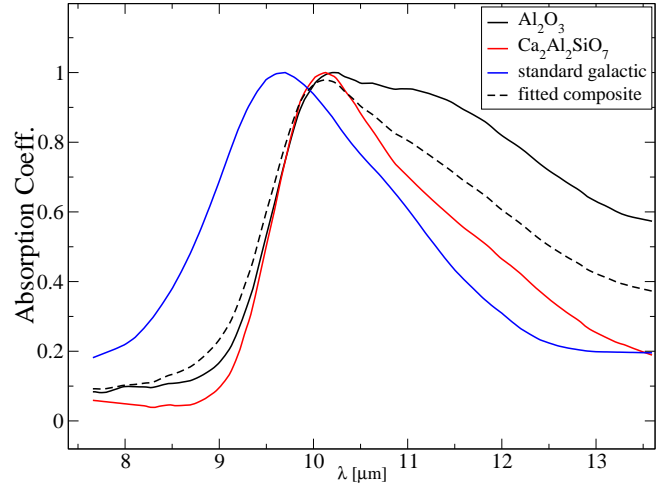
(2000)). Our aim here is not to unambiguously determine the chemical composition of the dust, which is not possible to do from the data, but rather to characterise the spectral template which will fit the data best, and to compare it with other known dust mineral templates. In this respect the template is any simple function $f(\lambda)$ which, when inserted into equation 3.1, will provide the best fit for the data. To achieve this, we first fit a combination of the minerals listed above and shown in Figure 3.6. The best-fit combination was improved on by allowing the value of τ at several key wavelengths (i.e. 8, 9, 9.7, 11.5 and 13μm) to vary and then interpolated between the new values using cubic spline. This method is able to mimic a typical absorption template. The resulting template, which we designate 'fitted composite', along with several other dust templates are plotted in Fig. 3.6 while the model parameters are given in Table 3.2. The parameter values in Table 3.2 are based on the results of different models that differ in the chemical composition of the dust. To determine the errors we fixed the value of all but one parameter at a time and noted the range of values resulting in significant changes to the model.

We label the two components in our model as components 1 and 2. Figures 3.3 and 3.4 plot the best fit model against the correlated fluxes, while Figure 3.2 plots the model's fit to the total flux plus the contribution from the individual components.

The fitting was done by finding the least-squares solution using the Levenberg-Marquardt technique. The general trend is for the quality of the fit to become worse with increasing baseline length, as one might expect from the lower spatial resolution of a short-baseline observation. In addition, component 2 only contributes to the correlated fluxes taken with shorter baselines, effectively increasing the number of fit parameters. Some of the features in the correlated fluxes, in particular the 'step' seen most clearly in correlated fluxes #4 and 5 at 10.5μm, cannot be reproduced by the simple model we propose. Our model will always generate smooth fluxes due to the smooth absorption templates we use, which not contain any such 'steps'. Furthermore, introducing more complicated templates will not help to fit these unsmooth features since any change made to the templates will affect each correlated flux, while these unsmooth features only appear in some of the correlated fluxes.

Seven out of sixteen modelled correlated fluxes (#7,8,9,10,11,15,16) are in excellent

Table 3.2.   Parameter fits for the two grey-body model of §3.4.1.

parameter	value[a]	error	units
Component 1			
FWHM major	20	± 3	mas
FWHM minor	6.4	± 1	mas
ϕ	-42	± 2	degrees
T	800*	± 150	K
τ	1.9	± 0.5	
η	0.25*	± 0.07	
Component 2			
FWHM major	56.5	± 5	mas
FWHM minor	42.4	± 5	mas
ϕ	0	$^{+70}_{-20}$	degrees
T	290	± 10	K
τ	0.42	± 0.2	
η	0.64	± 0.15	

[a]The temperature and scaling factor, η, are not independent. Temperatures as high as 1500K can be fitted with a low scaling factor, $\eta \sim 0.05$, although the resulting fit is not as good.

agreement with the data while the rest of the modelled fluxes are mostly in good to perfect agreement with the data either for $\lambda < 10\mu$m or for $\lambda > 10\mu$m. The two components are illustrated in Figure 3.5. Given the range of spatial resolutions of the different baselines (spanning a factor ~ 4 in length), the complex behaviour of the correlated fluxes and the striking simplicity of the model, it provides a surprisingly good fit to the data.

3.4.1.1 Symmetry issues

As stated before, only phaseless and therefore symmetric models were applied to the data. The lack of an absolute phase also implies a loss of astrometric information. We cannot, for example, determine the position of the mid-infrared emission in relation to other known components on similar scales for NGC 1068. In principle, we could constrain the relative position of our two model components by means of the l, m parameters in equation 3.2. If our two components are not symmetric with respect to each other, the resulting phase difference will also affect the sum of the Fourier amplitudes of both components, i.e. the observed correlated fluxes. In practice, we find that we do not have enough information on component 2 in order to determine its relative position. Models with offsets of up to a few tens of mas are virtually indistinguishable from models with zero offsets. In order to better constrain the relative positions, more observations on shorter baselines are needed, as component 2 is mostly over-resolved

Figure 3.7 — Maximum entropy reconstruction at 8μm. Image size is 30 × 30 pixels, with 1pix=2 mas. Colour scale is linear. The extended blobs are artifacts caused by the low *uv* coverage. Gaussian fitting to this image measures it to be 7.7 / 21 mas in FWHM with PA=−46°, very close values to the grey body model results, and in agreement with the results of the one Gaussian fitting at 8μm. The 'dirty map' is shown in the bottom left corner.
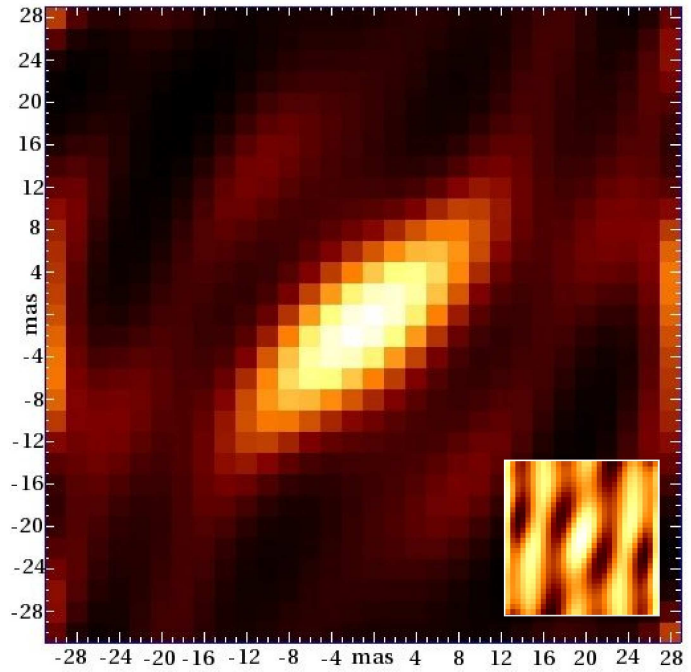
in our baseline sample. We do know from the differential phase that the mid-infrared emission is asymmetrical. However, we cannot tell whether this asymmetry is due to the geometry of the dust clouds or the result of asymmetrical absorption in the torus.

3.4.1.2 The infrared SED

The model used here is specifically designed to explain the MIDI data in the wavelength range of 8-13μm. It is not a full radiative transfer model, and therefore cannot be used to predict or account for the entire infrared SED of NGC 1068.

3.4.2 Maximum entropy imaging

The fits of the two blackbodies presented in §3.4.1 are not perfect fits to the data. Attempting to improve them, we explored different perturbations in the Gaussian distribution and although some of them can make the fit better, they are still ad-hoc. Finally we decided to reconstruct an image using maximum entropy (ME) methods, which guarantees that the resulting image will be the most statistically probable reconstruction given the information in the data. To our knowledge, this is the first time such a method has been used with infrared interferometric data. The ME reconstruction is based on the general algorithm by Skilling & Bryan (1984) and modified to the specific needs of dealing with MIDI data. The code was tested on simulated data with similar S/N as the original data and using the same *uv* coverage of NGC 1068 (Fig. 3.1). In general, the code is able to accurately reproduce Gaussian brightness distributions or similarly simple shapes without sharp edges. Attempting to reconstruct multiple component images (such as a binary) have not been successful for this *uv* coverage. We have chosen to reconstruct the image at 8μm, since in that wavelength a single component fits the data well and the silicate absorption does not come into play. The

resulting image is displayed and discussed in Fig. 3.7. The ME method is useful since it is not model-dependent and no prior assumptions about the source are needed to make use of it. Although the ME image details the basic properties of the source, and can provide a good starting point for any model, it does not provide a more detailed picture than parametric models which enable us to probe the wavelength dependence of the data as well as its brightness distribution. Nevertheless, the ME image does fit the data set at 8μm perfectly. Since the code, by definition, always prefers to get rid of complicated structures, we can gain insights into the deviations from the pure Gaussian shape in our models by looking at how the code chooses to reduce the χ^2 of the image. The central shape in the image fits well with component 1 from §3.4.1, while the extended blobs seen are needed to perfect the χ^2. We believe that the blobs correspond to extended emissions present in the source, while keeping in mind that the specific shape and positions of the blobs mostly reflect the low *uv* coverage of the data set. The contribution of the extended emission, as measured from the intensities in the image, is about 15% of the flux of component 1.

3.4.3 Channel by channel Gaussian fits

MIDI uses a grism to disperse the two beams into 261 channels before combining them. Per channel per time, we have a set of 16 correlated fluxes, or Fourier amplitudes, one for each baseline. From these amplitudes a Gaussian brightness distribution corresponding to infrared emission from this channel's wavelength is fitted. The fitting is done directly in the *uv* plane, and takes into account only the correlated fluxes. In each wavelength we fitted a single Gaussian, motivated by the successful Gaussian fitting of J04 to data composed of two baselines. The fit results are summarized in Fig. 3.8, which plots the values of the model's parameters (i.e. the major and minor FWHM sizes, height and position angle of the fitted Gaussian) and the resulting normalised χ^2 for each fit, determined by dividing the χ^2 by the number of degrees of freedom (16) minus the number of model parameters (4). The main results from this approach are:

1. The FWHM major and minor axis (Fig. 3.8a) lengths increase with wavelength. This is expected of centrally heated dust since longer wavelengths indicate cooler temperatures. and therefore larger radii. For optically thin dust in radiation equilibrium where $T \propto r^{-0.5}$, and for blackbody emission where λ scales as $1/T$ (Wien's law), we get $r \propto \sqrt{\lambda}$ as a crude estimate, which fits the trend seen in the fitting of the Gaussian's axis. The discontinuity at $\lambda \simeq 9.5\mu$m is due to the atmospheric 9.7μm Ozone feature and the intrinsic Silicate absorption.

2. The Gaussian flux density (Fig. 3.8b) is simply a response to the varying flux with wavelength.

3. The Gaussian's position angle (Fig. 3.8c) is perhaps the most interesting of results. First, we fit the same position angle from 8 to 9μm, followed by a jump of $\sim$10 degrees, which gradually rotates back but does not return to its original angle. The location of the jump in the position angle is indicative of the wavelength at which the Silicate absorption feature takes effect. The gradual, linear change in the position can be most easily interpreted as asymmetrical absorption, i.e. the absorption at 9 micron is more pronounced to the south-west of the Gaussian than at 12μm. In contrast, a constant PA will indicate a uniform absorption screen
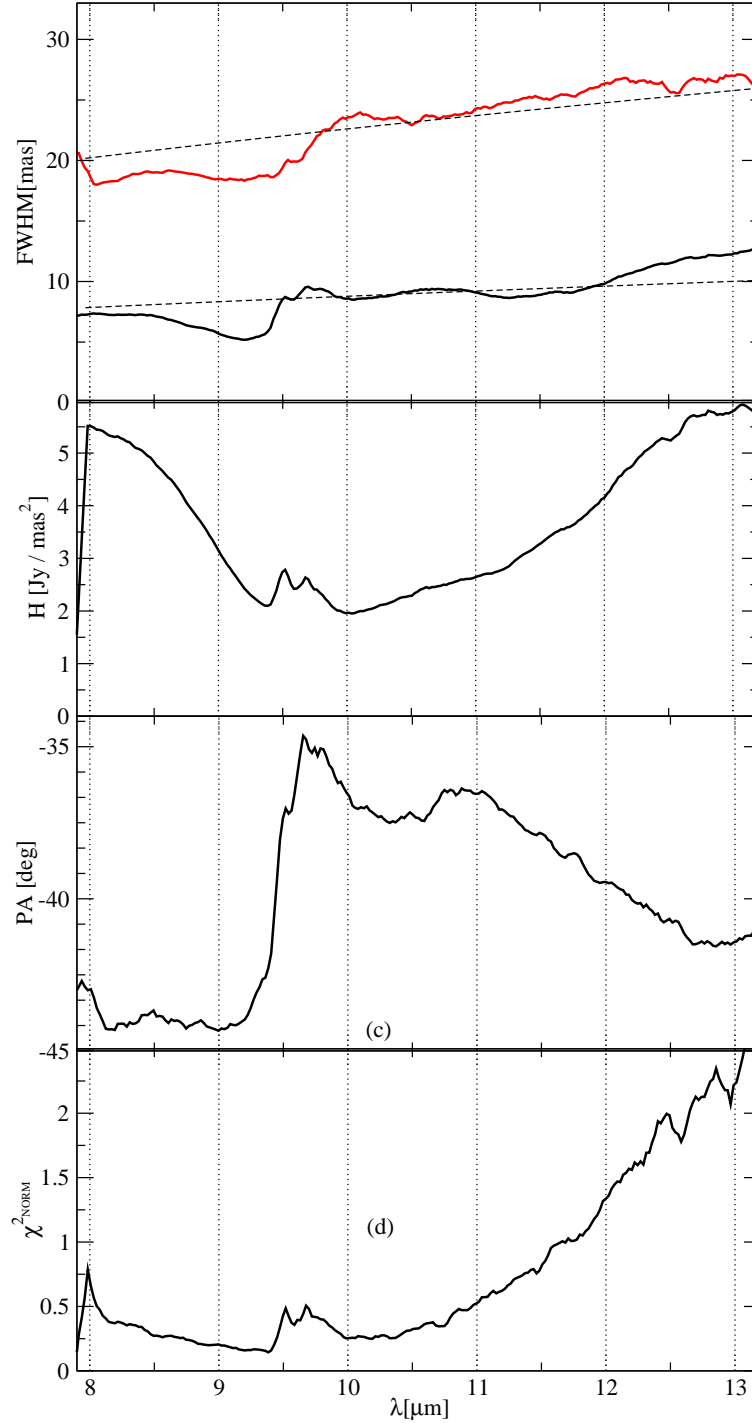
Figure 3.8 — Results of one Gaussian fitting. (a) FWHM sizes for the major (red) and minor (black) axes, overlaid with $r \propto \sqrt{\lambda}$ (dashed); (b) Gaussian peak; (c) position angle and (d) normalised χ^2, for each wavelength. We stress that in this model each wavelength was fitted independently, and the χ^2 in panel (d) is the minimized χ^2 found for each wavelength. The 'bumps' near 9.7μm are caused by the O_3 atmospheric feature.

is effectively present.

4. Further, we can deduce the presence of another dust component from the difference in PA between 8 and 13μm. The χ^2 (Fig. 3.8d) also supports the presence of an additional component, gradually becoming worse from 10μm (with increasing wavelengths). Although we cannot determine the geometry of this second component from this method, we can estimate that it consists of warm ($\sim$300K) dust, whose blackbody emission begins contributing to the flux at $\lambda >$10μm.

In general, the single Gaussian per wavelength model fits the data well, and helps to reduce the complex behaviour of the correlated fluxes to a set of four parameters that vary with λ. It is, however, a geometrical model and does not relate the different wavelengths in a physical way. We find it encouraging that the different parameters are continuous and behave in an 'orderly' fashion, although fitted independently.

3.4.4   The properties of each component

We now discuss in detail the properties of each component in the model, combining results from the different modelling methods.

3.4.4.1   Component 1

Component 1 is the dominant source of Mid-infrared emission on MIDI's scales. It is resolved in all of our observations and its geometrical properties are well constrained to have a major axis of 20 and a minor axis of 6.4 mas in FWHM with a PA=$-42°$. As Table 3.2 shows, and in contrast to the second component, the temperature and optical depth are not well constrained. Nevertheless we can establish that component 1 is composed of hot dust (T$\simeq$800K), with a low scaling factor ($\eta \sim$0.2). Although we cannot unambiguously determine the chemical composition of the dust, we observe that it differs from the profile of standard interstellar dust. Namely, the dust should begin absorbing towards 9μm and the optical depth should rise more sharply towards 10μm, followed by a shallower decline up to 14μm. Figure 3.8c indicates asymmetric absorption toward lower position angles, which may explain the deviations from a 'perfect' fit in both our models for the wavelength range $\lambda >$10μm. **Clumpiness:** Evidence for clumpiness comes from the small scaling factor, which is consistent with clumpy emission on unresolved scales that effectively reduces the surface brightness of the source independently of wavelength. Attempts to fit the data with models where the scaling factor is close to unity have not been successful. Extinction in the mid-infrared towards our line of sight probably contributes to the low value of η, but cannot fully account for it without invoking clumpiness. More direct evidence for clumpiness comes from the profile of the correlated flux of *uv* #4 at 8 μm, which is significantly less than our Gaussian model predicts. This is the observation with the longest baseline and as such it is most sensitive to small scale structure such as clumps. Given a resolution of 5.8 mas at 8μm for that baseline, we set an upper limit of 0.4pc (5.8 mas) for the size of a clump. Alternatively, one can interpret the missing flux at that *uv* point as a smooth (rather than clumpy), non-Gaussian flux distribution at sub-parsec scales.

3.4.4.2   Component 2

Since most of our observations were taken with long baselines, component 2 is mostly over-resolved. Figure 3.4 (filled curves) plots the contribution of this component to the correlated fluxes, illustrating its presence in only five of the sixteen baselines observed, corresponding to those shorter than sixty meters in telescope separation. As a result, its geometrical properties are not well constrained, while the temperature prediction is confirmed by that found in §3.4.3. As for the size of the flux distribution, component 2 is an extended Gaussian structure, with a minor axis of 42 mas and major axis of 56 mas in FWHM. It's orientation is best fitted as north-south, with a large uncertainty. Component 2 marks the colder, extended part of the torus-like structure, and is (together with comp 1) the unresolved source reported by Poncelet et al. (2007) and others (see introduction). Its north-south elongation is common with elongation of the mid-infrared tongue (Figure 3.5) of NGC 1068, which Bock et al. (2000) attribute to re-emission by dust and UV radiation concentrated in the ionization cone.

3.4.4.3   The physical distinction between the components

In our model the two components are separate and distinct, each with a fixed temperature. In reality, we expect the dust, on average, to have a smooth temperature and density distribution contained in one structure. In this sense, the two components are an abstraction. However, our findings here, and in particular the quality of the fit to the data, indicate that the two-component approximation is accurate regarding the brightness distribution of the dust, and this requires a steeper temperature gradient than the simple $T \propto \lambda^{-0.5}$ expected for centrally heated, optically thin dust.

3.4.5   Summary of modelling results

To summarise our main findings, the mid-infrared emission from the core of NGC 1068 within a beam size of 28 mas ($\sim$2 pc) is dominated by a warm Gaussian-shaped structure of dust (comp 1) with a chemical composition unlike that of dust towards our own galactic centre. The geometrical properties of this component are independently well constrained in each of our methods of investigation. Component 1 is co-linear with, and has similar size to the H_2O megamaser disk. It is tilted by $\sim 45°$ to the radio jet, and perhaps also by a lesser amount ($\sim$15°) to the ionization cone. The dust temperature is $\sim$800K, assuming a grey body model. Evidence for clumpiness is mostly indirect, and comes from the low grey body scaling factor and the deviation from a Gaussian fit for data obtained with the longest baseline. This single Gaussian component cannot account for the total flux as observed with an 8m telescope, as shown in Figure 3.2. It also does not fit the data as well for wavelengths longer that 10μm on our shortest baselines, suggesting the need for a second component (comp 2), which is extended so that it will become over-resolved with baselines longer than 60m. The filled curves in Figure 3.4, which plots the contribution of component 2 to the correlated fluxes, demonstrates how small that contribution is. As a result, the geometrical properties of this component, including its Gaussian nature, are not well constrained.

3.4.6   Comparison with previous MIDI studies of NGC 1068

Two previous studies of the core of NGC 1068 have been made using MIDI. Both studies were based on the same set of data: two *uv*-points with baseline lengths of 42 and 72 meters, obtained during the science demonstration time of the instrument. They were taken with the PRISM mode, which offers a low spectral resolution of $\lambda/\delta\lambda \simeq 30$. The first study, by Jaffe et al. (J04), used a simpler version of the two Gaussian greybody components used in this work (§3.4.1), and their findings are summarised in the introduction. In general, our findings here agree with those of J04, deviating from their results only in one parameter: the orientation of the extended component (component 2), which was then reported to be elongated east-west. This discrepancy is not surprising in light of our finding here that the extended component is over-resolved in observations with baseline lengths longer than 60m. This leaves just one observation (in J04) where component 2 contributes significantly to the correlated flux, not enough to determine its orientation. The FWHM sizes of the extended component in Jaffe et al. (30 and 49 mas) are smaller than the sizes reported here, and so the component was able to contribute to the correlated flux obtained with the longer baseline (72m), and an estimation of its orientation and axis ratio could be made. The second study, by Poncelet et al. (2006) (hereafter P06), used a different approach to modelling the same data set. Instead of Gaussian components, P06 used a combination of two uniform, circular disk components and visibilities rather than correlated fluxes as the quantity to be fitted. The derived angular sizes and temperatures of the two disk components are ∼35 and 83 mas, and ∼361K and 226K, respectively. Both approaches provided good fits to the data from the two short baselines. This is because the differences between a Gaussian model and a uniform disk is small for short baselines. With the addition of data taken at longer baselines, we can now determine that the circular disk model of P06 is inconsistent with the MIDI data presented here. This is mostly due to the sharp edge of the circular disk model: the visibility (and the correlated flux) of a circular disk is proportional to the absolute value of the J-Bessel function of the first order, which goes down to zero at specific baselines depending on the angular size of the disk and the baselines length in units of the observed wavelength. For the disk sizes of the P06 model, these zeroes fall between baseline lengths of 60m (at 8μm) to 100m (at 12.8μm), a range which is well sampled by our observations. Yet, no trace of the drop in the correlated flux predicted by the uniform disk model is seen in any of our observations. The zeroes in the visibility function appear for any flux distribution that possesses a sharp edge. Thus, our data is inconsistent with any such flux distribution.

3.5   Discussion

NGC 1068 is considered as the prototypical Seyfert II galaxy. It is also the first Seyfert II with broad emission lines seen in polarized, scattered light (Antonucci & Miller 1985). These observations proved that NGC 1068 harbours an obscured Seyfert I nucleus, and led to the AGN unification model, at least in its most simple form, uniting Seyfert I & II nuclei. This is **the** object for which the obscuring dusty torus was originally invented. The previous sections have described the *appearance* of this structure at mid-infrared wavelengths and sub-parsec scales, and its geometric relation to structures

Figure 3.9 — Picture summarising the multi-wavelength structures on parsec-scales in the nucleus of NGC 1068. The FWHM of the compact dust (component 1) is sketched in red, centred around the H_2O maser spots and 5GHz radio emission, both from Gallimore et al. (2004). Contour levels below the FWHM level have been removed to allow a better comparison between the radio and the mid-infrared. The ionization cones inferred from spectroscopy by Das et al. (2006) are shown in yellow, and the HST [OIII] (**reduced in scale by a factor** ~ 100) image contours (Evans et al. 1991) are shown in blue to indicate the visual orientation of the cone.
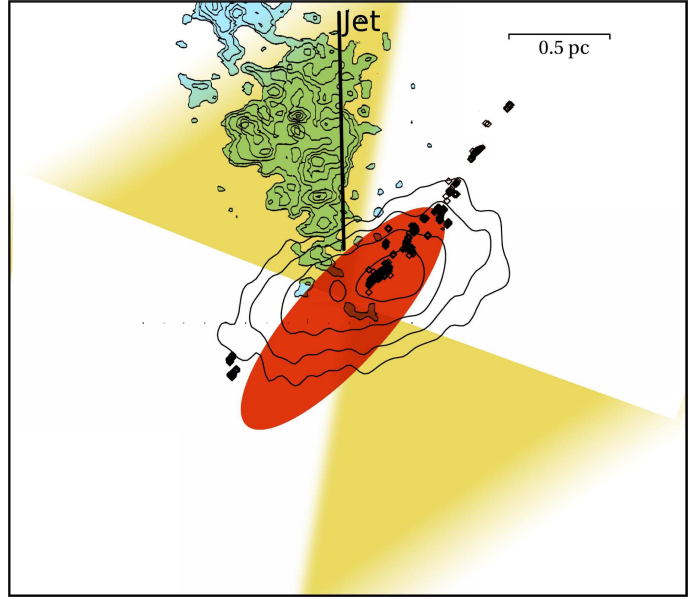
seen at other wavelengths.

The literature on the spectrum of NGC 1068, both observational and theoretical, is very extensive. Many authors have modelled the production of the overall SED of the galaxy within the context of the unified theories. Without detailed structural observations, however, they have found the problem underconstrained. The early interferometric work of J04 and W04 led modellers of the emitted spectrum in the direction of collections of optically thick inhomogeneous ("clumpy") systems. Following the pioneering work of Nenkova et al. (2002) on clumpy models, Hönig et al. (2006) and Schartmann et al. (2008) showed that three-dimensional radiative transfer models of clumpy tori were consistent with the low spatial resolution SED data and the J04 interferometric data of NGC 1068. The Hönig et al. (2006) model of a torus with an inclination of $i = 55°$ is also able to fit the K-band measurements of W04 to a factor of 2 in correlated flux. In a later work (Hönig et al. (2007)) the authors have revised the inclination angle of the torus to $i = 70°$, this time providing excellent fits to both the SED and the previous interferometric N-band data, though still falling short of reproducing the K-band interferometric data. Most recently, a model with an edge-on torus ($i = 90°$) was presented (Hönig et al. (2008)). This model was fitted to the SED and one of the interferometric data points of J04, reproducing a good fit to the former, and a fit correct to a factor of $\sim$2 for the latter. Their most important conclusion is that the random cloud arrangement has a significant effect on the SED and images, providing remarkably different SEDs for different cloud arrangements and for the same set of large-scale torus parameters. This accounts for the difficulty in determining the inclination angle.

The observational material presented here is considerably more detailed than that which was available to the authors cited above, and the results of their simulations of the production and redistribution of the radiative energy are generally not presented in a form that can be directly compared to our measured correlated fluxes as a function of wavelength and baseline and position angle. Hence, while these models seem globally consistent with our present data, we refrain from considering whether any of them do

or do not *fit* it in detail. Rather we focus on the physical structures we observe and their relations to the surrounding AGN components. We also consider the similarities and differences of the results for NGC 1068 with those of the nearby Circinus Seyfert II galaxy, (Tristram et al. 2007), and compare the implications of our N-band data with those measured on the same galaxy by W04 in the K-band.

3.5.1   The inclination and thickness of the dust

In this section we argue that the nuclear dust structure in NGC 1068 is circum-nuclear and inclined edge-on, and therefore its observed size and the 3:1 ratio of its major/minor axis is indicative of the thickness of its inner part rather than a projection effect of an inclined disk. Our main argument here is that the dust and the maser disk are co-spatial, and since the masers are seen edge-on, so is the dust. The possibility of detecting the hot dust through the cold dust that surrounds it has been demonstrated by several recent three dimensional radiative transfer calculation of tori:

Schartmann et al. (2005) find that "in a homogeneous dust distribution the observed mid-infrared emission is dominated by the inner funnel of the torus, even when observing along the equatorial plane". Similar results are also found by Hönig et al. (2006) and discussed in more detail in section 3.4.6. We show that this scenario of an edge-on geometrically thick torus not only agrees with 3D radiative transfer models, but also is consistent with other observed structures on milliarcseconds scales:

(a) The position angle of component 1 is virtually the same as the PA of the western maser spots. This can hardly be a coincidence. The theoretical relationship between water maser excitation and warm molecular dust has been well established (Neufeld et al. 1994, for example), and the masers are indeed expected to be embedded in warm (>600K) molecular dust.

(b) Apart from the position angle, the inner radius of the maser disk is approximately the radius at which dust sublimes (Greenhill 1998). Dust reverberation modelling for the maser disk (Gallimore et al 2001, Fig. 9) has established the geometry of the masers, with those closest to the nucleus outlining a ring 0.6 pc in radius. The diameter of the ring (1.2 pc) is similar to the FWHM size of the major axis of our component 1 (1.35 pc), supporting the conclusion that the masers and the hot dust component are co-spatial.

3.5.2   The orientation with respect to the jet

Although there seems to be little or no correlation between the relative angle of jets and the dust residing in the galactic disk for Seyfert galaxies (Kinney et al. 2000), the naive expectation is that the dust directly orbiting the black hole and the accretion disk is perpendicular to the jet. It is the common belief that the orientation of the jet is closely coupled to the spin axis of the black hole, which in turn is affected by the sum of all the angular momenta of the material accreted throughout its lifetime. Capetti et al. (1999) estimate the lifetime of the jet as $<1.5 \times 10^5$ years, a much shorter time compared to the lifetime of the black hole. The current phase of the AGN is not likely to have affected the spin axis of the black hole, and it is not surprising that the dust and the maser disk are not aligned with the jet. Still, it is interesting to consider the origin of the orienta-

tion of the dust component and the maser disk, since it seems related neither to the jet nor to the galactic plane. We now consider two mechanisms:

self warping. The sub-Keplerian velocities of the masers have been interpreted as evidence that the disk is supermassive and will warp due to self-irradiation (Lodato & Bertin 2003). This mechanism, however, only applies to thin structures and therefore cannot account for the orientation of the dust.

misaligned inflow. In this scenario the matter falls misaligned with respect to the current orientation of the jet. This can be the result of either matter infalling from outside the plane of the galaxy, or due to the influence of a torque, perhaps from a non-spherical nuclear star cluster. The presence of such a potential will be most likely due to a past minor merger, for which some evidence exists (Garcia-Lorenzo et al. 1997). Observations so far have determined that a dynamical mass of $6.5 \times 10^8 M_\odot$ is present inside a 50 pc radius (Thatte et al. 1997), but due to obscuration by dust there is no information on the gravitational potential at smaller scales. This mass is about 12 times the mass of the black hole (Lodato & Bertin 2003), and at a distance a few parsecs the black hole's potential still dominates over the potential of the star cluster. The influence of a star cluster may also explain the non-Keplarian velocity distribution of the masers. Finally, the generally linear, stable shape of the jet excludes non-continuous capture of material into the black hole such as individual stars or individual dust clouds, which may take an arbitrary route. To conclude, the identical orientation of both the thin maser disk and the thick dusty torus strongly indicate that it is the angular momentum of the infalling matter combined with the gravitational potential at the nucleus that are responsible for the current orientation of the maser (i.e. accretion) disk and the inner part of the dusty torus that surrounds it. When discussing the orientation of the central dust component and the orientations of other components related to the nucleus, it is interesting to point out that Galliano et al. (2003) have proposed to explain the asymmetrical appearance of the H_2 brightness distribution (on arcsecond scales) by suggesting that the Compton thick material located in the very central parts of the AGN is tilted with respect to the large scale molecular gas distribution with an orientation of 30 degrees, which is comparable to our findings.

3.5.3 Relation between the torus and the ionization cone

According to the AGN unification scheme, it is the obscuring torus that is responsible for the conical shape of the ionized gas in the narrow line region since it blocks the UV radiation from ionizing the material outside the cone. The cone's opening angle and orientation are then related to the orientation and geometry of the torus, and in particular to the arrangement of the clouds in its inner edge. Now that the inner part of the torus has been resolved, we can compare the two quantities and relate them to the predictions of the unification model. The position angle of the dust is well constrained to be $-42°$ (see Table 3.2). We then expect the ionization cone to be centred perpendicularly (i.e. at PA=48°). The opening angle in this scenario depends mainly on the inner geometry of the torus, as each cloud in itself is optically thick to UV and X-rays, and trivial geometrical considerations limit the cone's angular extent to within $\pm 90°$ of the torus axis (i.e. -42<PA<138).

The ionization cone, as seen in HST (Hubble Space Telescope) images, is centred

around PA=10°, with a small opening angle of $\sim 45°$ (see Evans et al. 1991, for example). As we can see in Figure 3.9, its axis of symmetry is not aligned with the axis of component 1, as it lies about 40 degrees further to the north. Yet, due to its small opening angle, the cone's angular extent is still within the bounds listed above. This discrepancy may be resolved by looking at the kinematics of the outflowing gas. Das et al. (2006) have applied bi-conical outflow models to high-resolution long-slit spectra of the narrow-line region obtained with the Space Telescope Imaging Spectrograph aboard the HST. These models require the cone to have a wider opening angle, $\sim 80°$, centred around PA=30°, rejecting models with PA=10° (Das, *private comm.*), and in agreement with the orientation of our component 1. Figure 3.9 plots the HST image on top of the kinematic model. The northern edge of the cone coincides in both the model and the image, and it appears as if only half of the bi-conical outflow described by the model is seen in the HST image. The UV radiation which ionizes the gas in the cone is partially blocked by the obscuring dust closest to the AGN and is therefore sensitive to the configuration of the obscuring clouds. It is not unreasonable to suggest that some of the UV radiation is blocked by a cloud of dust so that only a part of the gas in the cone is ionize, as seen in the HST images. Assuming this, the orientation of the dust component and the ionization cone roughly match our expectations and give further support to our interpretation of component 1 being the inner hot funnel of the torus-like obscuring object. This implies irregularities in the dust distribution and supports the idea of a clumpy dust distribution.

If this scenario holds then we expect a difference between the appearance of the cone in the optical and in the infrared. The infrared cone (i.e. narrow line region - NLR) should appear more symmetrical with respect to the dust since its appearance does not depend on the ionization of its material. The 12.8m image of Galliano et al. (2005) shows extended emission that is quite symmetrical to the north and the south of the central engine, although the northern emission is considerably more pronounced. The emission is centred on PA=$\sim$27 degrees, which is more symmetrical with respect to the dust, with a relatively small opening angle of $\sim$50 degrees. Alternatively, Poncelet, Sol & Perrin (2008) study the gas dynamic inside the NLR by looking at several mid-infrared emission lines by extracting spectra along two slit positions. They find the infrared cone to be centred on $PA = 10°$ with an opening angle of $\sim$80°. It seems then that in the infrared there is also disagreement between different methods of investigation. A case against this scenario of partial obscuration comes from the well defined shape of the cone over a scale of a few hundred pc, along with the linear shape of the radio jet both suggest that these irregularities in the dust distribution are stable over $\sim$1500 years.

To conclude, observations at infrared vs. optical wavelengths, and emission line analysis vs. imaging all disagree on the properties of the ionization cone / NLR. Further investigation is needed in order to clarify this puzzling aspect.

3.5.4   The dust and the radio emission

Radio observations at 5 and 8.4GHz of the nucleus of NGC 1068 show a parsec-sized component (hereafter: 'radio component'), most likely indicating free-free emission from the X-ray irradiated accretion disk (Gallimore et al. 2004). If so, we expect the ra-

dio component to have similar geometrical characteristics to our component 1. Figure 3.9 shows the 5GHZ contours (up to the FWHM level) against the FWHM of component 1. The radio component is 'thicker' with a major:minor ratio of $\sim 2:1$, as opposed to $3:1$ for component 1 with its PA of -57 degrees. The two components are indeed similar in size and orientation.

3.5.5 Comparison with Circinus

It is interesting to compare our findings with those for the nucleus of the Circinus galaxy, the only other active galactic nucleus for which the central mid-infrared source was studied in similar detail. The Circinus galaxy is similarly regarded as one of the typical representatives of a Seyfert II galaxy population. It shows many of the characteristic attributes of Seyfert II sources, such as narrow and broad emission lines (Oliva et al. 1994, 1998), an ionization cone (Veilleux & Bland-Hawthorn 1997), as well as a $0.4\,\mathrm{pc}$ edge-on, warped disk of H_2O masers (Greenhill et al. 2003). At about $4\,\mathrm{Mpc}$, the Circinus galaxy is located significantly closer to us than NGC 1068. However, due to its lower nuclear luminosity, $L_{\mathrm{acc}} = 10^{10}\,\mathrm{L_\odot}$ (Tristram et al. 2007), it appears slightly fainter in the mid-infrared than NGC 1068. Using an approach to analyse the MIDI data similar to the one used by us for NGC 1068, Tristram et al. (2007) have found the dust in the nucleus of the Circinus galaxy to be distributed in two components: (1) a dense, warm ($\sim$330K) component of $0.4\,\mathrm{pc}$ size and (2) a slightly cooler ($\sim$300K), geometrically thick torus component with a size of $2.0\,\mathrm{pc}$. The model fits to the data were improved by introducing clumpy-like perturbations in the flux distribution, mainly of the larger component, thereby providing arguably the first direct evidence of a clumpy structure in an AGN torus.

As for NGC 1068, the compact component coincides with the nuclear water maser disk in orientation and size and there is evidence for a clumpy or filamentary distribution of the dust. Hence there seems to be some similarity between the dust distributions in these two Seyfert galaxies. Especially striking is the agreement between the sizes when considering that the torus size is expected to scale with the square root of the luminosity of the central energy source, and the identical orientations of the dust and the masers. However, when the properties of the dust distributions are compared in more detail, there are several aspects in which the dust distribution in NGC 1068 deviates from that of the Circinus nucleus significantly. In the first place, while the temperatures of the extended components in the two galaxies are comparable, the compact component in the Circinus galaxy is significantly cooler ($T = 330\,\mathrm{K}$) than the one in NGC 1068 ($T = 800\,\mathrm{K}$). The shallow temperature decrease of the dust in the Circinus galaxy was attributed to a high degree of clumpiness in the torus (Schartmann et al. 2008). In fact, this torus seems to be lacking a significant amount of truly hot dust. And indeed, we are observing different physical dust structures: in NGC 1068 the compact component is interpreted as the dust in the inner funnel of the torus, which is heated up to near sublimation temperature. In the Circinus galaxy, on the other hand, the compact component is interpreted as a disk-like dust structure in the centre (or 'midplane') of the otherwise geometrically thick torus. This structure is co-spatial with the rotating disk of maser emitters. As a second difference, in the Circinus nucleus, there is less silicate absorption in the compact component than in the extended component.

This was interpreted to be due to the silicate feature in emission, as is expected from optically thin dust in the inner regions of the torus. In NGC 1068 the inverse is the case, the absorption feature deepens for the compact component. This, and the unusual spectral characteristics of the dust in NGC 1068, as opposed to the dust in the Circinus galaxy that was found to fit that of standard galactic dust, suggest the reprocessing of dust in NGC 1068, in analogy to the evolution of dust in protoplanetary disks. Several underlying properties can have a major influence on the observed temperatures and absorption depths: among them are the total luminosity of the central energy source, the exact inclination angle of the torus, and the volume filling factor of the torus. Proper radiative transfer calculations for the dust distributions in these two Seyfert galaxies are needed to bring more light to this issue. The relationship between the inner dust component and the maser disk found in both galaxies is the most striking of the features both objects have in common, and it may be that this is indeed the generic case in all Seyfert nuclei that also possess maser disks. To conclude, the existence of a thick configuration of obscuring dust was confirmed in both Circinus and NGC 1068. Both dust configuration are found to fit a two component Gaussian model with differences mostly in the temperature of the components, and both components are similarly related to the water maser disk and the ionization cone.

3.5.6   Comparison with other infrared interferometric measurements

This galaxy has been observed previously in the infrared with interferometric resolution in the N-band by us (Jaffe et al. (2004)) and in the K-band by Wittkowski et al. with the VINCI instrument, (Wittkowski et al. (2004) W04), and in speckle mode by Weigelt et al. (2004). These last observations were restricted to effective baselines shorter than 6 meters by the telescope used, corresponding to ~ 24 meters at our shortest baseline at 8 μm wavelength. Thus they are primarily sensitive to structures larger than any observed here, and we will not discuss them further. Here we summarize the findings of W04 and discuss possible nuclear structures that are consistent with both their observations and those reported here.

W04 found a squared visibility of 0.16±0.04 at a projected baseline length of 45.8 meters and position angle of 44.5 degrees, corresponding to a resolution of ∼5 mas. The authors favour a multi-component model where 52 mJy originates in an unresolved source of size $\lesssim$5 mas and 75 mJy arises on scales of the order of 40 mas or larger. Again this larger component will not be discussed here. The smaller emission was attributed to thermal emission from hot (1000-1500 K) dust at the inner cavity of the torus, with a possible contribution of direct plus scattered light from the central engine. The resolution achieved by VINCI at 2.2 μm is only $\sim 30\%$ smaller than that we reach on our longest baseline, 129 meters at our shortest wavelength, 8 μm, thus in spatial terms the measurements can be compared directly.

The interpretation of these measurements is clouded by several uncertainties. First, the interferometric observations provide no direct positional information. Thus we do not know the position of the small K-band component relative to the galactic nucleus or relative to the extended features seen with MIDI, except that it must lie within the 56 mas field of view of the VINCI fibers, presumably centered on the nucleus. Second, the extinction in front of the K-band component is uncertain. If this component is seen

through the same extinction as our Component 1 (Table 2), then the K-band absorption may be estimated by scaling the depth of the silicate absorption by a standard extinction curve (c.f. Schartmann et al. (2005), Fig. 3), yielding an optical depth of $\tau_K \sim 3$ but with large uncertainties, particularly if the dust is of non-standard composition. If the K-band component is not at the nucleus, e.g. represents a clump of warm dust clouds as suggested by W04 and Hönig et al. (2008), then perhaps our line of sight to it does not pass through the main body of dust absorption, and the extinction could be significantly smaller. Third, as we have seen in Section 4, the short wavelength, long baseline MIDI results can be well modelled by a smooth gaussian of size 20×6 mas, with no evidence of unresolved emission corresponding to that found by VINCI. However, the low scaling factor of Component 1, $\alpha = 0.25$ (Table 2), points to the possible existence of substructure on size scales below the resolution of MIDI. For the 8 μm flux of any of the sub-components we can then only set an upper limit of ~ 750 mJy corresponding to the correlated flux seen on a 129 meter baseline (Figure 3, panel 1). Assuming again a standard extinction law, its intrinsic 8 μm flux would be $\lesssim 1.3$ Jy.

Under these circumstances, we consider only two possibilities for the K-band source where reasonable additional assumptions can be made concerning the above uncertainties: either emission from the accretion disk around the central black hole, or from a small body of hot dust, as discussed by W04 and also proposed by Hönig et al. (2008).

3.5.6.1 Central Accretion Disk

In this case we assume that the source lies behind the absorption seen in N-band and assume that for the intrinsic flux from the accretion disk $S_\nu(2.2\mu) = 0.05 \times e^3 = 1$ Jy and $S_\nu(8\mu) \leq 1.3$ Jy. This would correspond to a $\nu^{-0.2}$ spectrum, not unreasonable for an accretion disk. In addition, this accretion disk flux is consistent with the total accretion disk luminosity: From the total infrared emission $\int \nu S_\nu d \ln \nu \simeq 2.5 \ 10^{15}$ Jy Hz (estimated from the data assembled in the *NASA/IPAC ExtraGalactic Database*) one infers the bolometric emission of the disk to be $\nu S_\nu(peak) \sim 7 \times 10^{15}$ Jy Hz (assuming that the UV luminosity exceeds the IR luminosity by a factor ~ 3, because light emitted out of the torus plane is not reprocessed into the infrared). At a distance of 14 Mpc this corresponds to $\sim 1.5 \ 10^{45}$ erg s^{-1}, similar to other estimates of the bolometric luminosity of NGC 1068. Schartmann et al. (2005) discuss likely SEDs for central accretion disks, based on observations of Type I AGNs (e.g. Walter et al., 1993, Zheng et al., 1997) and more modern theoretical models where observations are lacking. In most cases the spectrum is relatively flat in the optical-IR region, $-0.5 < \alpha_\nu < +0.3$ (where $S_\nu \propto \nu^{\alpha_\nu}$) and breaks sharply down shortwards of the Lyman edge ($\lambda_{peak} \sim 0.1 \mu m$ i.e. $\nu_{peak} \sim 3 \ 10^{15}$ Hz) With this value of ν_{peak} and the bolometric luminosity we find $S_\nu(peak) \sim 2$ Jy. The relatively flat spectrum thus inferred between ν_{peak} and 2.2 μm is consistent with the acceptable range of α_ν.

We conclude, therefore, that the fluxes and limits measured with the VLTI at 2 and 8 μm are consistent with an accretion disk spectrum. In fact, if the emission spectrum of the accretion disk and the (relatively low) foreground extinction value are correct we *expect* to see the accretion disk in the K-band measurements. [1]

---

[1]This is at variance with Hönig et al. (2008), who on the basis of a simple theoretical $\nu^{1/3}$ accretion

3.5.6.2 Dust Cloud Emission

Several authors (Nenkova et al., 2002, Hönig 2006, Dullemond et al 2005) have proposed that AGN dust tori are clumped and Hönig (2008) suggest that the small component of the VINCI observations is a warm dust cloud or compact cluster of such clouds. To evaluate this suggestion in the light of our observations requires an additional assumption about the K-band extinction. If, as above, we assume the clouds to be near the nucleus this would to be of order $\gtrsim 3$ mag, the intrinsic K-band flux is $\gtrsim 1$ Jy and the 8μm $\rightarrow 2.2\mu$m spectral index is $\alpha_\nu \lesssim -0.2$. For black-body emission this implies a color temperature $T_{color} > 1300$ K, which is rather warm for dust, but not excluded, particularly if the dust is more refractory than standard silicates. If, in fact, the dust clouds are in the immediate vicinity of the nucleus, i.e. $r < 2.5$ mas, their equilibrium temperature derived from the above luminosity would be much higher than this, making dust emission very unlikely. However, as discussed at the beginning of this section, there is no direct evidence that the emission feature is physically so close to the nucleus. If the unresolved K-band source is *not* centered on the nucleus but above the main body of dust clouds, or seen through a hole in these clouds, then its intrinsic K-band flux could be as low as the observed 50 mJy, in which case the N-band upper limit provides no useful information on its properties.

Thus we conclude that the K- and N- band interferometric data can be straightforwardly be explained as emission from a hot central accretion disk if reasonable assumptions are made on the foreground emission and the accretion disk spectrum. The data can also be explained as emission from a group of hot dust clouds, but then it is unlikely that these clouds are centered around the central source. Additionally in this case, the extinction towards the core must be sufficient (i.e. $\tau_K >> 3$) to suppress the expected K-band emission from the nuclear accretion disk below the observed 50 mJy level.

3.6 Conclusions

In this paper we present interferometric observations of the nucleus of NGC 1068, using MIDI at the VLT. Extensive *uv* coverage of sixteen baselines with a maximal resolution of 7 mas has allowed us to analyse the mid-infrared (8-13μm) emission from the obscuring torus in great detail. We find the measurements consistent with emission from a compact (0.45×1.35 pc) component with a Gaussian flux distribution that is composed of hot ($\sim$800K) silicate dust with an unusual absorption profile, which we identify as a funnel of hot dust associated with the obscuring torus. The emission is co-linear, and likely co-spatial, with the well studied H_2O megamaser disk, and therefore tilted by $45°$ with respect to the radio jet. A second, more extended (3×4 pc) component of warm ($\sim$300K) silicate dust is weakly detected, which we identify as 'body' of the torus. This second component is mostly over-resolved and its properties are not well constrained. We discuss the physical origin of the emission with respect to the torus, the masers, the ionization cone, and the radio jet. A direct image of the source at 8 μm, obtained with maximum entropy image reconstruction, is presented as well.

---

disk spectrum peaking at $\nu \sim 10^{17}$ Hz, for which little observational evidence exists, argued for an undetectably low accretion disk flux at $\lambda > 1\mu$m.

Since the obscuring torus is a crucial component in the accepted picture of an AGN, resolving the structure of the torus illuminates many aspects of the AGN picture. We show that in many aspects the nucleus of NGC 1068 is irregular: the orientation of the dust is tilted with respect to the jet; the PA of the visible ionization cone does not match the PA of the inner dust funnel; and the chemical composition of the dust in the torus is different than dust observed in the Milky Way.

Acknowledgements

References

Antonucci R., 1993, Ann. Rev. Astron. & Astrophys., 31, 473

Antonucci R. R. J., Miller J. S., 1985, Astrophys. J., 297, 621

Bock J. J., Neugebauer G., Matthews K., Soifer B. T., Becklin E. E., Ressler M., Marsh K., Werner M. W., Egami E., Blandford R., 2000, Astron. J., 120, 2904

Capetti A., Axon D. J., Macchetto F. D., Marconi A., Winge C., 1999, Astrophys. J., 516, 187

Claussen M. J., Lo K.-Y., 1986, Astrophys. J., 308, 592

Cohen M., Walker R. G., Carter B., Hammersley P., Kidger M., Noguchi K., 1999, Astron. J., 117, 1864

Das V., Crenshaw D. M., Kraemer S. B., Deo R. P., 2006, Astron. J., 132, 620

Dullemond C. P., van Bemmel I. M., 2005, Astron. & Astrophys., 436, 47

Evans I. N., Ford H. C., Kinney A. L., Antonucci R. R. J., Armus L., Caganoff S., 1991, Astrophys. J., 369, L27

Galliano E., Alloin D., Granato G. L., Villar-Martín M., 2003, Astron. & Astrophys., 412, 615

Galliano E., Pantin E., Alloin D., Lagage P. O., 2005, Mon. Not. R. Astron. Soc., 363, L1

Gallimore J. F., Baum S. A., O'Dea C. P., 2004, Astrophys. J., 613, 794

Gallimore J. F., Henkel C., Baum S. A., Glass I. S., Claussen M. J., Prieto M. A., Von Kap-herr A., 2001, Astrophys. J., 556, 694

Garcia-Lorenzo B., Mediavilla E., Arribas S., del Burgo C., 1997, Astrophys. J., 483, L99+

Greenhill L. J., 1998, in Zensus J. A., Taylor G. B., Wrobel J. M., eds, IAU Colloq. 164: Radio Emission from Galactic and Extragalactic Compact Sources Vol. 144 of Astronomical Society of the Pacific Conference Series, Water in NGC 1068. pp 221–+

Greenhill L. J., Booth R. S., Ellingsen S. P., Herrnstein J. R., Jauncey D. L., McCulloch P. M., Moran J. M., Norris R. P., Reynolds J. E., Tzioumis A. K., 2003, Astrophys. J., 590, 162

Hönig S. F., Beckert T., Ohnaka K., Weigelt G., 2006, Astron. & Astrophys., 452, 459

Hönig S. F., Beckert T., Ohnaka K., Weigelt G., 2007, in Ho L. C., Wang J.-W., eds, The Central Engine of Active Galactic Nuclei Vol. 373 of Astronomical Society of the Pacific Conference Series, 3D Radiative Transfer Modeling of Clumpy Dust Tori Around AGN. pp 487–+

Hönig S. F., Prieto M. A., Beckert T., 2008, Astron. & Astrophys., 485, 33

Huré J.-M., 2002, Astron. & Astrophys., 395, L21

Jaffe W., Meisenheimer K., Röttgering H. J. A., Leinert C., Richichi A., Chesneau O., Fraix-Burnet D., Glazenborg-Kluttig A., Granato G.-L., Graser U., Heijligers B., Köhler R., Malbet F., Miley G. K., Paresce F., Pel J.-W., Perrin G., Przygodda F., Schoeller M., Sol H., Waters L. B. F. M., Weigelt G., Woillez J., de Zeeuw P. T., 2004, Nature, 429, 47

Jaffe W. J., 2004, in Traub W. A., ed., New Frontiers in Stellar Interferometry, Proceedings of SPIE p.715 Vol. 5491

Kartje J. F., Königl A., 1996, Vistas in Astronomy, 40, 133

Kemper F., Vriend W. J., Tielens A. G. G. M., 2004, Astrophys. J., 609, 826

Kinney A. L., Schmitt H. R., Clarke C. J., Pringle J. E., Ulvestad J. S., Antonucci R. R. J., 2000, Astrophys. J., 537, 152

Krolik J. H., Begelman M. C., 1988, Astrophys. J., 329, 702

Kumar P., 1999, Astrophys. J., 519, 599

Leinert C., Graser U., Przygodda F., and 21 others *Astronomy & Space Science*, 286, 73

Lodato G., Bertin G., 2003, Astron. & Astrophys., 398, 517

Mason R. E., Geballe T. R., Packham C., Levenson N. A., Elitzur M., Fisher R. S., Perlman E., 2006, Astrophys. J., 640, 612

Nenkova M., Ivezić Ž., Elitzur M., 2002, Astrophys. J., 570, L9

Neufeld D. A., Maloney P. R., Conger S., 1994, Astrophys. J., 436, L127+

Oliva E., Marconi A., Cimatti A., Alighieri S. D. S., 1998, Astron. & Astrophys., 329, L21

Oliva E., Salvati M., Moorwood A. F. M., Marconi A., 1994, Astron. & Astrophys., 288, 457

Osterbrock D. E., Shaw R. A., 1988, Astrophys. J., 327, 89

Poncelet A., Doucet C., Perrin G., Sol H., Lagage P. O., 2007, Astron. & Astrophys., 472, 823

Poncelet A., Perrin G., Sol H., 2006, Astron. & Astrophys., 450, 483

Rhee J. H., Larkin J. E., 2006, Astrophys. J., 640, 625

Poncelet, A., Sol, H. , Perrin, G., 2008, Astron. & Astrophys., 481, 305

Sanders D. B., Phinney E. S., Neugebauer G., Soifer B. T., Matthews K., 1989, Astrophys. J., 347, 29

Schartmann M., Meisenheimer K., Camenzind M., Wolf S., Henning T., 2005, Astron. & Astrophys., 437, 861

Schartmann M., Meisenheimer K., Camenzind M., Wolf S., Tristram K. R. W., Henning T., 2008, Astron. & Astrophys., 482, 67

Speck A. K., Barlow M. J., Sylvester R. J., Hofmeister A. M., 2000, Astron. & Astrophys. Supp. Series, 146, 437

Sturm E., Lutz D., Tran D., Feuchtgruber H., Genzel R., Kunze D., Moorwood A. F. M., Thornley M. D., 2000, Astron. & Astrophys., 358, 481

Thatte N., Quirrenbach A., Genzel R., Maiolino R., Tecza M., 1997, Astrophys. J., 490, 238

Tomono D., Doi Y., Usuda T., Nishimura T., 2001, Astrophys. J., 557, 637

Tristram K. R. W., Meisenheimer K., Jaffe W., Schartmann M., Rix H.-W., Leinert C., Morel S., Wittkowski M., Röttgering H., Perrin G., Lopez B., Raban D., Cotton W. D., Graser U., Paresce F., Henning T., 2007, Astron. & Astrophys., 474, 837

Urry C. M., Padovani P., 1995, Pub. Astron. Soc. Pacific, 107, 803

Veilleux S., Bland-Hawthorn J., 1997, Astrophys. J., 479, L105+

Walter R., Fink H. H., 1993, Astron. & Astrophys., 274, 105

Weigelt G., Wittkowski M., Balega Y. Y., Beckert T., Duschl W. J., Hofmann K.-H., Men'shchikov A. B., Schertl D., 2004, Astron. & Astrophys., 425, 77

Weingartner J. C., Draine B. T., 2001, Astrophys. J., 548, 296

Wittkowski M., Kervella P., Arsenault R., Paresce F., Beckert T., Weigelt G., 2004, Astron. & Astrophys., 418, L39

Zheng W., Kriss G. A., Telfer R. C., Grimes J. P., Davidsen A. F., 1997, Astrophys. J., 475, 469

Chapter 4

Dust emission from a parsec-scale structure in the Seyfert 1 nucleus of NGC 4151

Abstract. We report mid-IR interferometric measurements with ~ 10 mas resolution, which resolve the warm (T $= 285^{+25}_{-50}$ K) thermal emission at the center of NGC 4151. Using pairs of VLT 8.2 m telescopes with MIDI, we determined the diameter of the dust emission region, albeit only along one position angle, to be (2.0 ± 0.4) pc. This is the first size and temperature estimate for the nuclear warm dust distribution in a Seyfert 1 galaxy. The parameters found are comparable to those in Seyfert 2 galaxies, thus providing direct support for the unified model. Using simple analytic temperature distributions, we find that the mid-infrared emission cannot be the smooth continuation of the hot nuclear source that is marginally resolved with K band interferometry. We also detected weak excess emission around 10.5 μm in our shorter baseline observation, possibly indicating that silicate emission is extended to the parsec scale.

L. Burtscher, W. Jaffe, D. Raban, K. Meisenheimer, K. Tristram, H. Röttgering

4.1   Introduction

IN the standard model of Active Galactic Nuclei (AGNs) (Antonucci 1993; Urry & Padovani 1995), the central engine (Black Hole + accretion disk + Broad Line Region) is embedded in a dusty torus. Galaxies where we see the center only through this torus are called "type 2" whereas ones where we receive direct radiation from the Broad Line Region are referred to as "type 1". For a long time, there was only indirect evidence for the existence of the enshrouding dust, until VLTI observations with MIDI actually resolved the parsec-scale AGN heated dust structures in two Seyfert 2 galaxies (Sy 2). (Jaffe et al. 2004; Tristram et al. 2007; Raban et al. 2009)

Further observations proved the existence of parsec sized dust structures in several Seyfert 1 galaxies (Sy 1) (Tristram et al. 2009), but so far, no Sy 1s have been observed in sufficient detail to test the central premise of the unified models: type 1 and type 2 dust distributions are identical and the observed differences are only due to differences in orientation with respect to the line of sight. These predictions can now be tested with the MIDI observations of NGC 4151 reported here.

At a distance $D = (14 \pm 1)$ Mpc (i.e. 1 mas ~ 0.068 pc)[1], NGC 4151 is the closest and brightest type 1 galaxy (classification: Seyfert 1.5). It is also one of the most variable Seyfert galaxies: The UV continuum flux varies on scales of days and weeks (Ulrich 2000) and the reverberation time to the hot dust on the sub-parsec scale varies on yearly timescales (Koshida et al. 2009).

Sy 1 galaxies have been observed previously with MIDI (NGC 3783, Beckert et al. 2008), (NGC 7469, Tristram et al. 2009), but NGC 4151 is the first multi-baseline case where the size of the nuclear dust distribution is clearly indicated.

Swain et al. (2003) reported near-IR, 2.2μm, observations with the Keck interferometer. They find that the majority of the K band emission comes from a largely unresolved source of ≤ 0.1 pc in diameter. Based onf this small size, they argued that the K band emission arises in the central hot accretion disk. They note, however, that their result is also consistent with very hot dust at the sublimation radius. This view is supported by the K band reverberation measurements of Minezaki et al. (2004) who find a lag time corresponding to ~ 0.04 pc.

Riffel et al. (2009) modelled the near-infrared spectrum of this source and found it to be composed of a powerlaw accretion-disk spectrum and a component likely arising from hot dust (T = 1285 K). The hot dust component dominates at $\lambda \gtrsim 1.3\mu$m, consistent with the interpretation of hot dust emitting at 2μm. They measured a K band flux of ~ 65 mJy.

In the mid-infrared, Radomski et al. (2003) presented images of NGC 4151 at 10.8μm with an aperture of $4.5''$ and a spatial resolution of $\sim$550 mas (35 pc). They find that the majority (73%) of the N band flux comes from an unresolved point source with a size ≤ 35pc, and the rest is extended emission from the narrow line region.

In this letter we report new mid-infrared interferometric observations of NGC 4151 which clearly resolve a thermal structure.

4.2 Instrument, observations and data reduction

Observations were performed in the N band ($\lambda \approx 8 \ldots 13\mu$m) with the MID-infrared Interferometric instrument (MIDI, Leinert et al. 2003) at the ESO Very Large Telescope Interferometer (VLTI) on Cerro Paranal, Chile, using pairs of 8.2 m Unit Telescopes (UTs). The observables with MIDI are the single-dish spectra and the correlated flux spectrum that is obtained from the interference pattern generated by the two beams. The spectra were dispersed with a NaCl prism with $R \equiv \lambda/\delta\lambda \sim 30$.

Observations were taken in the nights of April 21 and 23, 2008 with projected baseline length BL of 61 m and 89 m at position angles of $103°$ and $81°$ respectively. These provide effective spatial resolutions[2] ($\lambda/3BL$) at 10.3μm of 11 and 7 milliarcseconds (mas), respectively. The calibrators HD 133582 and HD 94336 were selected to be very close in airmass with $\Delta(\sec z) \lesssim 0.15$. This is especially important for this NGC 4151 (DEC $\sim +40°$) which, at Paranal, never rises higher than $\sim 25°$ ($\sec z \gtrsim 2.3$) above the

---

[1]from the NASA Extragalactic Database: http://nedwww.ipac.caltech.edu; distance from redshift with H_0=73 km/s/Mpc; other estimates range to 20 Mpc

[2]The resolution where the source is completely resolved is $\lambda/2BL$. However, given sufficient S/N, one can already distinguish models at lower resolutions, in our case at $\sim \lambda/3BL$.

horizon. The northern declination of the source also essentially limits the projected baselines and fringe patterns to East-West orientation at Paranal. The N band spectrum of HD 133582 (K2III) was taken to follow a Rayleigh-Jeans law, while that of HD 94336 (MIII) was taken from Cohen et al. (1999).

Data reduction was performed with the interferometric data reduction software *MIDI Interactive Analysis and Expert Work Station* (MIA+EWS, Jaffe 2004), specifically adapted for the analysis of low S/N sources.

4.3 Results and modelling

4.3.1 Single-dish spectrum

The resulting single-dish spectrum with an effective aperture of ~ 300 mas is shown in Fig. 4.1 together with a Spitzer IRS spectrum for this source (observed 8 Apr 2004; aperture $\sim 3.5''$, Weedman et al. 2005). The higher Spitzer flux most likely indicates emission from the Narrow Line Region (cf. Radomski et al. 2003).

The color temperature of the spectrum is (285^{+25}_{-50}) K. Additionally, we detect the [Ne II] 12.81 μm line commonly seen in star forming regions. The [S IV] (10.51 μm) line, clearly seen in the Spitzer spectrum, is not significant in the MIDI spectrum. The errors in the MIDI spectrum arise from incomplete thermal background subtraction and hence rise steeply with increasing wavelength.

4.3.2 Correlated spectra

The two correlated flux spectra are shown in Fig. 4.2.

The correlated flux observed with $BL = 61$m rises from (0.14 ± 0.02) Jy at 8.3 μm to (0.45 ± 0.05) Jy at 12.7 μm. The second spectrum ($BL = 89$m), rises from (0.12 ± 0.03) Jy at 8.3 μm to (0.30 ± 0.05) Jy at 12.7 μm. Correlated flux uncertainties arise primarily from background photon noise and increase with wavelength but are smaller than the single dish errors.

The correlated flux on the shorter baseline (the one that has a higher flux) shows a broad "bump" between 9 μm and 12 μm that we interpret as a silicate emission feature (see section 4.3.3). No [Ne II] emission is seen, indicating that this arises on a scale that is fully resolved by the interferometer (i.e. $\gtrsim 20$ mas ~ 1.3 pc). The fact that the correlated flux is lower on the longer baseline is a clear sign that the source is resolved by the interferometer.

Since the resolution of the interferometer $\theta_{min} \sim \lambda/3BL$ changes with wavelength, the correlated flux reflects both the source spectrum and the source structure. It is not possible to draw any conclusions from the spectral slope of a correlated flux spectrum without assuming a source geometry.

4.3.3 A possible silicate emission feature

Although the silicate absorption feature has often been detected in type 2 nuclei, the emission feature, predicted for type 1 nuclei by torus models (e.g. Pier & Krolik 1992; Schartmann et al. 2005), has not been detected except in a handful of objects, most of them quasars (Hao et al. 2005; Weedman et al. 2005; Buchanan et al. 2006).
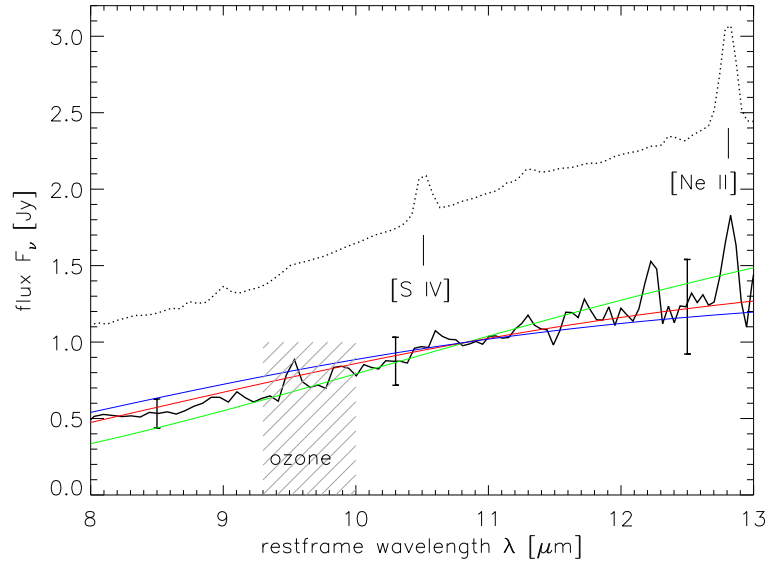
Figure 4.1 — Single-dish spectra for NGC 4151. Spitzer spectrum (3.5″, dotted, Weedman et al. 2005), MIDI spectrum (0.3″, black line with error bars). The MIDI single-dish errors were taken as the standard deviations from five observations. Also plotted are blackbody emission curves at $T = 235, 285, 310$ K (green, red, blue). The region of atmospheric ozone absorption, between 9.3 and 10 μm (hatched), is uncertain and not taken into account for the later analysis.
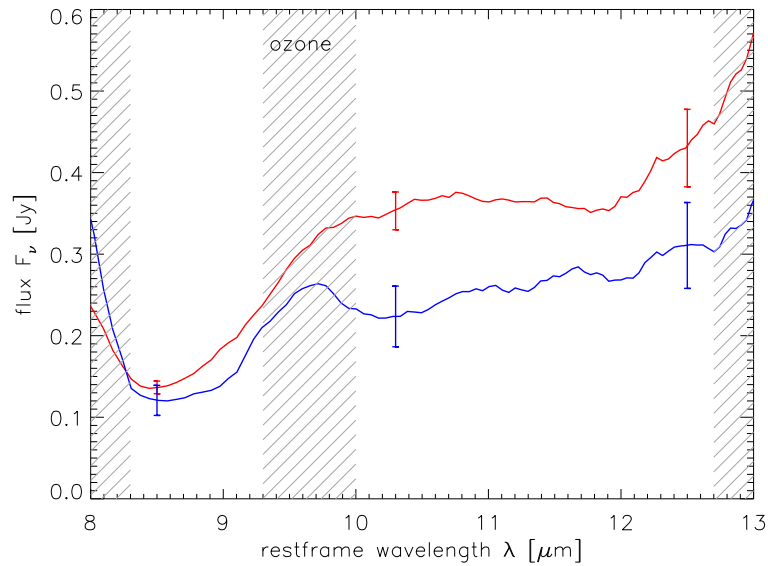
Figure 4.2 — Smoothed ($\Delta\lambda \sim 0.3\mu$m) correlated MIDI spectra at two different East-West projected baselines: 61m (red) and 89m (blue). The errors were taken as the standard deviations from multiple observations. The region of atmospheric ozone absorption, between 9.3 and 10 μm (hatched), is uncertain and not taken into account for the later analysis, as are the regions $\lambda < 8.3\mu$m and $\lambda > 12.7\mu$m (hatched), which have very low S/N.
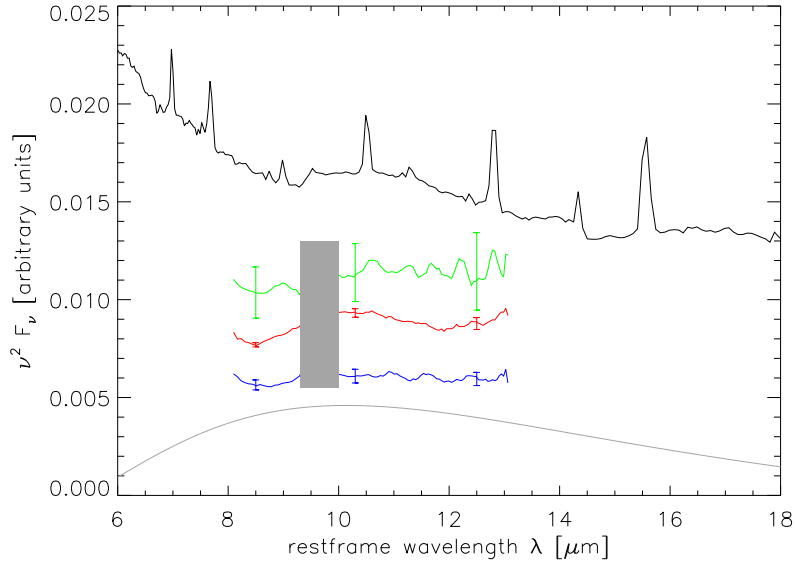
Figure 4.3 — The silicate emission feature as seen in $\nu^2 F_\nu$. In the Spitzer spectrum (black, Weedman et al. 2005), a broad weak emission feature at around 11 μm is clearly seen. The three MIDI spectra (green: single-dish, red: 61m baseline, blue: 89m baseline) are plotted with offsets. The grey line shows a 285 K blackbody. The region between 9.3μm and 10 μm is hard to calibrate in the MIDI spectra due to the atmospheric ozone feature and has been greyed to not mislead the eye.

As noted by Weedman et al. (2005) and Buchanan et al. (2006), Spitzer spectra (with an aperture of $\sim 3.5''$) of NGC 4151 show weak excess emission at 10 μm and 18 μm that is most easily seen when plotted as $\nu^2 F_\nu$ with a sufficiently large wavelength range. In Fig. 4.3 we plotted our spectra (that are limited to the atmospheric N band) in such a way together with a Spitzer spectrum.

The hypothesis of silicate emission is not inconsistent with our single dish spectrum (aperture $\sim 0.3''$) but since this spectrum suffers from incomplete background subtraction, especially at longer wavelengths, it is probably hidden in the resulting uncertainties. The emission feature seems to be most prominent in our observations on the 61m baseline observation and is clearly not detected on the 89m baseline.

This suggests that silicate emission is distributed over ~ 1 pc as derived from the 10.5 μm Gaussian model (see 4.3.4).

4.3.4 Simple Gaussian model

With the limited baselines available from Paranal, it is not possible to reconstruct an *image* of NGC 4151 from our data. Instead we consider simple model distributions of the emission on the sky and compare the predicted interferometric and single dish spectra with our measurements in order to fix parameters in such a model. We chose a model containing an unresolved point source (flux F_p) and an extended Gaussian distribution (flux normalization F_g, FWHM θ). Although we might expect the mid-IR brightness distribution in Sy 1 galaxies to have a hole in the middle, neither observed nor modelled fluxes change as long as the hole, whose radius is determined by the sublimation radius of the dust, is unresolved. This is certainly the case in NGC 4151 (see section 4.4). An upper limit to the size of our point source is given by the effective
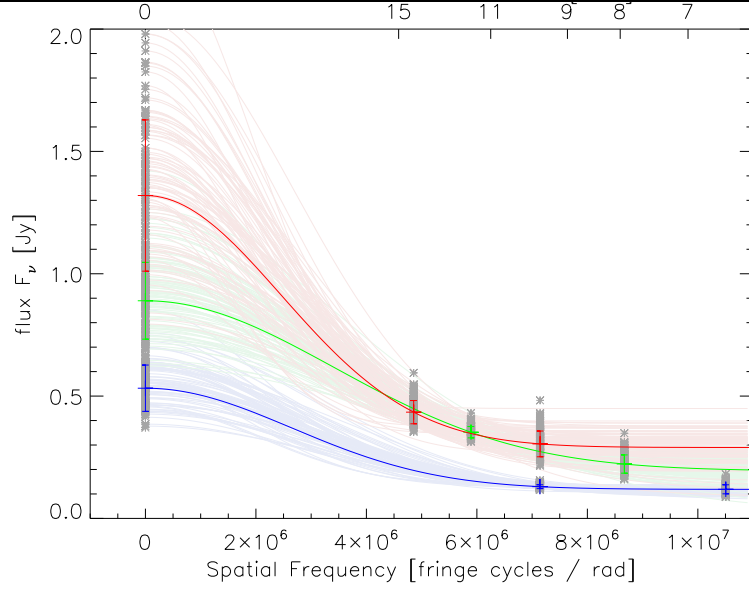
Figure 4.4 — Gaussian model for NGC 4151. On the upper x axis the resolution of the interferometer $\lambda/3BL$ is given. The three curves correspond to models at 8.5 μm (red), 10.3 μm (green) and 12.5 μm (blue). Data points and errors are taken from the single-dish (Fig. 4.1) and correlated fluxes (Fig. 4.2). The many thin lines represent the Monte-Carlo-like error determination for the Gauss model. For details see text.

Table 4.1. Parameters for the Gaussian models (see text).

λ [μm]	F_g [Jy]	θ [mas] (diameter [pc])	F_p [Jy]
8.5 ± 0.2	0.41 ± 0.10	29^{+3}_{-6} ($2.0^{+0.2}_{-0.4}$)	0.119 ± 0.016
10.3 ± 0.25	0.70 ± 0.16	23 ± 4 (1.5 ± 0.3)	0.194 ± 0.061
12.5 ± 0.3	1.03 ± 0.30	32 ± 6 (2.1 ± 0.4)	0.290 ± 0.070

resolution of the interferometer; this corresponds to a diameter of $\sim \lambda/3BL \sim 7$ mas, i.e. a radius of ~ 0.2 pc, at 10.3 μm.

Because of the East-West baseline orientation, the North-South distribution of emission is undetermined. Equivalently, we assume the source to be circularly symmetric on the sky.

The model flux density at wavelength λ is then given by $F_\nu(\lambda) = F_p(\lambda) + F_g(\lambda) \cdot \exp(-(BL/\lambda \cdot \pi/\theta)^2/\ln(2))$. We fitted such a model separately at 8.5, 10.3 and 12.5 μm where we are safely away from the regions of very low signal to noise (at the edges of the N band) and the ozone feature. At 10.3 μm this fit may be affected by the silicate feature. The modelled visibilities are shown in Fig. 4.4 and the resulting parameters are given in Table 4.1.

The errors of these parameters were estimated from a Monte-Carlo simulation in which we randomly placed 10000 measurements in a Gaussian distribution around the measured value with the σ as determined from our data reduction.

4.4 Discussion

4.4.1 The extended source and the Sy 1 / Sy 2 paradigm

In the strictest version of unified models, we expect for both a Sy 1 and a Sy 2 galaxy an extended dust structure with the same size, morphology and temperature distribution (at a given UV luminosity L_{UV}). In less strict versions this is only true statistically (e.g. Elitzur & Shlosman 2006). Additionally, Sy 1 galaxies should have an unobscured point source (the unresolved accretion disk and inner rim of the torus) – but the relative strength of these two components in the mid-IR is model-dependent.

To test this, we can compare our observations with other MIDI observations: In the Circinus galaxy ($L_{\mathrm{UV}} \sim 4 \times 10^{36}$ W, $L_{\mathrm{torus}} \sim 5 \times 10^{35}$ W), Tristram et al. (2007) found a warm ($T \sim 330$ K) disk with major axis FWHM ~ 0.4 pc and a larger, similarly warm, component of ~ 2 pc FWHM.

In NGC 1068 ($L_{\mathrm{UV}} \sim 3 \times 10^{37}$ W, $L_{\mathrm{torus}} \sim 10^{37}$ W), Raban et al. (2009) found a hot ($T \sim 800$ K) disk of 1.35 x 0.45 pc and a warm component 3 $\times$ 4 pc in FWHM. They identified the disks with the densest parts of the torus of the unified model.

For NGC 4151 ($L_{\mathrm{UV}} \sim 1.5 \times 10^{36}$ W – variable (from NED), $L_{\mathrm{torus}} \sim 4\pi D^2 \nu F_g \sim 6 \times 10^{35}$ W) we determined a torus size of $\sim (2.0 \pm 0.4)$ pc and a dust temperature of (285^{+25}_{-50}) K.

When scaled to the accretion disk luminosity L_{UV}, these values agree well with the torus sizes ($r \sim L_{\mathrm{UV}}^{1/2}$) and torus luminosities ($L_{\mathrm{torus}} \sim L_{\mathrm{UV}}$) of the two Seyfert 2 galaxies and the temperatures are also very similar. Note, however, that the torus luminosity used here is calculated from the 12μm flux density, not taking into account emission at longer wavelengths.

4.4.2 Greybody models and the nature of the extended source

In addition to the single-wavelength Gaussian models discussed above, we can also connect the various wavelengths together by constructing *greybody* models where we assume a smooth powerlaw dependence of temperature with radius: $T(r) \propto r^{-\alpha}$, and an essentially constant emissivity with radius and wavelength. With such models we get acceptable fits to both the total and the correlated flux spectra with $T(1\mathrm{pc}) \sim 250$ K and $0.35 \lesssim \alpha \lesssim 0.6$. These values of α are consistent with dust receiving direct radiation from a central source (e.g. Barvainis 1987), i.e. an optically thin medium with optically thick clumps in it.

These models can be extrapolated to shorter wavelengths to check their consistency with the K band measurements. All plausible extrapolations of the MIDI data yield K band fluxes of < 10 mJy, much less than observed by Swain et al. (2003) and Riffel et al. (2009) (see below). We therefore conclude that the K band emission arises from structures which cannot be extrapolated from the larger structure seen in the N band.

From the greybody models one can further infer an emissivity $\epsilon \sim 10^{-1}$ – similar to what has been seen in NGC 1068 and Circinus.

To conclude: The resolved nuclear mid-IR structure in NGC 4151 has a size, temperature and emissivity that is comparable to those in type 2 objects where the existence of clumpy tori is established. Apart from the similarities with type 2 tori and the temperature profile of the greybody models, there is further evidence for clumpiness in

the NGC 4151 torus from radio observations: Mundell et al. (2003) measured HI absorption against the radio jet ($PA \sim 77°$) and found a structure of ~ 3 pc in size. From the velocities they further suggest that the gas is distributed in clumps. Warm dust possibly traces the HI gas in the mid-IR.

It therefore seems reasonable to identify the warm dust structure resolved now in NGC 4151 with the clumpy tori seen in Sy 2 galaxies. Due to the limited observing geometry and the limited amount of observations we cannot reconstruct its apparent shape nor can we constrain a model with more than the two components discussed above.

4.4.3 The point source and its relation to K band measurements

K band interferometry measurements by Swain et al. (2003) and, with higher significance, more recent Keck observations (Pott et al. 2009, in prep.) revealed a marginally resolved source, compatible with hot dust at the sublimation radius of ~ 0.05 pc. Reverberation measurements by Minezaki et al. (2004) and Koshida et al. (2009) find lag times Δt between the UV/optical continuum and the K band corresponding to a radius of ~ 0.04 pc (variable) which they interpret as the sublimation radius of dust.

Riffel et al. (2009) measured a flux of ~ 65 mJy at 2.2 μm and from spectral fitting they found that, at 2.2 μm, this flux is entirely dominated by a blackbody with a temperature of (1285 ± 50) K – again consistent with hot dust at the sublimation radius and the K band interferometry, taking into account that L_{UV} is variable by at least a factor of 10 (Ulrich 2000). To account for that variability when comparing our observations with these K band observations of different epochs, we looked at the X-Ray flux as a proxy for the UV–optical radiation[3] and find that, at the date of our observations, the source was probably in a higher state than at the time of Riffel et al. (2009)'s observations and emitted ~ 0.2 Jy in the K band.

Since the flux density F_ν of a ~ 1285 K blackbody is roughly the same at 2.2μm as at 8.5 μm, we can compare the flux in the K band (~ 0.2 Jy at the time of our measurement) with our point source flux at 8.5 μm ($\sim (0.119 \pm 0.016)$ Jy). From this it seems likely that hot dust is contributing to our point source at 8.5 μm. The spectrum of the point source rises by more than a factor of two from 8.5 μm to 12.5 μm, however, and thus requires emission from an additional small, "red" component. This could be core synchrotron emission, although such sources usually have flat spectra, or emission from a small, cool, optically thick central dust structure, possibly shadowed from direct accretion disk radiation.

4.5 Conclusions

Using mid-IR interferometry, we have resolved a warm dusty structure in NGC 4151. Its size (2.0 ± 0.4 pc), temperature (285^{+25}_{-50} K) and emissivity (~ 0.1) are in good agreement with the clumpy tori seen in type 2 AGNs and are thus consistent with the unified

---

[3]Data from the All-Sky-Monitor (ASM) on the Rossi X-Ray Timing Explorer (RXTE), available online at http://xte.mit.edu/asmlc/srcs/ngc4151.html. The lag due to the light travel time $\sim c\Delta t \sim 48$ days was taken into account.

model of Active Galaxies. Excess emission around 10.5 μm on the intermediate baseline indicates that silicate emission might be distributed out to ~ 1 pc in AGNs.

Using simple models we compare our mid-IR fluxes with observations in the K band and find that the structure we resolve cannot be the smooth continuation of the nuclear source detected in the K band

Due to the limited number of measurements, no two-dimensional information could be gathered and questions about the unified model (such as: is the dust structure in Sy 1 galaxies thick and torus-like or rather disk-shaped?) remain unanswered. Since nuclear dust distributions are different even within the same class of AGNs, the ultimate question whether or not the unified model is valid will not be answered before a statistical study of numerous tori is performed.

Acknowledgements

References

Antonucci, R. 1993, Ann. Rev. Astron. & Astrophys., 31, 473

Barvainis, R. 1987, Astrophys. J., 320, 537

Beckert, T., Driebe, T., Hönig, S. F., & Weigelt, G. 2008, Astron. & Astrophys., 486, L17

Buchanan, C. L., Gallimore, J. F., O'Dea, C. P., Baum, S. A., Axon, D. J., Robinson, A., Elitzur, M., & Elvis, M. 2006, Astron. J., 132, 401

Cohen, M., Walker, R. G., Carter, B., Hammersley, P., Kidger, M., & Noguchi, K. 1999, Astron. J., 117, 1864

Elitzur, M., & Shlosman, I. 2006, Astrophys. J., 648, L101

Hao, L., et al. 2005, Astrophys. J., 625, L75

Jaffe, W., et al. 2004, Nature, 429, 47

Jaffe, W. J. 2004, in Society of Photo-Optical Instrumentation Engineers (SPIE) Conference Series, Vol. 5491, Society of Photo-Optical Instrumentation Engineers (SPIE) Conference Series, ed. W. A. Traub, 715–+

Koshida, S., et al. 2009, Astrophys. J., 700, L109

Leinert, C., et al. 2003, Astrophys. & Space Science, 286, 73

Minezaki, T., Yoshii, Y., Kobayashi, Y., Enya, K., Suganuma, M., Tomita, H., Aoki, T., & Peterson, B. A. 2004, Astrophys. J., 600, L35

Mundell, C. G., Wrobel, J. M., Pedlar, A., & Gallimore, J. F. 2003, Astrophys. J., 583, 192

Pier, E. A., & Krolik, J. H. 1992, Astrophys. J., 401, 99

Raban, D., Jaffe, W., Röttgering, H., Meisenheimer, K., & Tristram, K. R. W. 2009, Mon. Not. R. Astron. Soc., 394, 1325

Radomski, J. T., Piña, R. K., Packham, C., Telesco, C. M., De Buizer, J. M., Fisher, R. S., & Robinson, A. 2003, Astrophys. J., 587, 117

Riffel, R. A., Storchi-Bergmann, T., & McGregor, P. J. 2009, Astrophys. J., 698, 1767

Schartmann, M., Meisenheimer, K., Camenzind, M., Wolf, S., & Henning, T. 2005, Astron. & Astrophys., 437, 861

Swain, M., et al. 2003, Astrophys. J., 596, L163

Tristram, K. R. W., et al. 2007, Astron. & Astrophys., 474, 837

—. 2009, ArXiv e-prints

Ulrich, M.-H. 2000, A&A Rev., 10, 135

Urry, C. M., & Padovani, P. 1995, Pub. Astron. Soc. Pacific, 107, 803

Weedman, D. W., et al. 2005, Astrophys. J., 633, 706

Chapter 5

Resolved infrared emission from the QSO 3C 273

Abstract. In order to detect emission from a putative dusty torus, we obtained spectro-interferometric observations of the QSO 3C 273 with the MIDI instrument at the VLTI, in the wavelength range 7-11 μm. Two visibility measurements were obtained at similar baseline length (~ 35m) but at nearly perpendicular position angles. These measurements have been supplemented by VISIR N-band photometry and Spitzer spectrum.

Combined, these measurements show the infrared emission to be resolved with a projected size of 32 $\times$ 84 parsec. We also tentatively detect the 10μm silicate feature in emission in one of the correlated spectra. The spatial scale of the mid-infrared emission agrees with the luminosity-radius relation for the dusty torus in AGN. Therefore we conclude that the obscuring torus commonly found in Seyfert 2 nuclei and predicted by the AGN unification model can therefore also be present in type 1 sources such as 3C 273.

5.1 Introduction

$\rm I$N the standard model for Active Galactic Nuclei (AGNs), the central black hole, accretion disk and broad line region are surrounded by a thick, torus-shaped structure of dust: the obscuring torus. The torus absorbs UV photons from the accretion disk and re-emits the energy in the mid-infrared. Infrared observations are the obvious way to directly observe the obscuring torus, but conventional single-dish observations are unable to resolve the structure. The situation has changed with the introduction of near- and mid-infrared interferometers such as the Keck interferometer and the Very Large Telescope Interferometer (VLTI). These interferometers are able to resolve the dusty structure at the milliarcseconds scales, allowing for direct measurement of the properties of the dusty torus. The observations presented here are part of an ongoing campaign to detect tori with the Mid InfrareD Interferometer (MIDI), which is coupled to the VLTI. Previous observations of nearby Seyfert galaxies revealed the presence of parsec-scale dust distributions in the centres of those galaxies, much in agreement with the standard model (Jaffe et al. 2004; Meisenheimer et al. 2007; Tristram et al. 2007; Raban et al. 2009; Tristram et al. 2009). With the data presented here, we extend our sample of active galaxies to include a non-nearby, high luminosity object, the Quasar 3C 273.

3C 273 is a radio-loud quasar with redshift z=0.158 (Strauss et al. 1992) at a distance of $\sim 650 h^{-1}$ Mpc ($H_0 = 73\,\mathrm{km\,s^{-1}\,Mpc^{-1}}$, 1pc=0.3 mas). It is one of the most studied objects of its type, being the brightest quasar on the sky and the first one to be discovered (Schmidt 1963).

At millimetre and infrared wavelengths, the object's continuum spectral energy distribution is characterised by a power law of index 0.7 ± 0.1 (Courvoisier 1998). Thermal emission is also suspected as the presence of a 3μm bump was interpreted early on as evidence of the presence of hot dust (Neugebauer et al. 1979; Allen 1980). Robson et al. (1993) and Paltani et al. (1998) have established the presence of at least two components to the thermal infrared emission from 3C 273. Recently, due to a historical minimum in the synchrotron emission from the jet, Türler et al. (2006) identify three thermal (and unresolved) dust emission components in the infrared spectrum, with temperatures $\sim 45, 300$ and 1500 K.

3C 273 is notable for its extreme variability, with large variations at the millimetre and the infrared bands. For example, at infrared wavelengths unprecedented variations have been detected in 1988 (Courvoisier et al. 1988), when the infrared flux at 4.8, 10, 20 μm changed by a factor of two on a timescale as short as one day. The flux density measurements of the 1988 flare in the infrared fits a power-law spectrum with a spectral index of 1.2 ($f_\nu \sim \nu^{-\alpha}$). Paltani et al. (1998) identified two variable components as responsible for the short and long term variations, one associated with the accretion disk, and the other with the inner jet. However, the extreme variability of the source has been and still is unaccounted for, as has been noted by Robson et al. (1993) and Paltani et al. (1998), as well as others.

The 10μm silicate feature in emission was detected by the Spitzer space telescope (Hao et al. 2005). This emission supports the presence of centrally heated dust viewed face-on. Due to Spitzer's low spatial resolution, however, we do not know the size of

the silicate emitting region, or whether it is indeed related to the obscuring torus.

Correlations between the near-IR and the optical-UV emission (Soldi et al. 2008) find a lag of 0.8-1.2 years, corresponding to a distance of 0.24 - 0.35 parsecs, which may represent the light travelling time from the UV source to the dust location, i.e. the inner radius of the torus.

The main goal of this paper is to determine the nature of the infrared emission from 3C 273 at milliarcseconds resolution, and in particular to detect thermal emission from the putative torus predicted by AGN unification models, and to compare our findings with the predictions of the AGN unification model.

This paper is organised as follows. Section 5.2 describes the observations and data reduction procedures. In §6.4 we describe the results of the measurements. In §6.5 we discuss the size constraints, detection of the silicate emission feature, implications on AGN unification models, dust emission mechanism, variability, and the relative orientations of the dust and the jet. A summary and conclusions is presented in §5.5

5.2 Instrument, observations and data reduction

5.2.1 Observations

Spectro-Interferometric: MIDI is a classical Michelson interferometer, combining two beams from two 8.2m unit telescopes, after dispersing the beams using a prism. For a detailed description of the instrument see Leinert et al. (2003).

3C 273 was observed with MIDI on February 07, 2007 with a baseline length (BL) of 37m and position angle (PA) of $31°$ and April 21, 2008 (BL=30m, PA=$128°$). The obtained spectral resolution is $R = \lambda/\delta\lambda \simeq 30$. The correlated fluxes are normally accompanied by single-dish measurement of the flux of the source. During the data reduction these are then used to determine the visibility of the source and provide additional constraints on the size and emission mechanism. Due to technical difficulties we could not measure the single dish flux, only the correlated fluxes. In stead, we use data from the Spitzer Space Telescope accompanied by VISIR photometry to estimate the single dish flux. Both are described below.

Data was reduced with the EWS (Expert Work Station) reduction package (Jaffe 2004). In addition to standard reduction procedures, and in order to increase the signal to noise in the correlated fluxes, we estimated the level of noise by looking at frames where no interferometric signal was detected. These noise levels where then removed from the data.

Photometric: To obtain a rough estimate for the total flux of the source, intermediate band photometry with VISIR was obtained on March 1, 2007, 23 days after the first interferometric observation. VISIR, the VLT Imager and Spectrometer for the mid-InfraRed, provides a long-slit spectrometer as well as a high sensitivity imager in both the N and the Q bands. The two filters in which 3C 273 was observed were PAH1 ($\lambda_0 = 8.59\,\mu$m, $\Delta\lambda = 0.42\,\mu$m) and SiC ($\lambda_0 = 11.85\,\mu$m, $\Delta\lambda = 2.34\,\mu$m). The calibrator star for the VISIR observations was HD 124294. The VISIR data were reduced by combining the chopped and nodded frames in the standard procedures for such data. The photometry was extracted in a 2.25 arcsec aperture. For the calibration, the template spectrum of HD 124294 from the catalogue by Roy van Boekel (private comm.) was

used.

In addition, we used Spitzer data in order to compare the flux of Spitzer to the VISIR data and the correlated fluxes. The Spitzer data was obtained on two different dates: 2007 Feb 28 (one day before the observations with VISIR) and 2007 Jun 28, to which the 2005 Spitzer data of Hao et al. (2005) was added. All sets show within 10% an almost identical spectrum.

5.3 Results

The correlated fluxes as a function of wavelength, VISIR photometry and Spitzer spectra are displayed in Figure 5.1.

5.3.1 MIDI

The correlated flux of Feb. 4, 2007 rises with wavelength from 0.18 ± 0.02 Jy at 7μm to 0.35 ± 0.02 Jy at 11 μm. At the shorter wavelength end it is 30% lower than the Spitzer spectrum and the VISIR photometry. At 10-11 μm, the Feb. 4 correlated flux matches the Spitzer data. The source is therefore resolved in this case at shorter wavelengths only, where the spatial resolution is highest.

The correlated flux of April 22 ,2008 rises from 0.1 ± 0.02 Jy at 7 μm to 0.2 ± 0.02 Jy at 11 μm. Although is was taken with a shorter baseline (30m, as opposed to 37m for the Feb. 4 correlated flux), the correlated flux of April 22 in considerably lower. The difference between the two correlated fluxes is most likely due to the source having an elongated morphology, which is more extended towards PA=128°.

5.3.2 VISIR & Spitzer

In the VISIR images (not shown) the flux is contained within 1.5 arcsec and the FWHM of the PSF is 0.39 arcsec and 0.44 arcsec at 8.59 μm and 11.85 μm, respectively. This is only not significantly larger than the FWHM of the (unresolved) calibrator star. 3C 273 is hence not resolved by the VISIR imaging.

The Spitzer spectra is fully consistent with the VISIR photometry, as expected from an unresolved source, indicating that the mid-IR flux was stable over the period of the measurements. We therefore use the Spitzer spectrum to derive visibilities (and therefore size estimates) for both correlated fluxes.

Additional MIDI data acquired in May 2009 in DDT observations confirm the 2008 values for the total fluc.

5.4 Discussion

5.4.1 size constraints

The difference between the correlated fluxes indicates an elongated morphology for the source. In order to model both sets of data with a single elongated source model, at least three parameters are needed: the major and minor axis sizes and the position angle. With two data point we cannot unambiguously apply a single model of an elongated source. We therefore fit the two correlated fluxes independently. First, we derive

Table 5.1. Derived projected sizes for the mid-infrared emission

projected baseline degrees	FWHM mas	FWHM pc
31°	10.2 ±4	32 ±12
128°	27 ±4	84 ±12

visibilities for both correlated fluxes by dividing them by the Spitzer data. The resulting visibilities are displayed in Figure 5.2. Next, we fit the resulting visibilities with a model of a Gaussian flux distribution. With no prior information on the morphology of the source, a Gaussian model is the most general among the different modelling options, and is able to constrain the characteristic size of the emitter regardless of its actual shape. The source size, projected on a baseline with PA=31° is 10.2±4 mas, which translates to 32±12 parsec at the distance to the source. The size projected on a baseline with PA=128° is 27 ± 4 mas, which translate to 84 ± 12 parsec. The visibility fits to the data are shown in Figure 5.2, and the derived sizes are noted in Table 5.1.

5.4.2 A possible silicate feature in emission

The convex shape of the Feb. 28 correlated flux suggests the presence of the 10 μm silicate feature in emission. Due to the limited spectral range of MIDI we do not measure the full extent of the feature, nor we can separate the silicate emission from the underlying continuum, as has been done with Spitzer data by Hao et al. (2005). The same shape does not appear on the second correlated flux. A similar result was found in MIDI observations of the Seyfert 1 nucleus of NGC 4151 (Burtscher et al, in preparation), which was also observed with two u-v points, and showed a weak silicate feature in emission for the baseline observation which was less resolved. The tentative nature of the detection of the silicate feature in both cases makes it quite hard to draw robust conclusions. Further analysis must wait for more observations.

5.4.3 Implications on the AGN unification model

Here we compare our findings with specific predictions made by the standard AGN unification model, with additional insight from current state of the art simulations of clumpy tori. The standard model predicts the appearance of the 10μm silicate feature in emission in the case of a face-on torus (Pier & Krolik 1992). The lack of detection of the feature was considered a major drawback in accepting the standard model. In 2005, the silicate feature in emission was detected in a handful of objects, mostly PG quasars (Hao et al. 2005; Siebenmorgen et al. 2005) , including 3C 273. Our tentative detection of the silicate emission feature is then fully consistent with unification models.

The standard model relates in theory the inner (sublimation) radius of the torus, R_d, to the luminosity of the central engine (Nenkova et al. 2008):

$$R_d \simeq 0.4 \left(\frac{L}{10^{45}\,\mathrm{erg\,s^{-1}}} \right)^{1/2} \left(\frac{1500\,K}{T_{sub}} \right)^{2.6} \mathrm{pc}. \tag{5.1}$$

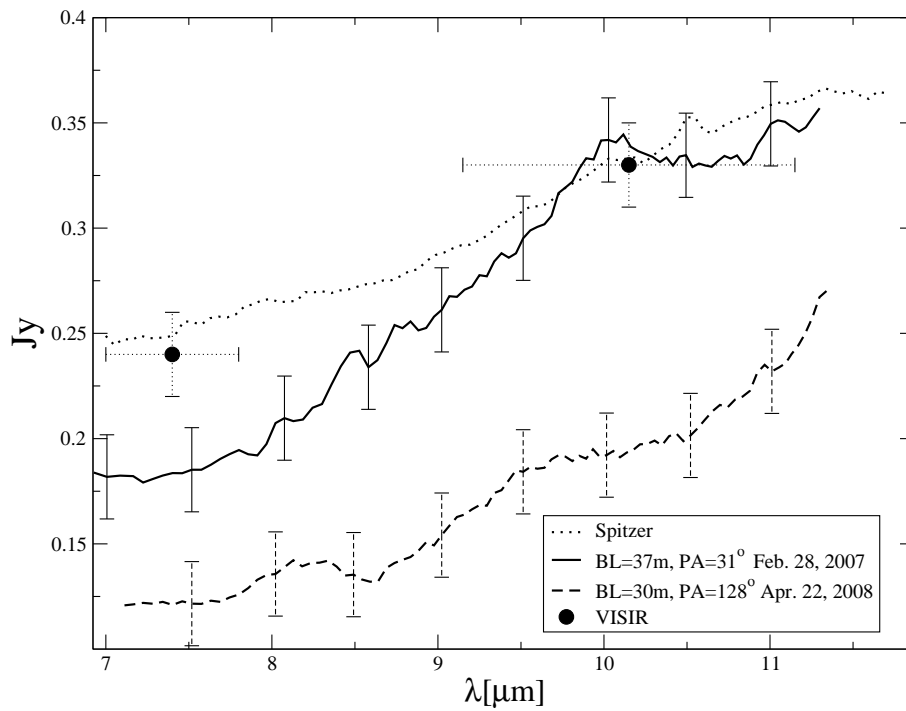**Figure 5.1 —** Redshift-corrected correlated fluxes, Spitzer and VISIR data. Solid: Feb. 28, 2007 correlated flux. Dashed: April 22, 2008 correlated flux. Dotted: Spitzer Spitzer spectrum of Hao et al. (2005). Filled circles: VISIR photometry.
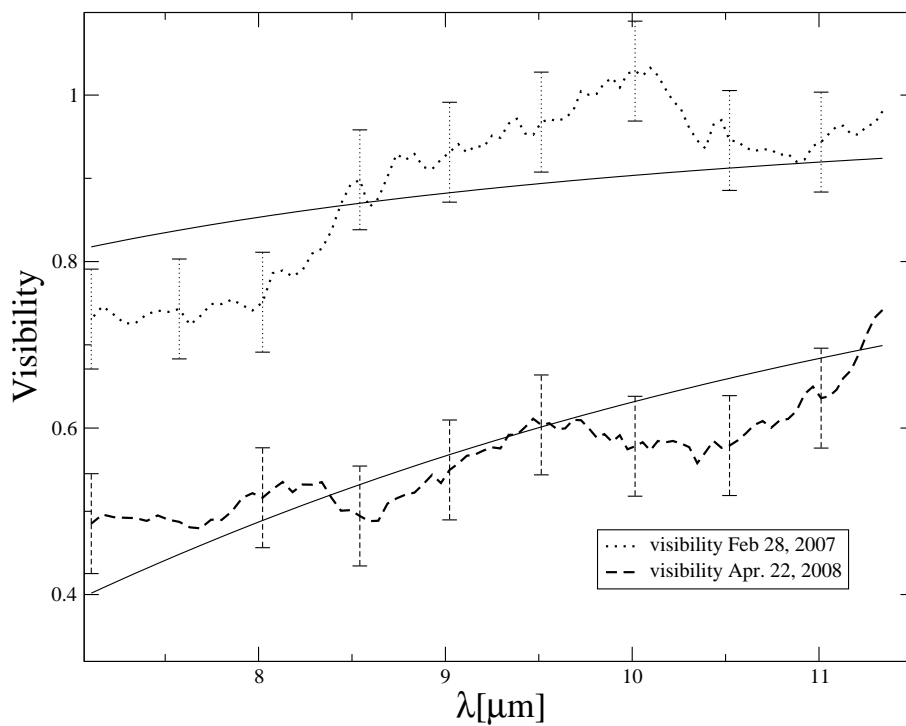

Figure 5.2 — Visibilities for the two u-v points and model fits. Dotted: data from Feb.8, 2007. Dashed: data from April 22, 2008. Solid: model fits to the data

For 3C 273, the central engine luminosity is $\sim 10^{47}\,\mathrm{erg\,s^{-1}}$ (Hao et al. 2005), which translates to a size of 4 pc for the sublimation radius of the dust, assuming a sublimation temperature of 1500 K, typical of many dust species. Further, recent three dimensional radiative transfer simulations of clumpy media (Nenkova et al. 2008; Schartmann et al. 2008) conclude that the outer radius of the torus is ~ 10 times its inner radius, in our case 40 pc. The projected size of the structure resolved by MIDI is, then, of the same order of magnitude as predicted from simulations. Thus, based on the size estimates given the luminosity of the source, we identify the resolved structure with the obscuring torus of the AGN unification models, and our findings are quite consistent with the predictions of such models.

5.4.4 Elongation and the inclination of the jet

An upper limit on the inclination of the jet in 3C 273 can be derived from the apparent super-luminar motion of the jet. The fastest radial jet speed measured for this object is $\beta = 13.4c$ (Lister et al. 2009). The upper limit on the viewing angle is then: $\theta < 2\arctan\beta^{-1} = 8.5°$.

The inclination of the jet raises the question of how to interpret the elongation we detect with MIDI. Simplistic (and likely naive) views on AGNs consider the obscuring torus to be perpendicular to the jet and circularly symmetric. In that respect, the inclination of the jet implies a nearly completely face-on torus, which should appear symmetric under the assumptions mentioned above. there are at least three mechanism which could produce an elongated appearance to the torus in 3C 273:

1. **Inclination of the dust with respect to the jet**. An elongated structure may appear if the axis of the torus is not perpendicular to the jet. Although at odds with the simplistic view of AGN, there is now a growing body of evidence which strongly suggests that this is, in fact, the general case: Statistically, Kinney et al. (2000) found little or no correlation between the relative angle of jets and the dust residing in the galactic disk for Seyfert galaxies. For individual objects, only two objects have data which directly relates the torus and the jet. The Seyfert 2 galaxy NGC 1068 has a dust distribution which is misaligned with the jet by $45°$ (Raban et al. 2009), while Circinus shows a dust distribution which is perpendicular to the jet (Tristram et al. 2007).

2. **An intrinsically elongated dust distribution**. Here, the dust structure itself possesses an elongation intrinsically. Although current theoretical models assume circular symmetry for the torus, this is mainly to simplify computation rather than a statement about the physical properties of the torus. In reality, there is neither an empirical nor a theoretical reason for the dust to be circular-symmetric. If the dust is accreted from circum-nuclear material (e.g. Schartmann et al. (2008)), then the dust might well be elongated in the direction from which it is fed. In the competing scenario (e.g. Elitzur & Shlosman (2006)), the exact morphology of the torus is determined by the little understood process of disk wind. Again, there is no reason to assume any symmetry as a result of this process. An elongated dust distribution is fully consistent with current knowledge of the obscuring torus.

3. **An unequal illumination of the torus.** The morphology and distribution of clouds in the broad line region (BLR) is not yet known, due to the compact size

of the BLR. Nevertheless, it is not unlikely that the distribution of clouds and the optical depth of the clouds are not symmetric about the nucleus. Some of the UV radiation from the accretion disk could be absorbed by the BLR, resulting in unequal illumination and temperature profile. Since MIDI observes dust at a certain temperature, those differences could appear to us an an elongation.

To conclude, any of the above mentioned scenarios (or a combination of them) could take place in an AGN. In light of this discussion, the elongation of the dust with respect of the inclination of the jet is not surprising.

5.4.5 Emission mechanism

Our findings are fully consistent with thermal emission from the obscuring torus as the dominant emission mechanism. However, we now briefly consider and dismiss the possibility that the correlated fluxes arise from synchrotron emission from the base of the jet. Radio data from the MOJAVE[1] program show extended structures in the core of 3C 273, of a size ~ 20 mas, quite similar to the size we report here. The elongated 2 cm structures, however, appear oriented at position angle PA=$\sim -50°$, a perpendicular PA compared to the structure seen by MIDI, which are elongated towards PA=$\sim 128°$. We conclude that the PA of the 2 cm emission is incompatible with the MIDI data.

Another indication that the emission from 3C 273 is thermal comes from the similarity between the shape of the 3C 273 correlated fluxes and the shapes of the correlated fluxes of type 1 sources observed in the MIDI snapshot survey (Tristram et al. 2009).

5.4.6 Variability

The above discussion, and in particular the derived projected sizes of the source, all assume that the emission from the source is constant in time, and therefore the differences in the correlated fluxes are a result of the morphology of the source. As mentioned in the introduction, the variability of 3C 273 has been well studied. In the infrared, variations of a factor 2 in flux were observed within a day (Courvoisier et al. 1988). Since our observations were obtained 1.5 years apart, which similar to the time lags between the correlations of the optical/UV and the infrared, we cannot neglect the possibility that at least some, if not all of the differences in correlated flux are a result of the variability of the source. Specifically, the differences in the correlated fluxes might result from the variability of a compact, unresolved source, for example thermal emission from the accretion disc or synchrotron from the base of the jet. As already mentioned in Tristram et al. (2009), there are indications that there were no long term (within a time-scale of years) variations in the infrared spectrum of 3C 273. Moreover, we have examined X-ray monitor RXTE data (averaged over 100 days) over the period 2006-2009. We find that the 2008.3 nuclear X-ray counts from 3C273 was *higher* than in 2007.3, thereby making less likely the possibility that long-term variability is responsible for the differences between the correlated fluxes. However, the possibility of extremely short time-scale variations (a few hours) cannot be fully discounted, given the behaviour of the source in the past.

---

[1]Monitoring Of Jets in Active galactic nuclei with VLBA Experiments, Lister et al. (2009)

5.5 Summary and conclusions

We have presented spectro-interferometric and photometric observations of the quasar 3C 273. Assuming the source was not significantly variable in the considered period, the two interferometric measurements of the 7-11 μm correlated fluxes, taken 14 month apart, reveal the source to be resolved with sizes of 32, 84 parsec projected on baselines with position angles of $31°$, $128°$, respectably. The 10 μm silicate feature in emission is tentatively detected in on of our correlated fluxes. We identify the resolved structure with the obscuring torus of AGN unification model.

Acknowledgements

References

Allen D. A., 1980, Nature, 284, 323

Courvoisier T. J.-L., 1998, A&A Rev., 9, 1

Courvoisier T. J.-L., Robson E. I., Hughes D. H., Blecha A., Bouchet P., Krisciunas K., Schwarz H. E., 1988, Nature, 335, 330

Elitzur M., Shlosman I., 2006, Astrophys. J., 648, L101

Hao L., Spoon H. W. W., Sloan G. C., Marshall J. A., Armus L., Tielens A. G. G. M., Sargent B., van Bemmel I. M., Charmandaris V., Weedman D. W., Houck J. R., 2005, Astrophys. J., 625, L75

Hönig S. F., Beckert T., Ohnaka K., Weigelt G., 2006, Astron. & Astrophys., 452, 459

Jaffe W., Meisenheimer K., Röttgering H. J. A., Leinert C., Richichi A., Chesneau O., Fraix-Burnet D., Glazenborg-Kluttig A., Granato G.-L., Graser U., Heijligers B., Köhler R., Malbet F., Miley G. K., Paresce F., Pel J.-W., Perrin G., Przygodda F., Schoeller M., Sol H., Waters L. B. F. M., Weigelt G., Woillez J., de Zeeuw P. T., 2004, Nature, 429, 47

Jaffe W. J., 2004, in Traub W. A., ed., Society of Photo-Optical Instrumentation Engineers (SPIE) Conference Series Vol. 549, pp 715–+

Kinney A. L., Schmitt H. R., Clarke C. J., Pringle J. E., Ulvestad J. S., Antonucci R. R. J., 2000, Astrophys. J., 537, 152

Meisenheimer K., Tristram K. R. W., Jaffe W., Israel F., Neumayer N., Raban D., Röttgering H., Cotton W. D., Graser U., Henning T., Leinert C., Lopez B., Perrin G., Prieto A., 2007, Astron. & Astrophys., 471, 453

Leinert C., Graser U., Przygodda F., Waters L. B. F. M., Perrin G., Jaffe W., Lopez B., Bakker E. J., Böhm A., Chesneau O., Cotton W. D., Damstra S., de Jong J., Glazenborg-Kluttig A. W., Grimm B., Hanenburg H., Laun W., Lenzen R., Ligori S., Mathar R. J., Meisner J., Morel S., Morr W., Neumann U., Pel J.-W., Schuller P., Rohloff R.-R., Stecklum B., Storz C., von der Lühe O., Wagner K., 2003, *Astrophysics and Space Science*, 286, 73

Lister M. L., Aller H. D., Aller M. F., Cohen M. H., Homan D. C., Kadler M., Kellermann K. I., Kovalev Y. Y., Ros E., Savolainen T., Zensus J. A., Vermeulen R. C., 2009, Astron. J., 137, 3718

Lister M. L., Homan D. C., Kadler M., Kellermann K. I., Kovalev Y. Y., Ros E., Savolainen T., Zensus J. A., 2009, Astrophys. J., 696, L22

Nenkova M., Sirocky M. M., Nikutta R., Ivezić Ž., Elitzur M., 2008, Astrophys. J., 685, 160

Neugebauer G., Oke J. B., Becklin E. E., Matthews K., 1979, Astrophys. J., 230, 79

Paltani S., Courvoisier T. J.-L., Walter R., 1998, Astron. & Astrophys., 340, 47

Pier E. A., Krolik J. H., 1992, Astrophys. J., 401, 99

Raban D., Jaffe W., Röttgering H., Meisenheimer K., Tristram K. R. W., 2009, Mon. Not. R. Astron. Soc., 394, 1325

Robson E. I., Gear W. K., Brown L. M. J., Courvoisier T. J.-L., Smith M. G., 1986, Nature, 323, 134

Robson E. I., Litchfield S. J., Gear W. K., Hughes D. H., Sandell G., Courvoisier T. J.-L., Paltani S., Valtaoja E., Terasranta H., Tornikoski M., Steppe H., Wright M. C. H., 1993, Mon. Not. R. Astron. Soc., 262, 249

Schartmann M., Meisenheimer K., Camenzind M., Wolf S., Tristram K. R. W., Henning T., 2008, Astron. & Astrophys., 482, 67

Schmidt M., 1963, Nature, 197, 1040

Siebenmorgen R., Haas M., Kruegel E., Schulz B., 2005, Astronomische Nachrichten, 326, 556

Soldi S., Türler M., Paltani S., Aller H. D., Aller M. F., Burki G., Chernyakova M., Lähteenmäki A., McHardy I. M., Robson E. I., Staubert R., Tornikoski M., Walter R., Courvoisier T. J.-L., 2008, Astron. & Astrophys., 486, 411

Strauss M. A., Huchra J. P., Davis M., Yahil A., Fisher K. B., Tonry J., 1992, ApJ, 83, 29

Tristram K. R. W., Meisenheimer K., Jaffe W., Schartmann M., Rix H.-W., Leinert C., Morel S., Wittkowski M., Röttgering H., Perrin G., Lopez B., Raban D., Cotton W. D., Graser U., Paresce F., Henning T., 2007, Astron. & Astrophys., 474, 837

Tristram K. R. W., Raban D., Meisenheimer K., Jaffe W., Röttgering H., Burtscher L., Cotton W. D., Graser U., Henning T., Leinert C., Lopez B., Morel S., Perrin G., Wittkowski M., 2009, ArXiv e-prints

Türler M., Chernyakova M., Courvoisier T. J.-L., Foellmi C., Aller M. F., Aller H. D., Kraus A., Krichbaum T. P., Lähteenmäki A., Marscher A., McHardy I. M., O'Brien P. T., Page K. L., Popescu L., Robson E. I., Tornikoski M., Ungerechts H., 2006, Astron. & Astrophys., 451, L1

Chapter 6

Parsec-scale dust distributions in Seyfert galaxies

Abstract.

Aims: To provide the necessary angular resolution to resolve the nuclear dust distribution which dominates the mid-infrared spectra of active galactic nuclei (AGN) and study its distribution and properties.

Methods: To this end, we carried out a "snapshot survey" with MIDI using Guaranteed Time Observations. In the survey, observations were attempted for 13 of the brightest AGN in the mid-infrared, which are visible from Paranal.

Results: . Here we present the interferometric observations for 8 of these. Size estimates or limits on the spatial extent of the AGN-heated dust can be derived from the interferometric data of 7 AGN. These indicate that the dust distributions are compact, with sizes on the order of a few parsec. The derived sizes roughly scale with the square root of the luminosity in the mid-infrared, $s \propto \sqrt{L_{\mathrm{MIR}}}$, with no clear differences between type 1 and type 2 objects. This is in agreement with nearly optically thick dust structures heated to $T \sim 300\,\mathrm{K}$. For several sources, we detect the $10\,\mu\mathrm{m}$ feature due to silicates tentatively either in emission or in absorption.

Conclusions: It seems that in the mid-infrared the individual differences between galactic nuclei are greater than the generic differences between type 1 and type 2 objects.

6.1 Introduction

IN the standard model for active galactic nuclei (AGN), the central engine, consisting of a hot accretion disk around a supermassive black hole in the centre of a galaxy, is assumed to be surrounded by a geometrically thick torus of obscuring gas and dust. These dusty tori are held responsible for redistributing the optical and UV radiation from the hot accretion disk into the mid- and far-infrared as well as for the type 1 / type 2 dichotomy of AGN. In type 2 AGN, the torus is thought to be oriented edge-on so that it blocks the view towards the central engine; in type 1 AGN, on the other hand, the torus is oriented face-on, allowing a direct view towards the central engine. The two types of AGN are hence considered to be intrinsically the same objects with any differences in their appearance arising from orientation effects (for a review, see Antonucci 1993). However, this concept faces difficulties, as geometrically thick structures orbiting compact objects are expected to collaps to a thin disk within a few orbital periods (Krolik & Begelman 1988). Therefore, different theoretical concepts for the nuclear dust distribution and obscuring medium are currently being discussed. These include clumpy dusty tori – either supported by radiation pressure(Pier & Krolik 1992; Krolik 2007), by elastic collisions of the clouds (Krolik & Begelman 1988; Beckert & Duschl 2004) or by supernova explosions (Wada & Norman 2002; Schartmann et al. 2009) –, clumpy disk winds (e.g. Königl & Kartje 1994; Elitzur & Shlosman 2006) or warped disks (e.g. Nayakshin 2005).

The dusty tori are too small to be significantly resolved with single dish telescopes in the thermal infrared ($\lambda \gtrsim 3\,\mu$m), even for $10\,$m class telescopes at the diffraction limit (with or without AO), which implies that the dust distributions are rather compact with sizes $\lesssim 10\,$pc (e.g. Soifer et al. 2003; Horst et al. 2009). Until recently, all arguments for the existence of these tori were hence based on theoretical considerations and indirect observational evidence such as the spectral energy distributions of AGN and the polarisation properties of Seyfert 2 nuclei.

Only with the advent of sufficiently sensitive interferometric instruments, the instrumental means to spatially resolve the nuclei of active galaxies at infrared wavelengths became available. One of these interferometric instruments is the MID-infrared interferometric Instrument (MIDI) at the Very Large Telescope Interferometer (VLTI), located on Cerro Paranal in northern Chile and operated by the European Southern Observatory (ESO). Apart from two observations in the near-infrared with other interferometric instruments, namely of the Seyfert 1 galaxy NGC 4151 with the Keck interferometer (Swain et al. 2003) and of the Seyfert 2 galaxy NGC 1068 with the VINCI instrument also at the VLTI (Wittkowski et al. 2004), MIDI is actually the only interferometric instrument to successfully observe active galactic nuclei in the infrared wavelength range.

The first AGN to be targeted by MIDI was NGC 1068, the brightest AGN in the mid-infrared. These observations, carried out in the Science Demonstration Time (SDT) of the instrument, indeed resolved the nuclear dust emission (Jaffe et al. 2004; Poncelet et al. 2006), showing the great potential of MIDI for the investigation of AGN. Further MIDI observations of NGC 1068 were subsequently carried out in Open Time (Raban et al. 2009).

Using mainly Guaranteed Time Observations (GTO), the two next brightest AGN, the radio galaxy Centaurus A and the Circinus galaxy, a Seyfert 2 galaxy, were studied with MIDI. The results were published in Meisenheimer et al. (2007) and Tristram et al. (2007) respectively. The MIDI observations of NGC 1068 and the Circinus galaxy have directly confirmed that, indeed, compact AGN heated dust structures on the scale of a few parsecs exist in Seyfert 2 galaxies and it was possible to determine their size as well as their orientation with respect to the source axis (Jaffe et al. 2004; Poncelet et al. 2006; Tristram et al. 2007 and Raban et al. 2009). The mid-infrared flux from Centaurus A, on the other hand, is dominated by an unresolved core (most likely the high-frequency tail of the radio core) which is surrounded by a low luminosity "dust disk" of about $0.6\,\mathrm{pc}$ diameter (Meisenheimer et al. 2007).

Apart from these three well studied sources, all other AGN which can potentially be observed with MIDI are less bright in the mid-infrared, close to or at the sensitivity limit of MIDI. In order to determine which AGN are suitable for further study with MIDI, a snapshot survey of potential targets was carried out during GTO. In the survey, every source on the target list was supposed to be observed at least once in order to test for the feasibility of MIDI observations and to obtain first estimates for the basic mid-infrared properties of the respective source. The results of this survey are presented in this paper.

The paper is organised as follows: Sect. 6.2 describes the original target list together with the properties of the sources; in Sect. 6.3, the general observational strategy as well as the general challenges for the data reduction are presented; in Sect. 6.4, the results for the individual sources are discussed while in Sect. Appendix A., a summary of the observational results is given. The discussion and the conclusions are found in Sects. 6.5 and 6.6 respectively. A more detailed discussion of the observations and the data reduction procedures for the individual sources is given in Appendix A.2.

6.2 Target list

The original list of targets for both the GTO and the SDTcontains those 16 active galaxies from Raban et al.(2008), plus NGC 1068, which are well visible from Paranal ($DEC < +25°$) and which were thought to be bright enough for MIDI observations (unresolved core flux $F_{\mathrm{core}} \gtrsim 0.35\,\mathrm{Jy}$). Additionally, the prototypical Seyfert 1 galaxy NGC 4151 was included in the list. Because of its northerly position at $DEC = +39°\,24'$, the latter does not rise more than $26°$ (corresponding to an airmass of 2.3) above the horizon at the location of the VLTI ($24°\,40'\,\mathrm{S}$). Despite the difficulty to observe it from Paranal, it was also included in the list of GTO targets in view of (1) its importance as the nearest and brightest type 1 AGN and of (2) it being one of the two AGN observed by other interferometric instruments.

In preparation for the MIDI observations, high resolution imaging in the near-infrared with NACO, the adaptive optics assisted multi mode instrument of the Very Large Telescope (Rousset et al. 2003; Lenzen et al. 2003), and in the mid-infrared with TIMMI2, the Thermal Infrared Multi-Mode Instrument 2(Käufl et al. 2003), was carried out for most of the AGN in the target list. Essentially, all nuclei remain unresolved both in the near and mid-infrared. The results of the investigation with TIMMI2 are pub-

Table 6.1.   List of all targets in the GTO program. The table columns are: objects name, type, distance (NED), 11.9 μm flux from(Raban et al. 2009), and relevant comments.[a]

Object	type	Distance	$\Delta 1\,$pc	$F_{11.9\,\mu m}$	comments
data presented here					
NGC 1365	Sy 1.8	18	1.3	0.61	
*MCG-05-23-016	Sy 2	35	6.0	0.65	
*Mrk 1239	Sy 1.5	80	2.5	0.64	
NGC 4151	Sy 1.5	14	15.1		
3C 273	QSO	650	0.3	0.35	
*IC 4329A	Sy 1.2	65	3.1	0.35	
NGC 5506	Sy 1.9	25	8.2	0.91	
NGC 7469	Sy 1.2	65	3.1	0.41	
data presented elsewhere					
*NGC 1068[b]	Sy 2	14	14.3		Raban et al. 2009
NGC 3783	Sy 1	40	.2	0.59	Beckert et al 2008
*Centaurus A	FR I	4	54.7	1.22	(Meisenheimer et al. 2007)
*Circinus[b]	Sy 2	4	50.0	9.70	(Tristram et al. 2007)
failed / not yet observed					
NGC 253	HII	3	60.0	2.04	observed by S. Hnig (failed)
IRAS 05189-2524	Sy 2	170	1.2	0.55	
NGC 3256	HII	40	5.3	0.55	not yet observed
NGC 3281	Sy 2	45	5.	0.63	
Mrk 463E	Sy 1/2	200	1.0	0.34	not yet observed
NGC 7582	Sy 2	22	10.0	0.67	observed by S. Hnig (failed)

[a] More observations than those listed here have been obtained in open time for the targets marked by an asterisk.

[b] The first observations of NGC 1068 and the Circinus galaxy were carried out on science demonstration time.

lished in Raban et al. (2008); those of the investigation with NACO will be presented in Prieto (In preparation). The photometry values of the targets at $11.9\,\mu$m from Raban et al. (2008) are listed in Table 6.1.

With progress of the observations, several galaxies from the original list were released from the GTO protection, without that observations were attempted. Among these galaxies are NGC 253, NGC 3256, NGC 3783, Mrk 463E, and NGC 7582. For some of these sources, observations were attempted by other authors: NGC 3783 was successfully observed in Open Time by Beckert et al. (2008), for NGC 253 and NGC 7582 no interferometric signal could be detected (S. Hönig, private comm.).

A summary of the observation attempts for all the sources from the original target list is given in Table 6.1. The ten objects discussed in detail in this paper, that is, the sources of the snapshot survey, are highlighted by boldface and marked by an asterisk.

6.3 Observations and data reduction

6.3.1 The MIDI instrument

MIDI is a two beam Michelson type interferometer producing dispersed fringes in the N band in a wavelength range from 8 to $13\,\mu$m (Leinert et al. 2003). For our observations, the light of two of the 8.2 m unit telescopes (UTs) was combined at any one time. The incoming wavefronts from the two telescopes were corrected using the Multi Application Curvature Adaptive Optics system (MACAO, Arsenault et al. 2003). All of the AGN in the snapshot survey were observed in high-sense mode and with low spectral resolution ($\lambda/\delta\lambda \approx 30$), that is, by the insertion of a NaCl prism into the light path after the beam combiner. As the main goal of this survey was to test for the feasibility of MIDI observations, the two shortest baselines, UT2 – UT3 and UT3 – UT4, were used for most of the observing runs so as to obtain the highest possible correlated fluxes. An observation run planned for 2007 May 05 with the longer UT2 – UT4 baseline was completely lost due to bad weather conditions on Paranal.

6.3.2 Observing sequence

We now briefly discuss the observing sequence and data reduction, while putting a special emphasis on the challenges in the context of sources at the detection limit of MIDI and the VLTI. A detailed description of the observing sequence can be found in Tristram (2007). The peculiarities of the observations and data reduction for the individual objects are discussed in Appendix A.2.

In a first step, after the telescopes have been pointed at the source, MACAO has to close the loop either on the nucleus of the source itself or – if available – on a suitable star with $V < 17$ mag and < 57 arcsec from the source, the so-called Coud guide star. For most of the sources the correction was perfomed on the nucleus itself. In several cases, this turned out to be at the limit of the abilities of the MACAO system resulting in difficulties to obtain a stable adaptive optics (AO) correction, especially under poor seeing conditions. The reason is not only that most of the nuclei are not very bright in the optical (due to obscuration), but also that the optical cores of the host galaxies are spatially extended sources. This issue will be further discussed in Sect. Appendix A..

In the next step of the observing sequence, acquisition images are taken to align the beams from the two telescopes and to ensure that the two beams overlap. For our observations, the number of individual exposures had to be increased significantly from the standard value of $NDIT = 1000$ to, for instance, $NDIT = 16000$ in order to make the source visible with respect to the residual background and to allow a proper alignment. Even for such increased integration times, several of our sources were hardly discernible against the residual background, as can be seen from Fig. 6.1. Since our
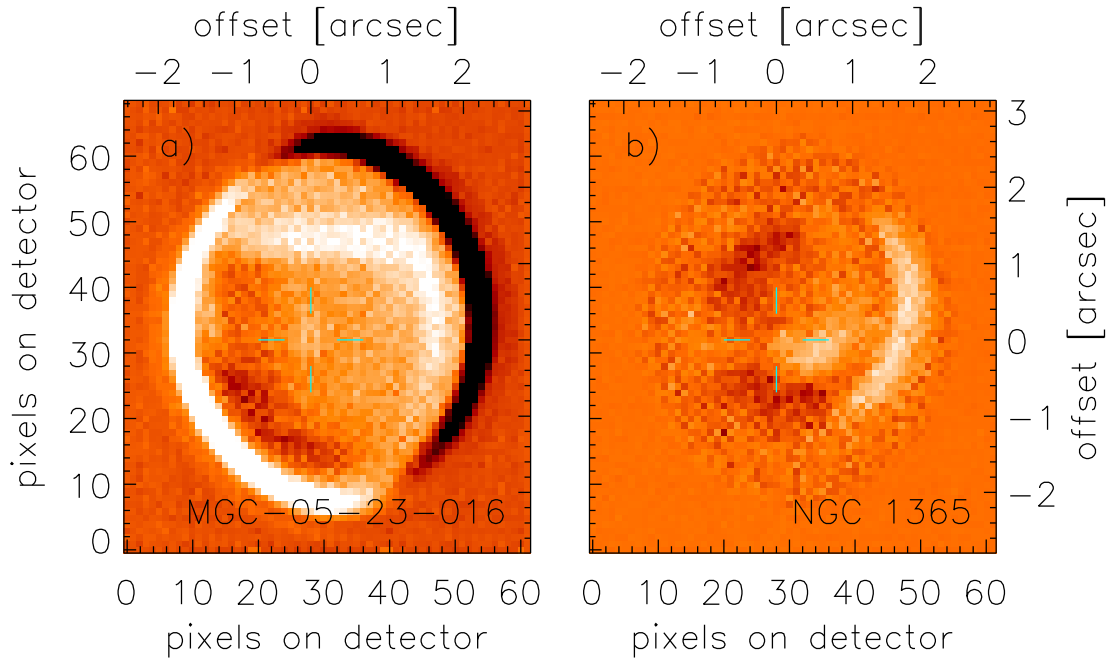
Figure 6.1 — Final acquisition images of **a)** MCG-05-23-016 (observed 2005 Dec 19) and **b)** NGC 1365 (observed 2006 Sep 11). Both sources have a total flux of about $F \sim 0.5$ Jy and $NDIT = 16000$ was used. The sources are still just about recognisable due to the high number of frames. The residual background from the VLTI tunnels is much stronger than the sources and a less even background would completely prevent a detection of the source position.

observations in September 2006, the VLTI infrared field-stabiliser IRIS (InfraRed Image Sensor, Gitton et al. 2004)) has been available. The purpose of IRIS is to stabilise the field of the beams by measuring the low-frequency tip-tilt directly in the VLTI laboratory, where MIDI is located. For sources bright enough in the near-infrared ($K < 14$ mag), IRIS guarantees the correct alignment of the beams during the observations. If one trusts that a good alignment of the beams in IRIS also produces a good alignment of the beams in MIDI[1], no acquisition images with MIDI itself have to be taken any more. Nevertheless, we continued to record acquisition images in later observing runs in order to verify the correct overlap of the beams and the quality of the

---

[1]The position of the photocentre of the source may, however, depend on the wavelength. Also, at high airmasses, the wavelength dependency of the atmospheric refraction leads to different apparent positions of the source in the near and mid-infrared which might lead to slightly different positions in MIDI and IRIS.

source image with respect to the background emission. Practically, only for two of the sources observed on 2007 Feb 07 (3C 273 and IC 4329A) and for the last observation of NGC 1365 on 2007 Nov 24, no acquisition images were obtained.

After the acquisition, the beamsplitter, a 0.52 arcsec wide slit and the prism are inserted into the light path and a so-called *fringe search* is performed in order to determine the position of the zero optical path difference (OPD) between the two beams. If an interferometric signal was detected in the fringe search, the path difference is stabilised (except for a small modulation) at or next to zero OPD while the spectrally dispersed interferometric signal is continuously recorded in order to increase the signal to noise ratio. This is the so-called *fringe track*. Because the strong background emission in the mid-infrared is uncorrelated, it can be effectively removed during the data reduction process by high pass filtering of the modulated fringe signal in delay and frequency space. Therfore, no chopping needs to be performed during the interferometric measurements and a more stable AO correction is achieved. All of our observations were carried out in "offset tracking" mode with the OPD stabilised at $50\,\mu$m from zero OPD. This tracking mode is of advantage for the sky removal using the high pass filter in frequency space as the signal is always modulated in wavelength direction; at zero OPD this is not the case.

Finally, photometric data, that is, single dish spectra, are recorded using only one telescope at a time for an otherwise identical optical set-up. As for the aquisition, chopping is used to suppress the background in the mid-infrared.

The entire procedure of acquisition, fringe search, fringe track and photometry is repeated for a calibrator star to obtain a single calibrated visibility point.

6.3.3 Data reduction

The data reduction was performed with EWS (Expert Work Station, Version 1.7), a data reduction package based on the coherent data reduction method. A detailed description of EWS is found in Jaffe (2004). The settings for the data reduction with EWS were `smooth` $= 10$, `gsmooth` $= 20$, `dave` $= 1$ and `nophot` $= 1$, the last parameter meaning that we chose to directly calibrate the correlated fluxes without using the photometric fluxes. The calibration of the data was performed using the database of stellar spectra from Roy van Boekel (private comm.).

During the data reduction process, we noticed a secular drift of the position of the dispersed signal on the MIDI detector. By November 2007, the shift had become so large (~ 3 pixels $= 0.26$ arcsec) that the dispersed fringes and the spectra of the photometry were moving outside the standard EWS mask. For this reason, we constructed a separate mask for every observing run, taking into account the position and the width (in spatial direction) of the spectra. Additionally, the sky bands used for the determination of the photometry were adjusted according to the new mask position.

The results of the data reduction process are the spectrally dispersed correlated flux $F_{\rm cor}(\lambda)$ (from the interferometric measurement), the total flux spectrum $F_{\rm tot}(\lambda)$ (from the photometric measurement, corresponding to an aperture of 0.52×1.1 arcsec^2) and the visibility spectrum $V(\lambda)$ (derived from both the interferometric and the photometric data). For an ideal measurement, $V = F_{\rm cor}/F_{\rm tot}$. In practice, however, this is often not the case (for a detailed discussion, we refer to Tristram 2007).

For sources as weak as those discussed here, the errors determined by EWS, which are statistical errors, have to be considered with caution. Especially the photometry can have unrealistically large errors. These come from the variations of the flux induced by the background residual. Extremely large errors were simply truncated corresponding to a relative error of $90\,\%$. The large errors of the photometry propagate into the visibility, but not into the correlated flux due to its direct calibration. The latter seems to have rather too small errors.

Due to the low quality or the incompleteness of several data sets, especially concerning the photometries, special data reduction procedures had to be applied to obtain meaningful results. The photometric data were completed or their quality improved by mainly using the three following methods: (1) where no photometry observations were carried out at all, photometry data obtained in conjunction with another fringe track were used to complete the data set; (2) if only one of the two photometries contains a useful signal (e.g. if there was no AO correction for one of the two telescopes during chopping), only that photometry was used to determine the total flux and (3) for strong background residuals, only those portions of the photometry integration where the background residual is relatively flat were used for the determination of the total flux spectrum. A description of which method and which additional steps were carried out for each of the individual sources is given in Appendix A.2.

6.3.4   Compilation of comparison spectra

In order to check whether the MIDI data are reasonable and in order to be able to interpret the correlated fluxes where no or only a questionable total flux spectrum was observed, additional mid-infrared spectra were compiled. Preference was given to data obtained with the highest angular resolution. For lack of alternative (no high resolution ground-based spectra available), Spitzer spectra were retrieved from the archive for several sources. The Spitzer spectra used for our comparison were observed with the Short-Low (SL, $\lambda/\delta\lambda \approx 60 - 120$) module of IRS, the InfraRed Spectrograph (Houck et al. 2004) on the Spitzer Space Telescope, in staring mode. The nuclear spectra directly delivered by the pipeline, version S15.3, were used, without applying any further correction factors. Note that a direct comparison of the Spitzer IRS spectra to MIDI data is only possible with reservations due to the large difference in the apertures of the two instruments ($3.6 \times 6.0\,\mathrm{arcsec}^2$ for IRS and $0.5 \times 1.1\,\mathrm{arcsec}^2$ for the total flux in MIDI). This is especially the case for sources also harbouring a nuclear starburst and thus displaying extended emission in the infrared, such as NGC 7469 (see Sect. 6.4.7). The Spitzer spectra thus have to be seen as upper limits to the ones measured by MIDI.

6.4   Results

The results of the measurements are presented for those seven sources where useful data could be obtained. These are namely NGC 1365, MCG-05-23-016, Mrk 1239, NGC 4151, 3C 273, IC 4329A and NGC 7469. For the remaining three sources of the snapshot survey, no useful data could be obtained: for NGC 3281 and NGC 5506, no measurements with MIDI were possible at all, because no stable AO correction could be achieved with MACAO using the extended nuclei for guiding. For IRAS 05189-2524

the interferometric signal was too weak for fringe tracking (see App. A.2.1).

For those sources where both an interferometric measurement as well as a proper measurement of the total flux spectrum was carried out with MIDI, a very crude estimate or a limit on the size of the emission region can be derived when assuming a Gaussian brightness distribution. A Gaussian flux distribution is the most simple and generalised initial guess for the shape of the source. Even if the true shape of the flux distribution differs from a Gaussian, it provides us with a correct scale of the spatial extent of the source.

The full width at half maximum $FWHM(\lambda)$ of the Gaussian brightness distribution is related to the visibility $V(\lambda)$ and the projected baseline length BL by

$$FWHM(\lambda) = \frac{\lambda}{BL} \cdot \frac{2}{\pi} \sqrt{-\ln 2 \cdot \ln V(\lambda)}. \tag{6.1}$$

By definition, $FWHM(\lambda) = 0$ when $V(\lambda) = 1^2$. Because of the nonlinear dependency of the $FWHM$ on the visibility in Eq. 6.1, the upper and lower limits on the $FWHM$ were calculated directly from the upper and lower limits of the visibility.

6.4.1 NGC 1365

The large, barred spiral galaxy NGC 1365 is located at a distance of $18.3 \pm 3.3\,\mathrm{Mpc}$ ($1\,\mathrm{arcsec} = 90\,\mathrm{pc}$, Silbermann et al. 1999) in the fornax cluster of galaxies. The Seyfert type of this galaxy is variable. This is seen as prime evidence for a clumpy torus (Risaliti et al. 2009 and references therein). An extensive overview of this galaxy is found in Lindblad (1999). In the mid infared, TIMMI2 data show that the nucleus is surrounded by 7 individual sources within $20\,\mathrm{arcsec}$ from the nucleus (Galliano et al. 2005; Raban et al. 2008), which are interpreted in terms of embedded young star clusters. The nuclear source itself shows a slight extension in E-W direction in the data from Galliano et al 2005, but this extension has not been confirmed by Raban et al. (2008). A TIMMI2 spectrum of the nucleus is presented in Siebenmorgen et al. (2004). It is featureless and flat, without any evidence for silicate absorption or emission.

The MIDI data are presented in Fig. 6.2. In the left column, the correlated and total flux spectra for the three different baseline lengths and orientations under which the source was observed are shown together with the TIMMI2 spectrum from Siebenmorgen et al. (2004). Both the total and the correlated fluxes show no indications for a silicate feature, consistent with the featureless TIMMI2 spectrum. Our total flux spectra show a continuous increase of the spectrum from $\sim 0.25\,\mathrm{Jy}$ at $8\,\mu\mathrm{m}$ to $\sim 0.50\,\mathrm{Jy}$ at $13\,\mu\mathrm{m}$, except for the second measurement (Fig. 6.2 **b)**), where up to $30\,\%$ lower flux values were measured. The MIDI spectra thus seem to be slightly lower than the spectrum obtained with TIMMI2. Nevertheless, all of the MIDI total flux spectra are consistent with each other and with the TIMMI2 spectrum when taking into account their large uncertainties. These uncertainties are caused by the residuals of the background subtraction which are especially strong for the second measurement. We hence consider the variations between our measurements as an indication for the applicability of our

---

^{2}Theoretically, $V(\lambda)$ cannot be greater than 1. Practically, however, it is not so uncommon to obtain $V(\lambda) \geq 1$ simply due to the error of the measurements. For such cases we set $FWHM = 0$.
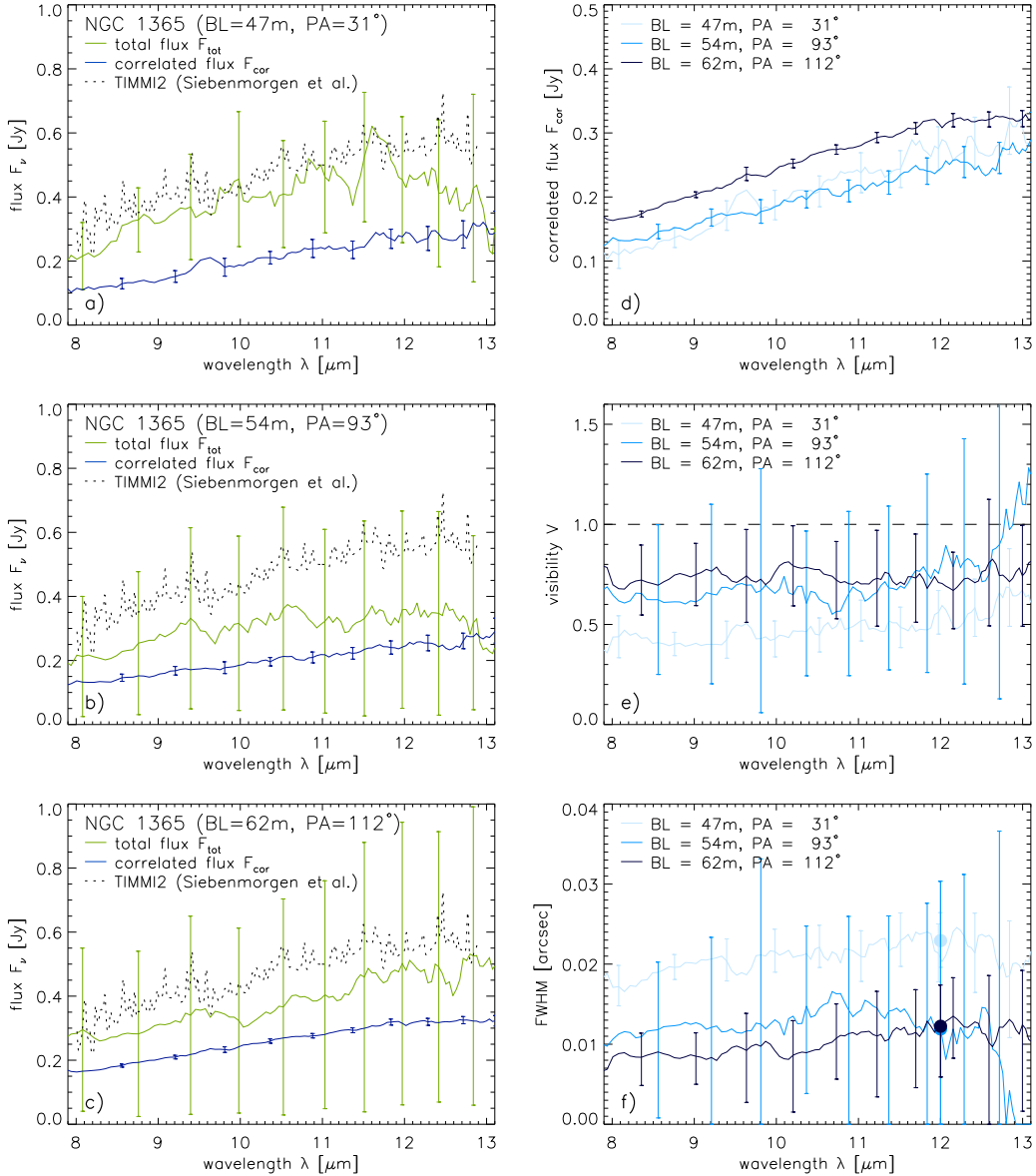
Figure 6.2 — Correlated and total flux spectra, visibilities and size estimates for the three interferometric measurements of NGC 1365. For sake of clarity, the error bars for the MIDI data are only given for every tenth wavelength bin. In the left column, panels **a)**, **b)** and **c)**, the correlated (blue) and total (green) flux spectra are displayed for each of the three baseline orientations. For comparison, the TIMMI2 spectrum from Siebenmorgen et al. (2004) is also shown (dotted line). In panel **d)** the three measurements of the correlated flux are shown together in a single plot. Panels **e)** and **f)** show the visibility spectra and the derived *FWHM* of a corresponding Gaussian flux distribution, respectively. The size estimates at $12\,\mu$m used in Sect. 6.5.2 are indicated in panel **f)** by filled circles.

data reduction methods and for the true uncertainty in the determination of the total flux. The correlated fluxes on the other hand rise from $\sim 0.15\,$Jy at $8\,\mu$m to $\sim 0.30\,$Jy at $13\,\mu$m and are hence below the level of the total flux ($F_{\mathrm{cor}} < F_{\mathrm{tot}}$). About 30 to $40\,\%$ of the nuclear mid-infrared flux is resolved by our interferometric set-up.

A comparison of the three correlated flux spectra and the corresponding visibility
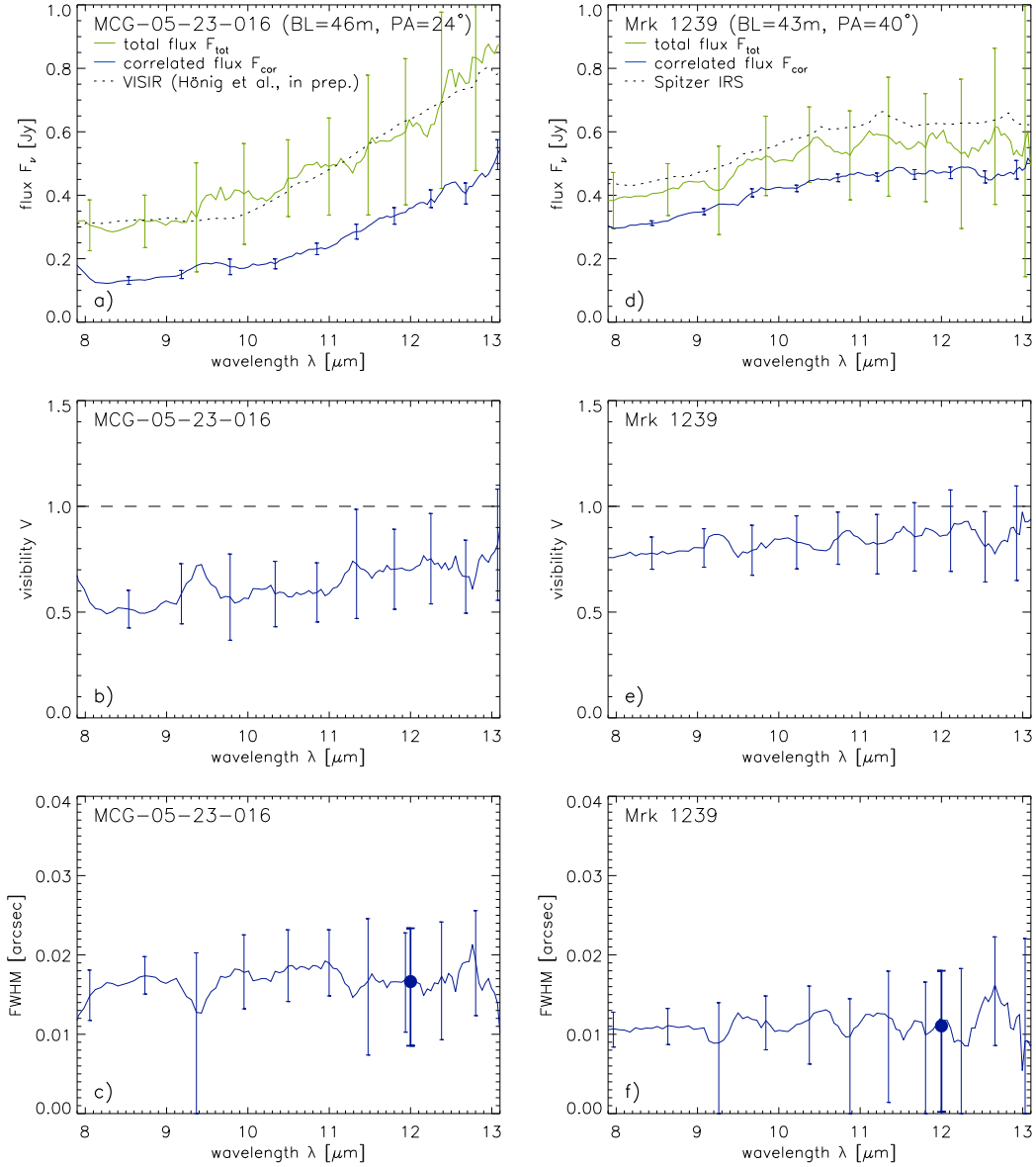
Figure 6.3 — Results of the interferometric measurements with MIDI for MCG-05-23-016 (left column) and for Mrk 1239 (right column). In the first row, the correlated (blue) and the total (green) flux spectra are displayed. For comparison, the VISIR spectrum for MCG-05-23-016 from Hönig et al. (in preparation) and the Spitzer spectrum for Mrk 1239 are also plotted (dotted lines). In the second row, the visibilities are shown. The last row shows the *FWHM* of a corresponding Gaussian flux distribution. The size estimates at $12\,\mu$m (see Sect. 6.5.2) are indicated by filled circles. For sake of clarity, the errors of the MIDI data are only indicated for every tenth wavelength bin.

spectra is given in Fig. 6.2 **d)** and **e)** respectively. Taking into account that a longer baseline length means a higher spatial resolution, it seems that the source is more extended along $PA = 31°$ than along along $PA = 112°$: the correlated flux for $PA = 31°$ tends to be slightly lower than that for $PA = 112°$, despite of the longer baseline and the consequently higher spatial resolution for the measurement at $PA = 112°$. The same conclusion follows from the visibilities: the two visibilities at $PA = 93°$ and $112°$ are still consistent with an unresolved source (i.e. with $V = 1$), while the visibility at $PA = 31°$ indicates that the source is partially resolved.

The angular sizes derived from the visibilities according to Eq. 6.1 are displayed in Fig. 6.2 **f)**. The assumed Gaussian brightness distribution has an angular extent somewhere between 5 and 30 mas. Like the correlated fluxes or the visibilities, also the size estimates show evidence for an asymmetry with a larger extent of the source (~ 20 mas) along $PA = 31°$ and a smaller size (~ 10 mas) along $PA = 112°$. At the distance of NGC 1365, 20 mas correspond to 2 pc, which sets a strong limit on the global size of the distribution of warm dust in the nucleus of this galaxy. We note that if our tentative detection of an elongated structure along $PA \sim 31°$ can be confirmed, it would not agree to the E-W elongation claimed by Galliano et al. 2005. It would, however, lie perpendicular to the ionisation cone at $PA \sim 130°$ (Wilson & Tsvetanov 1994; Hjelm & Lindblad 1996) and the radio "jet" at $PA = 125°$ (Kinney et al. 2000).

6.4.2 MCG-05-23-016

MCG-05-23-016 (ESO 434-G40) is a lenticular Seyfert 2 galaxy at a distance of 35 Mpc ($v_{hel} = 2544 \pm 12$ km s^{-1}, Wegner et al. 2003; 1 arcsec $= 170$ pc), which has been studied mostly for its X-ray emission(e.g. Balestra et al. 2004; Mattson & Weaver 2004). Its mid-infrared spectrum is characteristic for this type of nucleus rising strongly towards longer wavelengths and it displays a very shallow silicate absorption feature (see also Frogel et al. 1982).

The data obtained with MIDI are shown in the left column of Fig. 6.3. The values measured for the total flux are on the order of 0.3 Jy from 8 to 10 μm and then continuously increase to 0.8 Jy at 13 μm. Hence, the spectrum is in excellent agreement with the VISIR spectrum presented in Hönig et al. (in preparation) and with our TIMMI2 photometry: 0.65 ± 0.10 Jy at 11.9 μm. We are hence confident that the total flux values measured by MIDI are accurate for this galaxy. The correlated flux is considerably lower than the total flux ($F_{cor} < F_{tot}$), indicating that the emitter in the mid-infrared is partially resolved: roughly between 30% (at 13 μm) and 50% (at 8 μm) of the nuclear flux are resolved out by our interferometric measurement. This is also reflected by the visibility which is on the order of 50 to 70% (see Fig. 6.3**b)**).

Assuming a Gaussian flux distribution, an upper limit for the emission region in MCG-05-23-016 can be derived: at $\lambda = 12$ μm it has a size of less than 23 mas, which corresponds to less than 4.0 pc at the distance of this galaxy (see thick error bar at $\lambda = 12$ μm in Fig. 6.3 **b)**). From the fact that the source is slightly resolved, we similarly deduce a lower limit for the size of the emission region, which is roughly 9 mas and corresponds to 1.5 pc in MCG-05-23-016.
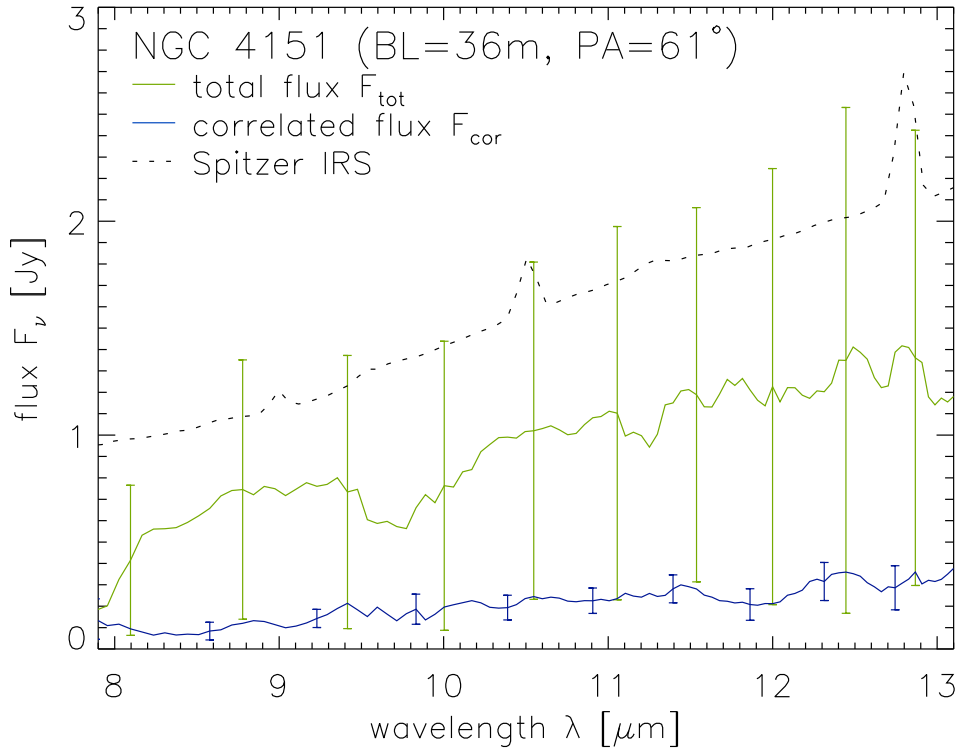
Figure 6.4 — Correlated (blue) and total (green) flux spectra for the nucleus of NGC 4151. Also plotted is the spectrum obtained with Spitzer (dotted line) which For sake of clarity, the errors of the MIDI data are only indicated for every tenth wavelength bin.

6.4.3 Mrk 1239

Mrk 1239 is a narrow-line Seyfert 1 (NLS1) galaxy located at a distance of about $80\,\mathrm{Mpc}$ ($v_{\mathrm{hel}} = 5747\,\mathrm{km\,s^{-1}}$, Beers et al. 1995; $1\,\mathrm{arcsec} = 380\,\mathrm{pc}$). Its unresolved near-infrared emission shows a strong bump at $2.2\,\mu\mathrm{m}$, which is interpreted in terms of very hot dust near its sublimation temperature ($T \sim 1200\,\mathrm{K}$), very likely located both in the upper layers of the torus and close to the apex of the polar scattering region(Rodrguez-Ardila & Mazzalay 2006). While the source appears unresolved with a flux of $0.64 \pm 0.10\,\mathrm{Jy}$ in the TIMMI2 image at $11.9\,\mu\mathrm{m}$ (Raban et al. 2008), Gorjian et al. 2004) detected an approximately $1\,\mathrm{arcsec}$ long extension from the nucleus to the northwest.

The correlated and total flux spectra, the visibility spectrum as well as the derived sizes for a Gaussian brightness distribution are displayed in the right column of Fig. 6.3, panels **d)**, **e)** and **f)**, respectively. The MIDI total flux spectrum is rising from 0.4 to $0.6\,\mathrm{Jy}$. It is slightly lower but still consistent with the Spitzer spectrum as well as with the $0.64\,\mathrm{Jy}$ measured with TIMMI2 at $11.9\,\mu\mathrm{m}$ (c.f. Table 6.1). The overall shapes of the MIDI and Spitzer spectra agree well: they both exhibit the silicate feature in emission (slightly convex shape of the spectra). The good agreement between the MIDI and Spitzer spectra despite the difference in apertures can be explained by the nature of Mrk 1239 as a Seyfert 1 galaxy without evidence for a starburst, thus implying a compact, solely AGN dominated emission region in the mid-infrared. The

correlated flux spectrum is slightly lower than the total flux spectrum, although they are consistent with each other within the errors. By consequence, the mid-infrared source in this nucleus is only slightly resolved, if at all. This can also be seen from the visibility, which is larger than 80%, with errors on the order of 20%. From the upper limit on the full width at half maximum of an assumed Gaussian flux distribution we conclude that the mid-infrared source in Mrk 1239 most likely has a size of less than $\sim 18\,\mathrm{mas}$, that is, less than $7\,\mathrm{pc}$.

6.4.4 NGC 4151

At a distance of $13.6\,\mathrm{Mpc}$ ($v_{\mathrm{hel}} = 997 \pm 3\,\mathrm{km\,s^{-1}}$, Pedlar et al. 1992; $1\,\mathrm{arcsec} = 65\,\mathrm{pc}$), NGC 4151 hosts the closest and brightest ($F_{\mathrm{N}} = 1.4\,\mathrm{Jy}$, Radomski et al. 2003)) Seyfert 1 nucleus. It has been extensively studied at all wavelengths. High resolution mid-infrared observations are presented in Neugebauer et al. (1990), Radomski et al. (2003) and Soifer et al. (2003).. They show that $\leq 70\%$ of the total mid-infrared flux comes from a core component with a size of $\lesssim 10\,\mathrm{pc}$, while the rest originates in extended emission from dust in the narrow line region. Observations with the Keck Interferometer have shown that the near-infrared emission of the nucleus is very compact ($\leq 0.1\,\mathrm{pc}$, Swain et al. 2003).

The result of the data on NGC 4151, obtained with MIDI in February 2007, is displayed in Fig. 6.4 together with the Spitzer spectrum. The total flux spectrum rises from $\sim 0.5\,\mathrm{Jy}$ at $8\,\mu\mathrm{m}$ to $\sim 1.3\,\mathrm{Jy}$ at $13\,\mu\mathrm{m}$. Its general shape agrees with the shape of the Spitzer spectrum, although it is lower by a factor of 30 to 50%. None of the smaller scale variations can be trusted and the decreases of flux below 8.2 and around $9.7\,\mu\mathrm{m}$ are due to an insufficient removal during the calibration of the absorption caused by water and ozone in the Earth's atmosphere especially for the high airmass at which this source was observed. The Spitzer and the MIDI spectra are consistent with the flux being distributed in an unresolved core and an extended component as described by Radomski et al. (2003) when taking into account the difference in the apertures. The correlated flux spectrum is even lower, on a level between 0.1 and $0.3\,\mathrm{Jy}$, implying that the mid-infrared source is clearly resolved. Assuming a visibility of $V = F_{\mathrm{cor}}/F_{\mathrm{tot}} \sim 20\%$ at $\lambda \sim 12\,\mu\mathrm{m}$ and for a baseline length of $BL = 35.8\,\mathrm{m}$, then a size on the order of $45\,\mathrm{mas}$, that is $\sim 3\,\mathrm{pc}$ at the distance of NGC 4151, can be derived for the emission region. That the emission appears to be resolved on such scales shows that most of the mid-infrared emission is of thermal origin. The size derived here is significantly smaller than the $10\,\mathrm{pc}$ from Neugebauer et al. (1990) but well above the estimated inner radius of the torus, $r_{\mathrm{inner}} = 0.04\,\mathrm{pc}$ (Minezaki et al. 2004). A full analysis of the MIDI data on this source will be given in Burtscher et al. in preparation.

6.4.5 3C 273

3C 273 (PG 1226+023) was the first quasar to be discovered (Schmid 1963). As it is the brightest object of its kind and because it exhibits a one-sided jet which is visible from the radio regime to γ-rays, it is one of the best observed and studied AGN. The quasar is located at a redshift of $z = 0.158$, which corresponds to a distance of $650\,\mathrm{Mpc}$ ($1\,\mathrm{arcsec} = 3.1\,\mathrm{kpc}$, Schmidt 1963). A detailed review of the source is given by Cour-
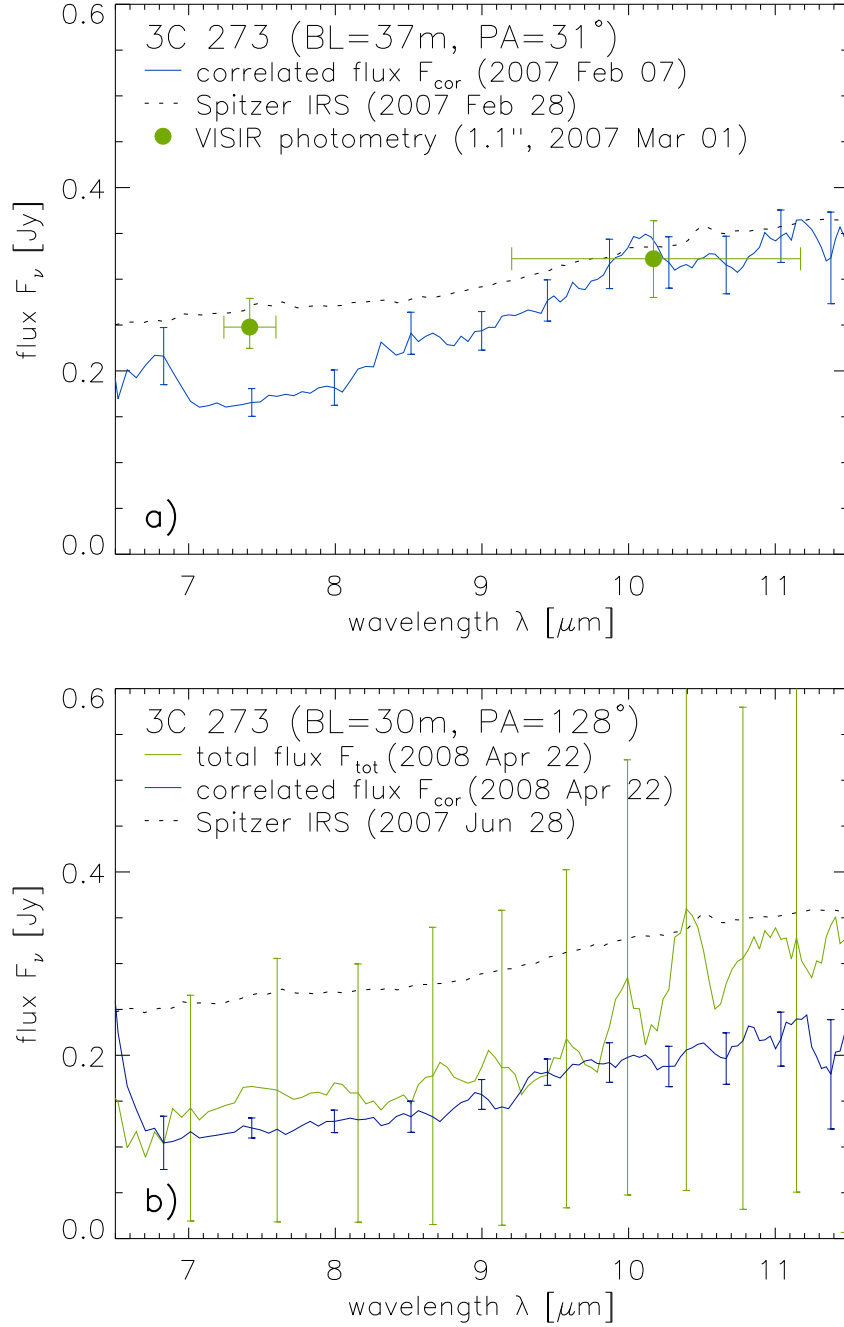
Figure 6.5 — Results for 3C 273. Panel **a)** shows the spectrum of the correlated flux measured with MIDI on 2007 Feb 07 (blue line) in comparison to intermediate band photometry with VISIR (green dots) and a Spitzer spectrum from 2007 Feb 28 (dotted line). For the VISIR data, the error bars in wavelength direction correspond to the width of the filter at half of the maximum transmission. In panel **b)**, the MIDI measurements from 2008 Apr 22 are plotted together with a Spitzer spectrum from 2007 Jun 28. The Spitzer spectrum in panel **b)** was observed four months after the one displayed in panel **a)**, nevertheless both are almost identical. Due to the relatively high redshift of this source ($z = 0.158$), the wavelength range plotted was shifted. For sake of clarity, the errors of the MIDI data are only indicated for every tenth wavelength bin.

voisier (1998).

The results of our measurements, are shown in Fig. 6.5. Due to the relatively high redshift, the restframe wavelengths probed by MIDI are between 6.5 and $11.5\,\mu$m. For the first measurement (panel **a)**), no total flux measurement could be obtained, only intermediate band photometry could be carried out with VISIR 21 days after the interferometric observations (see App. A.2.5). For the second measurement (panel **b)**), the total flux spectrum has very large errors. Therefore the interferometric data have to be compared to Spitzer spectra. These were obtained on two different dates: 2007 Feb 28 (one day before the observations with VISIR) and 2007 Jun 28. Both Spitzer spectra are almost identical. They are well suited for comparison to the MIDI data because of the pointlike nature of the nucleus in 3C 273: neither in our VISIR imaging (c.f. App. A.2.5) nor in our observations with TIMMI2 (Raban et al, 1998) there are signs for extended emission. Furthermore, the VISIR measurements are consistent with the Spitzer spectra, as is also the TIMMI2 measurement. We see this also as an indication that the total flux measured by MIDI in 2008 is rather underestimated.
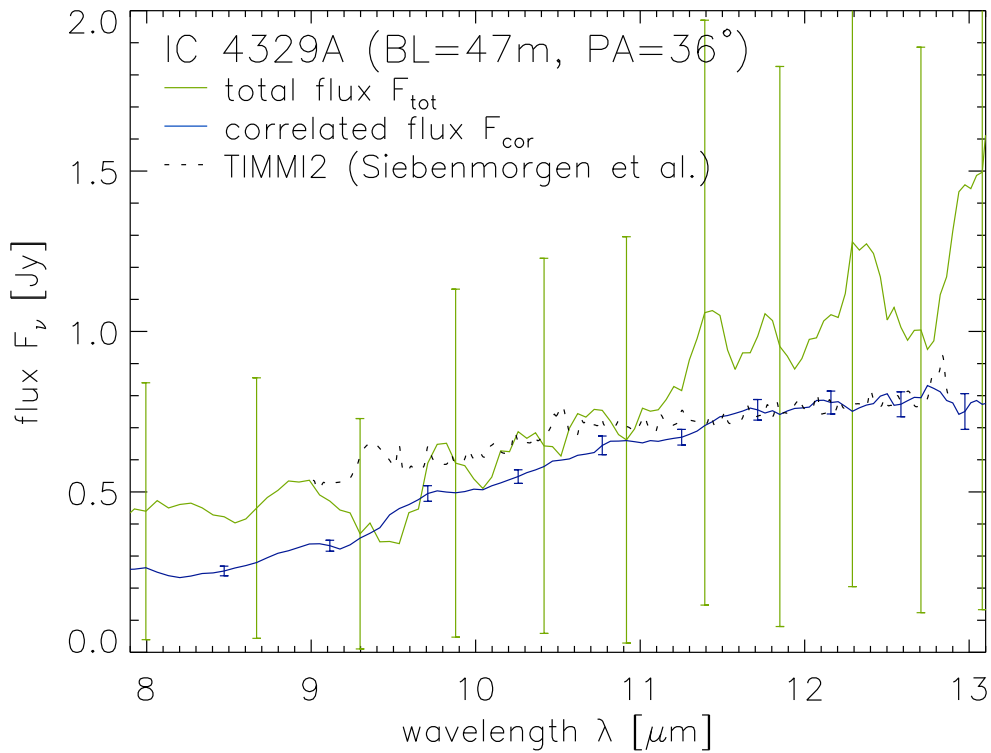
Figure 6.6 — Results of the MIDI measurements for IC 4329A. The correlated flux spectrum (blue) and the total flux spectrum (green) are compared to the TIMMI2 spectrum from Siebenmorgen et al (2004 dotted line). For sake of clarity, the errors of the MIDI data are only indicated for every tenth wavelength bin.

The correlated fluxes both rise between 6.5 and $11.5\,\mu$m. This is mainly due to the silicate feature in emission, which has its peak at $11\,\mu$m when looking at the entire mid-infrared spectrum (c.f. Fig. 1 in Hao et al (2005). The measurement on 2007 Feb 07 has a relatively steep, increasing spectrum and flux values consistent with the Spitzer

spectrum at the long wavelength end. The source appears to be only resolved to a minor fraction and only at shorter wavelengths. The correlated fluxes from 2008 Apr 22, on the other hand, follow the Spitzer spectrum at levels of 50 to 60%. It thus seems that up to half of the flux of the source is resolved, and this despite the shorter baseline length and thus smaller spatial resolution. The difference between the correlated fluxes may have two causes: (1) the difference in baselines or (2) the variability of the source. The two interferometric measurements were taken with almost perpendicular baseline orientations ($PA \sim 31°$ and $PA \sim 128°$). Changes in the correlated flux could thus be interpreted as an indication for an elongated morphology. On the other hand, variability of up to $\sim 60\%$ has been observed in the mid-infrared at $10.6\,\mu$m (Neugebauer & Matthews 1999) for 3C 273, so that the variations could have been caused by intrinsic changes in the spectrum of the quasar. All Spitzer spectra (the two Spitzer spectra shown in Fig. 6.5 from 2007 Feb 28 and 2007 Jun 28 as well as the spectrum in Hao et al. 2005 from 2004 Jan 06) show variations of less than 10% and are also consistent with the VISIR and TIMMI2 photometries. Hence we see no evidence for any significant variability during our observations. This is also supported by submm data of the source obtained as part of the monitoring program initiated by the SMA(Gurwell et al. 2007): 3C 273 appears in a relative quiescent state in February 2007 and April 2008. This leads to the conclusion that we mainly measured the emission from warm dust which is not expected to change on shorter timescales and that the change in the correlated flux is more likely caused by an elongated morphology. A more detailed analysis of the MIDI data for 3C 273 will be given in Jaffe et al. in preparation..

6.4.6   IC 4329A

IC 4329A is an edge-on spiral galaxy at a distance of $65\,$Mpc ($4793 \pm 27\,$km s^{-1}, $1\,$arcsec $= 320\,$pc, de Vaucouleurs et al. 1991) hosting a Seyfert 1.2 nucleus. The nuclear activity might be triggered by the proximity to IC 4329, a giant elliptical galaxy. As one of the brightest X-ray sources, it has been mainly studied in this wavelength range.

Fig. 6.6 shows the results of the MIDI measurements as well as the spectrum obtained with TIMMI2 from Siebenmorgen et al (2004). While the MIDI correlated flux spectrum seems to be well determined, the total flux spectrum has large uncertainities, mainly because the measured fluxes for the two telescopes differ by more than a factor of 2 (c.f. App. A.2.6). The total flux spectrum measured by MIDI lies between the slightly lower TIMMI2 spectrum and the slightly higher spectra obtained with larger apertures, e.g. the Spitzer IRS spectrum (not shown here) or the spectrum presented in Roche et al. (1991). As the total flux measurement with MIDI is consistent with these other spectra, we assume the total flux of the source to rise from $\sim 0.5\,$Jy at $8\,\mu$m to $1.1\,$Jy at $13\,\mu$m for the following. The correlated flux is slightly lower but nevertheless consistent with these values considering the uncertainties. The conclusion is that the nucleus in IC 4329A is essentially unresolved. This means that the bulk of the mid-infrared emission is concentrated on scales smaller than the spatial frequency corresponding to the baseline length for our measurement ($BL = 46.6\,$m), that is, on scales roughly smaller than $30\,$mas, which corresponds to $\sim 10\,$pc in IC 4329A.
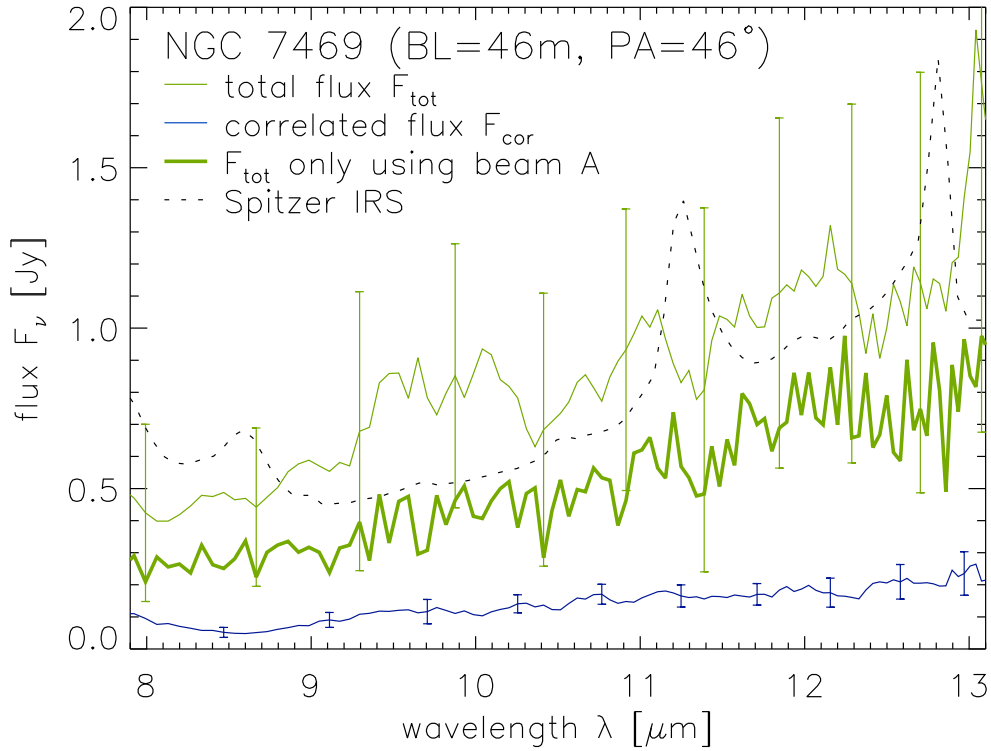
Figure 6.7 — Correlated (blue) and total (green) flux spectra of NGC 7469. For comparison, the flux measured by Spitzer is traced by the dotted line (c.f. also Fig. 6 in Weedman et al. 2005). The total flux, only determined using beam A (UT3), is plotted in dark green. The flux values at $8.3\,\mu$m and $12.8\,\mu$m used for the determination of the spectral index (see Sect. 6.5.1) are marked by filled circles. For sake of clarity, error bars are only given for every tenth wavelength bin.

6.4.7 NGC 7469

NGC 7469 is a well-studied, barred spiral galaxy at a distance of about $65\,$Mpc ($v_{\text{hel}} = 4843 \pm 5\,$km s^{-1}, Beswick et al. 2002; $1\,$arcsec $= 320\,$pc), which hosts a classical Seyfert 1 nucleus. It is also classified as a Luminous InfraRed Galaxy (LIRG) and it harbours a face-on circumnuclear starforming ring with a size of $1.0\,$kpc ($3\,$arcsec), which is detected at radio, optical and infrared wavelengths Díaz-Santos et al. 2007, and references therein). High resolution studies in the mid-infrared have been carried out by Miles et al. (1994); Soifer et al. (2003); Gorjian et al. (2004) and Galliano et al. (2005). They have found that 50 to $60\,\%$ of the total mid-infrared emission in the centre of this galaxy (i.e. within $\sim 6\,$arcsec $= 2\,$kpc) originate from the star forming ring, while only the remaining $40\,\%$ to $50\,\%$ ($\sim 0.5\,$Jy) can be ascribed to the compact nuclear source. Using deconvolved images obtained with the Keck telescope, Soifer et al. (2003) marginally resolve the nuclear source. They report a structure of $(< 0.04) \times 0.08\,$arcsec ($13 \times 26\,$pc) with a position angle of $135°$.

The results of the first MIDI observing run are shown in Fig. 6.7. These, however, need to be discussed: we find a significant difference between the pipeline reduced total flux spectrum (thin green line) and the one obtained only from beam A (UT3,

see Appendix A.2.8; thick green line). Which one is credible? The best mid-infrared spectrum available for comparison is from Spitzer. To a large degree, it contains the flux from the star forming ring, as can be deduced from the prominent PAH features and emission lines. It is hence an extremely conservative upper limit for the MIDI data and the expectation from the mid-infrared imaging is that the total flux measured by MIDI should be roughly half of that of Spitzer. As the pipeline reduced spectrum lies above that of Spitzer for most of the N band, we consider this determination as erroneous. On the other hand, the total flux spectrum only determined using beam A is on levels of roughly 50 to 80% of the continuum component in the Spitzer spectrum and it is consistent with the photometric values published for the nuclear component in Soifer et al. (2003); Galliano et al. (2005) and Raban et al. (2008):0.65 Jy at $12.5\,\mu$m, 0.56 Jy at $11.9\,\mu$m and 0.67 Jy at $11.9\,\mu$m respectively. We hence consider the total flux only using the A photometry as the best estimate for the total flux spectrum, F_{tot}.

From Fig. 6.7 it seems that the correlated flux spectrum, with $F_{\text{cor}} \sim 0.1 - 0.2$ Jy, is significantly lower than the total flux spectrum, i.e. $F_{\text{cor}} < F_{\text{tot}}$. Our interferometric observations were obtained with a position angle of $PA = 45°$, which is more or less along the minor axis of the extended structure from Soifer et al. The fringe spacing of the interferometric set-up for a baseline length of $BL = 46\,$m is on the order of $25\,$mas ($= 8\,$pc in NGC 7469). Due to the large errors in our data and especially the large uncertainty in the total flux spectrum, a determination of a size estimate is very ambitious. But considering that fringes could be tracked and that the correlated flux seems to be significantly lower than the total flux, the overall size of the source cannot be much different from the fringe spacing. We hence estimate the size of the dust distribution to be on the order of $10\,$pc. Note that, for the measurement on the second baseline with $BL = 51\,$m and $PA = 107°$, the correlated flux seems to have been even lower, because no fringes could be tracked (see Appendix A.2.8). This could be an indication that the source is slightly more resolved in this direction. This would be in rough agreement to the extended structure described by Soifer et al (2003). More data with a higher signal to noise ratio will be needed to confirm this speculation.

6.5 Discussion

Together with the other AGN observed by MIDI, the data presented here make up the spectra with the highest spatial resolution of cores of AGN in the mid-infrared. They allow us to directly analyse the properties of the circumnuclear dust which is heated by the central engine of the AGN.

In the following, two aspects of the sources will be discussed in greater detail, namely the properties of their spectra (Sect. 6.5.1) and the size of their emission region (Sect. 6.5.2). The size estimates used in the following discussion are those derived in Sect. 6.4, taken at a wavelength of $12\,\mu$m. For those galaxies where plots of the wavelength dependency of the size are given, i.e. for NGC 1365, MGC-05-23-016 and Mrk 1239, the values are marked by filled circles in the respective figures (Figs. 6.2 and 6.3).

The values of the sizes at $12\,\mu$m are listed in Table 6.2 for every visibility point together with the galaxy type, the distance of the galaxy and the baseline length of

Table 6.2 — Characteristics derived from the interferometric observations of the AGN in the snapshot survey (marked by asterisks) and other AGN studied by MIDI. The columns are (1) the name, (2) the type and (3) the distance of the galaxy (all repeated from Tab. 6.1); (4) the baseline length for the respective observation; (5) the total and (6) correlated fluxes at $12\,\mu$m as well as (7) the approximate size of the emitter at $12\,\mu$m.

Galaxy Name	Type	D [Mpc]	BL [m]	$F_{\mathrm{tot},12\mu\mathrm{m}}$ [Jy]	$F_{\mathrm{cor},12\mu\mathrm{m}}$ [Jy]	$s_{12\mu\mathrm{m}}$ [pc]
(1)	(2)	(3)	(4)	(5)	(6)	(7)
NGC 1068	Sy 2	14	33.6	16.50	4.00	3.2
NGC 1068	Sy 2	14	79.9	16.50	1.20	> 1.8
* NGC 1365	Sy 1.8	18	46.6	0.51	0.28	2.0
* NGC 1365	Sy 1.8	18	54.4	0.34	0.25	< 2.7
* NGC 1365	Sy 1.8	18	62.3	0.47	0.32	1.1
* MCG-05-23-016	Sy 2	35	46.1	0.60	0.35	2.8
* Mrk 1239	Sy 1.5	80	43.0	0.57	0.48	< 7.0
NGC 3783	Sy 1	40	68.6	1.25	0.50	3.6
NGC 3783	Sy 1	40	64.9	1.02	0.54	3.1
* NGC 4151	Sy 1.5	14	35.8	1.21	0.27	> 2.6
* 3C 273	QSO	650	36.7	0.32	0.32	< 67.3
* 3C 273	QSO	650	29.7	0.29	0.20	< 108.7
* IC 4329A	Sy 1.2	65	46.6	1.00	0.75	< 10.8
Circinus	Sy 2	4	20.7	10.20	1.80	> 1.5
Circinus	Sy 2	4	62.4	10.20	1.10	> 0.6
* NGC 7469	Sy 1.2	65	46.4	0.70	0.17	10.5

the MIDI observation. Also listed are the correlated and the total flux values at $12\,\mu$m, $F_{\text{cor},12\mu\text{m}}$ and $F_{\text{tot},12\mu\text{m}}$. For $\lambda = 12\,\mu$m, the MIDI measurements have the highest signal to noise ratio and they are least affected by the edges of the N band or the atmospheric ozone absorption feature.

The values for the sources of the snapshot survey were complemented by values for selected visibility points of other Seyfert galaxies, for which MIDI results have been published, that is, for NGC 1068 (Raban et al. 2009), for the Circinus galaxy (Tristram et al. 2009) and for NGC 3783 (Beckert et al. 2008). The sizes for these additional sources were determined in the same way as for the sources of the snapshot survey. Due to its nature as a radio galaxy with a strong non-thermal component in the mid-infrared, Centaurus A was not included in the current analysis.

6.5.1 Spectral features

The most characteristic feature of AGN in the N band is their absorption or emission by silicate dust, which leads to a broad absorption trough or emission bump covering almost the entire wavelength range between 8 and $13\,\mu$m. For typical geometries of AGN tori, the feature is expected to appear in absorption for type 2 objects and in emission for type 1 objects. Indeed, for most AGN, including the sources of the snapshot survey, a silicate absorption or emission feature is present in high signal to noise Spitzer spectra, even if the signature is very weak (see e.g. Hao et al. 2005; Weedman et al. 2005; Buchanan et al. 2006). The MIDI spectra presented here only show indications for silicate absorption or emission for three sources of the snapshot survey: MCG-05-23-016 (feature in absorption, Seyfert 2 galaxy), Mrk 1239 (feature in emission, Seyfert 1.5 galaxy) and 3C 273 (also in emission, type 1 quasar). The feature is relatively weak in all of these three sources, especially in comparison to the deep absorption features found in the two brighter Seyfert galaxies studied by MIDI, NGC 1068 and the Circinus galaxy (both Seyfert 2 galaxies;Tristram et al. 2007; Jaffe et al. 2004; Raban et al. 2009. In fact, it is surprising that the two brightest AGN in the mid-infrared also show the strongest absorption feature. For the Circinus galaxy and even more so for NGC 1068, changes in the silicate absorption depth are observed between the total flux spectra and the correlated flux spectra. For the sources of the snapshot survey however, we find no significant difference in the feature strength between the single dish measurements (or the comparison spectra) on the one side and the interferometric measurements on the other. While we can thus rule out any dramatic changes in the strength of the feature for the sizes probed by our interferometric measurements, any small changes may be hidden by the low signal to noise ratio of the data compared to that of the two bright sources. It is interesting to note that, for the two type 1 AGN, Mrk 1239 and 3C 273, the peak of the emission feature is located at $11\,\mu$m. The peak is thus offset to the maximum at $9.7\,\mu$m of the absorption coefficient of interstellar dust, which is dominated by amorphous Olivine ($[\text{Mg}, \text{Fe}]_2\text{SiO}_4$, Kemper et al. (2004). The shift of the position of the silicate feature is best explained by more aluminum-rich silica such as Augite ($\text{Ca}_2\text{Al}_2\text{SiO}_7$) which has a higher dissociation temperature and which also seems to be responsible for the changes in the absorption profile observed for NGC 1068 (Jaffe et al. 2004; Raban et al. 2009).

Finally, we note that there are no signs of the PAH features or the line emission,
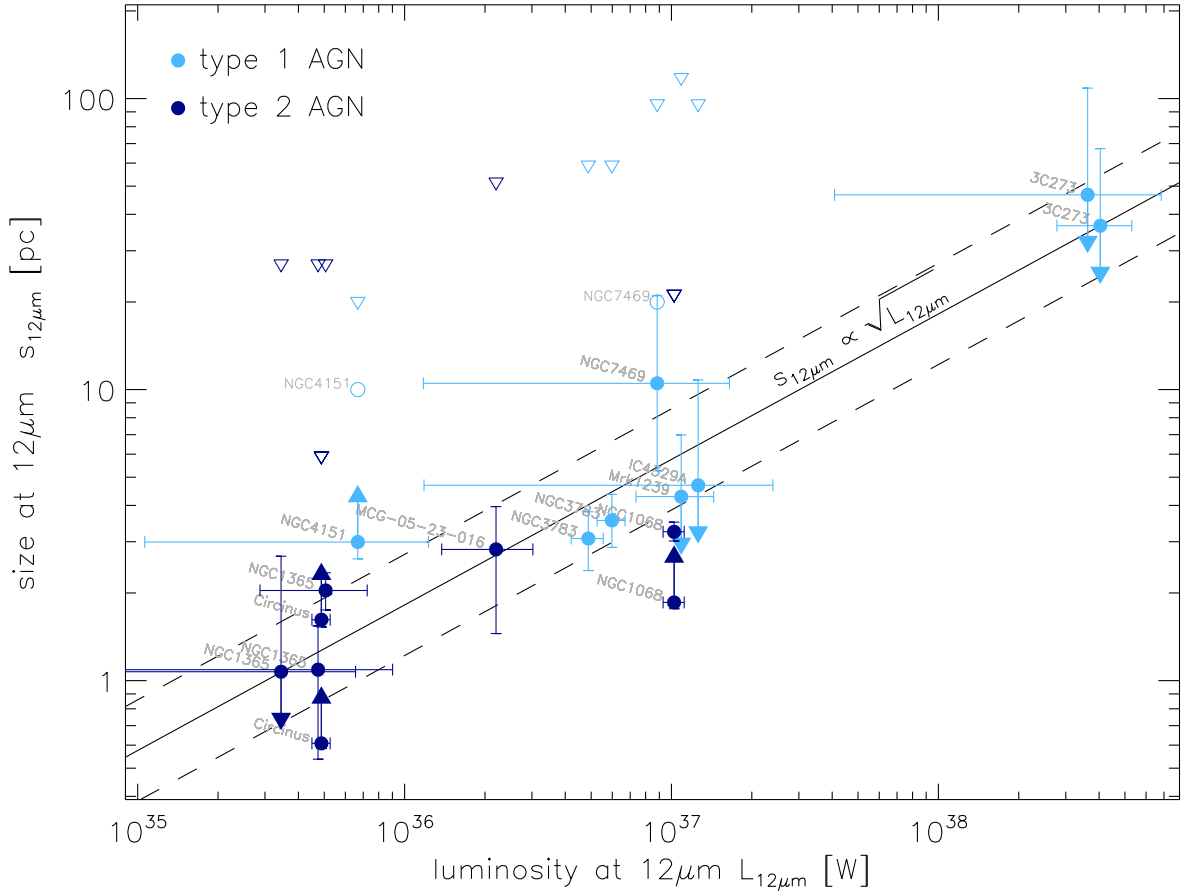
Figure 6.8 — Size of the mid-infrared emitter as a function of its monochromatic luminosity in the mid-infrared for the AGN studied with MIDI (filled circles with error bars). Upper and lower limits on the size estimates are marked by arrows. The fitted size–luminosity relation for $p = 1.8 \cdot 10^{-18}\,\mathrm{pc} \cdot (\mathrm{W})^{-0.5}$ is traced by the black line. The scatter of the measurements around this relation is $0.6\,\mathrm{dex}$ (black dashed lines). The physical scales in the respective galaxies corresponding to an angular resolution of $0.3\,\mathrm{arcsec}$ (diffraction limit of an $8\,\mathrm{m}$ class telescope at $12\,\mu\mathrm{m}$) are labelled by open triangles. The size of the resolved emission in NGC 4151 ($10\,\mathrm{pc}$) from Neugebauer et al (1990) and in NGC 7469 ($\sim 20\,\mathrm{pc}$) from Soifer et al. (2003) are also shown (open circles).

which are seen in the comparison spectra (especially for NGC 7469, see Fig. 6.7), in either the correlated flux spectra or in the total flux spectra. The PAH features are associated with star formation and they are destroyed by the hard UV radiation in the vicinity of the AGN. Their absence thus indicates that the regions we are probing are dominated by the radiation field of the AGN.

6.5.2 Sizes of the dust distributions

For simple geometries, the visibility reaches a first minimum when the fringe spacing $\Lambda = \lambda/BL$ (i.e. the "resolution") of the interferometer equals the characteristic size of the source. Therefore, the $FWHM$ of a Gaussian distribution is a good estimate for the spatial scales over which the bulk of the emission is distributed, as long as $0.2 \lesssim V \lesssim 0.8$. For $V \lesssim 0.2$ most of the flux has been resolved out while for $V \gtrsim 0.8$ the bulk of the emission remains unresolved. Only lower or upper limits on the sizes can be given in these cases.

One has to be careful not to overinterpret the size values derived from the interferometric measurements. As shown by models of AGN tori (e.g. Hönig et al. 2006; Schartmann et al. 2008) or revealed by our detailed studies of the Circinus galaxy and of NGC 1068 (Tristram et al. 2007; Raban et al. 2009), the nuclear mid-infrared emission of AGN is complex, with structures on a variety of size scales. An interferometric detection with MIDI merely indicates that the correlated flux that was measured is contained in a relatively compact region with a size not much more than Λ. The size scales sampled by the single dishes used to derive the total flux spectra are much larger than those probed by the interferometric set-up. It is not clear from only one (or very few) visibility measurements, how the flux is actually distributed between the two characteristic size scales and it is very unlikely that the real brightness distribution follows a Gaussian dependency. This is especially the case for type 1 AGN, where the infrared flux is possibly also affected by the flux from the accretion disk, which appears as a point source. The limits derived from the MIDI data for type 1 AGN are hence not only a measure for the size of the dust emission alone, but for the combination of the torus and the accretion disk flux. Because the point source adds a constant to the visibility, independent of the spatial frequency (i.e. also the baseline length), further measurements (with the same position angle but different baseline lengths) must be obtained in order to disentangle the individual components.

For NGC 1068 and the Circinus galaxy, our simple method to estimate the size assuming a Gaussian brightness distribution can be verified in comparison to fitting a model of the emitter to several interferometric measurements. In the present analysis, the measurements with the shortest and longest available baselines were included for these two galaxies. The sizes determined by our simple method (see Table 6.2) lie between the sizes of the two components of the models in Raban et al. (2009) and Tristram et al. (2007): 1.5 to $4.0\,\mathrm{pc}$ for NGC 1068 and 0.4 to $2.0\,\mathrm{pc}$ for the Circinus galaxy. We thus conclude that our size estimates are indeed realistic.

In Fig. 6.8, the sizes of the emission regions are compared to the monochromatic luminosity at $12\,\mu\mathrm{m}$, which is given by $L_{12\,\mu\mathrm{m}} = 4\pi D^2 \nu F_{\mathrm{tot},12\mu\mathrm{m}}$ with $\nu = 2.5 \cdot 10^{13}\,\mathrm{Hz}$. Studying the sizes as a function of $L_{12\,\mu\mathrm{m}}$ instead of $F_{\mathrm{tot},12\mu\mathrm{m}}$ breaks any dependency of the size on the distance D, except for selection effects (more distant objects being more

luminous). The physical scales corresponding to an angular resolution of $0.3\,$arcsec, which is the diffraction limit of an $8\,$m class telescope at $12\,\mu$m, are also shown for each galaxy. As the mid-infrared cores of all AGN are essentially unresolved by single dish observations, these size scales are strict upper limits for the sizes of the dust distributions.

For not too different geometries and especially volume filling factors, the size of the torus at a certain wavelength, s_λ, should be a function of its monochromatic luminosity, L_λ, at this wavelength: $s_\lambda = p_\lambda \cdot (L_\lambda)^{0.5}$ or $\log(s_\lambda/\mathrm{pc}) = q_\lambda + 0.5 \cdot \log(L_\lambda/\mathrm{W})$, where p_λ and q_λ are constants mainly depending on the volume filling factor and/or the optical depth of the torus. The relation simply accounts for an object of twice the size having four times more emitting surface. Indeed most of our measurements agree with the above relation and for $\lambda = 12\,\mu$m we find $p_{12\,\mu\mathrm{m}} = (1.8 \pm 0.3) \cdot 10^{-18}\,\mathrm{pc} \cdot (\mathrm{W})^{-0.5}$ and $q_{12\,\mu\mathrm{m}} = -17.7 \mp 0.2$, respectively. The scatter of the individual sources around the relation is $0.6\,$dex (see Fig. 6.8) and it can be largely explained by the uncertainties in our measurements. However, also differences in the actual geometry and orientation as well as in the filling factor of the dust distribution have a significant impact on the apparent size of the emission region. For an optically thick blackbody emitter with the size s, the luminosity is given as $L_\lambda = \pi s^2 \nu F_{\mathrm{bb}}(\nu, T)$. This can be rearranged to $s = (\pi \nu F_{\mathrm{bb}}(\nu, T))^{-0.5} \cdot (L_\lambda)^{0.5}$. For $p_\lambda = (\pi \nu F_{\mathrm{bb}}(\nu, T))^{-0.5}$ this is identical to the above relation. For a temperature of $T = 300\,$K, taken as an average value for the temperatures suggested by the slopes of the spectra, we receive $p_{12\,\mu\mathrm{m}} \sim 1.8 \cdot 10^{-18}\,\mathrm{pc} \cdot (\mathrm{W})^{-0.5}$. This implies that, indeed, the mid-infrared emission mainly originates from a more or less optically thick and thus compact dust distribution with an average temperature of $300\,$K.

At the first glance, there seems to be a tendency for type 1 objects to have more extended dust distributions than type 2 objects: while the nuclear dust distribution in NGC 1068 appears relatively compact in comparison to all other galaxies, the warm dust in NGC 4151 and NGC 7469 seems to be more extended than average. Further evidence in this direction comes from Neugebauer et al. (1990) and Soifer et al. (2003), who partially resolved the mid-infrared cores in just these two galaxies. Their size estimates, $10\,$pc for NGC 4151 and $(< 13) \times 26\,$pc for NGC 7469, are also shown in Fig. 6.8 (open circles; averaged to $\sim 20\,$pc in the case of NGC 7469) and suggest even more extended emission regions than measured by our interferometric measurements. In the case of NGC 7469, the apparently larger extent may partially be explained by contamination with extended emission from the surrounding starburst to the single dish spectra, although this contamination cannot be very large due to the lack of any PAH signatures in our total flux spectrum. In the case of NGC 4151, however, there is no circumnuclear starburst contribution that could contaminate the single dish measurements. It seems that the warm dust in this galaxy is extended more for its luminosity than in any other galaxy of our sample. This is probably caused by emission from dust in the ionisation cones, which is extended on the scales of $3.5\,$arcsec $= 230\,$pc (Radomski et al. 2003). Thus it seems that a major fraction of the mid-infrared emission in this source actually originates in the ionisation cones and not in the torus itself. Together with the relatively red spectrum at the centre, it seems that this galaxy is also a special case with respect to the standard picture, where most of the mid-infrared emission is

expected to originate in the dusty torus. A more detailed analysis of the interferometric data, including new observations, will be necessary to substantiate this finding.

Apart from these indications for individual outliers to the size-luminosity relation, there is no indication from our data that the size of the emission region is significantly different between type 1 and type 2 objects. That means that the sizes of the distributions of warm dust are of the same order in both types of nuclei. This is in strong support of the unified picture, where the dust distributions in both AGN types are assumed to be the same. The finding also agrees well to recent radiative transfer calculations of clumpy AGN tori, where the appearance of the tori is relatively similar in the mid-infrared (Schartmann et al. 2008, 2009).

6.5.3   Elongation of the dust emission

We also find tentative detections of an elongated mid-infrared emission region for three sources: NGC 1365, 3C 273 and NGC 7469. In the latter case, the elongation has been previously detected by Soifer et al. (2003). For NGC 1365, the elongation derived from our measurements is roughly oriented perpendicularly to the symmetry axis of the system, which is defined by the axis of the radio jet or the ionisation cone.

This is, again, in agreement with the expectation in the standard unified paradigm of AGN and to the results found for the three brighter AGN (NGC 1068, the Circinus galaxy and Centaurus A), where dust disks roughly perpendicular to the symmetry axis of the systems were found (Raban et al. 2009; Tristram et al. 2007; Meisenheimer et al. 2007).. More measurements are, however, needed to confirm these results.

6.6   Conclusions

In the MIDI AGN snapshot survey, high resolution interferometric observations of ten active galactic nuclei were attempted in the mid-infrared with MIDI at the VLTI. The goal was to determine, which further AGN, in addition to the previously investigated sources NGC 1068, the Circinus galaxy and Centaurus A, are suitable for studying with MIDI and to derive first estimates for the sizes of the emission regions in the mid-infrared.

The observations were performed at the sensitivity limit of MIDI and of the VLTI. We find that, currently, the main limitation for the observations lies in the possibility to assure a stable AO correction and to obtain a secure total flux (i.e. single dish) measurement. No interferometric measurements could be carried out for two sources, because the nuclei of these galaxies were too faint and too extended for the MACAO systems to provide an adaptive optics correction.

For the remaining eight sources, an interferometric signal could be detected and for seven of the sources the signal was strong enough to derive correlated flux spectra. Together with the three brighter targets NGC 1068, the Circinus galaxy and Centaurus A as well as two further AGN, NGC 3783 (Beckert et al. 2008) and NGC 424 (Hönig et al. in preparation b), this gives a total number of 12 extragalactic sources for which fringes could be tracked with MIDI. All of these objects are worth further investigations and more detailed observations are underway.

For the sources where size estimates for the emission regions could be determined, we find that the emission regions have sizes between 1 and $10\,\mathrm{pc}$ roughly scaling with $\sqrt{L_{\mathrm{MIR}}}$ and for close to optically thick emission. This "size-luminosity relation" is consistent with the emission originating in compact and warm ($T \sim 300\,\mathrm{K}$) dust distributions, which are heated by the central engines of the AGN. In both the spectral features as well as in their sizes we find no significant differences between type 1 and type 2 AGN, indicating that the types of objects have similar signatures of their dust distributions in the mid-infrared. The only evidence for a difference between type 1 and type 2 AGN in the MIDI data comes from the silicate feature appearing rather in emission for type 1 objects and in absorption for type 2 objects.

Larger differences in size appear between individual objects and we find that the individual members of a class differ from each other more than suggested by the standard picture of the dusty torus. This is in agreement with recent hydrodynamical models of AGN tori which show that the mid-infrared properties are significantly dependent on the detailed configuration of the non-smooth dust distribution.

acknowledgements

Appendix A.

A.1   General observational comments

In the MIDI AGN snapshot survey, interferometric observations in the mid-infrared were attempted for a set of ten AGN. Out of these ten sources, an interferometric signal could be detected for eight sources and only for two no measurement with MIDI was possible at all. For the latter two sources (NGC 3281 and NGC 5506, see Appendices A.2.3 and A.2.7), no stable AO correction could be performed with MACAO using the optical nuclei of these two galaxies. Hence the observation attempt failed during the acquisition process and not because no interferometric signal could be detected by MIDI. For all of the eight sources where a stable AO correction could be achieved at some point, an interferometric signal was detected. This means that the true detection rate of a fringe signal by MIDI itself for the AGN in the snapshot survey is $100\,\%$. For all except one of these eight sources, fringes could also be tracked, that is, the zero OPD position could be continuously determined. Only for IRAS 05189-2524, the online tracking software was not able to determine the zero OPD position. This was only possible in post-processing (see Appendix A.2.1). For six of the seven remaining sources, the faintness and extent of the nuclei in the optical were still challenging for MACAO. Mainly the photometric observations were affected by having to use the AO

systems at their limits: in many cases a stable AO correction was not possible while chopping. The chopping constitutes an additional complication for the AO system, since in every chopping cycle the AO loop has to be opened for the off target position (sky position) and then closed again for the on target position. For the interferometric measurement on the other hand, no chopping is needed and generally a more stable AO correction is achieved (see Sect. 6.3). Only for MCG-05-23-016 were there no AO problems at all. In fact, this is the only galaxy from the snapshot survey, where the AO correction was performed using a separate Coud guide star. For all other galaxies, the more or less extended and obscured nuclei were used.

The overall perfomance of the adaptive optics systems depends on several factors, the most important being (1) the performance of the individual adaptive optics units, (2) the brightness and spatial extent of the object used for guiding and (3) the atmospheric conditions. Ad (1) we note that, for our observations, mainly the MACAO unit on UT2 caused problems. In general, this unit produced a worse wavefront correction – resulting in a reduced PSF quality – than the other units and it was often this unit which failed totally to close the loop. Considering the object used for Coud guiding, a more robust correction is achieved for bright and pointlike sources. To date, for all except one of the faint sources observations have been tried with Coud guiding on the nucleus, although for some of the sources a possible guide star is in range. Especially in the case of NGC 7469, and maybe also for NGC 3281, future observations should be tried with the guide star available. Finally, the possibility of a stable AO correction sensitively depends on the atmospheric conditions at the time of observation: good seeing conditions and long coherence times increase the chances of a stable AO correction and are hence necessary for the interferometric observation of faint AGN with the VLTI. From the high detection rate of fringes in the snapshot survey, we deduce that the ultimate limit for the detection of an interferometric signal with MIDI has not been reached yet. From our data on IRAS 05189-2524, we infer that the limit for the detection and tracking of fringes with MIDI is on the order of 0.1 to $0.2\,\mathrm{Jy}$. This limit is however only reached when an optimised mask and optimised data reduction settings are applied. At the moment, this can only be done in post processing. For the current implementation of the software at the VLTI, the limit is approximately a factor of 2 higher, that is, on the order of $0.3\,\mathrm{Jy}$. Simply using longer integration times and redundant measurements will not improve the detectability of even weaker sources, as it will not be possible to continuously determine the zero OPD position in real time. An external fringe tracker will be necessary, if even fainter sources are to be observed. Furthermore, it has to be taken into account that normally the detection and the recording of the interferometric signal is not the only goal of a MIDI observation. Instead, full data sets consisting of both the interferometric signal as well as the photometry are required to scientifically evaluate the data. This is especially the case if only a few visibility points are observed (as is the case for the sources presented here) and if a direct comparison between several measurements of the correlated flux at different baseline lengths and orientations is not possible. Even if a stable AO correction is achieved, the main limitations are still connected to the robust determination of the total flux spectrum from the photometry: it is the total fluxes that show large (statistical) errors due to the permanent variation of the background in the mid-infrared. Even for stable

atmospheric conditions, total fluxes on the order of 1.0 Jy have a statistical error up to 20%. Less stable atmospheric conditions immediately lead to larger statistical errors, as can be directly deduced from the MIDI observations of Centaurus A ([see Fig. 1 in Meisenheimer et al. 2007). Due to these limitations, it should be considered to completely forego the measurement of the photometry for very faint sources and to only use the relative changes between the correlated fluxes to characterise the emitter. This is, in fact, how observations are commonly carried out in radio interferometry.

In general, the MIDI data nevertheless appears to be reasonable and trustworthy. Especially the good agreement between the MIDI measurements and the mid-infrared data used for comparison in the case of MCG-05-23-016 and Mrk 1239 is reassuring. It shows that MIDI produces reliable results even at its sensitivity limit when the observational strategy is adapted accordingly and when complete data sets are obtained. For faint sources it is imperative to carry out MIDI observations with significantly increased exposure times (e.g. NDIT $= 8000$ instead of NDIT $= 2000$ for the photometry) and a certain degree of redundancy (e.g. by repeating the error-prone photometric observations) in order to reach an acceptable signal-to-noise ratio. This and the often longer acquisition procedure lead to a considerably larger amount of time, up to 1 hour, needed for the measurement of the science target alone. Together with the calibrator observations, a full, calibrated visibility point for a faint source thus requires up to 1.5 hours of observing time.

A.2 Remarks on the observations and the data reduction for the individual sources

NGC 1365

This source was successfully observed several times during the observation runs on 2006 Sep 11 and on 2007 Nov 24, using the UT2 – UT3 and the UT3 – UT4 baselines, respectively.

During the first run, the ambient conditions were fair, with a seeing of 1.1 to 1.4 arcsec. Although the MACAO unit on UT2 was unable to securely lock on the extended nucleus under these conditions, a fringe signal could be detected and tracked. While the quality of the subsequent photometry of beam A is relatively good, no signal is present in the photometry of beam B: no stable AO correction could be achieved while chopping on UT2. For this reason, the photometry was replaced by a portion of the A photometry with little background variations in order to be able to reduce the data using the standard data reduction routines. Additionally to the standard reduction routine, which relies on both photometries and yields an "averaged two-dish total spectrum" of the source, we determined the total flux in a second way, which is only based on the photometry of beam A for both NGC 1365 and the associated calibrator HD 026967 (cal12). The information of beam B is disregarded completely. As for the standard data reduction, the calibration was carried out using the template spectrum of the star from the database by Roy van Boekel (private comm.). We find that the two determinations of the total flux spectrum are consistent with each other within a fraction of their errors.

Two further attempts (sci13 and sci14) to track the fringes of this source on 2007 Nov 24 failed, no stable tracking could be achieved.

More successful observations of the source were carried out during the second run

although the ambient conditions were comparable to those on 2006 Sep 11. A total of 4 successful fringe tracks and two sets of photometric data could be obtained. However the data reduction was again not straight forward due to problems with the photometry of the first data set (sci33): the background in the photometry of beam A (UT4) is extremely unstable, so that only a subset of the frames, where the background is relatively stable, were selected for the data reduction. The three last fringe tracks (sci35, sci36 and sci37) were observed consecutively without that the source was reacquired and the baseline orientation and length only changed insignificantly. Therefore, the three measurements are almost identical and they were averaged to give one visibility point.

A.2.1 IRAS 05189-2524

For IRAS 05189-2524 (LEDA 17155), a Seyfert 2 galaxy located at a distance of $170\,\mathrm{Mpc}$ ($12760 \pm 54\,\mathrm{km\,s^{-1}}$, Huchra et al. 1983; $1\,\mathrm{arcsec} = 850\,\mathrm{pc}$), two observation attempts were carried out. Although the acquisition succeeded with UT3 on 2006 Sep 11, it completely failed for UT2. Hence, no data was obtained on this occasion. Only during the second attempt on 2007 Nov 24 with the UT3 – UT4 baseline, a stable AO correction with MACAO was achieved. A very weak signal is present in the fringe search, although this was only noticed in post processing using the optimised mask and the parameter settings described in Sect. 6.3. The fringe track, which was observed "blind", i.e. without knowing the exact position of zero OPD at the time of the observation, also shows a very faint signal while the OPD drifted over the zero OPD position. However, the signal was too weak for the observing software to stabilise the OPD and hence not enough frames were recorded to allow a confident determination of the correlated flux. From the acquisition images it seems that the two beams were misaligned by more than 2 pixels ($= 0.17\,\mathrm{arcsec}$), which is slightly more than $HWHM = 0.15\,\mathrm{arcsec}$, the half width half maximum of the PSF averaged over the N band. This means the beam overlap was such that only $75\,\%$ of the flux was able to interfere. From the few frames where an interferometric signal is present we estimate that the correlated flux rises from $\sim 0.1\,\mathrm{Jy}$ at $8\,\mu\mathrm{m}$ to $\sim 0.2\,\mathrm{Jy}$ at $13\,\mu\mathrm{m}$. Taking into account the correction for the beam overlap, the correlated flux in IRAS 05189-2524 seems to have been on the order of 0.1 to $0.3\,\mathrm{Jy}$. This is significantly less than the total flux spectrum measured by Siebenmorgen et al. (2004), which rises from 0.3 to $1.0\,\mathrm{Jy}$ from the short to the long wavelength end of the N band, potentially indicating that the source is resolved. Unfortunately, no photometry confirming this conclusion was observed for IRAS 05189-2524 with MIDI. This case shows the importance to also obtain photometric information even for those sources where no fringes could be detected or tracked. Then a lower limit for the size of the emitter can be derived.

A.2.2 MCG-05-23-016 and Mrk 1239

One full visibility measurement for MCG-05-23-016 and two full measurements for Mrk 1239 were obtained on 2005 Dec 19. Double photometric measurements of 8000 frames each for every visibility point were carried out in order to increase the signal-to-noise and to obtain redundant measurements in case of problems. Indeed, for the

second observation of Mrk 1239, the MACAO loop was open for a portion of the second photometry of beam B (UT2). The faulty photometry was replaced by the corresponding one taken during the first observation.

The second observation of the calibrator HD 083618 was obtained at the end of the night and no photometric data could be recorded any more. The data set was completed using the photometry from the first observation of this calibrator (cal02).

To obtain the final fluxes and the visibility, the two individual measurements of Mrk 1239 were averaged. This is possible because the position angle and baseline length only differ insignificantly.

A.2.3 NGC 3281

An unsuccessful attempt to observe the Seyfert 2 galaxy NGC 3281 ($v_{hel} = 3200 \pm 22\,\mathrm{km\,s^{-1}}$, Theureau et al. 1998; $D = 45\,\mathrm{Mpc}$, $1\,\mathrm{arcsec} = 210\,\mathrm{pc}$) was made during the observing run on 2007 Feb 07. MACAO could not lock on the nucleus of this galaxy because it was too extended in the visible. By consequence, the source could also not be detected with IRIS and no data was obtained at all.

A.2.4 NGC 4151

Our first observation of NGC 4151 was carried out on 2007 Feb 07 using the UT2 – UT3 baseline. From the two fringe tracks that were attempted, only the second one contains useful data: fringes were clearly tracked for about $40\,\mathrm{sec}$ before they were lost. Only these $40\,\mathrm{sec}$ of tracking were used for the determination of the correlated flux. Due to the failure of MACAO to keep the loop closed on UT2 while chopping only the photometry for beam A contains useful data. A pipeline reduction with EWS was performed by also using the A photometry for beam B. The result was double checked by an additional determination of the total flux only using the A photometries of NGC 4151 and of HD 098430 alone, as described for the first observation of NGC 1365 (see App. A.2): the two total flux spectra agree within $30\,\%$.

More successful observations were carried out on 2008 Apr 22 and 2008 Apr 24 with the UT3 – UT4 and the UT2 – UT4 baselines, respectively. These new observations as well as a full analysis for the interferometric data will be presented in a separate paper, in preparation.

A.2.5 3C 273

3C 273 was first observed during the observation run on 2007 Feb 07. MACAO could not keep the loop closed during chopping and, by consequence, no acquisition images and photometry were obtained. Given the pointlike nucleus with $V = 12.8\,\mathrm{mag}$ (Türler et al. 2006) and the later success to close the loop on the nucleus (see below), the reason for this malfunction remains unexplained. Instead, the beams were aligned with IRIS in the K band alone. In total, four attempts to track fringes were performed, however only the last two contain an interferometric signal. For the data reduction, they were treated as a single, long track. Because no photometric data was available, only the calibrated correlated flux can be determined from the MIDI data. To obtain a rough estimate for the total flux of the source, intermediate band photometry with VISIR was

obtained on 2007 Mar 01, that is, 23 days after the interferometric observations. VISIR, the VLT Imager and Spectrometer for the mid-InfraRed, provides a long-slit spectrometer as well as a high sensitivity imager in both the N and the Q bands (Lagage et al. 2004). The two filters, in which 3C 273 was observed, were PAH1 ($\lambda_0 = 8.59\,\mu$m, $\Delta\lambda = 0.42\,\mu$m) and SiC ($\lambda_0 = 11.85\,\mu$m, $\Delta\lambda = 2.34\,\mu$m; Smette & Vanzi 2007). The calibrator star for the VISIR observations was HD 124294. The VISIR data were reduced by combining the chopped and nodded frames in the standard procedures for such data. The photometry was extracted in a 2.25 arcsec aperture. For the calibration, the template spectrum of HD 124294 from the catalogue by Roy van Boekel (private comm.) was used. The errors were estimated by increasing the aperture to 3.00 arcsec and by decreasing it to 1.50 arcsec – for both the calibrator and 3C 273 in the opposite way. In the VISIR images most of the flux is contained within 1.5 arcsec and the FWHM of the PSF is 0.39 arcsec and 0.44 arcsec at 8.59 μm and 11.85 μm, respectively. This is only slightly larger than the FWHM of the calibrator star. 3C 273 is hence not resolved by the VISIR imaging.

More successful observations of 3C 273 were obtained on 2008 Apr 22 with the UT3 – UT4 baseline. Two data sets (fringe track plus photometry) were observed directly one after the other in order to increase the signal to noise ratio. They were both reduced together because no significant change in baseline length and orientation took place between the measurements. The photometric measurements have a very low signal to noise ratio. This is mainly due to very strong variations in the background emission that are insufficiently removed by the chopping. In order to get non-negative fluxes for photometry A from the first data set, a special removal of the background was carried out by fitting a 5th order polynomial to the sky emission on both sides of the spectrum. During the reduction of the photometry we noticed that different total flux spectra can be obtained by changing the mask and the position of the sky bands. The alternative results are well represented by the error bars of the photometry from EWS.

A.2.6 IC 4329A

This target was also observed during the run on 2007 Feb 07. At first, the MACAO units on both telescopes could not keep the loop closed while chopping. During the interferometric measurement, however, a stable AO correction was possible. Strong fringes were found and tracked in two separate fringe tracks. These were combined and reduced as one data set. Only later, after the observation of the corresponding calibrator, HD 123123 (cal23), a stable AO correction could be achieved also while chopping. The photometry was thus observed in twilight, 1 hour after the fringe tracks. Because no proper alignment of the beams was carried out for the photometry, these are located at different positions on the detector than the interferometric signal. By consequence, the masks have to be adjusted accordingly. Still, the fluxes measured in the two beams differ by more than a factor of 2 and must hence be considered with caution.

A.2.7   NGC 5506

For the galaxy NGC 5506, which contains a Seyfert 1.9 nucleus and is located at a distance of $25\,\mathrm{Mpc}$ ($v_\mathrm{hel} = 1850 \pm 8\,\mathrm{km\,s^{-1}}$, Keel 1996; $1\,\mathrm{arcsec} = 120\,\mathrm{pc}$), observations were attempted on 2007 Feb 07. However, on both telescopes (UT2 and UT3) MACAO could not lock on the extended and faint nucleus. Hence no data was obtained.

A.2.8   NGC 7469

Two attempts to observe this source were carried out, the first one on 2006 Sep 11 with the baseline UT2 – UT3, the second one on 2007 Nov 24 with the baseline UT3 – UT4.

During the first attempt, a fringe track was successfully performed although the signal was extremely weak and the position of the OPD was not always determined correctly. As for NGC 1365, there was no AO correction by MACAO for the subsequent observation of the photometry of beam B (UT2). By consequence, the single dish spectrum is spatially very extended and it is actually unclear to what degree it is dominated by background fluctuations. For instance, no pronounced ozone absorption feature at $9.7\,\mu$m is present in the raw data, indicating that most of the signal is actually spurious. We therefore only selected those portions of the photometry for the data reduction where the background residual after chopping is relatively flat. Additionally, the total flux spectrum of the source was determined only using the information from beam A of the source and of the associated calibrator HD 220009 (cal11) as described in App. A.2.

During the second attempt to observe NGC 7469, the ambient conditions were similar to those of the first attempt with moderate wind and the seeing varying between $1.1\,\mathrm{arcsec}$ and $1.3\,\mathrm{arcsec}$. This time, however, MACAO could perform a stable AO correction on the nucleus. The source was successfully centered in MIDI after switching from the SiC to the N8.7 filter and increasing the chopping frequency to $2.3\,\mathrm{Hz}$[3]. Very faint fringes could be detected in the fringe search, however these were too faint to assure a stable finge tracking: in both of the two tracks that were performed, the OPD drifted away from the zero OPD value. From the few frames where an interferometric signal is present, it seems that the correlated flux was on the order of 0.1 to $0.2\,\mathrm{Jy}$, rising towards longer wavelengths. No photometry was observed on this occasion.

---

[3]The chopping frequency was set to a non-integer number in order to not have the same frequency as the gas-helium closed-cycle cooler of MIDI which runs at $1\,\mathrm{Hz}$. This should cancel out any differences in the background between target and sky position, which may be caused by a slight temperature change or vibrations with the frequency of the cooler.

References

Antonucci, R. 1993, ARA&A, 31, 473

Arsenault, R., Alonso, J., Bonnet, H., et al. 2003, in Adaptive Optical SystemTechnologies II. Edited by Wizinowich, Peter L.; Bonaccini, Domenico. Proceedings of the SPIE, Volume 4839, pp. 174-185 (2003)

Balestra, I., Bianchi, S., & Matt, G. 2004, A&A, 415, 437

Beckert, T., Driebe, T., Honig, S. F., & Weigelt, G. 2008, A&A, 486, L17

Beckert, T. & Duschl, W. J. 2004, A&A, 426, 445

Beers, T. C., Kriessler, J. R., Bird, C. M., & Huchra, J. P. 1995, AJ, 109, 874

Beswick, R. J., Pedlar, A., & McDonald, A. R. 2002, MNRAS, 335, 1091

Buchanan, C. L., Gallimore, J. F., ODea, C. P., et al. 2006, AJ, 132, 401

Burtscher, L., Raban, D., Tristram, K. R. W., et al. in preparation

Courvoisier, T. J.-L. 1998, A&A Rev., 9, 1

de Vaucouleurs, G., de Vaucouleurs, A., Corwin, Jr., H. G., et al. 1991, Third Reference Catalogue of Bright Galaxies (Volume 1-3, XII, 2069 pp. 7)

Díaz-Santos, T., Alonso-Herrero, A., Colina, L., Ryder, S. D., & Knapen, J. H. 2007, ApJ, 661, 149

Elitzur, M. & Shlosman, I. 2006, ApJ, 648, L101

Frogel, J. F., Elias, J. H., & Phillips, M. M. 1982, ApJ, 260, 70

Galliano, E., Alloin, D., Pantin, E., Lagage, P. O., & Marco, O. 2005, A&A, 438, 803

Gitton, P. B., Leveque, S. A., Avila, G.,& Phan Duc, T. 2004, in New Frontiers in Stellar Interferometry, Proceedings of SPIE Volume 5491. Bellingham, WA:

Gorjian, V., Werner, M. W., Jarrett, T. H., Cole, D. M., & Ressler, M. E. 2004, ApJ, 605, 156

Gurwell, M. A., Peck, A. B., Hostler, S. R., Darrah, M. R., & Katz, C. A. 2007, in Astronomical Society of the Pacific Conference Series, Vol. 375, From Z-Machines to ALMA: (Sub)Millimeter Spectroscopy of Galaxies, ed. A. J.

Baker, J. Glenn, A. I. Harris, J. G. Mangum, & M. S. Yun, 234

Hao, L., Spoon, H. W. W., Sloan, G. C., et al. 2005, ApJ, 625, L75

Hjelm, M. & Lindblad, P. O. 1996, A&A, 305, 727

Hönig, S. F., Beckert, T., Ohnaka, K., & Weigelt, G. 2006, A&A, 452, 459

Hönig, S. F., Horst, H., Smette, A., et al. in preparation a

Hönig, S. F., Kishimoto, M., & Weigelt, G. in preparation b

Horst, H., Duschl, W. J., Gandhi, P., & Smette, A. 2009, A&A, 495, 137

Houck, J. R., Roellig, T. L., van Cleve, J., et al. 2004, ApJS, 154, 18

Huchra, J., Davis, M., Latham, D., & Tonry, J. 1983, ApJS, 52, 89

Jaffe, W., Burtscher, L., Raban, D., et al. in preparation

Jaffe, W., Meisenheimer, K., Röttgering, H. J. A., et al. 2004, Nature, 429, 47

Jaffe, W. J. 2004, in New Frontiers in Stellar Interferometry, Proceedings of SPIE Volume 5491. Bellingham, WA: The International Society for Optical Engineering, ed. W. A. Traub, 715

Käufl, H.-U., Sterzik, M. F., Siebenmorgen, R., et al. 2003, in Presented at the Society of Photo-Optical Instrumentation Engineers (SPIE) Conference, Vol. 4841, Society of Photo-Optical Instrumentation Engineers (SPIE) Conference Series, ed. M. Iye & A. F. M. Moorwood, 117128

Keel, W. C. 1996, ApJS, 106, 27

Kemper, F., Vriend, W. J., & Tielens, A. G. G. M. 2004, ApJ, 609, 826

Kinney, A. L., Schmitt, H. R., Clarke, C. J., et al. 2000, ApJ, 537, 152

Königl, A. & Kartje, J. F. 1994, ApJ, 434, 446

Krolik, J. H. 2007, ApJ, 661, 52

Krolik, J. H. & Begelman, M. C. 1988, ApJ, 329, 702

Lagage, P. O., Pel, J. W., Authier, M., et al. 2004, The Messenger, 117, 12

Leinert, C., Graser, U., Przygodda, F., et al. 2003, Ap&SS, 286, 73

Lenzen, R., Hartung, M., Brandner, W., et al. 2003, in Presented at the Society of Photo-Optical Instrumentation Engineers (SPIE) Conference, Vol. 4841, Society of Photo-Optical Instrumentation Engineers (SPIE) Conference Series, ed. M. Iye & A. F. M. Moorwood, 944952

Lindblad, P. O. 1999, A&A Rev., 9, 221

Mattson, B. J. & Weaver, K. A. 2004, ApJ, 601, 771

Meisenheimer, K., Tristram, K. R. W., Jaffe, W., et al. 2007, A&A, 471, 453

Miles, J. W., Houck, J. R., & Hayward, T. L. 1994, ApJ, 425, L37

Minezaki, T., Yoshii, Y., Kobayashi, Y., et al. 2004, ApJ, 600, L35

Nayakshin, S. 2005, MNRAS, 359, 545

Neugebauer, G., Graham, J. R., Soifer, B. T., & Matthews, K. 1990, AJ, 99, 1456

Neugebauer, G. & Matthews, K. 1999, AJ, 118, 35

Pedlar, A., Howley, P., Axon, D. J., & Unger, S. W. 1992, MNRAS, 259, 369

Pier, E. A. & Krolik, J. H. 1992, ApJ, 399, L23

Poncelet, A., Perrin, G., & Sol, H. 2006, A&A, 450, 483

Prieto, M. A. e. a. in preparation, to be published in ApJ

Raban, D., Heijligers, B., Röttgering, H., et al. 2008, A&A, 484, 341

Raban, D., Jaffe, W., Röttgering, H., Meisenheimer, K., & Tristram, K. R. W. 2009, ArXiv e-prints

Radomski, J. T., Piña, R. K., Packham, C., et al. 2003, ApJ, 587, 117

Risaliti, G., Salvati, M., Elvis, M., et al. 2009, MNRAS, 393, L1

Roche, P. F., Aitken, D. K., Smith, C. H., & Ward, M. J. 1991, MNRAS, 248, 606

Rodríguez-Ardila, A. & Mazzalay, X. 2006, MNRAS, 367, L57 Rousset, G., Lacombe, F., Puget, P., et al. 2003, in Presented at the Society of Photo-Optical Instrumentation Engineers (SPIE) Conference, Vol. 4839, Society of Photo-Optical Instrumentation Engineers (SPIE) Conference Series, ed. P. L. Wizinowich & D. Bonaccini, 140149

Schartmann, M., Meisenheimer, K., Camenzind, M., et al. 2008, A&A, 482, 67

Schartmann, M., Meisenheimer, K., Klahr, H., et al. 2009, MNRAS, 393, 759

Schmidt, M. 1963, Nature, 197, 1040

Siebenmorgen, R., Kr ugel, E., & Spoon, H. W. W. 2004, A&A, 414, 123

Silbermann, N. A., Harding, P., Ferrarese, L., et al. 1999, ApJ, 515, 1 Smette, A. & Vanzi, L. 2007, VISIR User Manual, Tech. rep., VLT-MAN-ESO- 14300-3514, Issue 80

Soifer, B. T., Bock, J. J., Marsh, K., et al. 2003, AJ, 126, 143

Swain, M., Vasisht, G., Akeson, R., et al. 2003, ApJ, 596, L163

Theureau, G., Bottinelli, L., Coudreau-Durand, N., et al. 1998, A&AS, 130, 333

Tristram, K. R. W. 2007, PhD thesis, Max-Planck-Institut f ur Astronomie, Konigstuhl 17, 69117 Heidelberg, Germany

Tristram, K. R. W., Meisenheimer, K., Jaffe, W., et al. 2007, A&A, 474, 837

Türler, M., Chernyakova, M., Courvoisier, T. J.-L., et al. 2006, A&A, 451, L1

Wada, K. & Norman, C. A. 2002, ApJ, 566, L21

Weedman, D. W., Hao, L., Higdon, S. J. U., et al. 2005, ApJ, 633, 706

Wegner, G., Bernardi, M., Willmer, C. N. A., et al. 2003, AJ, 126, 2268

Wilson, A. S. & Tsvetanov, Z. I. 1994, AJ, 107, 1227

Wittkowski, M., Kervella, P., Arsenault, R., et al. 2004, A&A, 418, L39

Chapter 7

The millimeter-wave continuum spectrum of Centaurus A and its nucleus

Abstract. We study the radio emission mechanism of the FR-I AGN NGC 5128 (Centaurus A). We determine the centimeter and millimeter continuum spectrum of the whole Centaurus A radio source and measure at frequencies between 86 GHz (3.5 mm) and 345 GHz (0.85 mm) the continuum emission from the active radio galaxy nucleus at various times between 1989 and 2005. The integral radio source spectrum becomes steeper at frequencies above 5 GHz, where the spectral index changes from α_{low} = -0.70 to α_{high} = -0.82. The SW outer lobe has a steeper spectrum than the NE middle and outer lobes (α = -1.0 vs -0.6). Millimeter emission from the core of Centaurus A is variable, a variability that correlates appreciably better with the 20-200 keV X-ray variability than with 2 - 10 keV variability. In its quiescent state, the core has a spectral index α = -0.3, which steepens when the core brightens. The variability appears to be mostly associated with the inner nuclear jet components that have been detected in VLBI measurements. The densest nuclear components are optically thick below 45-80 GHz.

F.P. Israel, D. Raban, R.S. Booth and F.T. Rantakyrö

7.1   Introduction

CENTAURUS A (NGC 5128) is the nearest (D = 3.4 Mpc) radio galaxy with an active nucleus. Because of this, it has been extensively studied at various wavelengths over a very wide range in the electromagnetic spectrum; much of the observational database was reviewed by Israel (1998). The radio source spans more than eight degrees on the sky and shows structure on all scales down to milliarcseconds where VLBI techniques (e.g. Horiuchi et al. 2006) reveal an extremely compact core and bright nuclear jets. Notwithstanding the prominence of Centaurus A, relatively few measurements of the total radio emission of the source exist. The first comprehensive study of its decimetric emission and polarization by Cooper et al (1965) has, in more recent times, been supplemented only by the measurements summarized by Alvarez et al. In particular, no measurements of the Centaurus A total flux density at frequencies above 5 GHz are found in the astronomical literature. In this paper, we extend that range by providing new determinations between 20 GHz and 100 GHz derived from the WMAP all-sky surveys.

On much smaller scales, the flux densities of the compact Centaurus A core are also of interest. The central region of Centaurus A has been imaged at very high resolution with (space) VLBI techniques (Meier et al. 1989; Tingay et al. 1998, Fujisawa et al, 2000, Tingay, Preston & Jauncey 2001, Horiuchi et al. 2006) up to frequencies of 22 GHz, where both the selfabsorbed synchrotron emission from the core and the free-free absorbing foreground start to become optically thin (Tingay & Murphy 2001). Although Kellerman, Zensus & Cohen (1997) used the VLBA to observe Centaurus A at the significantly higher frequency 43 GHz, they did not actually measure nuclear flux densities. Hawarden et al. (1993) have provided the most recent systematic attempt to derive the core spectrum from single-dish measurements, and they conclude that it is essentially flat at millimeter wavelengths, a conclusion reiterated by Leeuw et al (2002).

Variability of the emission at frequencies of 22 and 43 GHz was explicitly noticed by Botti & Abraham (1993), de Mello & Abraham (1990), and Abraham et al. (2007). However, these results, as well as those by Tateyama & Strauss (1992), generally suffered from low spatial resolutions of 2–4 arcmin that do not allow separate identification of emission from the nucleus, the jets, and their surroundings. In this paper, we provide new flux density measurements of the compact core in the 90–345 GHz (sub)millimeter range, at resolutions between 0.8 and 0.2 arcmin. As these measurements were collected over a time period spanning more than a decade, we are also in a position to study the variable behavior of this emission.

7.2   Observations and reduction

7.2.1   WMAP data

The WMAP mission and its data products have been described in detail by Bennett et al (2003a, b, c). In our analysis, we used the data products from the official WMAP 5-year release, specifically the fully reduced and calibrated Stokes I, Q, and U maps of the entire sky, in nested HEALPIX format (Hinshaw et al. 2008). The maps were ob-
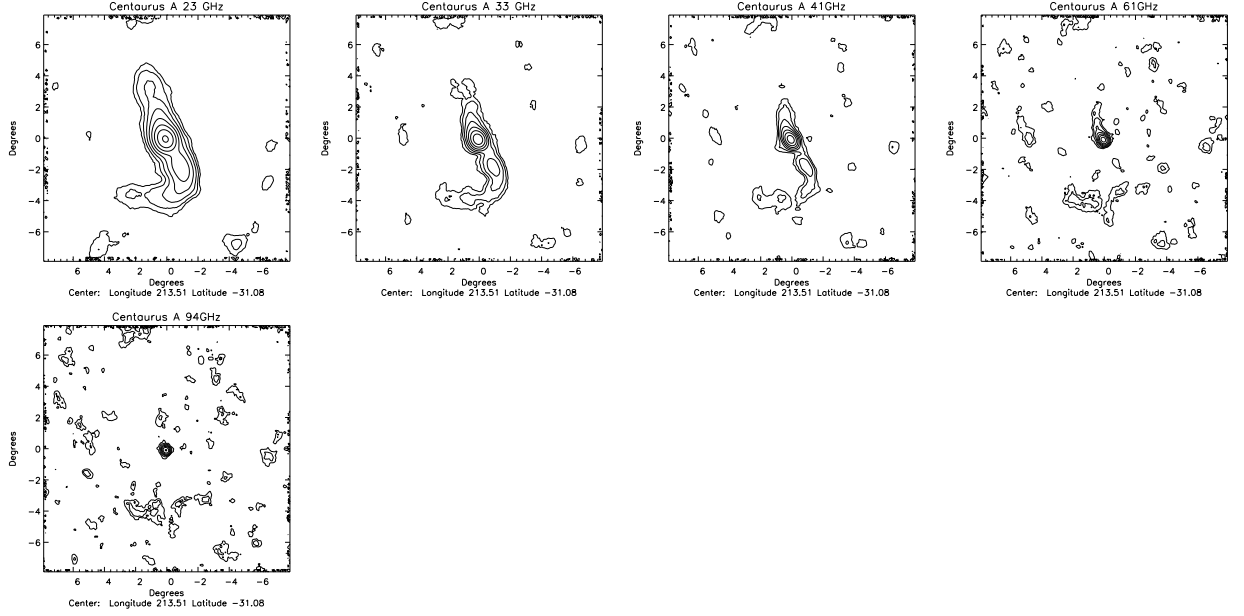
Figure 7.1 — Maps of the radio continuum emission of Centaurus A at (left to right) 23, 33, 41 GHz, 61 GHz, and 93 GHz. All images are at the nominal WMAP resolution. Contour levels are drawn at (23 GHz) 0.1, 0.19, 0.38, 0.74, 1.4, 2.8, 5.5, 10.7 mK, (33 GHz) 0.1, 0.19, 0.36, 0.68, 1.3, 2.4, 4.6 mK; (41 GHz) 0.1, 0.19, 0.34, 0.64, 1.2, 2.2, 4.1, 7.6 mK; (61 GHz) 0.1, 0.17, 0.31, 0.53, 0.94, 1.6, 2.9, 5.0 mK; (93 GHz) 0.1, 0.16, 0.25, 0.40 0.64 1.0, 1.6, 2.6 mK. Note the persistent diffuse emission features at +1.5°, -4° and at +2°, +8°, which are probably unrelated Galactic foreground emission (see Sect. 2.1.).
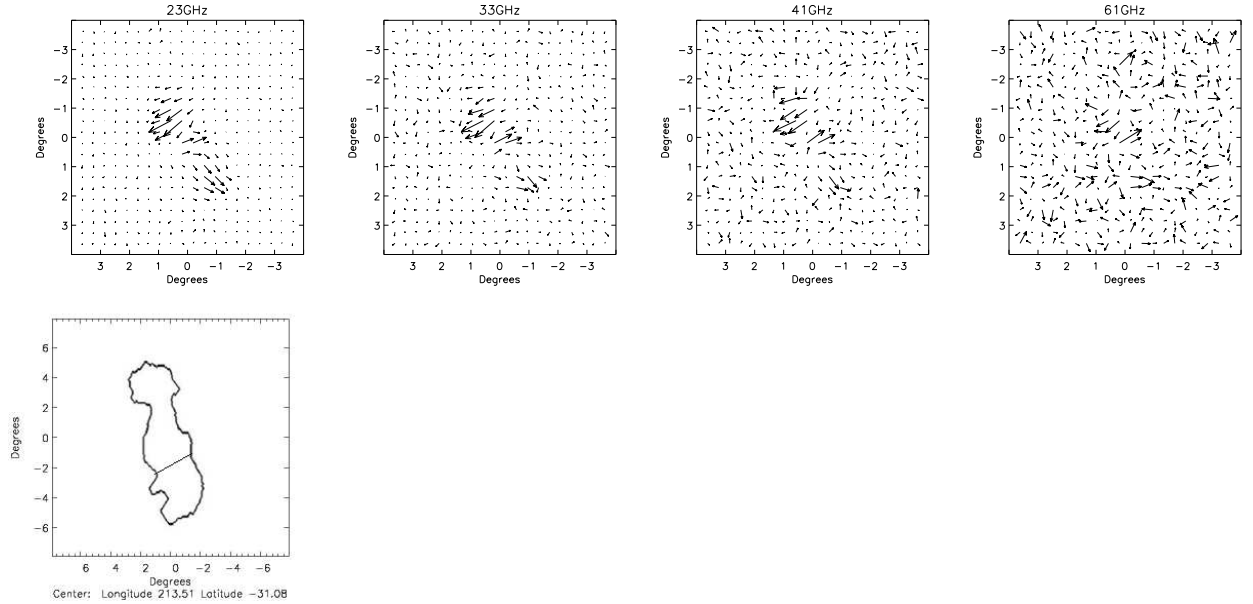
Figure 7.2 — Polarized vectors of the Centaurus A emission at (left to right) 23, 33, 41 GHz, and 61 GHz; the length of the vectors is proportional to the polarized intensity, but scaling is arbitrary. Far right: masks used to determine flux densities in Table 7.1.

Table 7.1 — WMAP observations of Centaurus A

Frequency	Flux Densities			Polarized Flux Densities		
	Total	NE Lobes+Core	SW Lobes	Total	NE Lobes+Core	SW Lobes
(GHz)			Jy			
23	112±13	76±9	29±4	6.8±0.5	5.0±0.3	1.8±0.2
33	82±12	62±8	20±4	4.6±0.6	3.6±0.3	0.8±0.2
41	72±9	56±6	16±3	3.8±0.5	3.4±0.5	0.4±0.2
61	56±15	48±12	8±3	4.0±1	4.0±1	—
93	41±18	47±18	-6±9	3.5±1	3.5±1	—

served at frequencies (assuming synchrotron spectra) ν = 22.5, 32.7, 40.6, 60.7, and 93.1 GHz with resolutions of 53, 40, 31, 21, and 13 arcmin respectively. As a first step, the HEALPIX data maps were converted with the use of standard software to flat maps in Zenithal Equal Area projection with pixel solid angles of $p(o) = 1.90644 \times 10^{-6}$ and intensities in mK. We first attempted to determine integrated flux densities by fitting in each map two-dimensional Gaussians to the emission corresponding to Centaurus A. However, with increasing frequency, both the beamsize and the total flux density decrease, resulting in a steep decline in flux density per beam. Our fitting results, not surprisingly, suggests that we were systematically missing low-surface-brightness extended emission. For this reason, we also integrated over the full extent of the Centaurus A radio source as shown in the maps by Cooper et al. (1965) - the mask used is depicted in Fig. 7.2, bottom right. We derived the flux densities given in Table 7.1 from the summed values with the conversion factor Jy/mK = $30.7 \times p(o) \times \nu^2$. This yielded the flux densities given in Table 7.1, which correspond to the maps shown in Fig. 7.2. We verified the accuracy of this procedure by also applying it to the strongest WMAP point sources J0319+4131, J0322-3711, J0423-0120, J1229-0203, J1230+1223, and J1256-0547 (Wright et al. 2008). For polarization measurements, the Q and U maps were reduced using the same conversion factors as the I maps; the polarized intensity was computed as $P = \sqrt{Q^2 + U^2}$. Only at 23 GHz are signal-to-noise ratios high enough to yield practically identical results for the gaussian-fitting and integration methods. We consider the integrated flux densities at 23, 33, and 41 GHz to be quite reliable, whereas at 61 GHz and 93 GHz much of the integration was over areas with a surface brightness very close to the noise, especially in the southern lobe. In the total-intensity (I) maps, the spatial resolution blends all components into the dominant emission of the NE and SW radio lobes, respectively. Even at the highest frequency, the compact core cannot be separated from the intense NE lobe. This is different in the polarized intensity (P) maps. In the 23, 33, and 41 GHz P-maps, the compact core can be seen separately. At the higher frequencies, the signal-to-noise ratio of the P-maps is too low to yield useful results. We note that the *central* 22 GHz flux densities of Cen A typically range between 16 and 29 Jy in a $4'$ beam (Fogarty & Schuch 1975; Botti & Abraham 1993), i.e. roughly 15–25% of the 23 GHz WMAP flux densities. At the same frequency, the VLBI milli-arcsec core (Tingay et al. 2001) contributes only 2% to the measured
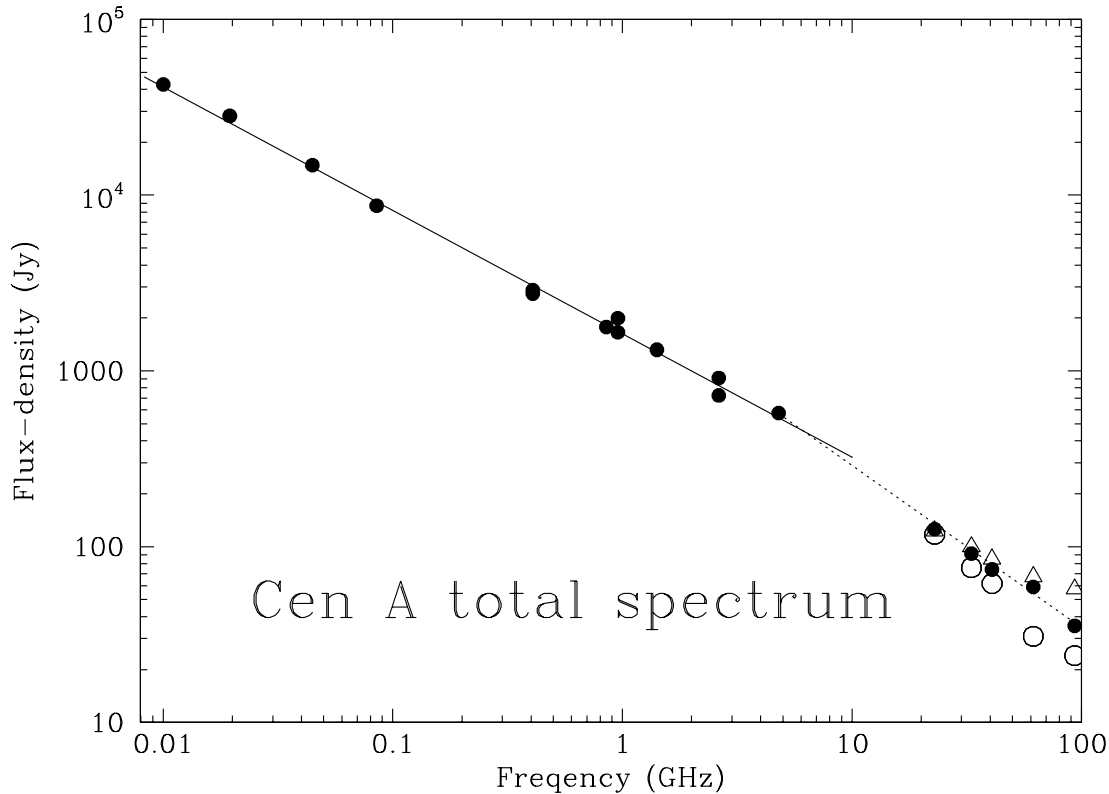
Figure 7.3 — The area-integrated continuum spectrum of the Centaurus A radio source from meters to millimeters. Filled circles represent integrated flux densities from the literature (cf. Alvarez et al. 2000) and from Table 7.1. For comparison, open triangles represent integrated flux densities including the SE feature which we suspect to be unrelated Milky Way foreground (see Sect. 2.1) whereas open circles represent the flux densities obtained from Gaussian fitting of the WMAP emission which is biased to regions of relatively high surface brightness. Solid lines mark fits to the literature and WMAP data.

WMAP emission.

Figure 7.2 shows the presence of an extended diffuse emission feature to the east of the SW lobe. This feature can be seen at all frequencies and is undoubtedly real. However, we do not consider it to be related to Centaurus A. (1) Large-scale maps show significant foreground emission from the Milky Way reaching up to the Galactic latitude of Centaurus A (see Bennett et al. 2003b). (2) Inclusion of this feature in the flux densities of the SW lobe causes its emission to first decrease with frequency but then to make a surprising jump at 61 GHz, and at 93 GHz the weak SW lobe would have become as strong as the NE lobe + core emission. (3) The lobes of Centaurus A are clearly polarized, whereas the diffuse feature does not show polarization at any frequency (Fig. 7.2, bottom row), which also argues against the feature being an extension of the SW lobe. Finally, (4) there is a similar but more obviously unrelated feature at +2°, 8°.
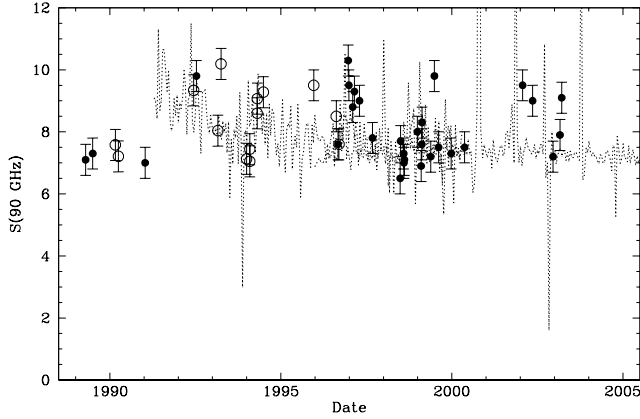
Figure 7.4 — Flux densities of the Centaurus A nucleus at 90 GHz in 1988-2005 taken from this paper (filled circles) and from published literature (open circles; see text). Dashed lines represent X-ray fluxes monitored by the BATSE and RXTE experiments on an arbitrary flux density scale

7.2.2   SEST data

The SEST was a 15 m radio telescope located at La Silla, Chile [1]. The main purpose of our observing program with the SEST was to obtain high-resolution molecular-line absorption spectra against the continuum of the Centaurus A core, with integration times ranging from 30 minutes to 4 hours per molecular transition per session, obtained by co-adding individual samples usually of 5 minutes each.

In the time period 1989-1993, observations were made with Schottky barrier diode receivers providing single-sideband (SSB) system temperatures, including the sky, of 500 K (3 mm band) and 1000 K (1.3 mm band). From 1996 onwards until the closure of the SEST in 2003, observations were made with Superconductor-Insulator-Superconductor (SIS) tunnel junction receivers operating simultaneously in either (i) the 3 mm and 2 mm bands, or (ii) the 3 mm and 1.3 mm bands. Typical system temperatures, including the sky, were 220 K in the 3 mm band and 330 K in the 1.3 mm bands. Continuum pointings were frequently performed on Centaurus A itself; monitoring the continuum level during the observations provided an additional and very valuable check on tracking accuracy. During the long integrations, the r.m.s. pointing was on average on the order of 5″ or better. All observations were made in double-beamswitching mode, with a 6 Hz switching frequency and a throw of 12′ because this procedure yielded excellent and stable baselines. SEST beam sizes and main-beam efficiencies at the various observing frequencies were listed by Israel (1992); they were 41″-57″ and 0.70-0.75 in the 3 mm band, and 23″ and 0.5 in the 1.3 mm band. Whenever feasible, we used the observatory high- and low- resolution acousto-optical spectrometers (AOS) in parallel.

For this paper, we extracted the continuum flux density from measurements with the low-resolution backend (bandwidth 500 MHz, resolution 1 MHz). To this end, we

---

[1]The Swedish-ESO Submillimeter Telescope was operated jointly by the European Southern Observatory (ESO) and the Swedish Science Research Council (NFR).

Table 7.2 — SEST observations of the Centaurus A nucleus

Day	Date	Frequency ν (GHz)	Brightness T_{mb} (mK)	Flux Density S_ν (Jy)
1989.29	Apr 15	87	373±45	7.2±0.9
1989.50	Jul 3	89	391±15	7.3±0.7
		98	393±7	7.5±0.8
		110	313±20	5.9±0.6
		113	353±9	6.6±0.7
		220	223±24	5.0±0.7
		227	208±44	4.3±0.8
1991.03	Nov 01	88	371±20	7.1±0.8
		89	369±21	7.0±0.8
		91	361±20	6.9±0.8
		114	361±25	6.8±0.9
1992.53	Jul 13	89	516±11	9.7±1.0
		91	516±7	9.7±1.0
		99	488±31	9.2±1.2
		218	263±11	5.5±0.6
		220	326±60	6.8±1.3
		226	289±35	5.8±0.8
		268	210±13	4.8±0.7
1993.55	Jul 20	218	384±40	8.0±0.8
		226	354±40	7.3±0.7
		268	329±37	7.6±0.8
		346	292±30	7.6±0.8
		357	238±35	5.6±0.6
1996.67	Aug 31	110	353±17	6.7±0.7
		115	333±31	6.3±0.6
		145	275±14	5.5±0.6
1996.97	Dec 19	90	410±20	10.3±1.0
		229	200±20	8.2±0.8
1996.99	Dec 29	90	380±20	9.5±1.0
		229	160±20	6.6±1.6
1997.10	Feb 06	90	350±10	8.8±0.9
1997.15	Feb 21	90	370±10	9.3±0.9
		150	290±10	8.7±0.9
1997.30	Apr 19	90	360±30	9.0±0.9
1997.68	Sep 05	87	440±20	8.3±0.8
		89	420±50	7.9±0.9

Note.– Table 7.2 is published in its entirety in the print & electronic edition of the *Astronomy & Astrophysics*. A portion is shown here for guidance regarding its form and content.
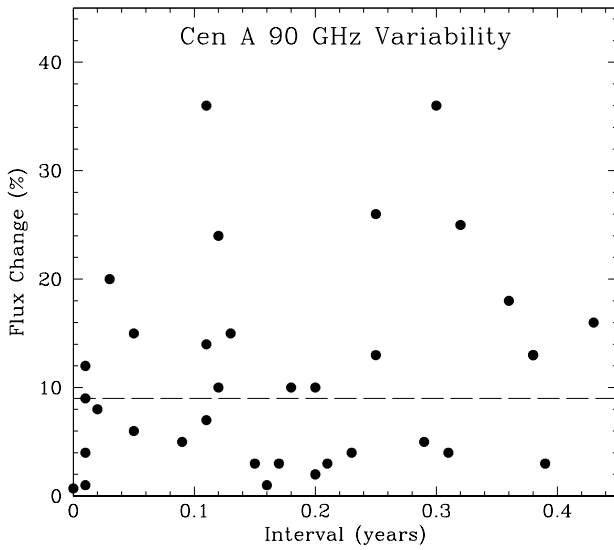
Figure 7.5 — Relative changes in 90 GHz flux densities as a function of observing interval. Changes above the horizontal thin line are highly significant and not influenced by observing errors or bias.

averaged, for each 5-minute sample, the continuum levels in the 0-300 km s^{-1} and 800-1100 km s^{-1} velocity intervals, straddling but avoiding the central line emission profiles. Individual sample continuum antenna temperatures were then converted to flux densities. The conversion typically ranged from 25 Jy/K at 86 GHz, 27 Jy/K at 115 GHz, 30 Jy/K at 147 GHz, to 41 Jy/K at 230 GHz. The flux densities listed in Table 7.2 for each observed frequency are the means of the individual samples observed at the frequency and run listed. Observing runs typically lasted four to eight days; the median date is given. In determining the means, we left out samples negatively affected by pointing drift, which were easily recognized by a slow but steadily decreasing continuum level.

From 1996 to 1999, the Centaurus A continuum intensity was also monitored every few months at frequencies of 90, 150, and 230 GHz in a dedicated program. The observations were performed in the dual beam switch mode with a 12$'$ throw, and the data were taken simultaneously at either 90/150 or 90/230 GHz. Individual exposures were kept short to minimize the effect of the atmosphere and to allow a filtering of spectra with poor quality. The r.m.s. values from the pointing runs were typically better than 3$''$. For each of the individual spectra, the continuum flux level was determined by fitting a zeroth-order line. Finally, the average was determined by a least-square fit to the fitted continuum levels and error of all the individual measurements.

The quality of the data is a function of the stability of the sky (which determines the accuracy of the double-beamswitch signal subtractions) and the accuracy of the pointing. As the pointing depends on the proper evaluation of a series of boresight observations taken in sequence, it is itself a function of sky stability. In general, observations in the 3 and 2 mm windows profited from transparent sky conditions superior
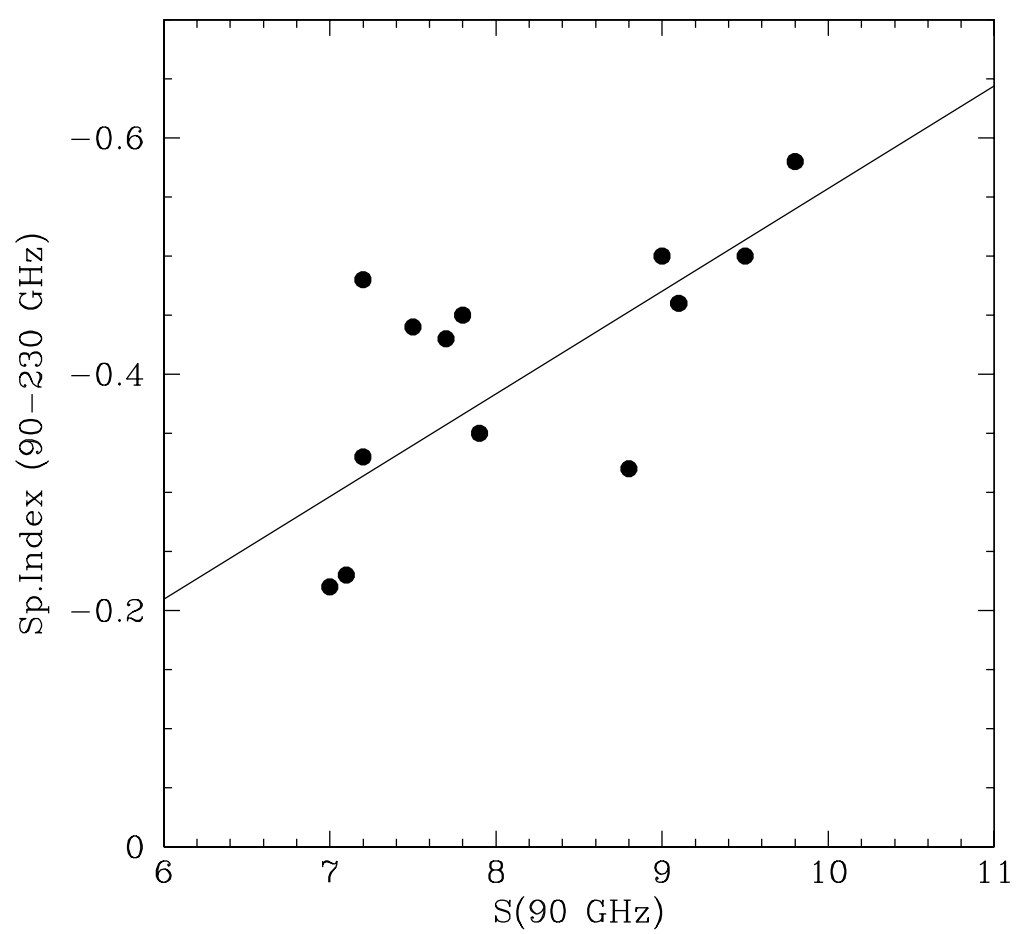
Figure 7.6 — Spectral index 90-230 GHz as a function of 90 GHz flux density.

Table 7.3 — JCMT observations of the Centaurus A nucleus

Day	Date	Frequency ν (GHz)	Main-Beam Brightness T_{mb} (mK)	Flux Density S_ν (Jy)
1997.09	Feb 01	330	327±22	5.8±0.6
2002.28	Apr 12	230		6.3±0.9
		268		5.9±0.9
2002.47		268		6.2±0.9
2003.24	Mar 30	268		6.1±0.9
		330		7.9±1.2
		345		5.2±0.8
2003.36	May 05	265		5.4±0.7
2003.50	Jul 01	265		4.1±0.6
		330		8.4±1.3
2004.30	Apr 17	345		7.2±1.1
2004.57	Jul 26	330		6.3±0.9
2005.23	Mar 23	330		4.4±0.7

to those encountered in the 1 mm window. In addition, a particular r.m.s. pointing error has a greater effect on smaller beamsizes, i.e. at higher frequencies. For this reason, observations around e.g. 90 GHz have the highest quality, and those at 220/230 GHz are associated with larger relative errors.

7.2.3 JCMT data

From 2002 through 2005, similar molecular line observations were made with the 15m James Clerk Maxwell Telescope (JCMT) on Mauna Kea (Hawaii). [2]. They were made in beamswitching mode with a throw of $3'$ in azimuth using the DAS digital autocorrelator system as a backend. As the low declination of Centaurus A brings the source to less than 30° above the horizon as seen from Hawaii, observations were performed in timeslots covering one hour at either side of transit. For all spectra, we scaled the observed continuum antenna temperature to flux densities by assuming aperture efficiencies η_{ap} = 0.57 at 230-270 GHz and η_{mb} = 0.49 at 330-345 GHz.

7.3 Results and analysis

7.3.1 The overall Centaurus A radio source spectrum

In Fig. 7.3 we show the spatially integrated radio spectrum of Centaurus A from 85 MHz to 90 GHz. The lower-frequency flux densities have all been taken from the literature as compiled, corrected, and discussed by Alvarez et al. (2000), who found

---

[2]The James Clerk Maxwell Telescope is operated on a joint basis by the United Kingdom Particle Physics and Astrophysics Council (PPARC), the Netherlands Organisation for Scientific Research (NWO), and the National Research Council of Canada (NRC).

a spectral index α = -0.70±0.01 ($S_\nu \propto \nu^\alpha$) corresponding to the solid line in Fig. 7.3. The higher-frequency points were taken from Table 7.1. A least-square fit indicates a slightly steeper spectrum with spectral index α = -0.82±0.07 and a spectral turnover by $\Delta\alpha \approx -0.12$ somewhere between 5 and 20 GHz (see also Junkes et al. 1997). The more poorly defined spectrum of the SW lobe is steeper than that of the NE lobe with $\alpha_{SW} = -1.0$ vs $\alpha_{NE+c} = -0.6$, but this difference is barely significant.

In these spectra and flux densities, we do not include the contribution by the extended emission feature east of the SW lobe discussed above. If we were to do so, its relatively strong presence at the higher frequencies would flatten the high-frequency spectrum to the one indicated by the open triangles in Fig. 7.3 (with $\alpha = -0.64 \pm 0.09$). The slope of that spectrum is very similar to that at the lower frequencies, but the spectrum itself is offset in flux density by about a factor of two and does not fit very well onto the lower-frequency spectrum. It is clear from Fig. 7.3 that the emission from the diffuse feature becomes negligible compared to the Centaurus A total at frequencies below frequencies 20 GHz. The low Galactic latitude of Centaurus A also has some effect at much lower frequencies. For instance, Cooper et al. (1965) briefly discuss the presence of a relatively weak spur of Galactic foreground synchrotron emission at the southeastern tip of Centaurus A. The location and extent of this spur is indicated in their Fig. 1. The WMAP diffuse feature is close to, but not coincident with, the spur and appears to be unrelated to it. Indeed, none of the radio continuum maps shown by Cooper et al. (1965) and Junkes et al. (1993) in the range of 0.4 to 4.8 GHz shows emission coincident with the WMAP feature.

There is some evidence that the ratio R_{NS} of the flux densities of the NE lobes (including the central core emission) and the SW lobes increases with frequency. At 0.4 and 1.4 GHz, R_{NS} = 1.5 (Cooper et al. 1965, Junkes et al. 1993), but this has increased to $R_{NS} \approx 3$ in the 23–41 GHz range (Table 7.1). Even if we were to add the suspected foreground emission to that of the SW lobe, we still would have a ratio $R_{NS} = 2$ in the well-determined 23–43 GHz range. We note that Alvarez et al. (2000) have found that, over the full 0.08–43 GHz range, at least the *inner* lobes also have a ratio R_{NS} = 1.5. For the giant *outer* lobes they find a lower ratio R_{NS} = 0.9, but this only applies to the limited 0.4–5.0 GHz range. The meaning of these apparent changes in ratio is not clear to us.

The fraction of polarized emission is well-defined between 23 GHz and 41 GHz. The lower-frequency, higher-resolution maps by Cooper et al. (1965) and Junkes et al. (1993) show overall polarization increasing from $P/I \approx 12\%$ at 960 MHz to $P/I \approx 30\%$ at 5 GHz/. We find much lower polarized fractions. The polarization of the entire source is within the errors constant over the 23–61 GHz range with $P/I = 6.0 \pm 0.3\%$. As Fig. 7.2 shows, the *beam-averaged* polarization direction is different for all three components. The low polarization fraction found by us most likely reflects the significant beam depolarization caused by the low resolution of the WMAP data.

7.3.2 Millimeter-wave emission of the Centaurus A core region

Although the extended radio emission from Centaurus A even at millimeter wavelengths significantly exceeds that of the core region, its surface brightness is low and declines rapidly with increasing frequency. Can it, however, be safely ignored in the

flux density measurements of the core with the SEST beam? The highest frequency measured with WMAP, 93 GHz, corresponding to a wavelength of 3.2 mm, is in the lowest band that the SEST offered for ground based millimeter-wave molecular line observations. The measured gaussian-fitted flux density at this frequency is $S_{93}(tot)$ = 24±5 Jy, well above the flux density S = 9±1 Jy that single-dish measurements suggest for the Centaurus A core region. Excluding the core, the mean surface brightness at 90 GHz of the extended synchrotron emission component is about 115 mJy/arcmin^2. The contribution of the extended nonthermal component can thus safely be neglected in the relatively high-resolution observations of the core.

At very high frequencies, thermal emission from dust may also contribute to measured intensities, but this is not the case in the frequency range of interest to us. The continuum emission seen at resolutions of a few tenths of an arcminute by telescopes such as the SEST and the JCMT, effectively originates in a point source as can clearly be seen in the 850μm (345 GHz) SCUBA images published by Mirabel et al. (1999) and Leeuw et al. (2002). From these and our own data, we deduce that the extended emission, after correction for 20% CO line contamination, contributes less than 4% to the central peak intensity at 345 GHz, and this contribution drops rapidly with decreasing frequency. In the next section we will return to this issue.

To study the temporal behavior of the mm-wave continuum spectrum of the core, we have reduced the measurements listed in Table 7.3 to standard frequencies of 90, 150, and 230 GHz. We performed a linear regression on all flux density/frequency pairs measured during a run, and for each run determined the best-fitting 'standard' flux densities by interpolation, as well as the effective spectral index between 90 and 230 GHz. As a consequence of this procedure, the results for each run, given in Table 7.4, are more robust than the individual measurements taken during that run. Typical uncertainties are about 0.3 Jy at 90 GHz and 0.6 at 230 GHz. Although the sampling in time was not uniform, we have given the mean flux density over the whole period for each frequency at the bottom of Table 7.4. If more detailed information is absent, these values are the best guess for the core flux densities at any time not covered by the monitor. We have also listed the rather flat spectral index defined by these 'best' points, with the important caveat that the three standard flux densities defining the means were not sampled at the same times.

7.3.3 Core variability at mm wavelengths

In Fig. 7.4 we have plotted all observed 90 GHz flux densities from Table 7.2 and added the available (SEST) values from the literature (Tornikoski et al., 1996; Wiklind & Combes 1997) fortunately filling in much of the gap created by our lack of monitoring Centaurus A in the period 1993-1997. It was clear from the start that the core of Centaurus A is variable. In Fig. 7.4 we illustrate this variability of core flux density. Over the period monitored, the flux density never drops much below 7 Jy, but at times may be higher than 10 Jy. Sustained periods of relatively high flux densities appear to have occurred in 1993/1994, 1997, and 2001/2002. There is no doubt that this variability is real. The excursions exceed the uncertainty associated with individual plotted values, and the behavior is similar at all observed frequencies. At 90 GHz, the core flux density is seen to change by as much as 20% in a few weeks. This is illustrated in Fig. 7.5, which plots

the percentage change from one observing date to another as a function of the elapsed time. Over the observed period, the greatest changes (more than 25%) take place over time intervals typically between 2 and 4 months. The high-frequency variability observed here should be compared to the variability deduced from the lower frequency monitoring observations by Botti & Abraham (1993) and Abraham (1996). Although there is, unfortunately, only limited temporal overlap, the pattern is very similar, with significant and sometimes rapid intensity changes. In particular, enhanced radio emission is seen in 1992 in both our sample and in the data by Abraham (1996). The 43 GHz variability has a large amplitude of 8 – 10 Jy (corresponding to factors of two change in brightness) and is about half as much (factor of 1.25) at 22 GHz. We note that those flux densities were determined with relatively large beams of 2.1′ and 4.2′, allowing significant contributions to the emission especially at 22 GHz, not related to the core.

The X-ray variability of the Centaurus A nucleus was monitored over the same period in the 20–200 keV band by the BATSE experiment onboard the Compton Gamma Ray Observatory from 1991 through 2000 and in the 2–10 keV band by the RXTE All Sky Monitor from 1996 onwards. We took the public data from the NASA Goddard SFC and MIT websites and constructed averages over 15-day bins. The results are plotted with the 90 GHz flux densities in Fig. 7.4. The correspondence between the SEST 90 GHz and the BATSE X-ray flux densities is quite good, suggesting closely related, perhaps even identical, radiative processes . The correlation between the millimeter-wave continuum and the relatively soft X ray emission sampled by the RXTE experiment is much poorer. Minor X-ray excursions (on the order of a factor of two) occurred in 1991/1992, during 1994, in late 1996 and early 1997, during 1999, and 2001. They correlate with radio maxima, although unfortunately we are lacking millimeter continuum coverage for 2001.

Although the behavior is the same at all frequencies observed by us, flux densities vary less at higher frequencies. As a result, the core spectral index changes with the degree of activity. In Table 7.4 we have calculated spectral index values α ($S_\nu \propto \nu^\alpha$) for the frequency range of 90 GHz to 230 GHz. To guarantee a reasonable accuracy (on the order of 0.10 or better in the index), we included only epochs at which measurements were available in three different frequency windows. In Fig. 7.6 we have plotted these spectral indexes as a function of the 90 GHz flux density. It is quite obvious that the mm-wave spectrum of the Centaurus A core becomes steeper (smaller spectral index) when the actual flux increases; i.e. increases are less in both absolute and relative senses at the higher frequencies. The points in Fig. 7.6, with their uncertainties of $\Delta\alpha \approx 0.10$, can be fitted with a linear-regression line α = -0.087 S_{90} + 0.311. For the observed lower limit of 7 Jy to the Centaurus A core flux density, this fit implies a fairly flat spectral index α = -0.3 (although the two actually measured values imply an even flatter spectrum with α = -0.22). Spectral indices α = -0.6 are approached at enhanced flux densities of 10 Jy.

Variations in the spectral index between 22 and 43 GHz were likewise deduced by Botti & Abraham (1993) and plotted as a function of time in their Figure 2. If we plot their data again, now with the spectral index as a function of the relatively strongly varying 43 GHz flux density, we find a behavior *opposite* to that deduced by us for the 90 – 230 GHz range. With relatively little scatter, α_{22-43} = + 0.11 S_{43} - 2.2; i.e. the

spectrum *flattens* when S_{43} increases! We do not have a full explanation for this, but some remarks are in order. First, we note that the 43 GHz flux density appears to vary even more than the 90 GHz flux density. Although there is very little temporal overlap, this is nevertheless consistent with our conclusion that the spectrum steepens when flux densities increase. Second, the 22 GHz emission would be expected to vary even more, but obviously fails to do so. This could be explained by high optical depths of the variable emission component at this frequency.

7.3.4   Nature of the core emission

In the quiet state, the core of Centaurus A has a high-frequency spectral index α_{high} = -0.3, but it must become optically thick around 80 GHz to allow flux densities to be a factor of two lower at 43 GHz than at 90 GHz. This implies that the emission at 22 GHz must arise almost entirely from non-core components. In the period covered by our observations, Centaurus A has not shown much activity, in any case less than in earlier decades (cf Abraham& Botti 1993). Nevertheless, we did observe a few episodes with slightly enhanced activity. In these mildly 'active' states, flux densities increase, the high-frequency spectral index steepens to α_{high} = -0.6, and the spectral turnover shifts to lower frequencies of about 45-50 GHz. In this state, there is a measurable 2–4 Jy contribution from the core to the total 22 GHz emission from the central 4 arcmin, such as the 4 Jy seen in the VLBI measurements by Tingay et al. during the 1995 episode, but most of the 22 GHz emission still represents non-core components.

Recent (April 2006) observations with the Smithsonian Millimeter Array (SMA) at a resolution of $2'' \times 6''$ show a point source with a continuum flux density S_{230GHz} = 6 Jy (Espada et al. 2007). Although we do not have a single-dish measurement at the same epoch, a glance at Table 7.4 will show that this is, in effect, the total flux to be expected at this frequency.

What does the observed core emission represent, and what is the meaning of the variability? Although our observing beams were much larger, essentially all observed emission arises from a region with a size of a few arcsec at most, as indicated by the SMA observations just mentioned, as well as the measurements described below. VLBI images at frequencies of 5 and 8 GHz (Tingay et al. 1998, 2001; Tingay & Murphy 2001; Horiuchi et al. 2006) show very considerable source structure concentrated within about 60 milliarcsec. We note that the *submillimeter core itself* suffers from both free-free absorption and synchrotron selfabsorption at these frequencies (see e.g. Tingay & Murphy 2001). Nevertheless, the images suggest that the emission observed by us arises from a nuclear source, as well as from bright nuclear jets extending over the better part of a parsec. This complicates the interpretation of the observed variability, since we have no means of determining where precisely it originates. The time sequences registered by Tingay et al. (1998, 2001) strongly suggest that nuclear jet evolution is a major source of variability in the emission, as total 8 GHz flux densities vary between 4 and 10 Jy, Their maps also show movement and variability of individual components in the nuclear jets. The 8 GHz 'core' component varies much less (between 1.8 and 3.3 Jy with a median of 2.4 Jy over the period 1991-2000) and the 8 GHz and 22 GHz core flux densities are almost identical at the only two epochs (1995.88 and 1997.23) for which a reliable measurement exists (Tingay et al. 1998, 2001). However, in the much higher

resolution (1.2×0.6 mas) maps by Horiuchi et al. (2006) this 'core' breaks up into at least four separate components. These extend over 7 milliarcsec (0.13 pc) and should presumably be considered as inner nuclear jet components. It is thus unclear whether the actual nuclear source (if any) itself is variable or not. Abraham et al. (2007) have interpreted rapid, day-to-day variations with amplitudes of 20% in the 43 GHz emission observed over a three-month period in 2003 as evidence of free-free absorption of the nuclear source by clouds in the center of NGC 5128. It is, however, by no means clear that such an explanation could also apply to longer term variations, or indeed to the pattern of variability at higher frequencies.

Figure 7.6 shows that the core spectrum steepens when it brightens, implying rapid energy loss of any electrons injected during active periods. We might assume that the emission from the Cen A core consists of a variable component and a component of constant emission. In that case, the spectral index of the variable emission is reasonably well-constrained with α_{var} = -1.6, especially if the 43 GHz peak excursions of about 9 Jy (Abraham 1996) correspond to the 3 Jy peak excursions at 90 GHz, which we do not know for certain. The relative flux densities of the two components and the spectral index of the constant component need an additional constraining assumption. The lowest flux densities measured at 43 GHz are 3-4 Jy, which puts an upper limit on the constant component. For instance, if we assume a flat spectrum for the latter (α_{cst} = 0.0), the minimum flux density of the variable component is $S_{90}^{min}(var)$ = 3 Jy. However, there does not seem to be a consistent model for the variation at all three frequencies without additional and ad-hoc assumptions. It appears that millimeter-wave VLBI monitoring is needed to provide the definitive answer to the question of the Centaurus A nuclear source properties. In particular, it would be quite interesting to compare the results of such monitoring with the results for the core of Centaurus A extracted by Meisenheimer et al. (2007) from mid-infrared interferometry at the ESO-VLT. After completion, the maximum resolution of the Atacama Large Millimeter Array (ALMA) will be about 50 mas at 100 GHz. This will close the gap between the centimeter-wavelength synthesis array *resolutions* and the centimeter-wavelength VLBI *fields of view* noted by Israel (1998, Sect. 5.4), and thus be invaluable for studies of the evolution of the nuclear and inner jets. The resolution falls far short, however, of those needed to separate processes occurring in the nuclear jets and in the core components. If THz imaging is feasible at the longest baselines, the resulting ALMA resolution of 5 mas is better suited to such studies. ALMA sensitivities will be amply sufficient to show the core, but it remains to be seen how much of the subparsec jet structure will be discernible.

7.4 Conclusions

We have extended the spatially integrated continuum spectrum of the Centaurus A radio source by using WMAP results between 23 and 93 GHz. The spectrum has now been explored over four frequency decades, from 10 MHz to 93 GHz. Between 10 MHz and 5 GHz, the spectral index $\alpha = -0.70$, as determined in the literature. Longwards of 5 GHz the spectrum appears to steepen, with $\alpha = -0.83 \pm 0.07$. The flux density ratio R_{NS} of the NE lobes (including the core) and the SW lobes increases with frequency

Table 7.4 — Normalized flux densities of the Centaurus A nucleus

| Epoch | Flux Density (Jy) | | | | Spectral |
	S_{90}	S_{150}	S_{230}	S_{345}	Index
1989.29	7.1	—	—	—	—
1989.50	7.3	—	4.5	—	—
1991.03	7.0	6.6	—	—	—
1992.53	9.8	7.3	5.7	—	-0.58
1993.55	—	—	7.7	6.6	—
1996.67	7.6	5.4	—	—	—
1996.97	10.3	—	8.2	—	—
1996.99	9.5	—	6.65	—	—
1997.10	8.8	7.5	—	5.7	-0.32
1997.15	9.3	8.7	—	—	—
1997.30	9.0	—	—	—	—
1997.68	7.8	6.2	5.1	—	-0.45
1998.49	6.5	9.0	—	—	—
1998.50	7.7	6.2	5.1	—	-0.43
1998.59	7.3	7.2	—	—	—
1998.60	7.0	6.3	5.7	—	-0.22
1998.61	7.1	6.3	5.7	—	-0.23
1998.99	8.0	6.8	—	—	—
1999.10	6.9	5.5	—	—	—
1999.12	7.6	8.5	—	—	—
1999.13	8.3	8.5	—	—	—
1999.38	7.2	6.1	5.3	—	-0.33
1999.49	9.8	8.9	—	—	—
1999.61	7.5	9.0	—	—	—
1999.98	7.3	7.5	—	—	—
2000.37	7.5	6.0	4.9	—	-0.44
2002.07	9.5	7.3	5.9	—	-0.50
2002.28	—	—	6.3	—	—
2002.36	9.0	7.0	5.8	—	-0.50
2002.47	—	—	6.6	—	—
2002.96	7.2	5.6	4.5	—	—
2003.16	7.9	6.6	5.7	—	-0.35
2003.21	9.1	7.2	5.9	—	-0.46
2003.24	—	—	6.5	6.6	—
2003.36	—	—	5.8	—	—
2004.30	—	—	—	7.2	—
2004.57	—	—	—	6.2	—
2005.23	—	—	—	4.3	—
Means	8.1	7.1	5.9	(6.1)	-0.33

from $R_{\mathrm{NS}} = 1.5$ at 0.4–1.4 GHz to $R_{NS} \approx 3$ in the 23–61 GHz range.

We monitored the emission from the Centaurus A core component at frequencies between 90 and 230 GHz over more than ten years. The core is variable in emission, but over the period 1989–2003, the 90 GHz flux density from the compact core was never below 7 Jy. The spectrum of the quiescent core is relatively flat with α = -0.3. Variability was less at higher frequencies, implying steepening of the continuum spectrum simultaneous with core brightening. During active periods, the emitted flux increases, but the spectral turnover frequency decreases. The nuclear component is optically thick below 45–80 GHz.

It appears that most if not all of the variability is associated with the inner nuclear jet components that have been detected in VLBI measurements, but the mechanism of variability is not yet clear.

acknowledgements

References

Abraham Z., 1996 in: Extragalactic Radio Sources, IAU Symposium 175, R. Ekers et als (eds), p. 25

Abraham Z., Barres de Almeida U., Dominici T.P., & Caproni A., 2007 MNRAS 375, 171

Alvarez H., Aparici J., May J., & Reich P., 2000 A&A 355, 863

Bennett C. L., Bay M., Halpern M., and 12 coauthors, 2003a, ApJ 583, 1

Bennett C. L., Halpern M., Hinshaw G., and 18 coauthors, 2003b, ApJS 148, 1

Bennett C. L., Hill R. S., Hinshaw G., and 13 coauthors, 2003c ApJS 148, 97

Bolton J.G., & Clark B.G., 1960 PASP 72, 29

Botti L.C.L., & Abraham Z., 1993 MNRAS 264, 807

Burns J.O., Feigelson E.D., & Schreier E.J., 1983ApJ 273, 128

Cooper B.F.C., Price R.M, & Cole D.J., 1965 Aust. J. Phys. 18, 589

Combi J.A., & Romero G.E., 1997 A&AS 121, 11

de Mello D.F., & Abraham Z., 1990 Rev. Mex. Astr. Ap. 21, 155

Fogarty W.G., & Schuch N.J., 1975 Nature, 254, 124

Fujisawa K., Inoue M., Kobayashi H., and 10 coauthors, 2000 PASJ 52, 1021

Hawarden T.G., Sanell G., Matthews H.E., et al. 1993 MNRAS 260, 844

Horiuchi S., Meier D.L., Preston R.A., & Tingay S.J., 2006, PASJ 58, 211

Israel F.P., 1998 A&A Rev. 8, 237

Hinshaw G., Weiland J.L., Hill R.S., and 18 coauthors, 2008, ApJS in press, (arXiv:0803.0732)

Junkes N, Haynes R.F., Harnett J.I., & Jauncey D.L, 1993 A&A 269, 29 (erratum 1993 A&A 274, 1009)

Junkes N., Haynes R. F., & Mack K.-H., 1997 Astron. Ges., Abstr. Ser., No. 13, p. 67

Kellerman K.I., Zensus J.A., & Cohen M.H., 1997, ApJL 475, L93

Leeuw L.L., Hawarden H.G., Matthews H.E., Robson E.I., & Eckart A., 2002 ApJ 565, 131

Meier D.L., Jauncey D.L., Prestion R.A., and 20 coauthors, 1989 AJ 98, 27

Meisenheimer K., Tristram K.R.W., Jaffe W., and 11 coauthors, 2007 A&A 471, 453

Mirabel I.F., Laurent O., Sauvage M., 1999 A&A 341, 667

Sheridan K.V., 1958 Austral. J. Phys. 11, 400

Tateyama C.E., & Strauss F.M., 1992 MNRAS 256, 8

Tingay S.J., Jauncey D.L., Reynolds, J.E., and 23 coauthors, 1998 AJ 115, 960

Tingay S.J., & Murphy D.W., 2001 ApJ 546, 210

Tingay S.J., Preston R.A., & Jauncey D.L., 2001 AJ 122, 1697

Tornikoski M., Valtaoja E., Teräsranta H., et al, 1996 A&AS 116, 157

Wiklind T., & Combes F., 1997 A&A 324, 51

Wright E.L., Chen X., Odegard N, and 18 coauthors, 2008, ApJS , submitted (arXiv:0803.0577)

Nederlandse samenvatting

Actieve Galactische Kernen

We weten nu dat er een super-massief zwart gat in het centrum van elk sterrenstelsel aanwezig is. In de meeste sterrenstelsels, bevat het zwarte gat niet veel materiaal en deze worden normale sterrenstelsels genoemd. In bepaalde gevallen, waarschijnlijk als gevolg van een samenvoeging/botsing met een ander sterrenstelsel, verkrijgt het zwarte gat meer en meer massa. Wanneer de materie in het zwarte gat valt, vormt zich een accretie schijf welke zeer efficient is in het converteren van potentiele energie door de zwaartekracht, naar warmte en licht. Als gevolg zijn de centra van deze sterrenstelsels zeer helder en stralen meer energie uit vanuit een gebied ter grootte van het zonnestelsel dan vanuit het gehele sterrenstelsel. De electromagnetische straling vanuit dit gebied varieert vaak sterk. Frequenties van de straling varieert van radio tot Röntgen. Deze sterrenstelsels worden 'actief' genoemd en hun kernen: 'Actieve Galactische Kernen' (engels: Active Galactic Nuclei: AGN)

AGN dierentuin

De eerste AGN werd in 1963 ontdekt. In eerste instantie leek het een gewone ster te zijn maar verscheidene emissielijnen hadden een roodverschuiving van z=0.158, de grootste roodverschuiving ooit gedetecteerd en derhalve het verste object dat bekend was in die tijd. Het was duidelijk dat dit geen normale ster kon zijn, gegeven de enorme afstand van 2 miljard lichtjaar. Het object werd vanaf toen 'quasi stellar object' of quasar genoemd.

We weten natuurlijk nu veel meer over deze mysterieuze en exotische objecten. Het belangrijkste kenmerk van AGN is de grote verscheidenheid van types. Dit heeft geleid tot de term 'AGN dierentuin'. Voorbeelden van de diversiteit zijn

- Verschillen in variabiliteit. Sommige stralen electromagnetische straling uit op een constant niveau, bij anderen kan dit dramatisch wijzigen binnen enkele uren
- Emissie bij verschillende golflengtes. Van sommige AGN worden geen energetische deeltjes zoals Röntgen en UV fotonen gemeten. Anderen laten weer geen radiostraling zien.
- Verschillend gedrag van nucleaire emissie lijnen. Sommige AGN laten brede nucleaire emissie lijnen zien terwijl die bij anderen weer heel nauw zijn.
- Verschillen in morfologie. Bijvoorbeeld, de radio-takken van AGN met radiostraling zijn soms helder aan de randen en soms helder in het centrum.

AGN zijn verdeeld in 2 klasses: Radiostil en radioluid. Radioluide AGN zijn degene waarbij de radiostraling domineert in de lichkracht. Anders worden ze radiostil genoemd. Elke klasse van AGN is verder onderverdeeld in types. Radiostille objecten zijn vooral verdeeld in type 1 en type 2 objecten. Als de lichtkracht van de AGN laag is,

worden ze Seyferts type 1 en 2 genoemd. Wanneer de bolometrische lichkracht van de
AGN hoog is, worden ze type 1 en type 2 quasars genoemd. Voor AGN van het Seyfert
type, is het gast-sterrenstelsel nog duidelijk te zien terwijl dit bij het Quasar type niet
het geval is. Het grootste verschil tussen type 2 en type 1 bronnen is het ontbreken
van Röntgen en UV emissie als ook de brede emissielijnen van het spectrum van type
2 bronnen. Radioluide objecten laten vooral verschillen zien in de morphologie van de
radiotakken en het variabele gedrag van de kern.

AGN bouwblokken:

De belangrijkste componenten waaruit een AGN bestaat, staan hieronder beschreven:
- Accretieschijf. Het invallen van gas in een zwart gat is de meest efficiënte
  methode van energieproductie die we kennen. Het is de energiebron voor AGNs.
  Zwaartekracht zorgt ervoor dat materiaal in de schijf naar binnen spiraliseert
  richting het supermassieve zwarte gat. Het invallend materiaal vormt een schijf.
  Wrijvinig tussen deeltjes in de schijf, die met hele hoge snelheden bewegen, zor-
  gen ervoor dat de schijf straalt. Accretieschijven in AGNs zenden elektromag-
  netische golven uit, die het hele spectrum van radio- tot Röntgen- en gammas-
  traling. Typische bolometrische helderheden van AGNs zijn van de orde van
  grootte van $10^{44} - 10^{47}$ ergs/s.
- Brede lijn regio (BLR). De BLR is een gebied waar emissielijnen waar te nemen
  zijn in het optische licht die breed zijn (>1000 km/s). Het emitterende materiaal
  bevindt zich zeer dicht bij het zwarte gat, aan de rand van de accretieschijf. De
  brede lijnen worden veroorzaakt door de grote rotatiesnelheden van het emit-
  terende materiaal. De BLR is te klein om opgelost te worden in huidige obser-
  vaties. Daardoor is de exacte morfologie van de BLR niet bekend.
- Nauwe lijn regio (NLR). De nauwe lijn regio is een gebied waar nauwe lijnen
  (<1000 km/s) worden waargenomen in het optische en infrarode licht. De NLR
  is orden van grootte groter dan de BLR, afhankelijk van het specifieke object.
  Ten gevolge hiervan kan de morfologie eenvoudig opgelost worden, zelfs met
  kleine spiegeltelescopen, zoals de Hubble ruimtelescoop. Normaliter is de NLR
  kegelvormig en bevat geïoniseerd materiaal. Daarom wordt zij ook wel de ion-
  isatiekegel genoemd.
- Verduisterende torus. Deze component van de AGN is het hoofdonderdeel van
  deze studie. De verduisterende torus is een structuur gemaakt van stofdeeltjes,
  die de accretieschijf en de BLR omgeven. De verduisterende torus absorbeert UV
  fotonen van de accretieschijf, wordt daardoor verhit en zendt de energie uit in
  het infrafood.
- Relativistische jets en lobben. Vaak worden enorme stromen van materiaal waar-
  genomen, die uit het centrum van een AGN komen. De materie vormt een
  nauwe, lineaire stroom, jet genaamd, met deeltjes die met bijna de snelheid van
  het licht bewegen. Het precieze mechanisme om jets te poduceren wordt nog
  niet volledig begrepen. We geloven dat jets uit het binnenste deel van de accreti-
  eschijf komen en dat hun oriëntatie is gekoppeld aan het impulsmoment van
  het binnenste deel van de schijf. Jets zijn vaak groot, typisch enkele kpc. Gi-

gantische opgeblazen lobben zijn dubbele, vaak redelijk symmetrische, ongeveer elliptische structuren aan beide zijden van de actieve kern. Ze zijn typisch enkele tientallen kilometers groot en zenden radiogolven uit. De lobben van een AGN kunnen een aantal keer groter zijn dan het sterrenstelsel.

Unificatie van AGN

AGN unificatie-theorieën proberen AGN-verschijnselen te vereenvoudigen door te suggereren dat de waargenomen verschillen tussen de verschillende AGN-types een gevolg zijn van de orientatie van de AGN ten opzichte van de waarnemer.

In lijn met de onderverdeling tussen radioluide en radiostille AGN zijn er unificatie-modellen voor zowel radiostille als radioluide objecten.

Deze hebben een gemeenschappelijke eigenschap: AGN van een bepaalde klasse zijn in wezen allemaal hetzelfde. Maar omdat het gaat om asymmetrische objecten, hangt hetgeen een waarnemer ziet af van de orintatie van de AGN. De uitstromen ('jets') zijn bijvoorbeeld een duidelijke bron van asymmetrie, en daardoor zou een object waarvan de uitstroom rechtstreeks naar de waarnemer gericht is er anders uitzien, dan een object waarvan de gezichtslijn van de waarnemer haaks op de uitstroomrichting staat.

Voor radiostille AGN, de belangrijkste objecten die in dit proefschrift worden bestudeerd, stelt de unificatie-theorie dat de verschillen tussen type 1 en type 2-objecten (zij het Seyferts of quasars) het resultaat zijn van verschillende orintatie van de waarnemer ten opzichte van de waargenomen 'torus'. Van bovenaf bekeken, dus met het gat naar de waarnemer toe, zouden de accretieschijf (Röntgenstraling) en de BLR waarneembaar moeten zijn, en zal het object geclassificeerd worden als type 1. Als de torus van de zijkant waargenomen wordt, verduistert de torus de accretieschijf en de BLR, en wordt het object geclassificeerd als type 2.

De unificatiemodellen zijn simpel en elegant, maar het is niet zo gemakkelijk om directe bewijzen te vinden die ze ondersteunen. De voornaamste reden is dat AGN erg compact zijn, en dat daardoor de accretieschijf, BLR en de verduisterende torus niet opgelost kunnen worden door conventionele telescopen. Daardoor bleef het bestaan van de verduisterende torus met zijn eigenschappen slechts een veronderstelling, tot een paar jaar geleden. Om direct bewijs te leveren voor de unificatie van type 1- en type 2-objecten moet men het bestaan de een torus-achtige stofverdeling aantonen in Seyferts en quasars. Het doel van dit proefschrift is, om dit te bereiken met behulp van interferometrische waarnemingen met hoge resolutie.

Interferometrie en de V.L.T.I

Interferometrie is het combineren van licht van twee of meer telescopen met als doel om een significante winst te maken in resolutie. Licht van elke telescoop afzonderlijk wordt opgevangen en geleid naar een gemeenschappelijke plaats waar het licht gecombineerd wordt in een interferentie patroon. Dit patroon bevat de informatie van de bron met een resolutie die afhangt van de telescoop configuratie. Als er genoeg waarnemingen van een bron gemaakt worden met een verscheidenheid aan telescoop

configuraties, dan kan het beeld van de bron gevormd worden. Als er slechts enkele telescoopconfiguraties beschikbaar zijn, kunnen met behulp van een model toch de verdeling in de ruimte van de bron bepaald worden. Interferometrie wordt traditioneel geassocieerd met radio-astronomie, waar al sinds decennia met antennes in plaats van telescopen wordt waargenomen, met als voordeel dat de radio golven niet fysiek getransporteerd hoeven te worden naar de combinatieruimte. Interferometrie voor infrarood licht is relatief nieuw, met eerste resultaten uit 2001. De interferometrische waarnemingen die hier gepresenteerd worden zijn verkregen met de Very Large Telescope Interferometer (VLTI), gesitueerd in the Atacama woestijn in het noorden van Chili. De VLTI bestaat uit vier 8.2 meter telescopen en verscheidene 1.8 meter telescopen. Voor het observeren van sterrenstelsels worden de grote telescopen gebruikt, terwijl de kleine telescopen gebruikt worden voor heldere en dichterbij staande objecten zoals sterren. Het licht, verzameld in de telscoop, wordt met spiegels geleid door tunnels onder de grond, waar het uiteindelijk gecombineerd wordt tot een interferentieplaatje die wordt opgeslagen. Er zijn verschillende instrumenten die het licht kunnen combineren en detecteren: Het instrument dat gebruikt wordt in dit werk is MIDI (Mid InfrareD Interferometer), die werkt als een klassieke Michelson interferometer in het infrarood (7-14 um) ?

Dit proefschrift

Dit proefschrift gaat voornamelijk over het gebruik van de ultra-hoge resolutie van interferometrie om informatie te vergaren over de ondoorzichtige torus. Het primaire doel is te bevestigen dat een ondoorzichtig, torus-vormig object aanwezig is in de kern van beide types Seyfert-sterrenstelsels. Vervolgens hopen we limieten te bepalen voor de fysische eigenschappen van de torus, zoals de grootte, temperatuur, verdeling, chemische samenstelling en de relatie tussen de torus en de andere bouwstenen van AGNs. Hieronder volgt een korte beschrijving van elk hoofdstuk.

Hoofdstuk 2

Interferometrische observaties zijn kostbaar en waarneemtijd wordt niet gemakkelijk verstrekt. Daarom moeten we van tevoren bepalen welke objecten de moeite waard zijn om te observeren, gegeven een gelimiteerde waarneemtijd met de interferometer. In dit hoofdstuk gebruiken we de 3.6 meter telescoop in La Silla, Chili, om 21 bronnen waar te nemen die mogelijke interessante doelwitten voor MIDI kunnen zijn. We trachten te bepalen welke bronnen helder genoeg zijn om te worden waargenomen, en voor welke bronnen de mid-infraroodstraling wordt opgelost. In de gevallen dat er structuur zichtbaar is worden afbeeldingen gepresenteerd.

Hoofdstuk 3

In dit hoofdstuk presenteren we waarnemingen van het Seyfert 2 sterrenstelsel NGC 1068. Voor dit object gebruiken we een uitgebreide UV-verdeling bestaande uit 16 verschillende basislijnen, één van de meest uitgebreide interferometrische infraroodwaarnemingen van een extragalactisch object. We lossen de stofstructuur volledig op en verrichten metingen aan belangrijke eigenschappen zoals grootte en temperatuur.

We presenteren ook een afbeelding van de bron op 8 micron, gegenereerd met behulp van maximale entropie beeldreconstructie. We zien dat de stofcomponent (de torus) samenvalt met de reeds bekende maser-schijf en bediscussiren de relatie tussen het stof en de ionisatiekegel. Het stof maakt een hoek van 45 graden ten opzichte van de jet, wat duidt op een gecompliceerde historie van accretie voor dit specifieke object. Vanwege het zijaanzicht van de torus in NGC 1068 kunnen we laten zien dat de opgeloste stofstructuur inderdaad een opgezwollen torus is. In vergelijking met de resultaten voor andere objecten is de waarneming van NGC 1068 het meest overtuigende geval van een ondoorzichtige torus.

Hoofdstuk 4

In dit hoofdstuk presenteren we waarnemingen die de stofverdeling in het Seyfert 1 sterrenstelsel NGC 4151 oplossen. De grootte en temperatuur van de opgeloste structuur zijn vergelijkbaar met die van Seyfert 2 sterrenstelsels, wat een sterke aanwijzing is ten gunste van unificatiemodellen. We voeren een gedetailleerde vergelijking uit tussen onze resultaten en interferometrische waarnemingen op kortere golflengtes en concluderen dat de onopgeloste bron in deze laatste waarnemingen geen voortzetting kan zijn van de opgeloste structuur die wordt waargenomen door MIDI. We detecteren het silicaat-kenmerk in emissie, zij het marginaal, en bediscussiren hoe de afgeleide grootte en temperatuur voor deze bron passen binnen de unificatiemodellen.

Hoofdstuk 5

In hoofdstuk 5 presenteren we waarnemingen van de quasar 3C 273. Deze bron is uniek binnen onze selektie, omdat dit een verafgelegen object is. Dit staat ons toe om de voorspellingen van de unificatiemodellen te toetsen op een zeer helder object op hoge roodverschuiving en om de resultaten voor dit object te vergelijken met die voor nabije AGNs. We nemen een opgeloste, uitgerekte structuur waar in de kern van 3C 273. De grootte van de structuur is consistent met de door unificatiemodellen voorspelde grootte van de stof-torus. Vergelijkbaar met NGC 4151 detecteren we ook hier het 10 micron silicaat-kenmerk in emissie, zij het marginaal. Deze waarnemingen tonen voor de eerste keer de opgeloste emissie van het stof in the centrum van een quasar op hoge roodverschuiving en leveren het eerste directe bewijs dat unificatie ook geldig blijft voor dit type objecten.

Hoofdstuk 6

In dit hoofdstuk presenteren we waarnemingen van een selektie van 10 Seyfert stelsels, een combinatie van beide soorten Seyfert sterrenstelsels. Voor elke bron hebben we één en drie UV-punten verkregen, waarmee we kunnen zien of het doelwit is opgelost en waarmee we basale eigenschappen kunnen meten zoals de grootte van de mid-IR emissiegebieden. Voor zeven van de tien waargenomen objecten zijn afmetingen of limieten van afmetingen bepaald van het door de AGN verwarmd stof. In deze gevallen zien we dat de grootte van het mid-IR emissiegebied in de orde van parsecs is. Verder zien we dat de afgeleide grootte grofweg schaalt met de wortel van de AGN

helderheid. Het 10 micron silicaat-kenmerk wordt marginaal gedetecteerd in emissie of absorptie.

Hoofdstuk 7

In dit hoofdstuk we onze aandacht weg van de ondoorzichtige torus, in de richting van milimeter en radio emissie afkomstig van de jet. Zijn alleen publiek toegankelijke gegevens gebruikt, inclusief WMAP metingen die zijn verzameld voor het bepalen van eigenschappen van de microgolf achtergrondstraling. In dit hoofdstuk gebruiken we de WMAP metingen om het radioemissie-mechanisme van FR-I AGN NGC 5128 (Centaurus A) te bestuderen. We bepalen het centimeter en milimeter continuum spectrum voor de gehele Centaurus A radiobron, en meten op frequenties tussen 86 GHz (3.5 mm) en 345 GHz (0.85 mm) de continuum emissie van de kern van het actieve radiostelsel op verschillende tijdstippen tussen 1989 en 2005. De gegevens laten zien dat het integrale radiospectrum steiler wordt bij frequencies boven de 5 GHz. De zuidwestelijke buitenste lob heeft een steiler spectrum dan het noordoostelijke middendeel en buitenste lob. De milimeter-emissie van de kern van Centaurus A is variabel, een variabiliteit die aanzienlijk beter correleert met 20-200 keV Röntgen-variabiliteit dan met 2 - 10 keV variabiliteit. In de niet-actieve toestand heeft de kern een spectrale index die steiler wordt naarmate de kern helderder is. De variabiliteit lijkt het meest samen te hangen met de binnenste nucleare jet-componenten die middels VLBI metingen zijn gedetecteerd. De meest dichte nucleaire componenten zijn optisch dik beneden de 45-80 GHz. Dit hoofdstuk is een voorbeeld van hoe bestaande, publiek toegankelijke gegevens kunnen worden gebruikt om resultaten te verkrijgen in een ander deel van de sterrenkunde dan waarvoor de gegevens oorspronkelijk bedoeld waren.

Acknowledgements

Four years is a long time, and during this time I learned many lessons, not all of them related to Astronomy. This has been a transforming time for myself. Being around so many talented people at the observatory have made me get to know myself better, my strengths and weaknesses, and get a much clearer idea of what I would like to do with my life than I had before. There are also many lessons to be learned from being a foreigner, living in a country where things are done in a different manner than what I have learned to take for granted. The biggest challenge I have encountered during these four years was the solitary nature of the work, and I would like to thank Rob Wiersma, Simon Albrecht and Martin Depken for their pleasant companionship, which helped a great deal.

This work could not have been completed in time without the help of many people, who have made every effort to allow me to do my work without interruption. First, I would like to thanks the human resource department and in particular Nori Poppeliers for getting my papers right with the local authorities and for the quick action they have taken whenever I needed them. The people at the Leiden Observatory are the friendliest people I have ever encountered in any working environment. Thanks for the computer support group, David Jansen and Tycho Bot, who have been extremely efficient in solving my computer problems. I thank Jan Lub for fixing up all the financial issues with a minimum of fuss for myself. Last but not least many thanks to Hilke Reckman, Marcel Haas, Eric Laan, Amir Vosteen, Liesbeth Vermaas, Huib intema and Freeke van de Voort for helping me with the Dutch summary.

But most of all, I would like to thank my parents, Ellen and Erez. I dedicate this thesis to them.

Curriculum vitae

I WAS born on February 4, 1976 in Petah-Tikva, Israel. From an early age, I have been fascinated by the workings on the world. Born to a mother who was one of the first women to ever study physics in Israel in the later sixties, I was often given books to read about scientific discoveries which have had an influence on me all my life.

After finishing my three years as a soldier, I travelled as a backpacker in Asia for a year, a journey that has had a deep influence over my outlook on life. In 1999 I started studying Physics in the Hebrew university of Jerusalem. After graduating in 2002 I started doing my Master's degree. In 2003 I moved to Tel Aviv University, where I completed my degree in 2005. During my time as a student I was also very busy with political and human rights work. Mainly advocating for the recognition of the freedom of conscience in Israel, and futilely working towards ending the occupation.

In 2005 I moved to the Netherlands and begun my PhD under the supervision of Dr. Walter Jaffe and Prof. Huub Röttgering. I am currently working for the Netherlands organisation for applied scientific research (TNO), as innovator.